Dissertation

submitted to the

Combined Faculty of Mathematics,
Engineering and Natural Sciences

of

Heidelberg University, Germany

for the degree of

Doctor of Natural Sciences

Put forward by

Gergana Dimitrova Borisova

born in Novi pazar (Bulgaria)

Oral examination:
16 January 2024

CONTROLLING TWO-ELECTRON SYSTEMS IN THEIR EXCITED STATE BY AN INTENSE LASER FIELD:

STRONG-FIELD IONIZATION OF ATOMIC HELIUM
&
WAVE-PACKET MANIPULATION IN MOLECULAR HYDROGEN

REFEREES:

Prof. Dr. Thomas Pfeifer

Prof. Dr. Selim Jochim

Controlling two-electron systems in their excited state by an intense laser field: Strong-field ionization of atomic helium & Wave-packet manipulation in molecular hydrogen

In this work fundamental light–matter interaction is studied in excited-state two-electron systems under the influence of an intense laser field in two respects: First, motivated by the results of a numerical simulation on the role of initial-state electron correlation for the ionization process, strong-field ionization out of selectively prepared doubly excited states (DESs) in helium is studied in a two-colour extreme ultraviolet (XUV)–infrared (IR) experiment using a reaction microscope (REMI). Detected recoil-ion and photoelectron momentum distributions help to identify a variety of different IR-induced ionization pathways for both single and double ionization out of different DESs as the initial state for strong-field interaction. Turning the focus from the atomic to the molecular two-electron system, in the second study, a novel all-optical approach enables visualisation of the dynamics of a vibrational wave packet in an electronically excited state of neutral H_2 through molecular self-probing by the ground state encoded in the reconstructed time-dependent dipole response of the excited system from XUV spectroscopy data. In a pump–control scheme, an additional interaction with a 5-fs near-infrared (NIR) pulse of adjustable intensity modifies the vibrational wave-packet revival. The adoption of an impulsive control mechanism together with state-resolved extraction of the accumulated strong-field induced phases leading to the observed revival shift brings access to state-dependent polarizability of different vibronic states in the excited wave packet. In future, both experimental approaches can be applied to multi-electron systems to study and control correlation in specifically prepared excited quantum systems.

Kontrolle von Zwei-Elektronen-Systemen in derem angeregten Zustand durch ein intensives Laserfeld: Starkfeldionisation von atomarem Helium & Wellenpaket-Manipulation in molekularem Wasserstoff

In dieser Arbeit wird die fundamentale Licht-Materie-Wechselwirkung in Zwei-Elektronen-Systemen in ihrem angeregten Zustand unter dem Einfluss eines intensiven Laserfeldes in zweierlei Hinsicht untersucht: Erstens, motiviert durch die Ergebnisse einer numerischen Simulation zur Rolle der Anfangszustandselektronenkorrelation für den Ionisationsprozess, wird die Starkfeldionisation aus selektiv präparierten doppelt angeregten Zuständen (DESs) in Helium in einem zweifarbigen Extrem-Ultraviolett (XUV)-Infrarot (IR)-Experiment unter Verwendung eines Reaktionsmikroskops (REMI) untersucht. Die detektierten Impulsverteilungen von Rückstoß-Ionen und Photoelektronen helfen bei der Identifizierung einer Vielzahl verschiedener IR-induzierter Ionisierungspfade sowohl für die Einzel- als auch für die Doppelionisation aus verschiedenen DESs als Ausgangszustand für die Starkfeldwechselwirkung. In der zweiten Studie wird der Schwerpunkt vom atomaren auf das molekulare Zwei-Elektronen-System verlagert. Ein neuartiger rein optischer Ansatz ermöglicht die Visualisierung der Dynamik eines Vibrationswellenpakets in einem elektronisch angeregten Zustand von neutralem H_2 durch molekulares Self-Probing durch den Grundzustand, kodiert in der aus XUV-Spektroskopiedaten rekonstruierten zeitabhängigen Dipolantwort des angeregten Systems. In einem Pump-Kontroll-Schema modifiziert eine zusätzliche Wechselwirkung mit einem 5-fs-Nahinfrarotimpuls (NIR) mit einstellbarer Intensität den Revival des Vibrationswellenpakets. Die Annahme eines impulsiven Kontrollmechanismus in Verbindung mit einer zustandsaufgelösten Extraktion der akkumulierten, durch das starke Feld induzierten Phasen, die zu der beobachteten Revivalverschiebung führen, ermöglicht den Zugang zu der zustandsabhängigen Polarisierbarkeit der verschiedenen vibronischen Zustände im angeregten Wellenpaket. In Zukunft können beide experimentellen Ansätze auf Mehrelektronensysteme angewendet werden, um die Korrelation in speziell präparierten angeregten Quantensystemen zu untersuchen und zu kontrollieren.

LIST OF PUBLICATIONS

Parts of this work have been published or prepared in the following articles:

- Gergana D. Borisova, Paula Barber Belda, Shuyuan Hu, Paul Birk, Veit Stooß, Maximilian Hartmann, Daniel Fan, Robert Moshammer, Alejandro Saenz, Christian Ott and Thomas Pfeifer
  Laser control of an excited-state vibrational wave packet in neutral H_2
  arXiv:2301.03908 (2023). For more information see [1].

- Gergana D. Borisova, Veit Stooß, Andreas Dingeldey, Andreas Kaldun, Thomas Ding, Paul Birk, Maximilian Hartmann, Tobias Heldt, Christian Ott and Thomas Pfeifer
  Strong-field-induced single and double ionization dynamics from single and double excitations in a two-electron atom
  Journal of Physics Communications **4,** 055012 (2020). For more information see [2].

- Veit Stooß, Maximilian Hartmann, Paul Birk, Gergana D. Borisova, Thomas Ding, Alexander Blättermann, Christian Ott and Thomas Pfeifer
  XUV-beamline for attosecond transient absorption measurements featuring a broadband common beam-path time-delay unit and in situ reference spectrometer for high stability and sensitivity
  Review of Scientific Instruments **90,** 053108 (2019). For more information see [3].

Further publications with own contributions:

- Tobias Heldt, Jonathan Dubois, Paul Birk, Gergana D. Borisova, Gabriel M. Lando, Christian Ott and Thomas Pfeifer
  Attosecond Real-Time Observation of Recolliding Electron Trajectories in Helium at Low Laser Intensities
  Phys. Rev. Lett. **130,** 183201 (2023). For more information see [4].

- Michael Straub, Thomas Ding, Marc Rebholz, Gergana D. Borisova, Alexander Magunia, Hannes Lindenblatt, Severin Meister, Florian Trost, Yimeng Wang, Steffen Palutke, Markus Braune, Stefan Düsterer, Rolf Treusch, Chris H. Greene, Robert Moshammer, Thomas Pfeifer and Christian Ott

Differential Measurement of Electron Ejection after Two-Photon Two-Electron Excitation of Helium
Phys. Rev. Lett. **129,** 183204 (2022). For more information see [5].

- Maximilian Hartmann, Lynda Hutcheson, Gergana D. Borisova, Paul Birk, Shuyuan Hu, Andrew C. Brown, Hugo W. van der Hart, Christian Ott and Thomas Pfeifer
Core-resonance line-shape analysis of atoms undergoing strong-field ionization
Journal of Physics B: Atomic, Molecular and Optical Physics **55,** 245601 (2022). For more information see [6].

- Marc Rebholz, Thomas Ding, Lennart Aufleger, Maximilian Hartmann, Kristina Meyer, Veit Stooß, Alexander Magunia, David Wachs, Paul Birk, Yonghao Mi, Gergana D. Borisova, Carina da Costa Castanheira, Patrick Rupprecht, Maia Magrakvelidze, Uwe Thumm, Sebastian Roling, Marco Butz, Helmut Zacharias, Stefan Düsterer, Rolf Treusch, Günter Brenner, Christian Ott and Thomas Pfeifer
XUV-Initiated Dissociation Dynamics of Molecular Oxygen (O_2)
The Journal of Physical Chemistry A **125,** 10138–10143 (2021). For more information see [7].

- Marc Rebholz, Thomas Ding, Victor Despré, Lennart Aufleger, Maximilian Hartmann, Kristina Meyer, Veit Stooß, Alexander Magunia, David Wachs, Paul Birk, Yonghao Mi, Gergana D. Borisova, Carina da Costa Castanheira, Patrick Rupprecht, Georg Schmid, Kirsten Schnorr, Claus Dieter Schröter, Robert Moshammer, Zhi-Heng Loh, Andrew R. Attar, Stephen R. Leone, Thomas Gaumnitz, Hans Jakob Wörner, Sebastian Roling, Marco Butz, Helmut Zacharias, Stefan Düsterer, Rolf Treusch, Günter Brenner, Jonas Vester, Alexander I. Kuleff, Christian Ott and Thomas Pfeifer
All-XUV Pump-Probe Transient Absorption Spectroscopy of the Structural Molecular Dynamics of Di-iodomethane
Phys. Rev. X **11,** 031001 (2021). For more information see [8].

- Thomas Ding, Marc Rebholz, Lennart Aufleger, Maximilian Hartmann, Veit Stooß, Alexander Magunia, Paul Birk, Gergana D. Borisova, David Wachs, Carina da Costa Castanheira, Patrick Rupprecht, Yonghao Mi, Andrew R. Attar, Thomas Gaumnitz, Zhi-Heng Loh, Sebastian Roling, Marco Butz, Helmut Zacharias, Stefan Düsterer, Rolf Treusch, Arvid Eislage, Stefano M. Cavaletto, Christian Ott and Thomas Pfeifer
Measuring the frequency chirp of extreme-ultraviolet free-electron laser pulses by transient absorption spectroscopy
Nature Communications **12,** 643 (2021). For more information see [9].

- Thomas Ding, Marc Rebholz, Lennart Aufleger, Maximilian Hartmann, Veit Stooß, Alexander Magunia, Paul Birk, Gergana D. Borisova, Carina da Costa Castanheira, Patrick Rupprecht, Yonghao Mi, Thomas Gaumnitz, Zhi-Heng Loh, Sebastian Roling, Marco Butz, Helmut Zacharias, Stefan Düsterer, Rolf Treusch, Christian Ott and Thomas Pfeifer
  XUV pump–XUV probe transient absorption spectroscopy at FELs
  Faraday Discuss. **228,** 519-536 (2021). For more information see [10].

- Veit Stooß, Paul Birk, Alexander Blättermann, Maximilian Hartmann, Gergana D. Borisova, Christian Ott and Thomas Pfeifer
  Strong-field-gated buildup of a Rydberg series
  Phys. Rev. Res. **2,** 032041 (2020). For more information see [11].

- Paul Birk, Veit Stooß, Maximilian Hartmann, Gergana D. Borisova, Alexander Blättermann, Tobias Heldt, Klaus Bartschat, Christian Ott and Thomas Pfeifer
  Attosecond transient absorption of a continuum threshold
  Journal of Physics B: Atomic, Molecular and Optical Physics **53,** 124002 (2020). For more information see [12].

- Christian Ott, Lennart Aufleger, Thomas Ding, Marc Rebholz, Alexander Magunia, Maximilian Hartmann, Veit Stooß, David Wachs, Paul Birk, Gergana D. Borisova, Kristina Meyer, Patrick Rupprecht, Carina da Costa Castanheira, Robert Moshammer, Attar, Andrew R., Thomas Gaumnitz, Zhi-Heng Loh, Stefan Düsterer, Rolf Treusch, Joachim Ullrich, Yuhai Jiang, Michael Meyer, Peter Lambropoulos and Thomas Pfeifer
  Strong-Field Extreme-Ultraviolet Dressing of Atomic Double Excitation
  Phys. Rev. Lett. **123,** 163201 (2019). For more information see [13].

- Thomas Ding, Marc Rebholz, Lennart Aufleger, Maximilian Hartmann, Kristina Meyer, Veit Stooß, Alexander Magunia, David Wachs, Paul Birk, Yonghao Mi, Gergana D. Borisova, Carina da Costa Castanheira, Patrick Rupprecht, Zhi-Heng Loh, Andrew R. Attar, Thomas Gaumnitz, Sebastian Roling, Marco Butz, Helmut Zacharias, Stefan Düsterer, Rolf Treusch, Stefano M. Cavaletto, Christian Ott and Thomas Pfeifer
  Nonlinear Coherence Effects in Transient-Absorption Ion Spectroscopy with Stochastic Extreme-Ultraviolet Free-Electron Laser Pulses
  Phys. Rev. Lett. **123,** 103001 (2019). For more information see [14].

Contents

1 INTRODUCTION

Physics as a word to describe "the scientific study of matter and energy and the relationships between them" has its origin in the Greek word *φυσική*, meaning "natural things" [15]. As the definition claims, the key subject in physics is the study of matter, or the "physical substance that everything in the world is made of" [16]. In the same lines, this thesis investigates quantum matter under the influence of external electromagnetic fields, aiming at understanding the structure and properties of the matter of interest and especially the possibilities to influence and even control those by the applied *light* fields.

With the invention of the first lasers [17, 18] two different directions in studies of light–matter interaction with fully coherent light emerged. On the one side, the development of highly stable laser sources with precisely defined narrow bandwidth has made possible high-resolution spectroscopy for the operation of atomic clocks, defining standards for frequency and through this also time [19]. On the other side, laser sources with ever decreasing pulse duration [20–24] have enabled tracking quantum dynamics in atoms and molecules on the natural timescales of the involved processes, all faster than nanoseconds, while also opening the way for studies of non-linear light–matter interaction, for which the short high-energy laser pulsed radiation is necessary.

The relevant timescales in quantum dynamics start at the level of picoseconds ($1\,\mathrm{ps} = 10^{-12}\,\mathrm{s}$), which is fast enough to follow molecular rotation, while even shorter pulse duration in the femtosecond regime ($1\,\mathrm{fs} = 10^{-15}\,\mathrm{s}$) is required to resolve molecular-bond dynamics. Here, ultrashort mode-locked lasers [20–24] have provided the temporal resolution for time-resolved investigation of chemical reactions in the field of femtochemistry [25] introducing the concept of quantum control in pump–probe spectroscopy studies [26]. The attosecond domain, however, ($1\,\mathrm{as} = 10^{-18}\,\mathrm{s}$), in which electronic processes evolve, remained out of reach until the discovery of high-order harmonic generation (HHG) [27–29], providing coherent broadband extreme ultraviolet (XUV) radiation in the form of attosecond pulse trains [30] or even isolated attosecond pulses [31]. The field of attosecond science aiming at real-time control of the electron motion in matter [32] was born.

In parallel, synchrotron facilities and their advanced version, free-electron lasers (FELs), have also developed to deliver XUV radiation with small bandwidth. While synchrotron light is not coherent, the radiation delivered by FELs is partially coherent, allowing pulse duration down to the femtosecond regime, thus fast enough for

studies of ultrafast dynamics. Additionally, FEL XUV radiation can reach high intensities in the XUV, which in contrast to HHG-based XUV light, restricted to the perturbative regime of light–matter interaction, can induce non-linear interactions in the studied quantum systems.

Extreme ultraviolet radiation for the excitation of matter from free-electron lasers as well as from high-harmonic generation has been used in the experimental studies, discussed in this thesis. In the two presented experiments the XUV sources have been utilised as a pump for the preparation of the studied systems, atomic helium and molecular hydrogen, in an excited state. The narrowband free-electron radiation allows for the selective excitation of specific doubly excited states in helium, while the broad XUV spectrum of the (nearly) isolated attosecond pulse excites a multitude of states, thus forming a molecular vibrational wave packet in an electronically excited state of neutral H_2. Having the initial state of interest prepared, an additional interaction with a moderately strong field (i.e. barely or not ionizing or changing the neutral system in its ground state, but very much influencing the excited state under investigation) is introduced as a control over the final state after interaction. In the case of helium, the IR pulse ionizes the system out of the specifically excited state, which allows to study the role of the initial-state electron correlation in strong-field ionization, as discussed in chapter 5, presenting the results of this project. In the H_2 study the dynamics of the excited molecular vibrational wave packet is visualised through the time-dependent electronic dipole reconstructed from XUV absorption spectra, while the few-fs short NIR field just impulsively changes the wave-packet's evolution without destroying it, thus allowing for control over the studied molecular vibration.

Structured around those two experiments, this thesis first introduces the fundamental concepts in light–matter interaction between classical light and quantum matter in chapter 2, distinguishing between the perturbation case and the strong-field interaction case, where both absorption and ionization are discussed. The focus is then shifted to the two-electron systems under study, presented in sections 2.2.1 and 2.2.2, respectively. Chapter 3 then introduces the laser sources employed for both presented experiments, while also delivering information on the basics of ultrashort laser pulses, as well as the working principles of free-electron lasers and high-harmonic generation. Not only different light sources are used in the two experiments, but also two complimentary in their concept experimental setups, both presented in chapter 4. While in the case of He the target is ionized, thus an apparatus for the detection of ionization products, here a reaction microscope (REMI) introduced in section 4.1, is required, the excited vibrating H_2 molecule remains intact after the interaction process and the bound-state dynamics is accessed in an XUV time-domain absorption spectroscopy setup, section 4.2. The next two chapters present both experimental studies, giving details on the experiments and the data evaluation procedure before presenting the results, either motivated by or compared to model simulations. Here, chapter 5 elaborates on strong-field ionization of the FEL-prepared doubly excited states in the helium atom, whereas in chapter 6

laser control over a vibrational wave packet in the hydrogen molecule is demonstrated. The final chapter 7 provides a summary of the findings in both studies of light–matter interaction.

2 CLASSICAL LIGHT AND QUANTUM MATTER

This chapter aims to bring an insight into the key physical concepts addressed throughout this thesis, all centred around light–matter interaction. The light fields are treated throughout classically, while matter is considered to be fully quantised in the adopted semiclassical formalism, section 2.1.1. Different photoabsorption and photoionization processes are discussed in the context of perturbation theory, section 2.1.2, and in the strong-field limit in section 2.1.4.5, as well as from the macroscopic perspective 2.1.3. Those types of processes are studied in the benchmark two-electron systems – atomic helium and molecular hydrogen, where the presence of two interacting electrons opens possibilities to the occurrence of dynamics not otherwise observed in single-active electron systems. Relevant structural details of both systems under investigation are presented in section 2.2. While the ionization process is characterised by ion yields and photoelectron momentum distributions, the absorption process is best studied in spectroscopy experiments able to detect changes of the observed absorption Beutler-Fano resonance line shapes discussed in section 2.3.

2.1 Light–matter interactions

The subject of this thesis is the investigation of matter under the influence of external electromagnetic *light* fields, which makes the following discussion of light–matter interaction unavoidable.

2.1.1 Semiclassical description

Two systems of matter are studied throughout this thesis - atomic helium and molecular hydrogen, both in the gas phase. Both systems are considered quantum and are treated in the scope of quantum mechanics. The involved light sources interacting with the quantum matter, on the other side, are classical and can be entirely described using classical electrodynamics. Therefore, all quantum-mechanical considerations throughout this thesis are semiclassical.

2.1.1.1 Classical light fields

Classical light fields can be fully described using classical electrodynamics with Maxwell's equation at its heart, from which also the wave equation can be derived:

$$\nabla^2 u - \frac{1}{c^2}\frac{\partial^2 u}{\partial t^2} = 0. \tag{2.1}$$

Its solutions u are possible optical waves describing electromagnetic radiation. The simplest solution of the wave equation (2.1) is a monochromatic wave with harmonic time dependence,

$$u(\mathbf{r},t) = \tilde{u}(\mathbf{r})\cos(\omega t + \phi(\mathbf{r})), \tag{2.2}$$

with the (in general) position-dependent amplitude $\tilde{u}(\mathbf{r})$ and phase $\phi(\mathbf{r})$ of the wave having an angular frequency $\omega = 2\pi\nu$.

Since complex-valued functions are mathematically easy to work with, it is convenient to represent the real wave function $u(\mathbf{r},t)$, being an observable in the real world, in terms of a complex function

$$U(\mathbf{r},t) = \tilde{u}(\mathbf{r})\exp^{i(\omega t+\phi(\mathbf{r}))}, \tag{2.3}$$

such that the monochromatic wave in Eq. (2.2) is restored through taking the real part of expression (2.3):

$$u(\mathbf{r},t) = \Re\mathrm{e}U(\mathbf{r},t) = \frac{1}{2}[U(\mathbf{r},t) + U^*(\mathbf{r},t)]. \tag{2.4}$$

Here, $U(\mathbf{r},t)$ is known as the complex wave function and completely describes the wave. It also satisfies the wave equation. Defining the complex-valued position-dependent amplitude of $U(\mathbf{r},t)$ as

$$U(\mathbf{r}) = \tilde{u}(\mathbf{r})\exp^{i\phi(\mathbf{r})} \tag{2.5}$$

and rewriting Eq. (2.3), one arrives at the Helmholtz equation:

$$\nabla^2 U + k^2 U = 0, \tag{2.6}$$

with the definition of the wavenumber $k = \omega/c$. The choice of boundary conditions leads to different solutions of the Helmholtz equation, with the simplest being a plane wave and a spherical wave [33].

For the purpose to describe the fundamental principles of light–matter interaction, it is sufficient to consider monochromatic plane waves with the electric field vector $\boldsymbol{F}(\boldsymbol{r},t))$ given through the expression

$$\boldsymbol{F}(\boldsymbol{r},t)) = \frac{i}{2}F_0\left(\boldsymbol{e}\mathrm{e}^{i(\boldsymbol{k}\boldsymbol{r}-\omega t)} - \boldsymbol{e}^*\mathrm{e}^{-i(\boldsymbol{k}\boldsymbol{r}-\omega t)}\right), \tag{2.7}$$

where F_0 is the field amplitude, $\boldsymbol{e}$ the unit polarization vector and $\boldsymbol{k}$ the wave vector, with the previously defined wavenumber being its amplitude. The optical intensity of the field is given through the square of the field amplitude

$$I = \frac{1}{2}\epsilon_0 c F_0^2. \tag{2.8}$$

2.1.1.2 Quantum matter

Matter, on the other side, is treated fully quantum-mechanically and its stationary states $\psi_n(\boldsymbol{r})$ are eigenvectors of the time-independent Schrödinger equation

$$\hat{\mathcal{H}}_0 \psi_n(\boldsymbol{r}) = E_n \psi_n(\boldsymbol{r}), \tag{2.9}$$

where $\hat{\mathcal{H}}_0$ is the stationary Hamilton operator and E_n the eigenenergies belonging to each of the stationary states. Their time evolution is found as a solution of the time-dependent Schrödinger equation (TDSE)

$$i\hbar \frac{\partial}{\partial t} \psi_n(\boldsymbol{r}, t) = \hat{\mathcal{H}}_0 \psi_n(\boldsymbol{r}, t), \tag{2.10}$$

leading to the time-propagation of a state, given by

$$\psi_n(\boldsymbol{r}, t) = \mathrm{e}^{-\frac{i}{\hbar} E_n t} \psi_n(\boldsymbol{r}, t = 0) = \mathrm{e}^{-i\omega_n t} \psi_n(\boldsymbol{r}) \tag{2.11}$$

with $E_n = \hbar\omega_n$.

An arbitrary time-dependent wave packet describing the free system is then a linear superposition of all possible states

$$\Psi(\boldsymbol{r}, t) = \sum_{n=0}^{\infty} c_n(t) \mathrm{e}^{-i\omega_n t} \psi_n(\boldsymbol{r}), \tag{2.12}$$

where $c_n(t)$ are the time-dependent probability amplitudes of the states $\psi_n(\boldsymbol{r})$ with the population probability of the state given by the square of the coefficients $c_n(t)$

$$w_n(t) = |c_n(t)|^2. \tag{2.13}$$

2.1.2 Time-dependent perturbation theory

In the semiclassical approximation light–matter interaction can be treated in the context of time-dependent perturbation theory. The following discussion closely follows [34] and [35].

Time-dependent perturbation theory is applicable whenever the total Hamiltonian of the system can be represented as a sum of the stationary Hamiltonian of the

unperturbed system $\hat{\mathcal{H}}_0$ and a small time-dependent perturbation $\hat{\mathcal{H}}'(t)$:

$$\hat{\mathcal{H}}(t) = \hat{\mathcal{H}}_0 + \hat{\mathcal{H}}'(t). \tag{2.14}$$

Here, the perturbation has a general time dependence but can typically be given in relation to the time-dependent electric field $\boldsymbol{F}(\boldsymbol{r},t)$, as for example in the length gauge of the dipole approximation. Considering a wave packet of states as an *ansatz* for the solution of the TDSE corresponding to the time-dependent Hamiltonian, in the bra-ket notation, which explicitly shows the orthogonality of the included states, the time-dependent wave-function takes the form

$$|\Psi(t)\rangle = \sum_n c_n(t) \mathrm{e}^{-i\omega_n t} |\psi_n\rangle . \tag{2.15}$$

The TDSE to be solved then reads

$$i\hbar \frac{\partial}{\partial t} |\Psi(t)\rangle = \left[\hat{\mathcal{H}}_0 + \hat{\mathcal{H}}'(t)\right] |\Psi(t)\rangle . \tag{2.16}$$

Evaluating Eq. (2.16) after insertion of expression (2.15) and making use of the orthogonality of the states $|\psi_n\rangle$, one arrives to a set of linear differential equations for the time-dependent coefficients $c_n(t)$

$$\frac{\mathrm{d}c_b(t)}{\mathrm{d}t} = -\frac{i}{\hbar} \sum_n c_n(t) \langle \psi_b | \hat{\mathcal{H}}'(t) | \psi_n \rangle \mathrm{e}^{i\omega_{bn}t}, \tag{2.17}$$

with the angular transition frequency $\omega_{bn} = (E_b - E_n)/\hbar$.

Making use of the fact that the perturbation is small, in 0-th order, the initial conditions will change very slightly, such that the population of the initial state a will remain the same for all times, i.e. $c_a^{(0)}(t) = 1$ and all other coefficients will vanish, $c_a^{(n)}(t) = 0$ for all $n \neq a$. This leads to

$$\frac{\mathrm{d}c_b(t)}{\mathrm{d}t} = -\frac{i}{\hbar} \langle \psi_b | \hat{\mathcal{H}}'(t) | \psi_a \rangle \mathrm{e}^{i\omega_{ba}t}. \tag{2.18}$$

For an interaction starting at time $t = 0$, the time-dependent transition amplitude in 1-st order perturbation theory is given by

$$c_b(t) = -\frac{i}{\hbar} \int_0^t \langle \psi_b | \hat{\mathcal{H}}'(t') | \psi_a \rangle \mathrm{e}^{i\omega_{ba}t'} \mathrm{d}t' \tag{2.19}$$

and the full solution in first order takes the form

$$|\Psi(t)\rangle \approx \mathrm{e}^{-i\omega_a t} |\psi_a\rangle + \sum_{n\neq a} c_n(t) \mathrm{e}^{-i\omega_n t} |\psi_n\rangle , \tag{2.20}$$

while higher-order solutions can be obtained iteratively.

Photoabsorption and photoemission naturally arise in time-dependent perturbation theory, when the time-dependent perturbation is specified through a perturbation amplitude dependent on an acting electromagnetic field as eF_0, and a transition operator $\hat{\mathbf{T}}$ with $\hat{T}_{ba} = \langle\psi_b|\hat{\mathbf{T}}|\psi_a\rangle$, where typically the transition dipole operator is considered.

One-photon interaction

The time-dependent transition amplitude in 1st order perturbation theory then becomes

$$c_b(t) = \frac{eF_0}{2\hbar}\int_0^t \left(\hat{T}_{ba}\mathrm{e}^{i(\omega_{ba}-\omega)t'} - \hat{T}^\dagger_{ba}\mathrm{e}^{i(\omega_{ba}+\omega)t'}\right)\mathrm{d}t' \tag{2.21}$$

$$= \frac{eF_0}{2\hbar}\left(\frac{\hat{T}_{ba}\mathrm{e}^{i(\omega_{ba}-\omega)t}}{i(\omega_{ba}-\omega)} - \frac{\hat{T}^\dagger_{ba}\mathrm{e}^{i(\omega_{ba}+\omega)t}}{i(\omega_{ba}+\omega)}\right)\mathrm{d}t'. \tag{2.22}$$

The two terms lead to significant contribution only in the cases $\omega_{ba} \mp \omega \approx 0$, since otherwise the exponential functions oscillate rapidly and disappear taking the limit $t \to \infty$. Because the angular frequency of the electromagnetic field is defined positive, $\omega > 0$, the first term in Eq. (2.21) describes absorption and the second emission of a single photon:

$$\text{absorption} \quad b \leftarrow a: \quad \omega_{ba} > 0 \tag{2.23}$$

$$\text{emission} \quad a \leftarrow b: \quad \omega_{ba} < 0. \tag{2.24}$$

The transition probability to state b from state a scales linearly with the laser-field intensity, since

$$R_{ba}(t) = |c_b(t)|^2 \propto F_0^2 \propto I. \tag{2.25}$$

Multi-photon interaction

The computation of the N-photon transition probability requires insertion of the one-photon solution from Eq. (2.21) on the right hand side of Eq. (2.19) iteratively N times. The obtained solution is valid for a transition from state $|\psi_a\rangle$ to state $|\psi_b\rangle$ in a quantum system S requiring N photons to become resonant:

$$\mathrm{S}(|\psi_a\rangle) + N\hbar\omega \to \mathrm{S}(|\psi_b\rangle). \tag{2.26}$$

The N-photon transition rate then becomes proportional to the N-th power of the laser intensity I:

$$R^{(N)}_{ba}(t) = \sigma^{(N)}_{ba}\Phi^N \propto I^N, \tag{2.27}$$

with the generalised cross section $\sigma^{(N)}_{ba}$ and the photon flux $\Phi = I/(\hbar\omega)$. Because of the exponential scaling, N-photon processes become possible for higher intensities.

2.1.3 Absorption in atoms and molecules

While the previous section discussed absorption in quantum systems in time-dependent perturbation theory from the state-perspective, the following discussion looks at absorption as a process occurring in a macroscopic system consisting of many atoms or molecules of the same kind. If a considerable amount of atoms or molecules in the target system absorb light with the same photon energy, then the transmitted light spectrum would lack photons at a specific position in the spectrum. The dips of the spectrum are called resonances and since they exactly correspond to energy differences in the system, one finds information on the system's structure in the absorption spectra.

Due to the absorption, the transmitted light spectrum through the spectroscopic sample will be attenuated. According to Lambert-Beer's law of attenuation, in the case of light propagation along the z direction, the transmitted signal is given by

$$I(\omega, z) = I_0(\omega)\mathrm{e}^{-\alpha(\omega)z}, \tag{2.28}$$

with the macroscopic absorption coefficient $\alpha(\omega)$ proportional to the microscopic absorption cross section $\sigma(\omega)$ of a quantum system through the number of atoms/molecules ρ_N interacting with the incoming light of intensity $I_0(\omega)$:

$$\alpha(\omega) = \rho_N \sigma(\omega), \tag{2.29}$$

with the assumption that all atoms/molecules in the target interact with the laser field independently of each other. The absorption cross section obtained in this manner is a phenomenological observable quantifying the probability of interaction between an absorber and an incident photon with energy $\hbar\omega$ and has still to be related to the intrinsic cross section for light–matter interaction of a quantum system.

The discussion in this section, following Ref. [36], shows that the absorption cross section can be related to the microscopic dipole of a quantum system, thus relating the microscopic response of a system to an interaction with a laser field with the macroscopic observable of light attenuation passing through a medium.

Starting from the wave equation for a light electric field $\boldsymbol{F}(\boldsymbol{x}, t)$ propagating through a homogeneous medium without currents and charges

$$\left(\boldsymbol{\nabla}^2 - \frac{1}{c^2}\frac{\partial^2}{\partial t^2}\right)\boldsymbol{F}(\boldsymbol{x}, t) = \mu_0 \frac{\partial^2}{\partial t^2}\boldsymbol{P}(\boldsymbol{x}, t), \tag{2.30}$$

with μ_0 being the vacuum permeability and $\boldsymbol{P}(\boldsymbol{x}, t)$ the linear polarization, one can restrict the derivation for a plane wave propagating along the z direction. The one-dimensional wave equation then takes the form

$$\left(\frac{\partial^2}{\partial z^2} - \frac{1}{c^2}\frac{\partial^2}{\partial t^2}\right)F(z, t) = \mu_0 \frac{\partial^2}{\partial t^2}P(z, t). \tag{2.31}$$

In the frequency domain, this relation between the linear-response polarization and the electric field takes the form

$$\tilde{P}(z,\omega) = \epsilon_0 \chi(\omega) \tilde{F}(z,\omega). \tag{2.32}$$

In general, $\chi(\omega)$ is a tensor quantity. However, in the linear approximation only its first order component is taken into account and the polarization is then just linearly proportional to the electric field, as denoted in Eq. (2.32).

For the discussed case of a plane wave propagating in z direction approximating the electric field, the dispersion relation takes the form

$$k^2 - \frac{\omega^2}{c^2}(1 + \chi(\omega)) = 0, \tag{2.33}$$

with its usual form involving the index of refraction n restored through the relation $n = \sqrt{1+\chi(\omega)}$. In complex notation, $\chi(\omega)$ can be decomposed into a real and imaginary part,

$$\chi(\omega) = \Re\mathfrak{e}[\chi(\omega)] + i\Im\mathfrak{m}[\chi(\omega)]. \tag{2.34}$$

For a dilute gas-phase sample $\chi(\omega)$ is smaller than unity, such that

$$k \approx \frac{\omega}{c}\left(1 + \frac{\Re\mathfrak{e}[\chi(\omega)]}{2} + \frac{i\Im\mathfrak{m}[\chi(\omega)]}{2}\right) \tag{2.35}$$

also takes a complex form. The real part of the complex wave number is related to the dispersion whereas the imaginary part relates to the absorption coefficient $\alpha(\omega)$

$$\alpha(\omega) = \frac{\omega}{c}\Im\mathfrak{m}[\chi(\omega)]. \tag{2.36}$$

Thus, the atomic cross section can be related to the susceptibility and through Eq. (2.32) to the polarization

$$\sigma(\omega) = \frac{1}{\rho_\mathrm{N}}\frac{\omega}{c}\Im\mathfrak{m}[\chi](\omega) = \frac{1}{\rho_\mathrm{N}}\frac{\omega}{c\epsilon_0}\Im\mathfrak{m}\left[\frac{\tilde{P}(\omega)}{\tilde{F}(\omega)}\right] \tag{2.37}$$

Classically the polarization $\tilde{P}(z,\omega)$ is interpreted as the average dipole moment per atom or molecule $d(\omega)$, multiplied by the atomic number density ρ_N. This leads to the relation between the atomic cross section and the dipole moment

$$\sigma(\omega) = \frac{\omega}{\epsilon_0 c}\Im\mathfrak{m}\left[\frac{d(\omega)}{\tilde{F}(\omega)}\right]. \tag{2.38}$$

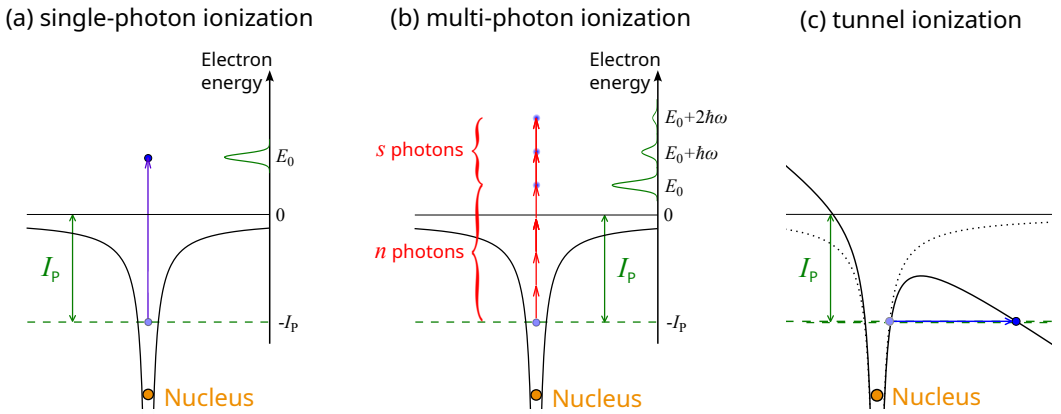

Figure 2.1: Ionization processes. **(a)** Single-photon ionization as a result of interaction with one photon with energy $\hbar\omega > I_P$ (purple arrow). **(b)** Multi-photon ionization requiring interaction with $n+s$ photons (red arrows), with n photons being necessary to overcome the ionization potential barrier. **(c)** Tunnel ionization, where the strong laser field lowers the potential and an electron can tunnel outside the binding region of the potential (blue arrow).

2.1.4 Ionization processes

Light-matter interaction does not only lead to absorption and (stimulated) emission, which are bound-bound transitions but can also couple bound states to free states, thus causing ionization with the emission of (at least) one photoelectron.

2.1.4.1 Single-photon ionization

To free an electron from its bound state in a system S, the electron has to absorb a minimal amount of energy, corresponding to its binding energy I_p, with all the excess energy being transferred to the freed particles upon ionization, Fig. 2.1 (a). The induced transition takes place starting from a bound state $|\psi_a\rangle$ and going to a continuum state $|\epsilon\rangle$, describing a free electron with an asymptotic kinetic energy ϵ. The continuum energy is a function of the wavenumber k_e of the electron in the asymptotic limit of being infinitely far away from the nucleus:

$$\epsilon = \frac{\hbar^2 k_e^2}{2m_e}. \tag{2.39}$$

The photoionization reaction can be written schematically in the following notation:

$$S(|\psi_a\rangle) + \hbar\omega \rightarrow S^+ + e^-(\epsilon) \quad \text{with} \quad \epsilon = \hbar\omega - I_p. \tag{2.40}$$

The photoionization cross section in this case is similar to the photoexcitation cross section for a one-photon transition, thus

$$\sigma_{\epsilon a}(\hbar\omega) = 4\pi^2\alpha\hbar\omega|\hat{T}_{\epsilon a}|^2, \tag{2.41}$$

where the transition-matrix element is defined between the initial bound state $|\psi_a\rangle$ and the final continuum state $|\epsilon\rangle$.

2.1.4.2 Multi-photon ionization

As it was shown for the absorption process, at high enough intensities multiple photons can be absorbed simultaneously to make a bound-bound transition possible. The N-th order process in perturbation theory can be used also to describe bound-free transitions, i.e. multi-photon ionization, Fig. 2.1 (b). The photoionization reaction of this process is given by

$$\mathrm{S}(|\psi_a\rangle) + N\hbar\omega \rightarrow \mathrm{S}^+ + \mathrm{e}^-(\epsilon) \quad \text{with} \quad \epsilon = N\hbar\omega - I_p. \tag{2.42}$$

Exactly as in the absorption case, the transition rate for multi-photon ionization depends on the photon flux Φ and through this on the field intensity to the power of N:

$$R^{(N)}_{\epsilon a}(t) = \sigma^{(N)}_{\epsilon a}\Phi^N \propto I^N, \tag{2.43}$$

with the generalised cross section for the bound-free transition $\sigma^{(N)}_{\epsilon a}$.

As illustrated in Fig. 2.1 (b), it is possible that not just the minimal amount of n photons are absorbed to overcome the ionization threshold but also that additional absorption of s photons above the threshold, i.e. above-threshold ionization (ATI), takes place. A signature of this process are discrete peaks in the electron-energy distribution, ATI peaks, spaced by the energy $\hbar\omega$ of the ionizing field [37–39].

2.1.4.3 Tunneling ionization

At intensities of the interacting field where the laser electric field strength is comparable to the binding potential strength, perturbation theory is not applicable any more. In this case, the binding potential is strongly distorted by the interacting field, as sketched in Fig. 2.1 (c). Here, an electron can tunnel through the created Coulomb barrier. The rate of tunnel ionization can be derived from ADK-theory, named after M. V. Ammosov, N. B. Delone and V. P. Krainov [40–42] treating the atom in the single-active electron approximation:

$$\begin{aligned}\Gamma_{ADK}(t) = \sqrt{\left(\frac{2\mathrm{e}}{n^*}\right)\frac{1}{2\pi n^*}}\frac{(2l+1)(l+|m|)!}{2^{|m|}(|m|)!(l-|m|)!}I_\mathrm{P}\left(\frac{3F(t)}{\pi(2I_\mathrm{P})^{3/2}}\right)^{1/2}\times \\ \left(\frac{2(2I_\mathrm{P})^{3/2}}{F(t)}\right)^{2n^*-|m|-1}\exp\left[-\frac{2(2I_\mathrm{P})^{3/2}}{3F(t)}\right].\end{aligned} \tag{2.44}$$

The ionization rate Γ_{ADK} does not only depend on the electric field $F(t)$ but also on the ionized quantum state with effective principal quantum number $n^* = Z/\sqrt{2I_\mathrm{P}}$, the angular momentum and magnetic quantum numbers l and m, as well as the ionization potential I_p and charge number Z.

2.1.4.4 Over-the-barrier ionization

In the case that the Coulomb barrier is suppressed such that the initially bound electron is *freed* in the laser field, over-the-barrier ionization takes places. Electric-field strengths at which this process becomes relevant are achieved for fields higher than a critical field

$$F_0^\mathrm{crit} = \frac{I_\mathrm{P}^2}{4Z}, \tag{2.45}$$

with the ionization potential I_P and the charge after ionization Z. While this limit holds in the case of a classical barrier and considering the electron as a particle with a given momentum, it is only approximative when the electron is treated as a wave function [43].

2.1.4.5 Strong-field ionization

If perturbation theory or ADK-theory should be considered for the description of a particular ionization case, i.e. if multi-photon or tunneling ionization takes place, can be decided, calculating the corresponding Keldysh parameter γ [44] quantifying the transition from the multi-photon to the tunneling regime. The Keldysh parameter is an adiabaticity parameter depending on the ionized target species through the ionization potential I_P, the laser intensity I and the carrier frequency ω:

$$\gamma = \omega\sqrt{\frac{2I_\mathrm{P}}{I}}. \tag{2.46}$$

It can be expressed in terms of the ponderomotive potential, given by

$$U_\mathrm{P} = \frac{e^2F_0^2}{4m_\mathrm{e}\omega^2} = \frac{I}{4\omega^2}, \tag{2.47}$$

which is defined as the averaged kinetic energy of an electron in a periodic laser field of frequency ω and intensity I. With this,

$$\gamma = \sqrt{\frac{I_\mathrm{P}}{2U_\mathrm{P}}}. \tag{2.48}$$

For $\gamma \ll 1$ the ionization is best described by tunneling, whereas for $\gamma \gg 1$, or even $\gamma \gtrsim 1$, multi-photon interaction should be considered. In reality, however, with laser intensities of strong infrared ($\hbar\omega \approx 1.6\,\mathrm{eV}$) lasers on the order of $10^{14}\,\mathrm{W/cm^2}$ and

ionization potential starting from the ground state $\sim 10\,\mathrm{eV}$, the Keldysh parameter $\gamma \approx 1$, so that no clear classification is possible.

The ponderomotive shift U_P can be interpreted as an increase of the ionization threshold with increasing intensity. In the same way, the bound states also get an energy shift with increasing intensity due to the Stark shift

$$\Delta E_\mathrm{Stark} = -\frac{\alpha}{2} F_0^2, \tag{2.49}$$

depending on the polarizability of the state α and the field strength F_0. As α can be state dependent, different states get a different Stark shift, and it was found that loser bound states experience a bigger Stark shift [45, 46]. Both the ponderomotive shift and the Stark shift thus affect the photoelectron kinetic energy gained upon ionization.

2.1.4.6 Multiple ionization

In an ionization processes involving the liberation of multiple (at least two) electrons, in contrast to single-ionization processes, multiple ionization takes place. Here, the different electrons can be freed either independently one after each other in the process of sequential ionization or together in non-sequential ionization. If sequential ionization takes place, every step in the sequential process can be treated as a single-electron ionization, but with a (typically) larger ionization potential I_P and a different initial and final charge state Z. If the obtained results would deviate from the expected in the case of the sequential treatment, this would indicate the occurrence of a non-sequential process, thus indicating electron correlations during the ionization process.

A prominent example of electron correlation is occurring knee-like structure for double-ionization yield as a function of increasing intensity [47, 48], where a significant increase in the yield of doubly charged ions was found compared to the predictions from ADK-theory. The discrepancy has been closed through consideration of recollision, where the initially freed electron interacts with the ion, while being driven back to it during the electric-field cycle [49, 50]. Different types of processes can happen upon recollision [32]:

- radiative recombination leading to high-harmonic generation [27–29], as it will be discussed in chapter 3.2.2;
- elastical back-scattering at the ion causing high-order above-threshold ionization (HATI) used for characterisation of ultrashort laser pulses [51, 52];
- non-radiative recombination leading to frustrated tunneling ionization [53];
- inelastic recollision causing either ionization of the electron itself or ionization of the ion in non-sequential double ionization (NSDI) [47, 48].

2.2 Two-electron systems

In this work, both an atomic system and a molecular system having two electrons are investigated - the helium atom and the hydrogen molecule, both being in an excited state. The present section gives information on the main states in both systems studied throughout this thesis.

2.2.1 The helium atom

The helium atom consists of two protons and two neutrons, bound together in a nucleus, as well as two electrons in the electron shell of the atom. The total two-electron wave function $\Psi(\mathrm{e}_1, \mathrm{e}_2)$ can be written as a product of the spatial and spin wave functions in the form [34]

$$\Psi(\mathrm{e}_1, \mathrm{e}_2) = \Psi(\boldsymbol{r}_1, \boldsymbol{r}_2)\chi(s_1, s_2). \tag{2.50}$$

In the cases discussed in this thesis, the spin degrees of freedom are decoupled from the electron degrees of freedom. Thus, not considering spin-spin interaction, the total spin quantum number is preserved in all studied transitions starting from the ground state with $S = 0$, which implies that the spin wave function of the excited states is also antisymmetric and therefore the spatial wave function must be symmetric according to Pauli's principle for fermions.

The spectroscopic notation for two-electron systems is

$$^{2S+1}L^{\pi}, \tag{2.51}$$

with $L \in \{0, 1, 2, \ldots\} \cong \{\mathrm{S}, \mathrm{P}, \mathrm{D}, \ldots\}$ and S being the total angular momentum and total spin quantum number, respectively. The parity of the state is given by π with "o" for odd and "e" for even parity. For single-photon transitions in the dipole approximation only coupling of different parity states is allowed, such as $^1\mathrm{S}^{\mathrm{e}}$ to $^1\mathrm{P}^{\mathrm{o}}$.

Singly excited states of the helium atom can be understood as states, where only one of the electrons is excited and the other one remains in the 1s shell. All singly excited states have energies between 21.22 eV, the energy level of the first excited state, and the first ionization threshold I_1 at 24.588 eV. For dipole transitions involving absorption of just one photon, the 1snp singly-excited states series is accessible, where $n = 2, 3, 4, \ldots$. The energy levels of those states, converging to the N = 1 ionization threshold, are listed in table 2.1 together with the states' decay rate back to the ground state.

All doubly excited states in the helium atom have energies higher than the first ionization threshold and are classified in different series, converging to the higher lying ionization thresholds $\mathrm{I}_n \in \{\mathrm{I}_2, \mathrm{I}_3, \mathrm{I}_4, \ldots, \mathrm{I}_\infty\}$, where the lower excited electron can be thought of being in the corresponding n shell and the other electron in a higher excited shell. The ionization thresholds, relevant for the ionization studies

Table 2.1: Energies and decay rates of considered singly and doubly excited states in the helium atom [54–57].

Series	State configuration	Energy (eV)	Energy (a.u.)	Decay rate (meV)
Singly excited states, N=1	$1s^2$	0	0	
	1s2p	21.2180	0.77979	0.0074
	1s3p	23.0870	0.84847	0.0023
	1s4p	23.7421	0.87255	0.0010
	1s5p	24.0458	0.88371	0.0005
	1s6p	24.2110	0.88978	0.0003
	1s7p	24.3107	0.89345	0.0002
Doubly excited states, N=2	2s2p	60.147	2.2105	37.4
	$sp_{2,3+}$	63.658	2.3395	8.2
	$sp_{2,4+}$	64.466	2.3692	3.5
	$sp_{2,5+}$	64.816	2.3821	1.8
	$sp_{2,6+}$	65.000	2.3888	1.0
	$sp_{2,7+}$	65.110	2.3929	0.7
	$sp_{2,8+}$	65.179	2.3951	0.4
	$sp_{2,3-}$	62.758	2.3065	0.5
	$sp_{2,4-}$	64.135	2.357	0.3
	$sp_{2,5-}$	64.657	2.376	<0.1
Doubly excited states, N=3	3s3p	69.873(9)	2.568	181(10)
	$sp_{3,4+}$	71.623(4)	2.632	82(5)
	$sp_{3,5+}$	72.179(2)	2.653	39(3)

out of doubly excited states presented in chapter 5, are listed in table 2.2 according to reference [56].

High-resolution studies of double-excitation states in helium [55, 56] have revealed multiple series of states converging to the respective ionization threshold of the excitation manifold. For the doubly excited states with $N = 2$, the possible dipole-allowed configurations are the 2snp, 2pns and 2pnd. Initial detection of at first only two series [58] has lead to the definition of superposition states as linear combination of states [59]

$$sp_{2,n\pm} = \frac{1}{\sqrt{2}}(2snp \pm 2pns) \tag{2.52}$$

forming a strong "+" and a weak "-" series, whereas the third even weaker series has only been detected in spectroscopic studies with higher resolution [56, 57].

Table 2.2: Energy positions of the ionization thresholds in the helium atom reported in [56].

Ionization threshold	Energy position
I_1	24.588 eV
I_2	65.399 eV
I_3	72.957 eV
I_4	75.602 eV
I_5	76.826 eV
I_6	77.491 eV
I_∞	79.003 eV

The classification of doubly excited states for increasing lowest quantum number N becomes ever more challenging and in the context of this work is kept up to the $N = 3$ series. Introduction of new set of correlation quantum numbers, which classify correlations between the electrons in the radial and angular coordinates (hyperspherical coordinates) allow for better classification of the highest Rydberg series in the helium atom [60–63].

Being embedded in the single-ionization continuum, all doubly excited states can autoionize through a configuration-interaction coupling to the continuum [64] and have lifetimes ranging between 18 fs for the 2s2p state and $\sim$ 100 fs for the higher excited states. The energies of states relevant to the ionization studies in chapter 5, are listed in table 2.1 together with other important state parameters, such as the decay rate, which is inversely proportional to the state's lifetime.

2.2.2 The hydrogen molecule

The hydrogen molecule, just like the helium atom, has two electrons, but also two separate nuclei, each consisting of one proton. Using the fact that the mass of the electrons m_e is much smaller than the mass of its nuclei M, the nuclear and electronic degrees of freedom can typically be decoupled adiabatically in the Born-Oppenheimer approximation [65]. The total molecular wave function then reduces to a product between the electronic and nuclear wave functions for a given electronic state s and nuclear centre-of-mass coordinate $\boldsymbol{R}$

$$\Psi_s(\mathbf{r}_1, \mathbf{r}_2, \boldsymbol{R}) = \eta(\boldsymbol{R})\psi_s(\boldsymbol{R}; \mathbf{r}_1, \mathbf{r}_2). \tag{2.53}$$

The nuclear wave function $\eta(\boldsymbol{R})$ describes both vibration and rotation for the electronic states s with its wave function $\psi_s(\boldsymbol{R}; \mathbf{r}_1, \mathbf{r}_2)$.

In analogy to the spectroscopic notation introduced for atoms, the electronic state in the hydrogen molecule can also be characterized by a molecular term sym-

Table 2.3: Character table for the point group of a two-atomic homonuclear molecules. The symmetry operation of the point group are the identity E, the rotation around the molecular axis C_∞^ϕ, reflection at planes including the molecular axis σ_v, inversion i, improper rotations around the molecular axis S_∞^ϕ and the 2-fold rotations C_2.

Molecular state	**Symmetry operations**					
	E	C_∞^ϕ	σ_v	i	S_∞^ϕ	C_2
Σ_g^+	1	1	1	1	1	1
Σ_u^+	1	1	1	-1	-1	-1
Σ_g^-	1	1	-1	1	1	-1
Σ_u^-	1	1	-1	-1	-1	1
Π_g	2	$2\cos(\phi)$	0	2	$-2\cos(\phi)$	0
Π_u	2	$2\cos(\phi)$	0	-2	$2\cos(\phi)$	0
Δ_g	2	$2\cos(2\phi)$	0	2	$2\cos(\phi)$	0
Δ_u	2	$2\cos(2\phi)$	0	-2	$-2\cos(\phi)$	0

bol of the form

$$^{2S+1}\Lambda_{g,u}^{\pm}, \tag{2.54}$$

with S being the total spin and $\Lambda \in \{0,1,2,\dots\} \cong \{\Sigma,\Pi,\Delta,\dots\}$ the z-component of the total angular momentum, whereas $\pm$ stands for symmetry, antisymmetry under the σ_v transformation (reflection at a plane including the molecular axis) and the subscript g,u for $\mathrm{sgn}(\Lambda) = 1,-1$, respectively. Thus, the molecular term symbol also shows the symmetry properties of the electron wave function under different transformations, as listed in table 2.3.

To specify a certain electronic state in a molecule, a letter is typically also added before the term symbol, where X is used for the ground state, as in the ground-state notation of the H_2 molecule $X^1\Sigma_g^+$. The excited states are labelled alphabetically, in ascending order, $A,B,C,\dots$ or $a,b,c,\dots$. Here, capital letters are used for spin singlet states ($S=0$) and lower-case letters for triplet states ($S=1$) [66]. For diatomic molecules, also the one-electronic molecular-orbital designators for the united atom configuration of the type $1s\sigma 2p\pi$ are typically given next to the term symbol, where if an electron is assumed to be in the $1s\sigma$ orbital, only the orbital of the excited electron is listed [67].

With XUV light having photon energies bellow 20 eV, as used in the nuclear wave-packet study presented in chapter 6, one can reach the singly excited electronic states in the H_2 molecule, with the notation of the first lowest states: $B^1\Sigma_u^+ 2p\sigma$, $C^1\Pi_g 2p\pi$ $B'^1\Sigma_u^+ 3p\sigma$, $D^1\Pi_u 3p\pi$, which are all accessible via a dipole transition from the molecular ground state $X^1\Sigma_g^+ 1s\sigma$. Those excited states can be dipole-coupled to states which are dipole-forbidden for transitions from the ground state as for example the $EF^1\Sigma_g^+ 2s\sigma + 2p\sigma^2$ or the $H^1\Sigma_g^+ 3s\sigma$. A summary of accu-

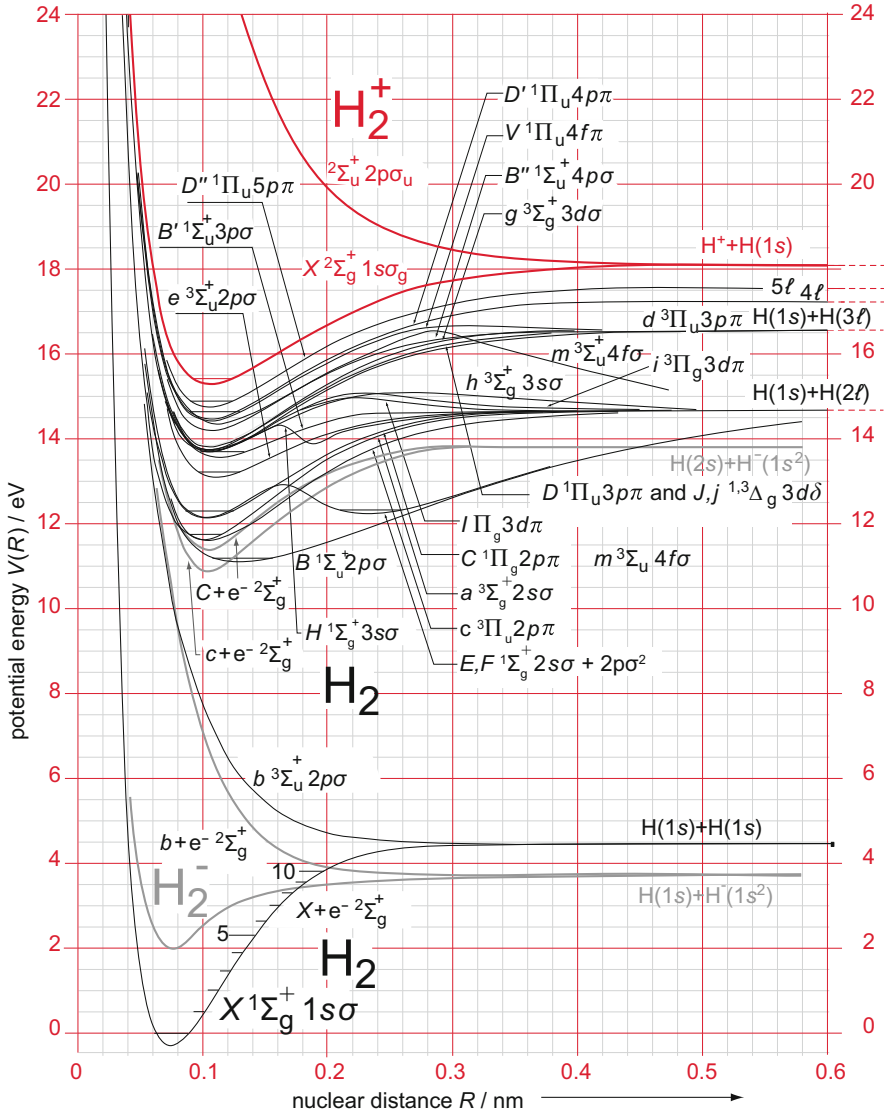

Figure 2.2: Potential-energy curves of the most important states of the H_2 molecule after [67]. Figure reprinted from [68].

rate potential-energy curves for the hydrogen molecule, shown in Fig. 2.2, is given in [67, 68].

Some of the singly excited states in the H_2 molecule have a predissociating character, because they are located above the H(1s)+H(2l) dissociation limit at

14.676 eV and can non-adiabatically couple to it as well as to other states. A prominent example of a state with predissociative character is the $D^1\Pi_u 3p\pi$ state. Already after the first observation of its absorption lines [69, 70] broadening due to dissociation was identified and later asymmetrical Beutler-Fano line shapes were measured, followed by many spectroscopic studies summarized in [71], with the most accurate spectroscopic study [72] and theory description of predissociation in the D vibronic resonances [73] to date. Due to the predissociative broadening of the vibronic resonances of the D state, they are easier to detect spectroscopically in an XUV absorption-spectroscopy experiment and thus were chosen as the focus of the studies in chapter 6 investigating vibrational wave-packet dynamics in the excited electronic state.

2.3 Beutler-Fano line shapes

Line shapes of resonances belonging to states with autoionizing or predissociative character have an asymmetric form arising due to couplings with the energetically degenerate continuum or dissosciation states through configuration interaction [64]. A summary of Fano's theory of configuration interaction is found in [74, 75], leading to a general Beutler-Fano line shape profile described by its absorption cross section

$$\sigma \propto \frac{|q+\epsilon|^2}{1+\epsilon^2}, \tag{2.55}$$

depending on the reduced energy variable

$$\epsilon = \frac{E - E_{\mathrm{res}}}{\Gamma/2}. \tag{2.56}$$

The linewidth $\Gamma = 2\pi|V_E|^2$ depends on the interaction $V_E = \langle c_E|\hat{\boldsymbol{V}}|b\rangle$ between the bound $|b\rangle$ and continuum $|c_b\rangle$ states introducing a finite life time of the state $\tau \propto 1/\Gamma$ due to the loss channel in the continuum. The asymmetry parameter q is connected to the strength of the interaction to the continuum and the transition probabilities between the ground and bound state and between the ground and continuum state in the system. Figure 2.3 illustrates the dependence of the generalised Beutler-Fano profile on the asymmetry parameter q.

Experimentally obtained spectroscopic data is fitted with a Fano line profile of the form

$$\sigma_{\mathrm{exp}} = a\frac{|q+\epsilon|^2}{1+\epsilon^2} + \sigma_{\mathrm{NR}}, \tag{2.57}$$

with the parameter a scaling with the strength of the asymmetric profile and the non-resonant background contribution σ_{NR}.

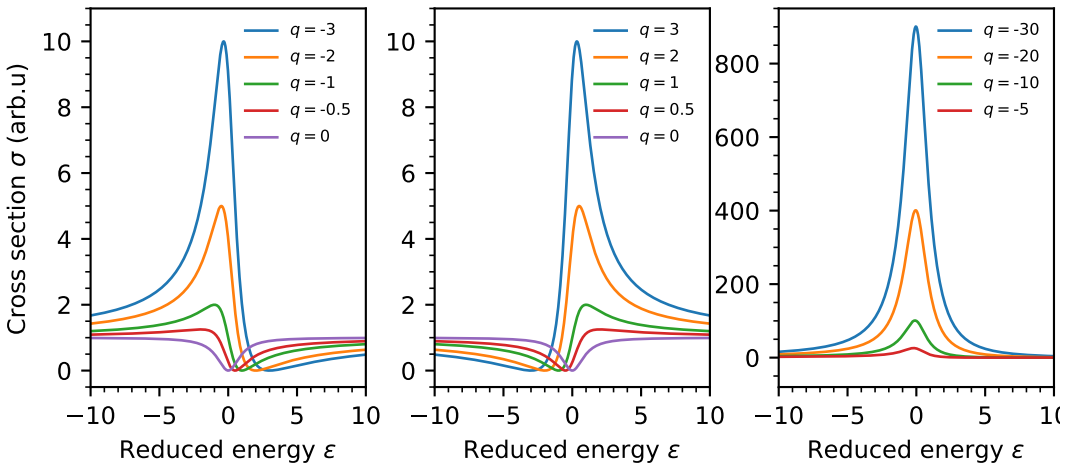

Figure 2.3: Beutler-Fano line shapes for different values of the asymmetry q parameter. In the limits $|q| \to \infty$ and $|q| = 0$ the line shape becomes symmetrical.

3 LIGHT SOURCES

For the investigations presented in this thesis different light sources have been used. This chapter discusses their most important characteristics, starting from the used light sources with the longest time duration on the order of a few tens of femtoseconds and going to light pulses with duration on the attosecond timescale.

3.1 Ultrashort laser pulses

Laser pulses with duration on the picosecond and femtosecond time-scale are referred to as ultrashort laser pulses [76]. In this thesis, ultrashort laser pulses refer to light fields with temporal duration less than 100 fs, distinguishing between multi-cycle laser pulses with duration ~ 70 fs and few-cycle laser pulses with duration ~ 5 fs.

In the time-domain, ultrashort laser pulses are described by a time-dependent electric field $F(t)$, typically defined as the product between a slowly varying envelope $\mathcal{F}(t)$, often a Gaussian or a $\cos^2$ function [33], and an oscillating part with a time-dependent phase $\phi(t)$:

$$F(t) = \mathcal{F}(t)\mathrm{e}^{i\phi(t)}, \tag{3.1}$$

which for convenience, as noted in the discussion on classical light fields in section 2.1.1.1, is preferably treated in the complex plane. The temporal field $F(t)$ is related to the spectral field $\tilde{F}(\omega)$ in the frequency domain via a Fourier transformation $\mathfrak{F}$:

$$\tilde{F}(\omega) = \mathfrak{F}\{F(t)\}(\omega) = \frac{1}{2\sqrt{\pi}} \int_{-\infty}^{\infty} F(t)\mathrm{e}^{-i\omega t}\mathrm{d}t, \tag{3.2}$$

$$F(t) = \mathfrak{F}^{-1}\{\tilde{F}(\omega)\}(t) = \frac{1}{2\sqrt{\pi}} \int_{-\infty}^{\infty} \tilde{F}(\omega)\mathrm{e}^{i\omega t}\mathrm{d}\omega, \tag{3.3}$$

with ω being the angular frequency of the oscillating field. The Fourier relationship between the electric-field representation in the time and in the frequency domain implies, that a stretch in one of the domains leads to a contraction and amplitude change in the other domain. According to this inverse relationship between the temporal ΔT_{FWHM} and spectral $\Delta\omega_{\mathrm{FWHM}}$ width ultrashort light pulses have to be supported by a broadband spectrum.

While a broad spectrum is a necessary condition for a short laser pulse, the phase relationship of the frequencies in the laser pulse is the deciding factor for the production of ultrashort light pulses. The temporal phase $\phi(t)$ can be expanded in a Taylor series

$$\phi(t) = \sum_{n=0}^{\infty} \frac{\phi_n}{n!} t^n = \phi_{\mathrm{CEP}} + \omega_{\mathrm{c}} t + \Phi(t). \tag{3.4}$$

Here, ϕ_{CEP} is the constant offset phase between the carrier oscillation and the maximum of the envelope amplitude function, i.e. the carrier-envelope phase (CEP). The carrier frequency ω_{c} is typically defined as the average of all spectral components or as the frequency with maximal spectral amplitude. The remaining term in the expansion $\Phi(t)$ contains all higher-order phase contributions, which affect the instantaneous pulse frequency $\omega(t)$, defined as the derivative of the temporal phase with respect to time:

$$\omega(t) = \frac{\mathrm{d}}{\mathrm{d}t}\phi(t) = \omega_{\mathrm{c}} + \frac{\mathrm{d}}{\mathrm{d}t}\Phi(t). \tag{3.5}$$

In the case that $\Phi(t)$ has no temporal dependence, the instantaneous frequency is constant for all times and the resulting Fourier-transform limited pulse (FTL) has the shortest possible duration supported by the spectral bandwidth of the pulse. If $\frac{\mathrm{d}}{\mathrm{d}t}\Phi(t) \neq 0$, then $\omega(t)$ changes with time and the pulse is referred to as chirped, as the frequencies increase or decrease during the time-propagation of the pulse, in the cases of up-chirp and down-chirp, respectively. The temporal phase is connected to the spectral phase of the pulse, which can also be expanded around the carrier-envelope frequency ω_{c} in a Taylor series

$$\varphi(\omega) = \sum_{n=0}^{\infty} \frac{\varphi_n}{n!}(\omega-\omega_{\mathrm{c}})^n = \varphi_{\mathrm{CEP}} + GD(\omega-\omega_{\mathrm{c}}) + \frac{GDD}{2}(\omega-\omega_{\mathrm{c}})^2 + \frac{TOD}{6}(\omega-\omega_{\mathrm{c}})^3 + \ldots \tag{3.6}$$

Here, as in the case of the temporal phase, the constant term corresponds to the CEP offset. The group delay GD shifts the absolute time-position of the pulse, while the higher components introduce a frequency-dependent delay of the different spectral components. The group-delay dispersion GDD leads to a time-chirp of the laser pulse, with positive GDD causing an up-chirped pulse (with increasing frequency over time) and a negative GDD leading to a down-chirped pulse (with decreasing frequency over time). The third-order dispersion TOD leads to pre- and post-pulses around the main pulse. All higher-order frequency dependences, GD, GDD, TOD, can be induced through propagation of the pulses in a medium over a given distance, as for example through air, and have to be taken into account when designing the optical path of a laser beam, such that the shortest possible pulse is detected at the position of interaction with the target under study.

3.1.1 Laser system for strong-field ionization of excited states in the helium atom

In the experiments discussed in chapter 5 an ultrashort light pulse with intensity on the order of $10^{13}\,\mathrm{W/cm^2}$ is used to strong-field ionize initially prepared doubly excited states in the helium atom. The laser setup for the production of those IR pulses with central wavelength of $\sim 800\,\mathrm{nm}$ is a flexible high repetition laser source for pump-probe experiments at FLASH2 [77] based on the process of optical parametric chirped pulse amplification (OPCPA) [78]. It features a hybrid Yb:fibre laser, Yb:YAG by Innoslab [79], as a pump and a YAG-generated supercontinuum seed as a seed of the OPCPA setup. The output of the OPCPA delivers intensity-stable output pulses with energy $> 500\,\mu\mathrm{J}$ synchronised to the FLASH master oscillator in a 10 Hz burst mode and an intraburst repetition rate of 100 kHz.

The OPCPA-output laser pulses are transported to two FLASH2 experimental end-stations via a transport beamline with length more than 40 m, which requires pointing stabilisation of the laser beam. Directly at the FL26 end-station, where the experiments of chapter 5 were performed, pulse diagnostics, pulse compression, attenuation and focussing to the experimental chamber were carried out. Here, a grating compressor is used for the adjustment of the time duration of the pulse, set for the experiments $\sim 70\,\mathrm{fs}$, such that temporal overlap with the time-jittering FEL pulses is ensured. The measured energy per pulse directly before incoupling in the experimental setup amounts to $\approx 130\,\mu\mathrm{J}$.

The IR beam is focussed in the experimental setup with an IR-focussing lens with focal length of 50 cm and is coupled in the FEL beamline under 90° by a silver-coated planar mirror with a 4-mm whole in its center, through which the FEL pulse can pass through. Both beams propagate collinearly downstream and spatially overlap in the target-interaction region. While spatial overlap is found optically on a Ce:YAG-coated screen, temporal overlap is found with nanosecond precision with a fast photodiode placed in the reaction microscope [80] and with femtosecond precision in a target with well-known pump–probe ionization signal, like a ground-state noble gas. For the presented experiments Ar was used.

3.1.2 Laser system for the generation of short and strong laser pulses

In the experiment discussed in chapter 6, demonstrating the all-optical visualisation of a vibrational wave packet in the neutral excited hydrogen molecule, together with the possibility to control the wave-packet evolution, a short and strong NIR pulse is used twofold:

1) as a driving pulse in the process of high-harmonic generation for the production of coherent XUV radiation and

2) as a control pulse of the XUV-initiated wave-packet dynamics.

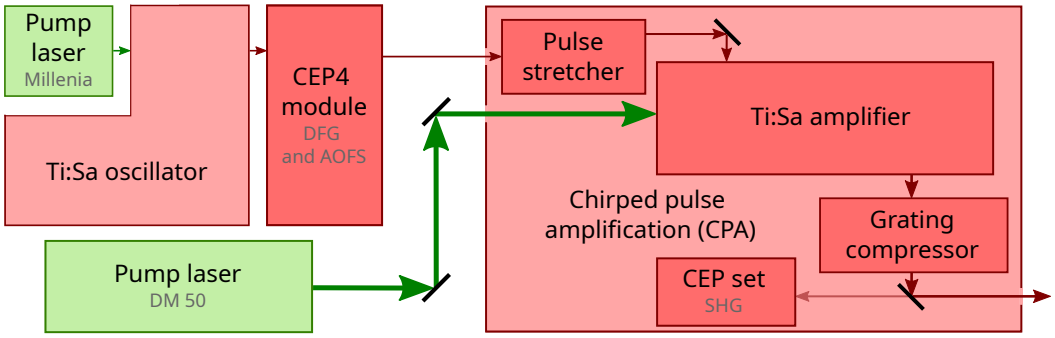

Figure 3.1: Illustration of the main components of the laser setup for the generation of ultrashort laser pulses.

For the first purpose, high peak intensity of the laser radiation, on the order of $10^{14}\,\mathrm{W/cm^2}$, is required. Such intensities can be reached in the small focal size of ultrashort laser pulses, on the order of a few tens of fs or shorter, delivering also high pulse energy. Because the produced HHG XUV radiation has to span over all resonances of the $D^1\Pi_u 3p\pi$ potential-energy curve to excite the whole D vibrational wave packet, a few-cycle laser pulse leading to the generation of continuous XUV spectrum is needed. All those laser requirements are met by the specifications of the commercially available laser system Femtopower™ HR/HE CEP4 by Femtolasers GmbH in combination with a home-built hollow-core-fibre (HCF) based system for spectral broadening followed by a suitable chirped-mirrors compression stage.

3.1.2.1 Femtosecond laser system

The Femtopower™ HR/HE CEP4 laser system delivers sub-20 fs pulses centred at the wavelength of 790 nm with repetition rate of 3 kHz and energy per pulse up to 3 mJ. It consists of two main parts: an actively dispersion-controlled Kerr-lens mode-locked oscillator [22,23] and a multi-pass chirped-pulse amplifier (CPA) [81], both using a titanium-doped sapphire crystal (Ti:Sa, or Ti:Al_2O_3) as the gain medium. A sketch of the laser system with its main components is shown in Fig. 3.1.

The oscillator Ti:Sa crystal is pumped by a Spectra Physics Millenia solid-state laser with continuous power of 3.5 W at 532 nm to generate broadband, almost octave-spanning, output pulses centred around 800 nm with duration less than 10 fs and pulse energy up to 3.5 nJ at 75 MHz repetition rate. Before seeding the amplifier, the oscillator output pulses are carrier-envelope-phase (CEP) stabilised in the CEP4 module by passing through an acousto-optic frequency shifter (AOFS), where the fluctuating CEP is shifted by the amount measured in an f–$2f$ interferometer [82, 83].

In the amplifier, the passively CEP-stable pulses are first stretched to a duration of a few-tens of picoseconds before entering the multipass section. After the first four passes through the amplifier Ti:Sa crystal, pumped by a Q-switched pump laser

(DM-50 by Photonics Industries) with average power of $\backsim 50\,\mathrm{W}$ the repetition rate is reduced to 3 kHz through selection of a single pulse from the pulse train by a fast-switching Pockels cell. To compensate for higher order dispersion and reduce the gain-narrowing in the amplification process by shaping the spectral amplitude of the selected pulse from around the maximum of the gain envelope, the beam is steered through an acousto-optic programmable filter (Dazzler by Fastlite). After the following 4 passes through the amplifier crystal the beam divergence is changed for the last two passes to prevent damage to the Ti:Sa crystal and optimize the efficiency of the amplification process, arriving to pulse energies above 3.5 mJ. After the tenth and final pass through the crystal the beam is directed trough a grating compressor combined with chirped mirrors to increase the peak intensity and lower the pulse duration of the output pulses back to the sub-20 fs range.

3.1.2.2 Laser pulse compression to the few-cycle regime

To come back to the single-digit femtosecond pulse length, i.e. to few cycle laser pulses, the output pulses need to be spectrally broadened and all new light frequencies have to be brought back together in phase. In the laser setup, sketched in Fig. 3.2, a helium-gas-filled hollow-core fibre is used for the spectral broadening through self-phase modulation of the light in the gas medium [84, 85]. The fibre capillary with the inner diameter 310 µm and length of 1.5 m is cut in two equally long parts in the middle and the two parts are again brought back together very tightly in the original rotation to each other, with the proper procedure for fibre installation described in [86, 87]. The separation of the glass capillary in two parts enables the seamless propagation of the beam mode through the two adjacent parts, while allowing for double differential pumping of the fibre system: the helium gas, typically under 2 bar pressure fills the fibre through the cut in the middle and is pumped through both fibre ends down to $\backsim 4\,\mathrm{mbar}$. Lowering the pressure on the in- and out-coupling end of the HCF reduces plasma generation in the focus area due to the high pulse power and with this extends the lifetime of the fibre.

The broad bandwidth of the laser pulse spectrum however does not necessarily mean short pulses. Due to dispersion in the conversion medium and the nonlinearity of the self-phase modulation process, the spectral phase of the pulse is chirped and all frequencies have to be brought back in phase. To achieve this, the laser beam passes through a chirped mirror compressor with seven pairs of double-angle chirped mirrors (PC70 by UltraFast Innovations GmbH), where each pair introduces negative GDD of $-40\,\mathrm{fs}^2$, pre-compensating also the dispersion introduced by the subsequent propagation in air over the distance of around 4 m until entrance of the vacuum beamline. Fine tuning of the dispersion is achieved with a pair of motorized glass wedges (fused silica with anti-reflective coating in the range 450 nm to 950 nm and 4° apex angle by Lens Optics).

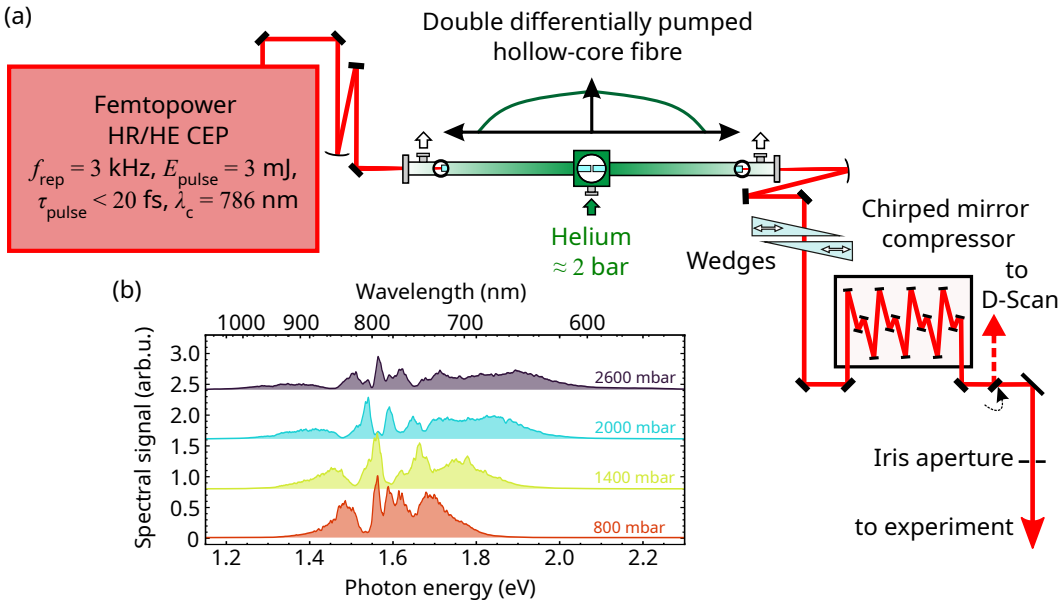

Figure 3.2: Laser pulse compression to the few-cycle regime. **(a)** Setup for pulse compression of ultrashort laser pulses from 20 fs to < 5 fs, including a differentially pumped hollow-core fibre for spectral broadening, a pair of wedges for dispersion control and a chirped mirror compressor. **(b)** Pulse broadening after propagation through the hollow-core fibre as a function of input helium pressure. Data from [86]. Figure adapted from [87].

3.1.2.3 Laser pulse characterisation

Before guiding the NIR laser pulses used for both the HHG process and for the target interaction in the experimental setup, the few-cycle NIR pulses are characterised in a dispersion scan, or short D-Scan, setup [88, 89]. As the name suggests, this pulse characterisation technique relies on the controlled change of the dispersion in the pulse through glass insertion in the beam path. Measuring the fundamental spectrum and spectra generated in a non-linear process around the optimum glass insertion for best pulse compression, in combination with a numerical retrieval algorithm, allows for full temporal characterisation of the few-cycle short NIR pulses.

A pulse characterisation trace together with the retrieved pulse shape and spectral phase, measured directly before the experiment presented in chapter 6, is shown in Fig. 3.3. The measured pulse spectrum, Fig. 3.3(c), spans between 1.2 eV and 2.5 eV. The measured temporal pulse shape shows a duration of FWHM = 4.45 fs. Because the retrieved spectral phase is not constant, the pulse duration is considerably longer than the Fourier-transform-limited (FTL) pulse with FWHM_{FTL} = 3.67 fs. The peak intensity of the retrieved pulse is only around half of the peak intensity of the FTL pulse, which is important for the intensity calibration, presented in section 6.3.2.4.

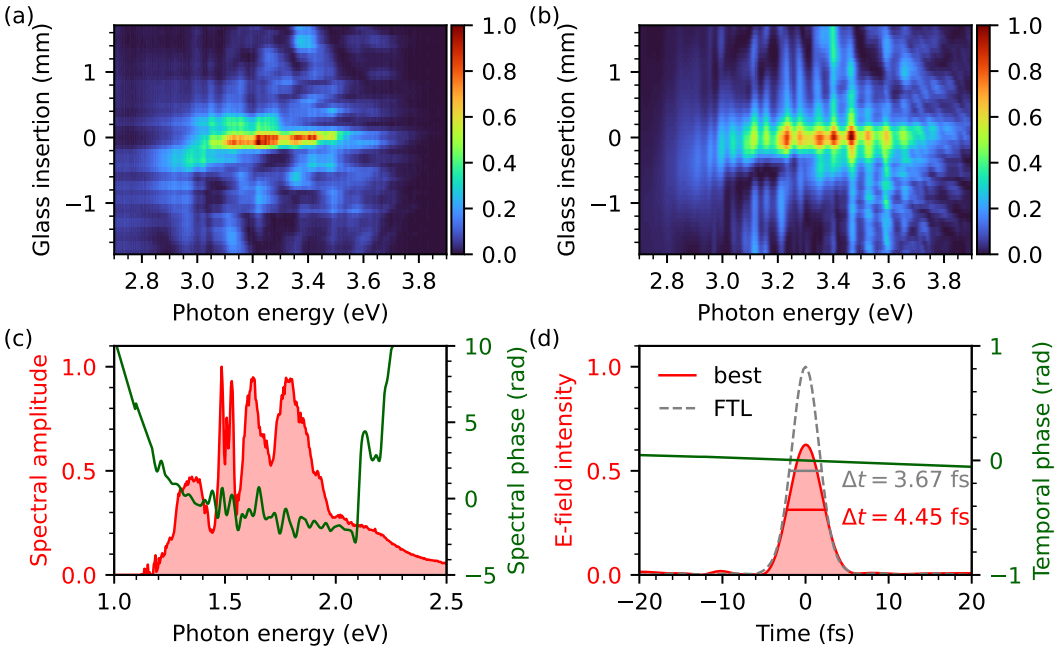

Figure 3.3: NIR-pulse characterisation applying the D-Scan technique. **(a)** Measured D-Scan trace, composed by the recorded SHG spectrum as a function of glass insertion, i.e. pulse dispersion. **(b)** Retrieved D-Scan trace, obtained through variation of the spectral phase to fit the measured data. **(c)** Measured fundamental spectrum together with the retrieved spectral phase, yielding the shortest pulse in time domain. **(d)** Shortest retrieved pulse in the time domain with duration of 4.45 fs obtained via Fourier transformation, shown together with a Fourier-transform-limited (FTL) pulse with a flat spectral phase.

3.2 Light sources for XUV radiation

To access excited states in the helium atom or the hydrogen molecule in a one-photon transition, excitation pulses in the XUV spectral region should be used. Here, different XUV sources are available. While monochromatic XUV radiation can be used for precision measurements of line-shapes and absorption/ionization cross section, pulsed (coherent) XUV laser sources are required for studies of dynamics in atoms and molecules. Two kinds of XUV pulsed radiation sources are free-electron lasers (FELs) and high-order harmonic generation (HHG). While the HHG process, depending on the properties of the driving pulse, can produce attosecond pulse trains or single attosecond pulses with a broad spectral range allowing simultaneous excitation of multiple transitions, FEL-produced XUV light has a narrow bandwidth, enabling selective excitation to chosen states. Doe to those differences, in the ionization study out of selectively prepared doubly excited states, chapter 5, FEL XUV light was used, whereas in the studies of wave-packet dynam-

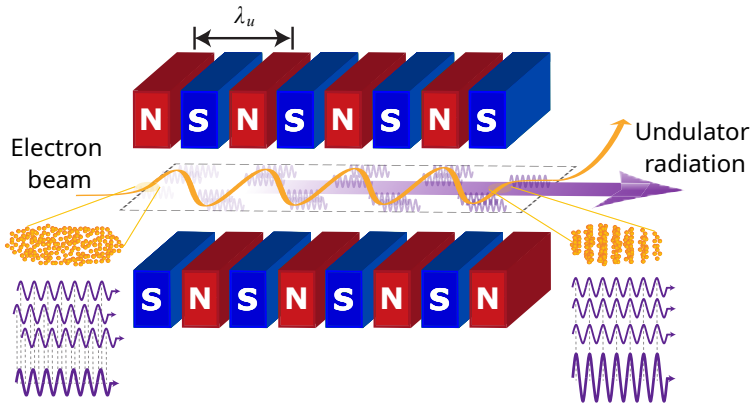

Figure 3.4: Schematic representation of the working principle of an FEL, with focus on the production of undulator radiation, together with illustration of the microbunching induced in the SASE process over the length of the undulator. Figure adapted from [98].

ics in the H_2 molecule, high-harmonic generation was the preferred technique for XUV light production.

3.2.1 Free-electron laser radiation

A free-electron laser is an accelerator-based light source emitting light with laser-like properties: low divergence, high photon density, spatial coherence and (partial) temporal coherence. FEL light sources can produce light starting from the IR [90], through the XUV [91–94] up to the X-ray regime [95–97]. The basic principle of the light generation, sketched in Fig. 3.4, is discussed in the following.

For the generation of XUV and X-ray light in FELs, free electrons are accelerated to relativistic speeds, typically in linear accelerators [99], and forced on sinusoidal motion perpendicular to their propagation direction by an arrangement of oppositely poled magnets (undulators), which decelerates the electrons such that they start emitting synchrotron radiation in a small cone along the propagation direction [100]. The fundamental wavelength of the emitted radiation depends on parameters of the electron bunch and the undulator:

$$\lambda_0 = \frac{\lambda_\mathrm{u}}{2\gamma^2}\left(1+\frac{K^2}{2}\right). \tag{3.7}$$

Here, λ_u is the period of the undulator segments, i.e. the distance between the differently poled magnets, $\gamma = \sqrt{1-v^2/c^2}$ is the Lorentz factor of the relativistic electrons and K is an undulator parameter depending on the magnetic field strength B_0 and on the undulator period λ_u:

$$K = \frac{eB_0\lambda_\mathrm{u}}{2\pi m_\mathrm{e}c}, \tag{3.8}$$

with e and m_e being the electron charge and mass, and c the speed of light. The relation in Eq. (3.7) shows that to change the wavelength, both the electron accelerator settings as well as the undulator settings can be changed. In the majority of FEL facilities the emitted photon wavelength is adjusted by changing the electron-accelerator settings, while the FLASH2 facility features variable-gap undulators, allowing for quick change of the photon wavelength [101]. This possibility has been exploited for the measurements, presented in chapter 5.

While Eq. (3.7) describes the process of emitting synchrotron radiation by the relativistic electrons, free-electrons lasers, in contrast to synchrotrons, are partially coherent high-gain light sources, where the electrons emit in phase. The process leading to high gain and partial coherence is called microbunching and is a self-arrangement mechanism due to the ponderomotive back-action of the electromagnetic field on the electrons. The process causes the emergence of microbunches of electrons spaced at the radiation wavelength. The microbunching leads to increase in the radiation power, which in turn further amplifies the bunching as in a self-consistent feedback loop. If all electrons are bunched in phase, no further amplification is possible and the FEL process is saturated. The microbunching process starts from statistical fluctuations in the density of the electron beam, which are then self-amplified, thus coining the term self-amplified spontaneous emission (SASE) [102–104].

A characteristic feature of FEL radiation is the shot-to-shot fluctuation between different light pulses in intensity, temporal structure as well as spectral distribution, caused by the stochastic character of the SASE process. The temporal structure of an FEL XUV pulse can be retrieved by THz streaking [105]. Here, the kinetic energy of the photoelectrons ionized by the XUV pulse is modified by a superimposed THz streaking field. This allows for mapping of the temporal structure of the electron wave packet induced by the ionizing XUV field onto the photoelectron kinetic energy distribution after measuring the kinetic energy parallel and perpendicular to the THz polarization. On the other hand, XUV spectrometers, based on diffraction gratings and detection with a CCD camera, can measure the spectral structure of SASE pulses [106–109] on a shot-to-shot basis, revealing a distinct spikes in the spectrum.

The free-electron laser in Hamburg (FLASH)

The Free-electron LASer in Hamburg (FLASH) at DESY is a user facility providing very intense and ultrashort-pulsed XUV and soft x-ray radiation for light–matter interaction experiments with extremely intense and ultrashort-pulsed XUV and soft x-ray radiation. FLASH operates two parallel SASE beamlines, FLASH1 and FLASH2 [101], that share the same electron pulses. Radiation from the FLASH2 beamline with its variable gab undulators for precise and quick adjustment of the wavelength of the emitted light was used for the experiments presented in chapter 5. Figure 3.5 illustrates the main components of the FLASH facility. Details on the capabilities of the light sources at FLASH can be found in [101, 110],

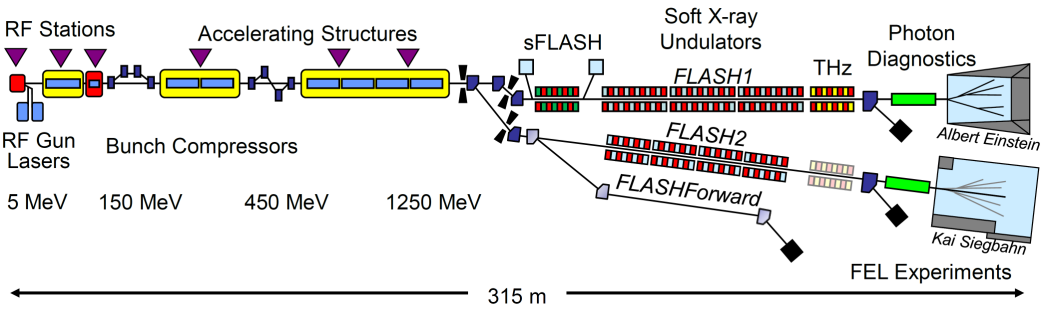

Figure 3.5: Schematic drawing of the main components of the Free-electron laser in Hamburg FLASH. The linear accelerator is shared for both beamlines FLASH1 and FLASH2, where the separation of the electron beam between both beamlines is enabled with a fast-switching magnet. The FLASH-REMI endstation FL26 used for the experiments presented in chapter 5 is located in the experimental hall "Kai Siegbahn" of the FLASH2 beamline. Figure reprinted from reference [110], licensed under CC BY 3.0.

while the following paragraph gives a short overview of the range of possible FLASH2 settings.

The possible wavelength range of light radiation provided by FLASH2 spans between 4 nm and 90 nm, which due to the shared electron accelerator is restricted between 1 and 3 times the wavelength at FLASH1 for simultaneous operation of both FLASH beamlines. Pulses with duration from 10 fs to 200 fs and energy ranging between 1 µJ and 500 µJ are provided in burst mode of 10 Hz, such that each pulse train in the burst contains pulses with 1 MHz repetition rate.

3.2.2 High-harmonic generation for the production of attosecond pulses

High-harmonic generation is a non-linear process for the production of XUV light pulses either in an attosecond pulse train or as a single isolated attosecond pulse [32, 111, 112].

The process of high-harmonic generation requires a strong driving pulse, typically an IR or NIR pulse centred at a wavelength of around 800 nm, focussed into a conversion gas medium at intensities of at least $10^{14}\,\mathrm{W/cm^2}$. With a peak field strength approaching the order of magnitude of the binding potential in the target, a laser pulse of this intensity considerably deforms the atomic potential, allowing a part of the valence-electron wave function to tunnel out into the continuum. The free electron is then accelerated away from the ionic core, gaining energy in the strong laser electric field. Upon reversion of the laser field direction after its oscillation-period maximum, the electron is decelerated, while being driven back towards the atom. The returning electron, having gained energy in the laser field, can radiatively

Table 3.1: Ionization potential I_p for neutral rare gas atoms, which are typically used as the conversion medium in the process of high-harmonic generation.

Species	Ionization potential, I_p	
	(eV)	(a.u.)
helium	24.59	0.9036
neon	21.56	0.7925
argon	15.76	0.5792
krypton	14.00	0.5145
xenon	12.13	0.4458

recombine with the atom, releasing energy equal to the sum of the gained kinetic energy E_{kin} and the ionization potential I_P:

$$\hbar\omega_{\text{HHG}} = E_{\text{kin}} + I_P. \tag{3.9}$$

where I_P depends on the used conversion medium. The ionization potential of the six noble gases typically used in HHG production are listed in table 3.1. The gained kinetic energy by the electron reaches a maximum, depending on the laser field strength, so that a cut-off in the frequency spectrum of the XUV radiation field appears at energies:

$$\hbar\omega_{\text{cut-off}} = 3.17U_P + I_P, \tag{3.10}$$

with U_P being the ponderomotive potential.

Despite involving highly non-linear light-matter interaction, including quantum-mechanical tunneling, the process of high-harmonic generation can, to a good approximation, be described by a quasi-classical three-step model, considering independent interaction of the laser field with the HHG target in separate steps [50, 113]. The three steps are illustrated in Fig. 3.6: the first tunneling step takes place usually at around the laser-field maximum, followed by the quasi-free propagation in the next three-quarters of a cycle until the recombination at nearly zero electric field strength. The three steps repeat every half a cycle of the driving laser field, so that a three-step process takes place twice per cycle. The light irradiated upon recombination from the different three-step processes can interfere, which due to the half-cycle periodicity leads to a harmonic spectrum, consisting of only the odd harmonics of the fundamental laser frequency spaced by $2\hbar\omega$.

In a semiclassical treatment of the HHG process [114], the strong-field approximation is applied to neglect the influence of the ion core after the tunneling ionization process [115, 116]. Here, the conversion medium is considered fully quantum-mechanically, such that the HHG process begins with part of the ground-state wave function being ionized, which then propagates in the continuum before it interferes with the remaining part of the wave function around the parent ion. This inter-

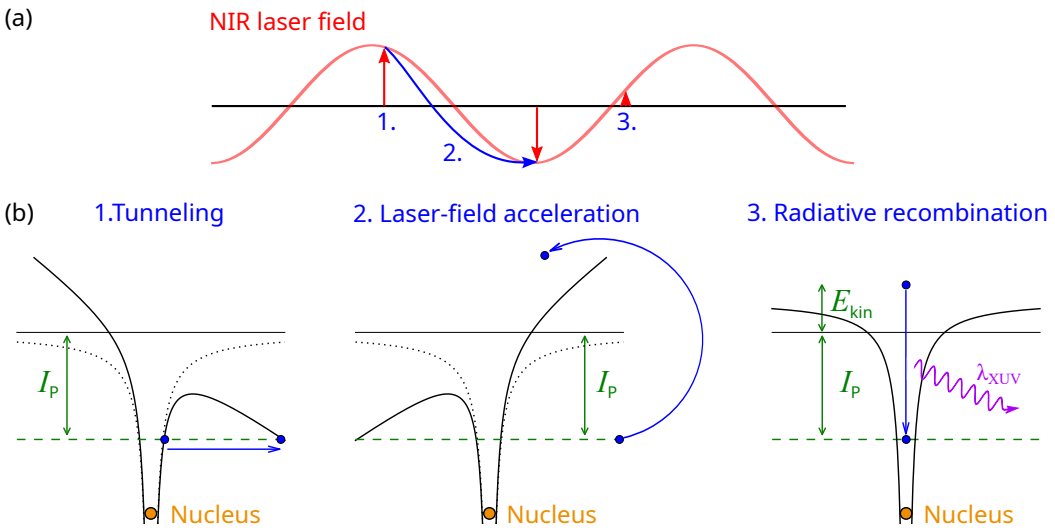

Figure 3.6: The three-step model of high-harmonic generation: tunneling, acceleration and radiative recombination. The points in time along the laser-field amplitude illustrated when the different steps take place.

ference induces a rapidly oscillating dipole moment which is the source for the emission of the high-energy harmonic radiation.

With a long incident pulse with many cycles, the emitted radiation appears as a comb of intense isolated harmonics of the driving laser, corresponding to an attosecond pulse train. To generate single XUV pulses with attosecond duration [117], on the other hand, few-cycle incident NIR pulses (only a few fs long) should be used in an intensity-gating [118] or a polarization-gating technique [119–122].

While ensuring excellent coherence and temporal properties of the produced XUV radiation, the process of high-harmonic generation in a gas conversion medium has a very low conversion efficiency, which in a simplistic argument could be understood due to the low tunneling probability and the low probability for radiative recombination, leading to conversion efficiency on the order 10^{-6}. Thus, HHG-produced XUV pulses with low intensity cannot initiate nonlinear processes and interaction with them can be treated in the context of perturbation theory. High-harmonic generation in liquids [123] or solid medium [124] are alternative approaches to improve the XUV photon flux.

4 EXPERIMENTAL INSTRUMENTATION

This thesis investigates two different two-electron targets - atomic helium and the hydrogen molecule - both of them in an excited state being influenced by an intense laser field. While in the case of helium the intense laser field ionizes the atom out of specifically prepared initial states, for H_2 a strong field is used only as a control knob to change an excited wave packet inside the molecule, leaving it intact after the interaction. The nature of those different kinds of experiments, one relying on ionization products as observables for helium, and another investigating a bound molecular system, requires different instrumentation to access the right observables. For the helium measurement of strong-field ionization out of doubly excited states a reaction microscope (REMI) capable of full-coincidence detection of ionization products has been used. For the control of an excited wave packet in the neutral hydrogen molecule, on the other hand, the bound state dynamics is accessed in an XUV time-domain absorption spectroscopy setup. This chapter presents the details on the experimental instrumentation utilised in both experiments, starting with the reaction microscope setup in section 4.1 followed by the description of the setup for XUV time-domain absorption spectroscopy in section 4.2.

4.1 The reaction microscope: an experimental setup for full-coincidence measurements of ionization products

A reaction microscope is a multi-particle coincidence spectrometer for kinematically complete studies of fundamental atomic and molecular processes [125]. It is an extension of Cold Target Recoil Ion Momentum Spectroscopy (COLTRIMS) [126] enabling the detection of all produced charged particles, ions and electrons, upon laser interaction as well as electron or ion impact [127]. The reaction fragments are accelerated onto large-area time- and position-sensitive detectors, measuring the time-of-flight (TOF) and the particle's impact position, from which the initial three-dimensional momentum vectors of the particle can be reconstructed to reveal information about the electronic structure of the investigated system as well as about the nuclear dynamics during reaction. The combination of a homogeneous magnetic and electric field makes a solid angle acceptance of 4π possible for both electrons and ions.

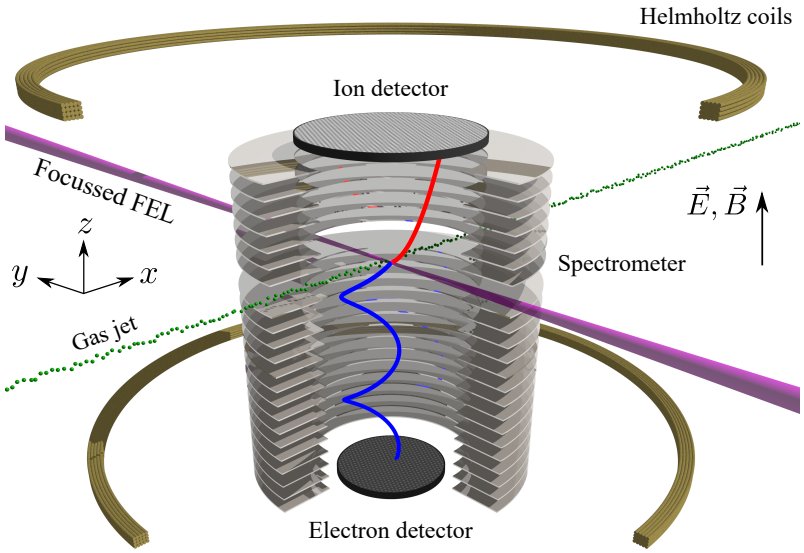

Figure 4.1: Illustration of the reaction microscope setup. The target gas jet propagates along the x-axis through the spectrometer, in the middle of which it meets the FEL beam propagating in $-y$ direction. The particles freed upon interaction are accelerated to the top (ion) and bottom (electron) detector by a homogeneous electric field produced by the spectrometer along the z-axis. The pair of Helmholtz coils around the spectrometer produces a homogeneous magnetic field in the interaction region, forcing the electrons and ions on curved trajectories and thereby preventing them to leave the REMI in transverse direction. Image adapted from Ref. [130] with permission.

A detailed description of the reaction microscope endstation FL26 at FLASH2, used as the experimental tool to investigate strong-field ionization out of selectively prepared doubly excited states in helium, is found in [128–130]. A schematic of the REMI setup is shown in Fig. 4.1 to illustrate its main components: a supersonic gas jet containing the target atoms or molecules and a time-of-flight spectrometer together with Helmholtz coils to guide the created ions and electrons to the respective detector on the opposite spectrometer ends. A short description of those main parts is provided in the present section.

4.1.1 Target delivery by a supersonic gas jet

In reaction-microscope experiments the target is typically in the gas phase and is prepared through supersonic gas expansion. In this process, gas from a high-pressure reservoir is expanded through a nozzle into vacuum, thus forming a supersonic jet by transforming the thermal energy of the gas particles into directed kinetic energy while cooling the particles. The final temperature in the jet depends on the gas medium, the nozzle diameter, the backing pressure and the initial temperature

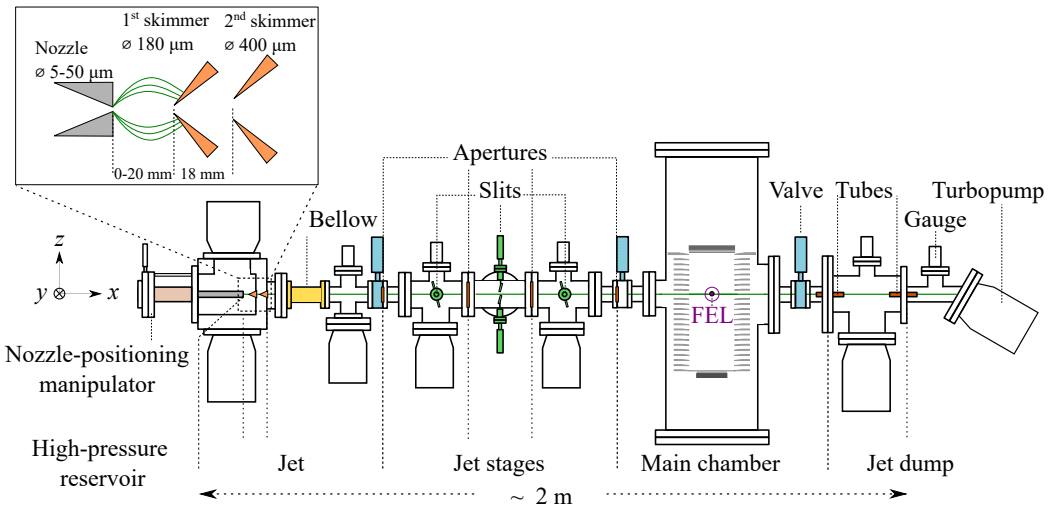

Figure 4.2: Schematic of the target-delivery apparatus with detail view of its components creating the supersonic gas jet. Figure adapted from reference [130].

of the gas before expansion [131]. Typical temperature of less than 20 K at a particle density of $\leq 10^{10}$ particles per cm^3 is achieved, ensuring well-defined initial target state and low enough target density allowing for single-event detection.

The apparatus producing the supersonic gas jet at the reaction microscope at the FLASH2 endstation consists of six differentially pumped vacuum stages, Fig. 4.2. After its initial creation through expansion in vacuum from a high-pressure reservoir, the gas jet passes through a set of conical skimmers for selection of the cold gas particles and through apertures, serving as differential pumping stages before entering the main spectrometer chamber. Additional pairs of slits allow for tuning of the target density in the jet through change of its divergence in the plane perpendicular to the jet propagation direction. Neutral particles, which have not been ionized in the interaction region, are collected in a jet dumb.

4.1.2 Charged-particle spectrometer

The purpose of the spectrometer in the reaction microscope is twofold: on the one side, it has to guide all created charged particles in the interaction region to their respective detector, and on the other side, it should separate the particles by species. Both of these requirements are enabled by the application of a homogeneous electric field along the spectrometer axis. This electric field accelerates the ions and electrons in opposite direction towards the corresponding detector. The orientation of the electric field is along the z-axis, such that the ions are guided to the top and the electrons to the bottom detector. The separation by species is achieved through the different time-of-flight t_{TOF}, depending on the mass-to-charge ration of the ions

created at the laser interaction position:

$$t_{\mathrm{TOF}} = d\sqrt{\frac{2m}{qU}} \propto \sqrt{\frac{m}{q}}, \tag{4.1}$$

where m and q are the mass and charge of the ion, respectively, U is the applied voltage and d is the distance between the interaction position and the detector. No field-free drift region for time focussing [132] is implemented in the spectrometer, since the FEL focal spot with a diameter of $< 10\,\mu\mathrm{m}$ defines a sufficiently small interaction region as a starting point of the created electrons and ions.

The spectrometer, sketched in Fig. 4.3, consists of 22 equidistantly spaced ring-like steel plates across the overall $\approx 275\,\mathrm{mm}$ spectrometer length, with the exception of the two plates around the reaction point, which have the double spacing to allow the FEL beam to reach the interaction region without scattering. To create the electric field in the spectrometer, external voltage is applied to the uppermost and lowest spectrometer rings. Because two neighbouring rings are connected via $100\,\mathrm{k}\Omega$ resistors, a constant voltage gradient is created along the whole spectrometer length. The homogeneous electric field extends to both ends of the spectrometer due to the high-transmission gratings (transmission $\sim 80\%$) positioned between the spectrometer electrodes and the two detectors. The gratings shield the electric field from distortions due to the high detector voltages. Additional gratings on both spectrometer ends are mounted behind the transmission gratings but before the detectors for post-acceleration of the ions and electrons to their respective detector, which ensures better detector sensitivity.

The distance between the interaction region and the electron detector is roughly two times longer than the distance to the ion detector. This allows for longer flight times of the electrons to the detector, and therefore for better momentum resolution. The electric field applied for the conduction of the experiment presented in chapter 5 is around $127\,\mathrm{V/m}$. For the collection of the electrons, additionally a homogeneous magnetic field is applied along the spectrometer axis, which forces the electrons (and ions) onto a spiral trajectory towards the detectors, such that a 4π acceptance angle is also reachable for the electrons. The magnetic field, typically on the order of 10 Gauss, is generated by a pair of Helmholtz coils positioned around the spectrometer.

4.1.3 Particle detectors

The time-of-flight and the impact position of the electrons and ions is detected by large-area detectors, consisting of two main components: charge-multiplying microchannel plates (MCPs) for the TOF extraction and delay-line anodes positioned behind the MCPs for the position information. An overview of the detector assembly and its working principle is shown in Fig. 4.4.

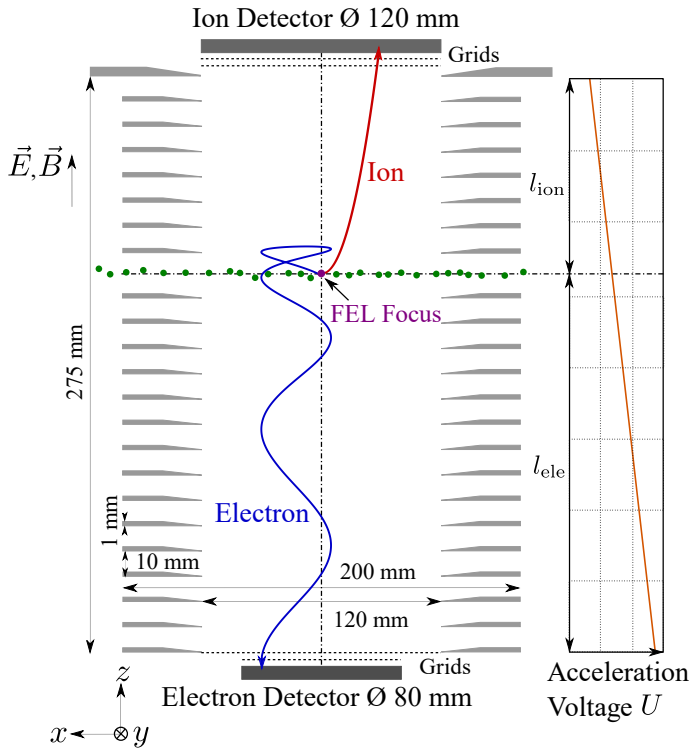

Figure 4.3: Sketch of the reaction-microscope spectrometer illustrating its working principle to guide the electrons and ions created in the interaction region towards their respective detector. Figure reprinted with permission from reference [130].

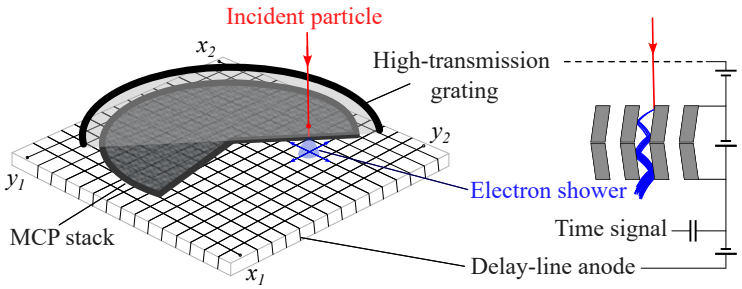

Figure 4.4: Illustration of the working principle of the particle detector, consisting of a stack of MCPs for TOF detection and delay-line anodes for position extraction. An incident particle, here an ion, hits the high-transmission grating and is accelerated towards the MCP stack, were it causes an electron shower (blue), delivering both the time signal and the raw position signal (blue arrows) travelling towards the ends of the two perpendicularly to each other arranged delay-line anodes, with ends x_1 and x_2 and y_1 and y_2, respectively. Figure adapted from reference [130].

The ion detector includes a stack of two MCPs with a diameter of 120 mm, arranged in a chevron configuration, and a delay-line anode consisting of two perpendicularly oriented quadratic wire layers (quadanode). For better multi-electron hit sensitivity also to very low-energy electrons, the electron detector is equipped with three 80-mm MCPs in a Z-arrangement and a delay-line hexanode, made of three wire layers rotated by 60° relative to each other. This arrangement improves the detection efficiency for simultaneous particle hits through the redundancy of the layers [133].

4.1.3.1 Microchannel plates for time-of-flight extraction

A microchannel plate is a large array of micrometer-size electron multipliers embedded in a thick glass disk with electrodes on its front and back side [134]. When an incident charged particle hits the wall of a channel in the MCP, it creates secondary electrons, which are accelerated between the two electrodes with a potential difference of typically around 3 kV. After multiple hits on the inner side of the microchannels, the initial signal is amplified by a factor of 10^4 until the cloud of secondary electrons leaves the MCP on the back side. A tilt of all channels of typically 8° to the surface normal ensures that a hit of a wall in the MCP will happen to trigger the avalanche process. Further amplification of the signal is achieved by stacking a second MCP behind the first one, in a V-shape orientation of the channels of the two plates. This *chevron* geometry enhances the gain to $10^5 - 10^6$ [135] and ensures that each incoming particle will hit a wall in the channels of one of the two MCPs, while reducing background signal from ions created by electron impact ionization inside the channels. The addition of a third MCP to the stack, as in the electron detector, enables reaching a gain of more than 10^7.

The electron avalanche caused by a particle hitting the MCP configuration leads to a drop in the MCP voltage, which is registered as a measured signal. This voltage drop, referenced to the FEL trigger, corresponds to the time-of-flight of the incoming particle (ion or electron):

$$t_{\mathrm{TOF}} = t_{\mathrm{MCP}} - t_{\mathrm{trigger}}. \tag{4.2}$$

Imaging the MCP onto a phosphor screen would also make extraction of position information possible directly out of the MCP signal, since every electron avalanche is localised inside one of the MCP channels. Velocity map imaging, where a lot of different particles can be detected simultaneously, for example, makes use of this imaging technique [136, 137]. In a reaction microscope measurement, with the aim of a kinematically complete coincidence experiment, single particle resolution and readout is required, such that delay-line anodes are preferred for the electron cloud imaging [138].

4.1.3.2 Delay-line anodes for position detection

A delay-line anode is a long copper-alloy wire wound around an insulator [139], set at a positive voltage with respect to the rear side of the MCP stack in order to attract the electron cloud leaving the MCP. Arriving at the delay line, the electron cloud induces a signal, which propagates with a constant velocity v_w towards both ends of the wire. To obtain two-dimensional position information, a second wire layer, mounted perpendicularly to the first one, is needed [140]. The x and y coordinates of a hit on such a quadanode are given by [141]

$$x = \frac{v_{\mathrm{w}_x}}{2}(t_{x_1} - t_{x_2}) \quad \text{and} \quad y = \frac{v_{\mathrm{w}_y}}{2}(t_{y_1} - t_{y_2}), \tag{4.3}$$

with arrival times of the signal on each wire to one of its two ends $t_{x/y_{1/2}} = t^*_{x/y_{1/2}} - t_\mathrm{MCP}$ with respect to the MCP timing signal t_MCP. The effective propagation velocity v_w is extracted from the detector size.

Typically, each anode layer consists of two parallel wires: a signal and a reference wire. The signal wire, set to a more positive potential, attracts the electron cloud, whereas the reference wire records the signal from noise at the same time. Electronic subtraction of the reference from the signal delivers a noise-reduced signal.

To allow for detection of delay-line signals closer in time than the signal run-time on the wire, the time-sum condition, stating that the overall run-time towards both wire ends is constant for one wire, has to be fulfilled [133]:

$$t_\mathrm{sum} = t_1 + t_2 = \text{const.} \tag{4.4}$$

Adding a third wire layer, as in the hexanode used at the electron detector, the hit-position (x, y) of the electrons is determined from the combination of two of the three layer coordinates u, v and w [133]

$$\begin{aligned} x_{uv} &= u & x_{uw} &= u & x_{vw} &= v - w \\ y_{uv} &= \frac{1}{\sqrt{3}}(u - 2v) & y_{uw} &= -\frac{1}{\sqrt{3}}(u + 2w) & y_{vw} &= -\frac{1}{\sqrt{3}}(v + w) \end{aligned} \tag{4.5}$$

for the coordinate orientation sketched in Fig. 4.5(a).

To combine the position information from Eq. (4.5) to one pair of (x, y) coordinates, the positions calculated from any combinations of pairs must overlap. This is possible when scaling all hexanode coordinates u, v and w with scale factors f_u, f_v and f_w as well as through adding an offset a to one of the coordinates. With those additions, the wire coordinates are then calculated similarly as in Eq. (4.3):

$$u = \frac{v_u}{2} f_u (t_{u_1} - t_{u_2}), \quad v = \frac{v_v}{2} f_v (t_{v_1} - t_{v_2}) \quad \text{and} \quad w = \frac{v_w}{2} f_w (t_{w_1} - t_{w_2}) + a_w. \tag{4.6}$$

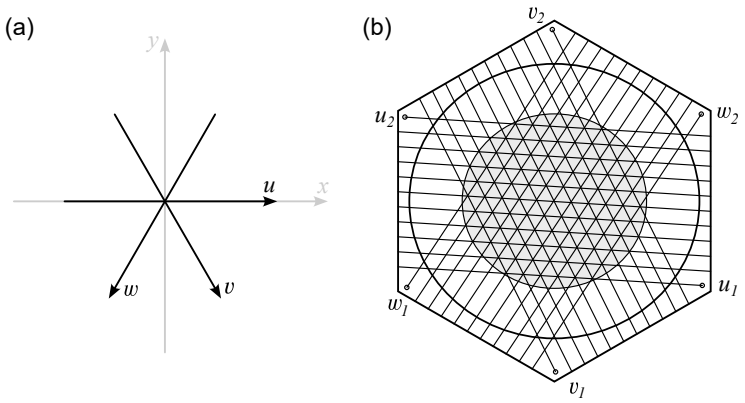

Figure 4.5: Sketch of the delay-line hexanode used for position determination of particle hits at the electron detector. **(a)** Coordinate arrangement for a hexanode delay line. **(b)** Wiring principle of the delay-line hexanode.

Here, $t_{u/v/w_{1/2}}$ are the propagation times of the signal to both ends of the respective layer u, v or w, as shown in the hexanode sketch in Fig. 4.5(b). To determine the scale factors, the x or y values calculated from the different combinations are plotted against the difference of the values of the other two combinations, while varying the parameters such that the difference is 0 for all coordinate values.

From the obtained time-of-flight and position information for each particle the initial momenta of the ions and electrons are reconstructed, as described in section 5.2.

4.2 The attosecond beamline: an experimental setup for XUV time-domain absorption spectroscopy

A typical XUV time-domain absorption spectroscopy setup consists of four main parts: an XUV source, a time-delay unit for precise time adjustment of the used laser pulses, a target interaction region and a suitable XUV spectrometer. Figure 4.6 shows a 3D model of the beamline depicting those key components of the setup, while Fig. 4.7 illustrates their function. A detailed review of the beamline and its full capabilities is presented in reference [3], while the following only discusses the main components of the XUV time-domain absorption spectroscopy setup.

4.2.1 Generation of attosecond XUV pulses

The first crucial component in an XUV spectroscopy setup is the XUV source. Here, attosecond pulses are generated in the process of high-harmonic generation by focusing intense laser light on a rare-gas conversion medium. For this, the laser

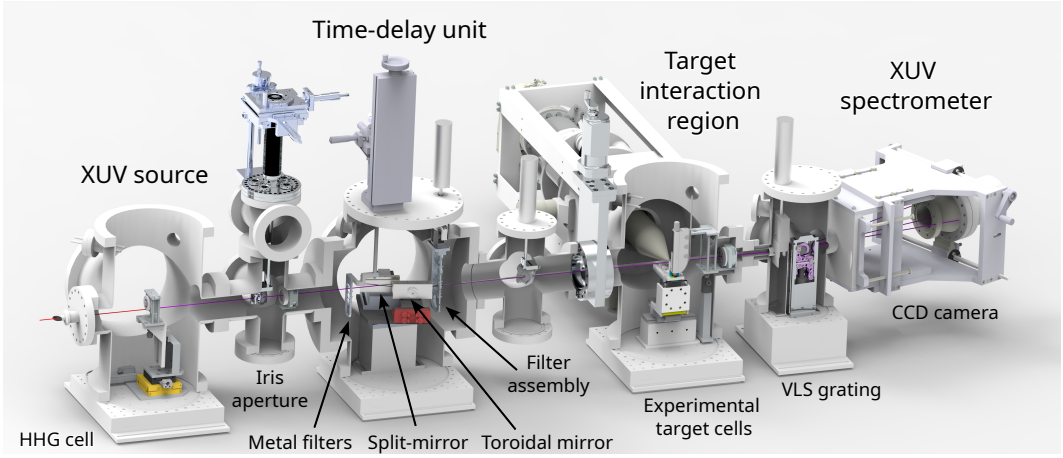

Figure 4.6: Setup for XUV time-domain absorption spectroscopy, with its four main parts: an XUV source, a time-delay unit for time-delay control between the used laser pulses, a target interaction region and an XUV spectrometer, all indicated in the upper part of the figure. The main setup components described in this section are depicted on the bottom of the 3D model of the beamline.

pulses delivered by the laser setup, described in detail in chapter 3.1.2, are focused down to a spot size of $\approx 60\,\mu m$ in the middle of the first vacuum chamber of the beamline, called the HHG chamber, where a gas cell containing the HHG conversion medium is placed. The gas cell made of the glass-ceramic MACOR® has an inner diameter of 2 mm and machine-drilled wholes with 150 µm diameter for the laser beam to pass through. This material has been chosen because of its heat and radiation resistance [142] making the gas cell more durable than stainless steel cells, which are easily damaged by the high laser intensity in the focus. With pulse energy up to 1 mJ, peak intensities between 10^{14} and $10^{16}\,W/cm^2$ are reached in the focus of the beam. The intensity is very much dependent on the NIR focal spot size, which can easily be tuned with an iris aperture positioned in the far field of the beam outside the HHG chamber. For the experiment presented in chapter 6 this iris aperture was partially closed, thereby enlarging the focus size and reducing the intensity, which is necessary in order to reduce plasma production in the rare-gas conversion medium, chosen to be xenon for high low-order harmonics efficiency. With the intensity adjustment and precise positioning of the gas cell along the laser propagation direction, as well as tuning of the wedges in front of the beamline for shortest laser pulses, best conversion efficiency was found for a backing pressure of 65 mbar.

4.2.2 NIR intensity control

After the generation of XUV light in the HHG process in the first part of the experimental setup, both the HHG-driving NIR pulse and the XUV pulse propagate temporally locked and spatially overlapped through the beamline. The two of

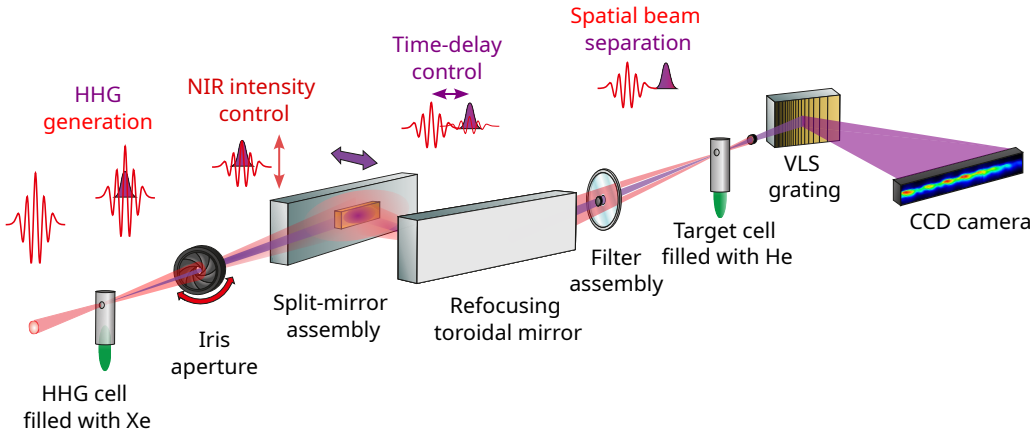

Figure 4.7: Schematic illustration of the components in the experimental setup together with their influence on the NIR (red) and XUV (violet) beams, depicted through the shown pulse configurations in the upper part of the figure.

them pass through a closed-loop motorized iris aperture concentrically placed in the combined beam path. Due to the considerable wavelength difference between the XUV and NIR radiation the divergence of both beams differs significantly, ≈ 1 mrad for the XUV compared to ≈ 15 mrad for the NIR for the focussing geometry of the beamline, therefore the iris aperture can be used to concentrically cut a variable fraction of the larger-diameter NIR beam and with this control its intensity without affecting the XUV beam. A calibration of the NIR intensity in the target region as a function of the iris opening is presented in the section on experimental details in chapter 6.

4.2.3 Time and space separation of the XUV and NIR pulse

Before reaching the target interaction region, the co-propagating NIR and XUV pulse have to be separated in time and space to make time-resolved experiments possible. The time delay between the two pulses is adjusted by the split-and-delay unit, which is an interferometric mirror setup, consisting of a pair of flat mirrors. Just as for the NIR intensity control, the time-delay unit also takes advantage of the different divergence of the NIR and XUV light. Therefore the unit consists of an outer and an inner mirror, reflecting predominantly the NIR and XUV beam, respectively. The precise adjustment of the time delay is controlled by moving the smaller inner mirror on a piezo stage in or out in the plane perpendicular to the reflecting surface of the outer mirror. This movement introduces a path length difference of the XUV beam compared to the constant path length of the NIR beam and thereby a time delay between the two pulses. The relation between the displacement of the inner mirror and the introduced time delay for the incident angle $\theta = 15°$ was calibrated with a helium-neon (HeNe) laser to $\tau/\Delta d = 1.701\,\mathrm{fs}/\mu\mathrm{m}$. The analysis of the intensity-modulation of the HeNe laser, reflected by the split-mirror arrange-

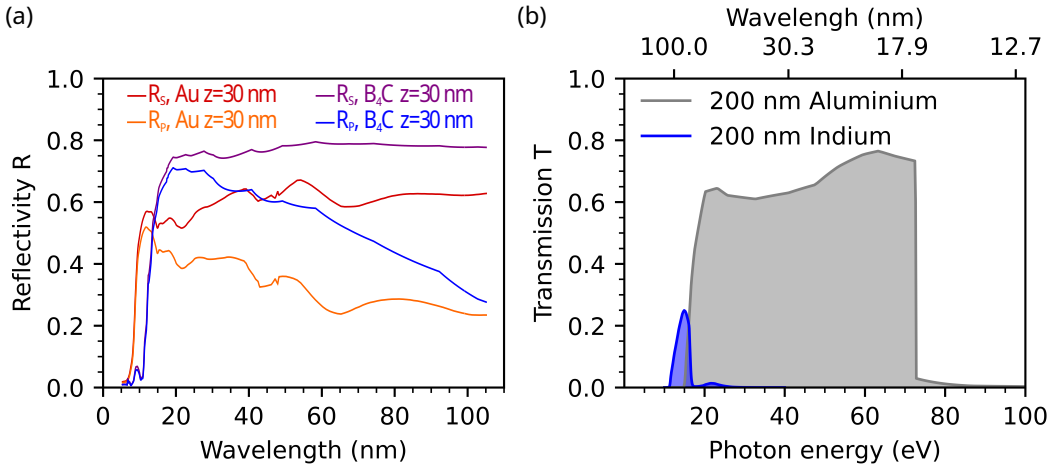

Figure 4.8: Reflectivity and transmission of XUV optical components. **(a)** Reflectivity of gold (Au) and boron carbide (B_4C) coatings of 30 nm thickness for *s* and *p* polarization of light incident under 15 deg gracing incidence. Data provided by optiXfab GmbH. **(b)** Transmission curves for 200 nm metal foil filters typically used in the XUV absorption beamline. Data from [143].

ment, determined also the interferometric stability of the split-and-delay unit to be 26.9 as [3]. For better reflectivity in the respective spectral range, the outer mirror is silver coated, whereas the coating of the inner mirror is of boron carbide (B_4C), which, compared to the gold coating previously used, see Fig. 4.8 (a), has a considerably better reflectivity in the low-photon-energy range, the spectral range of the experiments, presented in chapter 6. At the same time, B_4C has lower reflectivity for the NIR, which considerably reduces the intensity of the NIR reflected off the inner mirror and co-propagating with the XUV light [87]. To block this remaining NIR light and the XUV reflected off the outer mirror, after refocusing by a gold-coated toroidal mirror installed in a 1:1 focusing geometry (f = 350 mm by OptixFab®), the co-propagating beams pass through a filter unit of concentrically arranged filters. The inner filter, mounted on a home-built filter support, is a metal foil filter provided by LEBOW® Company, which blocks the NIR, but is transparent in a certain XUV range, depending on the material. Typically, here 200 nm aluminium foil filters are used in the spectral range above 17 eV, but for the experiments in the energy range of the singly excited states in H_2, 200 nm indium filters, with considerably worse transmission efficiency than aluminium had to be used, see Fig. 4.8 (b). The outside filter is an organic material, either 2 µm nitrocellulose membrane by National Photo Color® with a 2 mm concentric hole, or a 7 µm Kapton foil mounted concentrically around an aluminium filter. For the experiments in this thesis, the combination of a nitrocellulose membrane with an indium filter was preferred. It has also the advantage of introducing less group delay and group delay dispersion to the NIR pulse due to its lower membrane thickness.

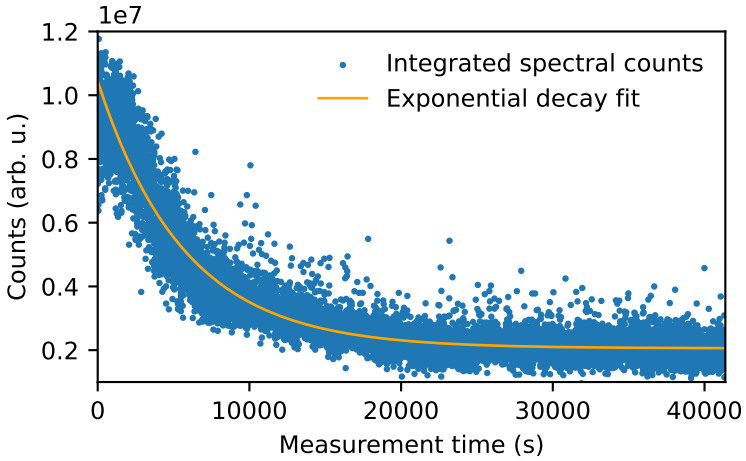

Figure 4.9: Spectral counts integrated over the whole detected photon-energy region as a function of measurement time in seconds. The decaying data signal (blue) is fitted with an exponentially decaying function to extract the decay time of the reflectivity of the XUV mirror.

During the experiments in the low-energy spectral range 12 – 17 eV, a disadvantage of having the filter array mounted after the mirror assembly became apparent. Due to the high low-harmonics rate in the xenon conversion medium, a fast degrading of the reflectivity of the inner mirror and the toroidal mirror was noticed, which over the time of the experiment lowered the detected XUV counts. Figure 4.9 shows the overall detected counts in each acquired spectrum as a function of measurement time in one measurement run together with a fit of an exponentially decaying function. The decay constant determined to be (5674 ± 28) s/counts accounts for the decay rate of the XUV optics. The most obvious short-term solution at first was to exchange all mirrors, both the inner and outer mirror, as well as the toroidal mirror with new ones directly before the experiment, which very much improved the XUV detection. A long-term solution, realised after the measurement campaign was the design of a filter array, which can be installed in front of all mirrors in the beamline, as shown in the 3D model of the mirror chamber in Fig. 4.6. Here, the metal foil filters mounted on home-built filter holders already block the remaining NIR light as well as the low-energy XUV.

4.2.4 Target interaction

After adjusting the desired time delay between the NIR and XUV pulse, both beams are then focused into a gas cell containing the target medium. The target cell used for the experiments presented in chapter 6 has the same design as the HHG cell, but is mounted on a high-precision high-velocity closed-loop XYZ stage, allowing for precise and reproducible positioning of the target cell in the overlapping foci of the XUV and NIR beams. The closed-loop position determination allows for a

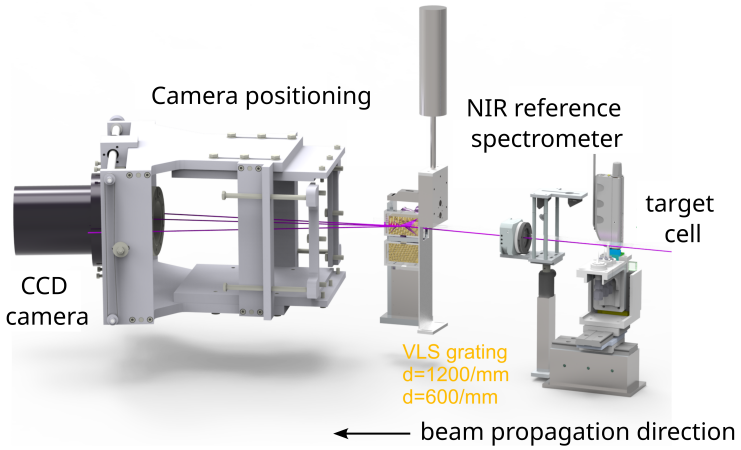

Figure 4.10: Schematic drawing of the XUV spectrometer, showing its main components, as well as the target cell. Figure adapted from [75].

measurement mode of taking the target cell in and out of the beam focus in order to sequentially measure absorption and reference spectra for optical density determination. Similarly, with the nm-precision of the stage positioning, also a small correction of the target position perpendicular to the beam propagation direction can be introduced, in order to correct for the walk-off of the XUV focus with respect to the NIR focus when adjusting a specific time delay through movement of the inner mirror. This cell-tracking procedure effectively extends the accessible time-delay range to about 80 fs compared to the range of 60 fs otherwise [144].

Additionally to the aforementioned absorption cell, two different cell designs, not used in the scope of this thesis, were developed: on the one hand, the *in situ* reference cell for simultaneous measurement of absorption and reference spectra [3], and on the other hand, the hybrid cell for simultaneous measurement of a streaking trace and absorption data [87, 145]. While the *in situ* reference cell used in a combination with a transmission electron microscopy (TEM) grid with suitable grid constant allows for the simultaneous measurement of absorption and reference spectra with sensitivity of the obtained absorption signal down to the order of mOD, its use proved very difficult in the energy region below 17 eV because of the low transmission efficiency of the indium filters used, which then forces for data taking on the order of minutes for just one spectrum. For this reason, the standard absorption cell was preferred. In a succeeding study, the hybrid cell might be used for experiments allowing also for detection of ionized electrons or ions out of the hydrogen molecule, opening the possibility to detect and analyse bound state transitions spectroscopically and ionized products of the NIR interaction in a time-of-flight measurement.

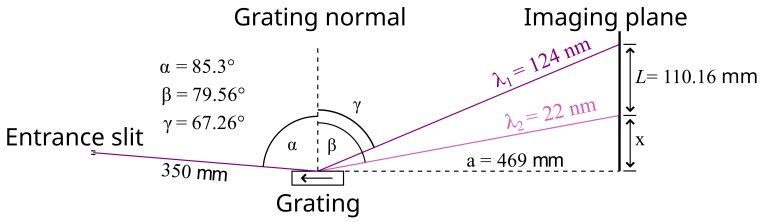

Figure 4.11: Imaging geometry of the VLS grating spectrometer. The flat-field grating spectrally disperses the incident light on a flat imaging plane across the distance L. The angles α,β,γ denote the incidence angle, the maximal and the minimal angle of diffraction in the first diffraction order in the region for which the grating is specified. To achieve best resolution a careful alignment according the specified geometry is required.

4.2.5 Flat-field XUV spectrometer

The spectrometer for XUV light detection consists of two aberration corrected, concave gratings by HITACHI® [146] that can be used interchangeably depending on the desired spectral range either $10-56\,\mathrm{eV}$ or $20-112\,\mathrm{eV}$, and a thermo-electrically cooled, back-illuminated CCD camera, PIXIS series by Princeton Instruments®, Fig. 4.10. Despite the drop of grating efficiency for higher spectral energies even measurements at photon energy up to $180\,\mathrm{eV}$ are possible with this kind of gratings in a spectrometer given a suitable XUV source [147, 148]. The grooves of the gratings are edged with variable line spacing (VLS) such that the spectra are focused on a flat field instead on a Rowland circle as for a grating with fixed line spacing. This allows for imaging on the flat camera chip without blurring of the signal. The whole camera can be moved along the imaging plane on a home-built mount to access the whole accessible spectral region with either one of the spectrometer gratings, which is necessary due to the small chip size of the camera not being able to cover the whole resolved spectrum at once. On the other hand, the 1340×400 pixels with a size of $20\,\mu\mathrm{m} \times 20\,\mu\mathrm{m}$ allows for remarkably good resolving power in the XUV of $E/\Delta E > 1500$. After careful alignment of the CCD camera in the focal plane of the grating according to the specified grating geometry, Fig. 4.11, for the measurements presented in chapter 6 in the spectral range $12-17\,\mathrm{eV}$ a resolving power of better than 4000 was achieved, corresponding to a resolution of less than $5\,\mathrm{meV}$.

5 STRONG-FIELD IONIZATION OF FEL-PREPARED DOUBLY EXCITED STATES IN THE HELIUM ATOM

An initial step towards the goal to control the quantum dynamics of any atomic or molecular system in a desired way is the development of understanding of the complex dynamics in multi-electron systems exposed to external electromagnetic fields. In a bottom-up approach, studies of the simplest atomic system of this kind, the helium atom, give first insight into electron-correlation effects in their great complexity [48, 149–154]. In this context, photoionization is one of the most fundamental electronic processes, the dynamics of which are fully encoded in the released electron (wave packet) as well as in the final ionic state. The properties of those are directly accessible in full-coincidence experiments [127] applied broadly together with other electron-detection techniques as time-of-flight and velocity-map-imaging spectroscopy, to capture the ionization dynamics through the direct detection and characterization of the outgoing electrons [155–159]. A complementary approach, keeping track of the bound-state dynamics and couplings between states by identifying absorption lines and their changes upon light-matter interaction is the all-optical technique of transient-absorption spectroscopy (TAS) [153, 160, 161].

Theoretical investigations on helium solve the time-dependent Schrödinger equation of the system under laser interaction either in its full dimensionality [151] or for models with reduced complexity [162–164], or specifically address the structure of the excitation spectrum [165], to examine the effect of light-matter interaction on observables accessible in the previously mentioned experiments. Typically, the effects of strong IR fields on the electron dynamics have been studied starting from the ground state influenced by a single (N)IR laser pulse [162, 163] or a combination of an NIR and a time-delayed extreme ultraviolet (XUV) pulse [166–168] or a single or two XUV pulses [169–171].

This chapter summarises the results of a project studying the ionization out of specifically excited states in the atomic benchmark system helium. The excited states under consideration here are doubly excited autoionizing states, created through the interaction of a narrow-band XUV pulse produced by the free-electron laser source in Hamburg FLASH. A moderately intense IR pulse then causes ionization behaviour out of the excited states. The aim of the project is to discover the dominating ionization processes taking place, differentiating between single and

double ionization, both detected in a full-coincidence reaction-microscope experiment. This interplay between single and double ionization in doubly excited states but also in singly excited states of helium was studied in a prior theoretical project. Its main results, published in a recent publication [2], showing increased double-ionization yield for doubly excited states motivated the experimental investigation of ionization out of selectively prepared doubly excited states.

5.1 Motivating theoretical study of single and double ionization in He out of specifically excited states

The experiment presented in this chapter, was motivated by a theoretical study comparing single and double ionization from single and double excitations in a two-electron helium-like model atom. This section summarizes the results of this study following closely the original publication:

Strong-field-induced single and double ionization dynamics from single and double excitations in a two-electron atom

Gergana D. Borisova, Veit Stooß, Andreas Dingeldey, Andreas Kaldun, Thomas Ding, Paul Birk, Maximilian Hartmann, Tobias Heldt, Christian Ott and Thomas Pfeifer

Journal of Physics Communications **4,** 055012 (2020).

Concentrating on the electron dynamics in excited states accessible from the ground state via dipole-allowed transitions, this study considers both single and double excitations as the initial states in laser-induced strong-field ionization. Both single and double ionization contribute as ionization mechanisms in the two considered initial-state cases. Double ionization, however, is considerably enhanced for doubly excited states (DESs) compared to singly excited states (SESs), with both direct and sequential processes contributing to the enhanced double-ionization yield as a result of interaction with a moderately intense NIR field with intensity $I_{\mathrm{NIR}} \sim 10^{13}\,\mathrm{W/cm^2}$.

5.1.1 Two-electron model system

To investigate the dynamics of strong-field ionization arising from single and double excitations in a helium-like model system, a numerical approach for the solution of the time-dependent Schrödinger equation (TDSE) for two electrons in a linearly polarised laser field is adopted, allowing to restrict the motion of each of the electrons to a one-dimensional (1D) discretized grid. After separation of the electronic and nuclear degrees of freedom, the motion of the nucleus is not considered further. The described grid-based simulation approach is based on a non-perturbative two-electron model [172, 173]. It comprehensively accounts for full electron-electron correlation, as well as for both linear and non-linear light-matter interaction under the influence of an external laser field.

The non-relativistic Hamiltonian of the model system in the length gauge of the dipole approximation (in atomic units) takes the form

$$\mathscr{H}(x_1, x_2, p_1, p_2; t) = \frac{1}{2}\sum_{i=1}^{2} p_i^2 - \sum_{i=1}^{2} \frac{2}{\sqrt{x_i^2 + a^2}} + \frac{1}{\sqrt{(x_1 - x_2)^2 + b^2}} + (x_1 + x_2)E(x_0, t). \tag{5.1}$$

All electromagnetic interactions are given by the Coulomb force, including the interaction between the two electrons. Each Coulomb potential, approximated by a Rochester one-dimensional potential [174, 175], is modified by a soft-core parameter, a for the electron-nucleus interaction and b for the electron-electron repulsion. All results presented in the following were obtained for $a = b = 1\,\mathrm{a.u.}$ The choice for the values of the soft-core parameters changes slightly the energies of the bound states in the model atom, compared to a real helium atom.

The NIR laser field, interacting with the model system, is approximated by an oscillating cosine wave under a Gaussian envelope as

$$E(x_0, t) \equiv E(t) = E_0 \cos(\omega t + \phi) \mathrm{e}^{-\left(\frac{t-t_0}{\tau_\mathrm{G}}\right)^2}, \tag{5.2}$$

with E_0 being the maximum of the electric field strength, ω the laser frequency, ϕ the carrier envelope phase of the pulse and τ_G the Gaussian width of the pulse. The duration of the laser pulse τ_P, defined as the full width at half maximum (FWHM) of $|E(t)|^2$, is connected to the Gaussian width through $\tau_\mathrm{P} = \sqrt{2\ln 2}\tau_\mathrm{G}$. Here, only the electric-field component of the electromagnetic field with polarization parallel to the direction of the electrons' motion is considered, since the electrons have no access to the perpendicular space direction. The magnetic field, with two orders of magnitude smaller amplitude than the electric field ($E_0/B_0 = c = 137$; in atomic units), is therefore neglected in the model.

With the Hamiltonian of the model system at hand, Eq. (5.1), including also laser interaction, the time-dependent Schrödinger equation

$$i\frac{\partial}{\partial t}|\psi(x_1, x_2; t)\rangle = \mathscr{H}(x_1, x_2, p_1, p_2; t)\,|\psi(x_1, x_2; t)\rangle \tag{5.3}$$

is solved via a split-step algorithm method with second order accuracy [176]. Here, $|\psi(x_1, x_2; t)\rangle$ denotes a time-dependent state vector of the model system and the TDSE solution gives the time evolution of this state. The time-evolution operator, making use of the separation of the system's Hamiltonian into a spatial and momentum part takes the form

$$U(t + \Delta t, t) = e^{-i\left(\mathscr{H}_p(t) + \mathscr{H}_x(t)\right)\cdot\Delta t} = e^{-\frac{i}{2}\mathscr{H}_x\Delta t} e^{-i\mathscr{H}_p\Delta t} e^{-\frac{i}{2}\mathscr{H}_x\Delta t} + O(\Delta t^3), \tag{5.4}$$

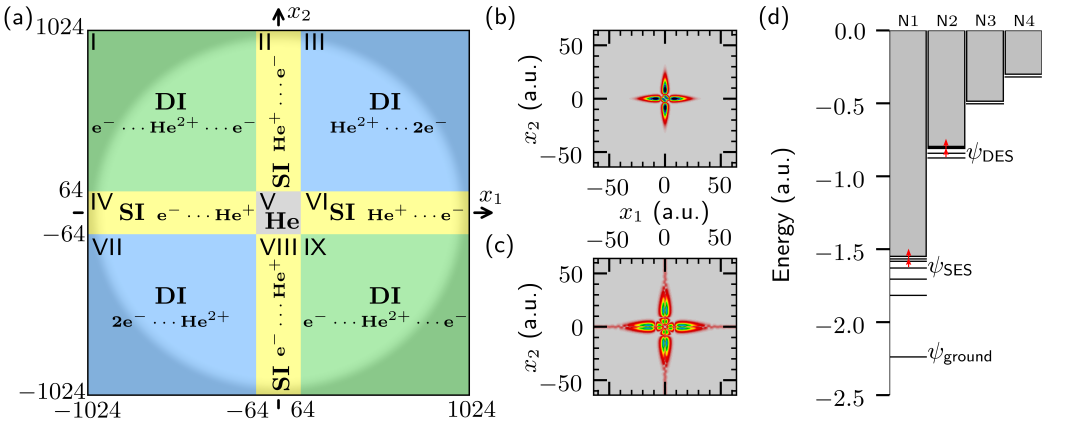

Figure 5.1: Wave function partition scheme. **(a)** Partition scheme of the two-electron wave function, represented on a two-dimensional grid: Section V (grey) specifies the extension of the neutral atom. Sections II, IV, VI, VIII (yellow) are populated in case of single ionization (SI), while population of sections I, III, VII and IX means double ionization (DI). The shadowed region displays the absorbing boundary around the edges of the grid. **(b)** and **(c)** Spatial representation of the wave function of the considered singly and doubly excited state, respectively. (d) Energy-level diagram of the model system with indicated energy position of the two compared states. The red arrows illustrate two-photon ionization due to the NIR laser field with photon energy centred at $\omega = 0.064\,\mathrm{a\,u}$

such that the propagation of the wave function for one time-step Δt becomes

$$|\psi(t+\Delta t)\rangle = e^{-\frac{i}{2}\mathscr{H}_x\Delta t}\,\mathscr{F}^{-1}\,e^{-i\mathscr{H}_p\Delta t}\,\mathscr{F}\,e^{-\frac{i}{2}\mathscr{H}_x\Delta t}|\psi(t)\rangle\,, \tag{5.5}$$

where the Fourier transform and its inverse $\mathscr{F}$ and $\mathscr{F}^{-1}$ are applied for the transformation between position and momentum space in the two directions.

The time-dependent wave function of the model system in position space $|\psi(x_1,x_2;t)\rangle$ is represented on a discrete 4096×4096 grid with complex number entries at each grid point $\boldsymbol{x} = (x_1,x_2)$. For each position, the absolute squared value of the complex number entry gives the local electron probability density. The coordinates x_1 and x_2 span between $-1023.5\,\mathrm{a\,u}$ and $1024\,\mathrm{a\,u}$ with $\Delta x_i = 0.5\,\mathrm{a\,u}$. To avoid propagation of the wave-function probability density over the edge of the grid, and to additionally account for ionization effects, a cylindrically symmetric imaginary potential $\mathscr{V}$ is included to absorb the electron probability density at the outer boundary of the grid. The absorbing boundary as a function of $r = \sqrt{(x_1^2+x_2^2)}$ is defined as

$$\mathrm{Im}(\mathscr{V}) = \begin{cases} -\cos^2\left(\frac{\pi}{2}\frac{r}{(R_{max}-R_{min})}\right) & \text{for } r\in[R_{\mathrm{min}},R_{\mathrm{max}}] \\ 0 & \text{for } r < R_{\mathrm{min}} \\ -1 & \text{for } r > R_{\mathrm{max}} \end{cases}, \tag{5.6}$$

with $R_{\mathrm{min}} = 925\,\mathrm{a\,u}$ and $R_{\mathrm{max}} = 1024\,\mathrm{a\,u}$ The absolute value of the boundary is shown as a grey shadowed area in Fig. 5.1(a), illustrating the grid representation of the wave function.

The wave function grid representation is partitioned into different sections, Fig. 5.1(a). Time-dependent changes in the electronic probability density in each of the grid parts, segments I to IX, indicate dynamical evolution as a result of the interaction with an external laser field. Here, the electron-electron correlation has the biggest influence on the distribution of the electronic density in the different regions. Such a partitioning technique has been successfully implemented in theoretical studies of the ionization out of the ground state of small atoms and molecules [177–184]. The partitioning of the wave function is done around section V, defining the size of the atom, with $d_{\mathrm{atom}} = 64\,\mathrm{a\,u}$. This neutral atomic region contains at least 99% of the unperturbed two-electron probability density of the considered singly and doubly excited states. If electronic density penetrates in regions II, IV, VI and VIII (yellow sections), this would mean high probability of one of the electrons to move away from the nucleus, while the other electron remains bounds, which is the process of single ionization (SI). If also the second electron moves away from region V, i.e. inside sections I, III, VII and IX (green and blue sections), both electrons leave the atom in the process of double ionization (DI), such that these regions are called DI sections, in contrast to the SI sections. In the double-ionization regions one can distinguish between a uni-directional two-electron emission pattern [157, 185, 186] in sections III and VII, and back-to-back emission [155, 186] in sections I and IX.

5.1.2 Comparative study of the ionization dynamics from single and double excitations

To study the difference between ionization from a singly and a doubly excited states exposed to interaction with a moderately strong NIR laser field, a pair of a singly and a doubly excited state was selected and their NIR strong-field ionization dynamics was compared. The considered NIR pulse is centred at photon energy $\hbar\omega = 1.74\,\mathrm{eV} = 0.064\,\mathrm{a\,u}$, has a temporal duration of $\tau_{\mathrm{P}} = 5\,\mathrm{fs}$ and its intensity is varied between 0 and $14\,\mathrm{TW/cm^2}$. Experimentally, ionization out of selectively excited states is realized after a preceding population of the excited states from the ground state by narrow-band XUV radiation, populating only a specific excited state. The experimental demonstration of this scenario is presented in section 5.3 of this chapter. In the simulation, on the other hand, the excited bound states with known energy are prepared as excited eigenfunctions of the free Hamiltonian of the model system according to the methods presented in [187] and extended to doubly excited states in [188]. With the initial preparation of the excited states, the XUV excitation step can be omitted in the calculations, such that effects of NIR interaction with the ground state of the system are also excluded from the calculation. The two compared states are chosen according to their single-ionization

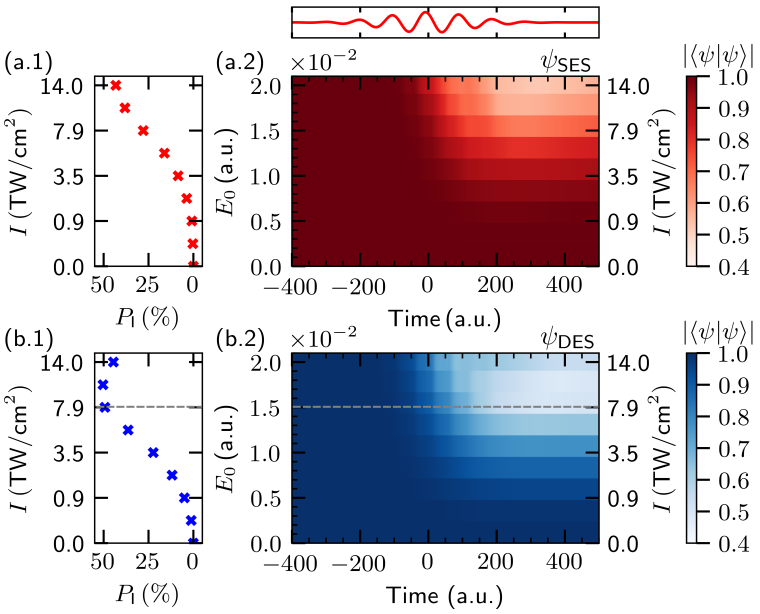

Figure 5.2: Ionization probability and population of the excited states. **(a.1)** and **(a.2)** Ionization probability P_I after NIR interaction as a function of the laser field strength and time evolution of the state probability density $P_\psi(t)$ of the singly excited state ψ_{SES}. **(b.1)** and **(b.2)** Ionization probability P_I and state probability density $P_\psi(t)$ of the doubly excited state ψ_{DES}.

potential, which for both states is around 0.1 a u , specifically, 0.081 a u for the SES and 0.114 a u for the DES. Those are the labelled states in the level scheme of the field-free model system, Fig. 5.1(d).

5.1.2.1 Ionization probability

To gain a first insight into the ionization process, initially the time-dependent state probability density $P_\psi(t) = \langle\psi(t)|\psi(t)\rangle$ is studied for both excited states. Hereby, the population in the central grid part, section V, is regarded as containing the electronic bound state, such that $P_\psi(t)$ for this grid area is calculated as a measure of the remaining bound electronic probability density, Fig. 5.2 (a.2) and (b.2) for the SES and the DES, respectively. The ionization probability $P_{\mathrm{I}} = 1 - P_\psi(t)$, on the other hand, is defined as the probability density of the unbound fraction distributed over all remaining grid sections. Figures 5.2 (a.1) and (b.1) depict P_{I} right after the end of the NIR pulse, at $t = 500\,\mathrm{a\,u}$, as a function of the NIR field strength for both states ψ_{SES} and ψ_{DES}, respectively. The NIR field strength E_0 is scanned between $0\,\mathrm{a\,u}$ and $0.0225\,\mathrm{a\,u}$, corresponding to NIR-intensity variation between 0 and $14\,\mathrm{TW/cm^2}$.

While the exact values for the calculated ionization probability depends on the choice of the box partition, as long as region V is chosen big enough to fit in the field-free wave function and small enough such that population can leave it upon

NIR interaction, the qualitative trend would remain the same regardless of the arbitrary choice of d_{atom}. In the here considered geometry, for both excited states, the ionization probability increases with increasing intensity and for $I_{\text{NIR}} \sim 10\,\text{TW/cm}^2$ approaches 50%, meaning that nearly half of the two-electron probability density has left the original neutral region, i.e. ionization is getting increasingly likely. In the considered moderate NIR-intensity regime, the Keldysh parameter depending on the state's ionization potential I_P and the ponderomotive shift U_P

$$\gamma = \sqrt{\frac{I_\text{P}}{2U_\text{P}}} \quad \text{with} \quad U_\text{P} = \frac{E_0^2}{4\omega^2} \tag{5.7}$$

for both considered states is larger than 1, which points toward a multi-photon ionization process responsible for the observed rising ionization probability. With the rising ponderomotive shift for increasing NIR intensity, the condition for channel closing $m\omega \leqslant I_\text{P} + U_\text{P}$ in the two-photon ionization channel for the doubly excited states is met for NIR-intensity of $8\,\text{TW/cm}^2$, marked by the horizontal dashed line in Fig. 5.2. The three-photon ionization channel then becomes the dominant one, as observed in studies of strong-field ionization in noble gases [189, 190]. Thus, channel closing due to the rising ponderomotive energy shift might be responsible for the slightly decreasing DES ionization probability for NIR intensity higher than $10\,\text{TW/cm}^2$.

5.1.2.2 Directionality of the ionization process

A significant amount of the electron density of both states spreads out of the neutral atom region for increasing laser intensity, which requires examination of the wave-packet dynamics in the outer ionization regions. For this, part of the probability density of the SES and DES wave function in position space is displayed in Fig. 5.3 at 6 points in time during the interaction with an NIR field with field strength $E_0 = 0.02\,\text{a.u.}$ In the singly excited state, the electrons occupy almost exclusively the SI sections, where one of them remains closely bound to the nucleus but the other one leaves the neutral atom. Only a very small part of the electron probability density, on the level of the numerical precision, leaves the SI regions and propagates towards the DI regions. This is not the case for the evolution of the doubly excited state. Until shortly before the maximum of the laser field, at time point (2) in Fig. 5.3 (b), the DES is also localised in the SI regions, after which, however, a considerable amount of $|\psi_{\text{DES}}|^2$ enters the diagonal regions, where both electrons simultaneously move away from the neutral atom region, time point (3) and onwards. In the back-to-back regions I and IX, the electronic probability density moves perpendicularly out of the SI sections, which is manifested as rectangular structures in the DES time evolution. This indicates an ionization mechanism, where first one of the electrons is driven away from the bound state, i.e. ionized, and subsequently also the second electron leaves the bound single-ionized state. Horizontal or vertical flow of the wave function perpendicularly out of the closest SI region is

therefore a signature of an independent, thus sequential double-ionization process. In the unidirectional regions III and VII, on the other hand, direct double ionization pathways are manifested. Here, the electrons move predominantly diagonally either out of the central (bound) region or out of the nearest SI domains (indicated by black arrows in Fig. 5.3(b)) but also perpendicularly out of the SI regions, as in the back-to-back case. In earlier studies, involving interaction with an NIR field of intensity on the order of $10^{14}\,\mathrm{W/cm^2}$, recollision-induced non-sequential ionization is found to play a significant role in strong-field ionization out of the atomic or molecular ground state [156, 157, 162, 179]. In the here considered lower intensity regime up to $I_{\mathrm{NIR}} \approx 10^{13}\,\mathrm{W/cm^2}$ the maximum energy of a recolliding electron amounts only to $3.17I_{\mathrm{P}} = 0.076\,\mathrm{a\,u} = 2.07\,\mathrm{eV}$, which is insufficient for ionization of the still bound electron in the ion with binding energy of $1.5664\,\mathrm{a\,u} = 42.6\,\mathrm{eV}$ in the case of the singly excited state and $0.5\,\mathrm{a\,u} = 13.6\,\mathrm{eV}$ for the doubly excited state. Recollision-induced double ionization is therefore not expected to play a dominant role for the here considered NIR intensity, where recollision causes recolliding periodic orbits [4, 191].

To determine the share between single and double ionization, the partition technique is made use of through calculation of the population in the SI and DI regions as a measure of the single and double ionization yield (SIY and DIY) for the two states under comparison. Here, similarly as already discussed for the overall ionization probability, the ionization yields depend on the exact choice of the box partition. The results for the here considered case are shown in Fig. 5.4, where the left panels show the time evolution of the SIY and DIY, for the singly excited state, as a dependence on the maximum field strength of the NIR pulse, while the right panels present the data for the doubly excited state. Due to its autoionizing nature the SIY of the doubly excited state is higher than the initial SIY for the SES. Autoionization is also the cause of decreasing SIY before and after the laser interaction. For both excited states the increase in single ionization arises at earlier times compared to the double ionization, where the latter sets in around the envelope maximum of the laser pulse. The increase in DIY after an initial rise of the SIY suggests a sequential process contributing to the observed double ionization, as also deduced from the directionality of ionization observed in the spatial distribution of the DES. Hereby, the double ionization yield of the doubly excited state, being more loosely bound to the double ionization continuum, is increased by four orders of magnitude during the interaction with the NIR laser field. For the SES, however, the major role in ionization is played by single ionization, as suggester by the small DIY for all considered NIR intensities.

In the case of the doubly excited state two double-ionization scenarios contribute to the overall double ionization yield: back-to-back and uni-directional ionization. Integration over regions I and IX for the back-to-back case and regions III and VII for the uni-directional double ionization allows for quantisation of the ionization yield in the respective scenario, Fig. 5.5. For all considered NIR field strengths the back-to-back DIY exceeds the uni-directional yield due to suppression of the uni-

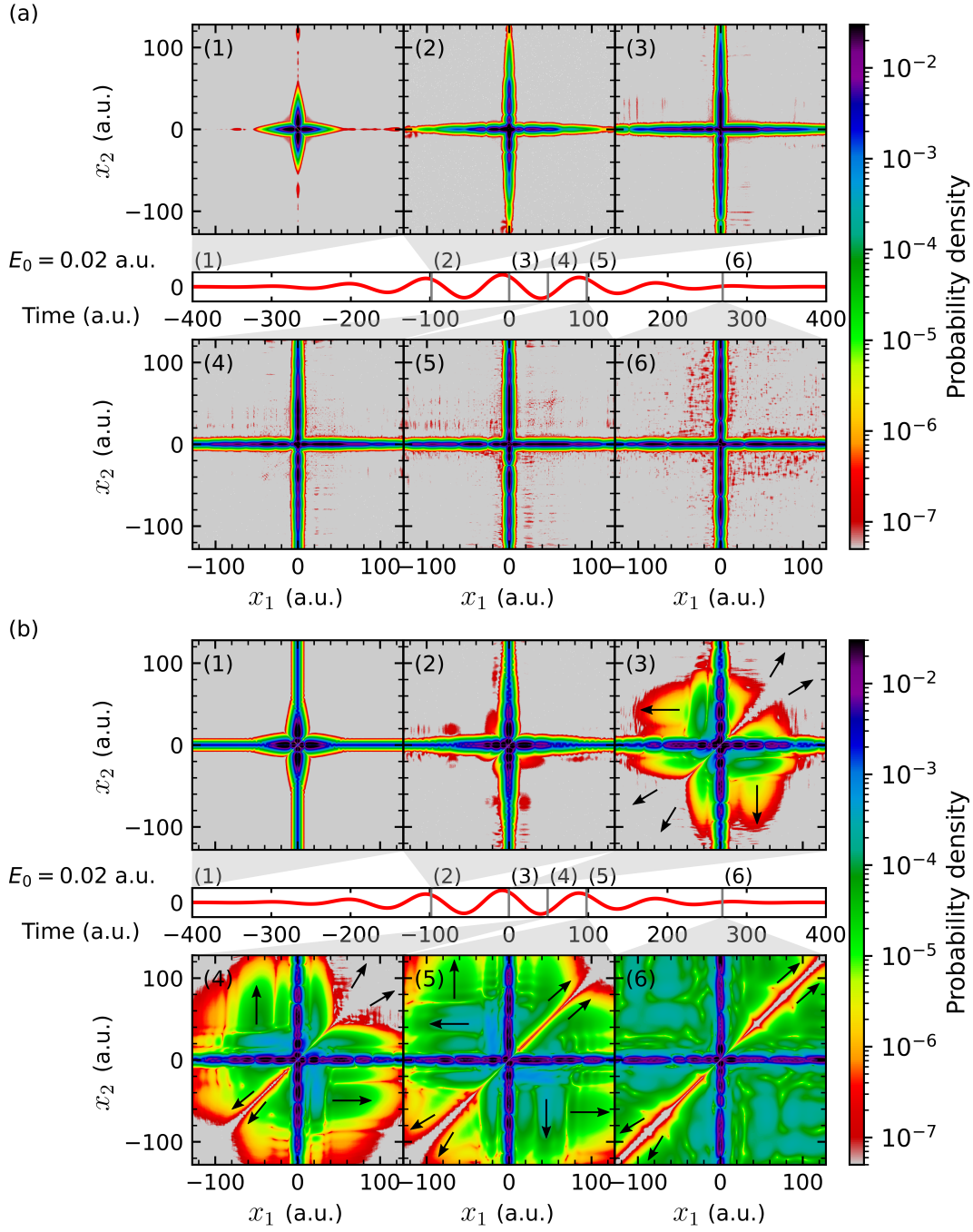

Figure 5.3: Time evolution $|\psi|^2$ of the spatial wave function of **(a)** the singly excited state ψ_{SES} and **(b)** the doubly excited state ψ_{DES} at different times during the interaction with an NIR field of strength $E_0 = 0.02\,\mathrm{a.u.}$ The chosen time instances (1) to (6) are shown over the E-field illustration in both subfigures. The black arrows are guides to the eye to follow the electron flux during ionization.

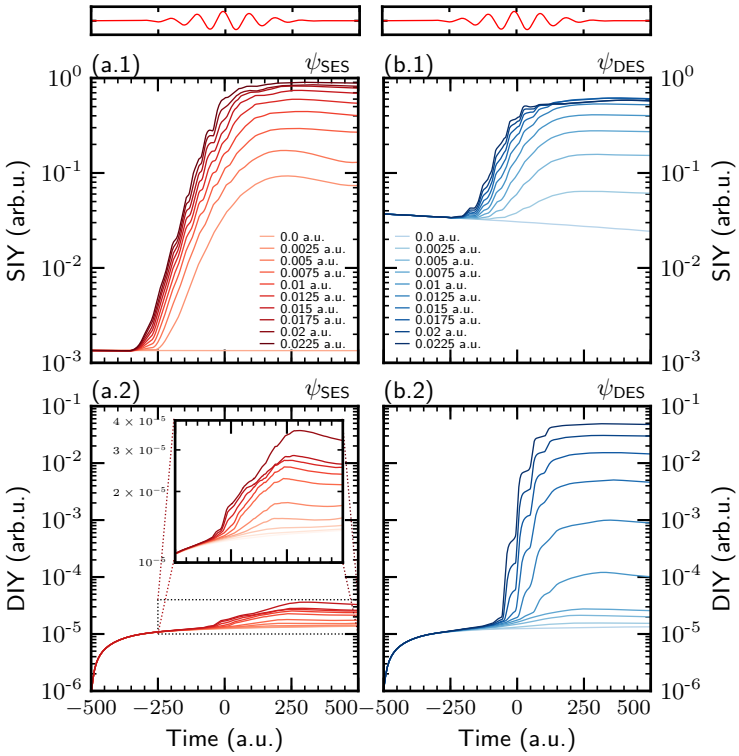

Figure 5.4: Single and double ionization yield as a function of laser interaction field strength. **(a.1)** and **(a.2)** Time evolution of $|\psi|^2$ integrated over the SI and DI regions for the singly excited state ψ_{SES} and **(b.1)** and **(b.2)** for the doubly excited state ψ_{DES}.

directional channel through the Coulomb repulsion between the electrons. To gain an insight into the motion of one of the electrons in the double ionization regions, the electron probability density is integrated over the distribution of the second electron. All data shown in Fig. 5.5 depicts the motion of the electron moving along the x_1 coordinate, as the integration is done along the x_2-axis. The left panels of the figure shown the projection signal in the back-to-back regions (green) and the right panels in the uni-directional regions, all for NIR field strength of $E_0 = 0.02\,\mathrm{a.u.}$ Electron probability density enters the double ionization regions upon the envelope maximum of the laser field and subsequently the electrons are driven by the oscillating laser field in both back-to-back and uni-directional regions. Back-to-back ionization, however, starts before the uni-directional ionization, as the electron probability density reaches the unidirectional region later than the back-to-back region. Furthermore, suggested by to the lack of electron bursts in the uni-directional case after the laser-field maximum, electrons escape the atom in the same direction predominantly for higher laser intensities, necessary for the electrons to overcome the additional Coulomb repulsion when escaping into the regions III and VII.

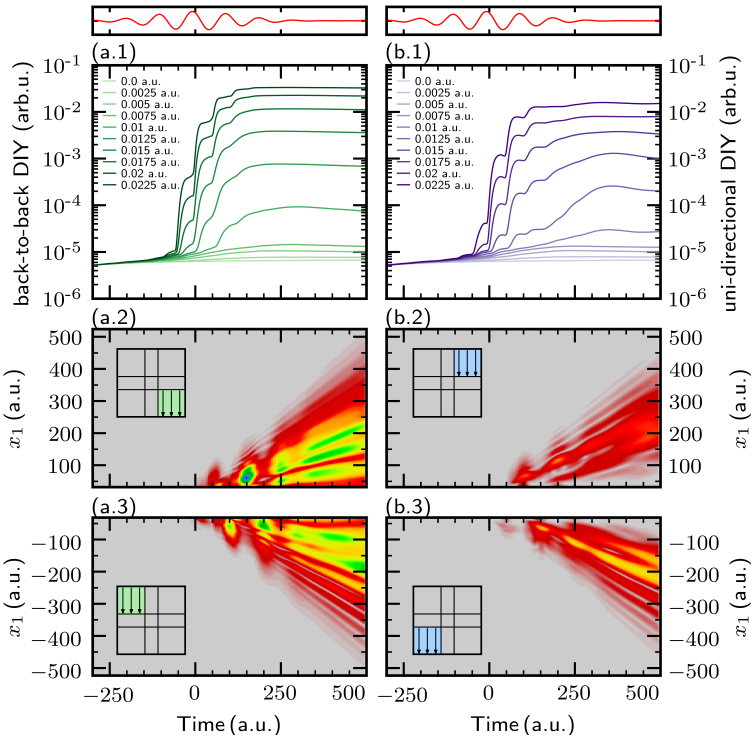

Figure 5.5: Contributions of the back-to-back **(a.1)** and the uni-directional **(b.1)** double ionization yield to the double ionization of the doubly excited state ψ_{DES} as a function of electric field strengths E_0. **(a.2)** and **(a.3)** Projection of the electron probability density on the x_1-axis in the back-to-back regions (green). **(b.2)** and **(b.3)** Projection on the x_1-axis in the uni-directional regions (blue). All shown projections are obtained for NIR field of strength $E_0 = 0.02\,\mathrm{a.u.}$

Exploring the role of the initial state in light–matter interaction by comparing the strong-field ionization dynamics of single- and two-electron excited atomic states in the limit of moderately strong fields provides a new platform for single and double ionization studies, especially towards understanding the peculiarities of the sequential and direct mechanisms beyond recollision. While singly excited states appear to ionize predominantly in the single ionization process, doubly excited states, additionally exhibit significant double ionization. Here, a back-to-back emission pattern in a sequential manner dominates the double ionization process. Uni-directional emission, on the other side, is not initiated sequentially, but also non-sequentially. The emerging different pathways for double ionization motivated experimental measurements of ionization dynamics out of selectively prepared excited states, thus being sensitive to the role of the electron correlation within the initial state.

5.2 Experimental details

This section presents the details of the XUV-IR pump-probe experiment for studies of ionization processes out of specifically excited states. First, the setup for the XUV-IR experiment, with characterisation of both XUV and IR pulses, is introduced, followed by a detailed presentation of the data analysis procedure, delivering particle momenta and finding coincidence events.

5.2.1 Experimental setup for the XUV-IR experiment

The experimental results presented in this chapter were obtained during a beamtime at the FL26 REMI beamline at FLASH2, during which the variable-gap undulator setup at FLASH2 was used to scan the whole range of doubly excited states in helium starting at the photon energy of 59 eV, just below the 2s2p resonance, up to 80 eV, just above the double ionization continuum at 79.03 eV. The XUV photon energy in this region was scanned in steps of 0.2 eV. Longer data acquisition for better statistics were conducted at the photon energies of (63.6 ± 0.1) eV and (70.0 ± 0.4) eV, which correspond to the position of the sp_{23+} and the 3s3p resonance, respectively. The FEL-pulse duration was characterised to be on the order of 50 fs, with more details presented in the following. A time-synchronised IR laser pulse with a central wavelength of 780 nm was spatially superimposed with the FEL beam. Despite the time-synchronisation, both the XUV and IR pulses have an intrinsic timing jitter, which is why an IR pulse-duration of ~ 70 fs was set to ensure best temporal overlap with the FEL pulses. The FEL pulses are delivered in bunches of 87 individual pulses with 10 Hz bunch repetition rate and pulse repetition rate inside the bunch of 201 kHz. Similarly, the IR pulses arrive in bunches of 70 individual pulses with 10 Hz bunch repetition rate and pulse repetition rate inside the bunch of 100.5 kHz. This way every second FEL pulse is synchronised with an IR pulse which enables measuring the FEL-only background reaction products, as well as IR-only background products, which are, in fact, on the detection noise level since the IR is not strong enough to cause ionization out of the ground state.

Both the FEL and IR beam, propagating collinearly, are focussed onto the supersonic gas jet of helium atoms with injection pressure of 10 bar. The FEL beam is focussed by an ellipsoidal mirror to a diameter of approximately 10 µm [130]. The slightly larger IR focus with diameter ~ 40 µm ensures spatial overlap of both pulses. Both the XUV and IR beams are linearly polarised, with the possibility of parallel and perpendicular polarisation of the IR light with respect to the FEL light, polarised along the x-axis.

The FEL pulse energy was adjusted through a set of apertures in the tunnel section and in the experimental hall, as well as by the addition of two 400 nm Si filters, further ensuring suppression of higher harmonics of the FEL radiation. A filter wheel with mounted neutral density (ND) filters (ND 0.5, 1, 2, 3, 4) enables adjust-

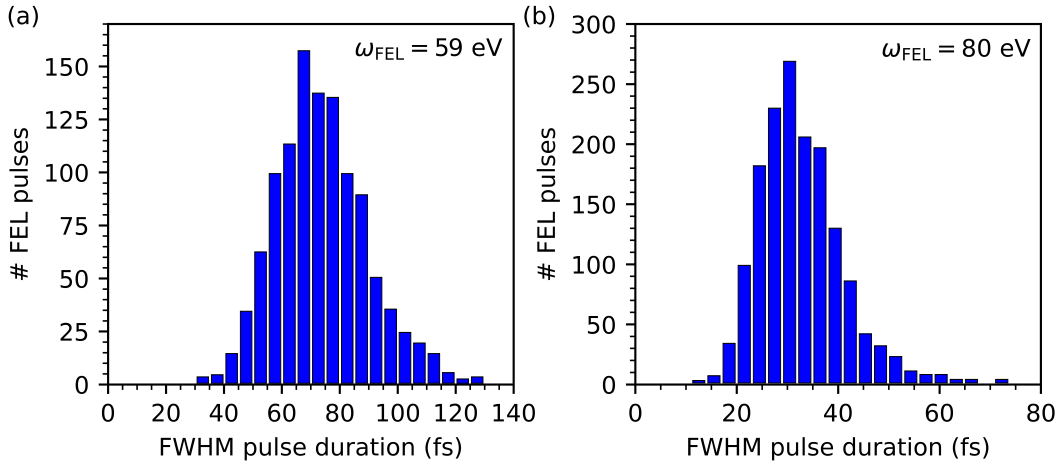

Figure 5.6: Temporal characterisation of the FEL pulses through a THz streaking measurement for FEL photon energy of **(a)** 59 eV and **(b)** 80 eV.

ment of the IR intensity, which without attenuation is on the order of $10^{13}\,\mathrm{W/cm^2}$, such that no strong-field ionization out of the helium ground state is possible.

5.2.1.1 Temporal characterisation of the FEL pulses

With variation of the FEL photon energy, also the spectral bandwidth, optimised to $< 1\%$ of the central photon energy of a pulse, changes. This was confirmed by a THz streaking measurement [192, 193] at the FLASH2 beamline FL21, conducted directly before the start of the beamtime for the FEL wavelengths of 15.5 nm and 21.0 nm, or 80 eV and 59 eV, respectively, i.e., on the two ends of the scanned photon-energy region, see Fig. 5.6. The measurement was carried out by the FEL THz team consisting of I. Bermudez, R. Ivanov, S. Düsterer. At both photon-energy settings a few 100 pulses were measured. The average pulse duration was determined to be (73 ± 17) fs at photon energy 59 eV and (33 ± 9) fs at photon energy 80 eV. Additionally, a slight chirp of the pulses was found by measuring at the two different THz slopes [194, 195]. The extracted value of the chirp is $\sim (3 \pm 1)$ meV/fs, with blue photons preceding red photons. Even though the pulse-length characterisation was carried out only for the highest and lowest photon energy, these measurement results confirm the expectation that with increasing photon energy, i.e. increasing spectral bandwidth, the FEL pulses become shorter in time.

5.2.1.2 Characterisation of the IR pulses

Both time and spectral characterisation of the IR pulses was conducted before and after the data acquisition. Figure 5.7 shows a typical IR spectrum with a maximum at 785 nm and a FWHM bandwidth of (18.2 ± 0.5) nm. The pulse spectrum is not ideally Gaussian with a shoulder on the red side of the spectrum extending the

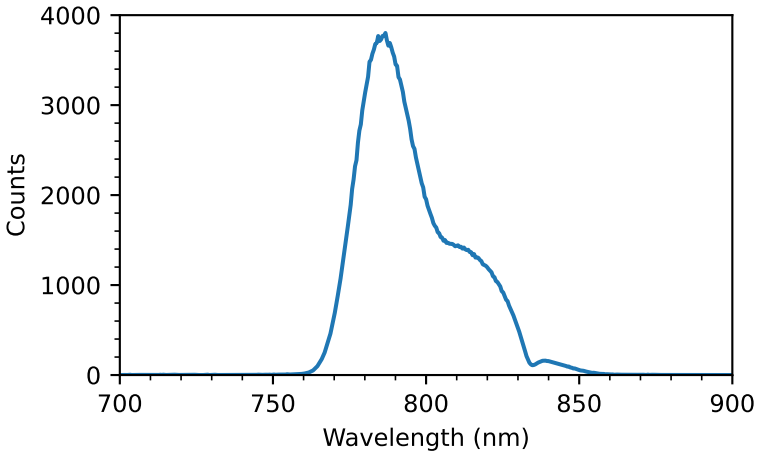

Figure 5.7: Spectrum of the IR pulses used in the XUV-IR experiment with a maximum at 785 nm.

spectrum to wavelengths up to 850 nm. The temporal pulse length was measured in an intensity autocorrelator to be (74 ± 7) fs.

5.2.2 Data analysis

During the analysis of the data recorded with a reaction microscope the aim is to convert the stored detector voltage traces to ion momentum information for all measured charged particles. The main steps of the analysis procedure are implemented in the Grand unifiEd reactioN microscopE souRce Code (GENERiC), which has been under continuous development since its original implementation for the analysis of the thesis project [196]. The GENERiC code is accessible as a shared library implemented in the GSI Object Oriented On-line Off-line system (Go4) framework [197], based on CERN's ROOT data analysis framework [198]. The analysis software used in the scope of this thesis is adapted to the experimental conditions at FLASH, especially including the pulse delivery in burst mode. The basic procedures for the data analysis, including three main steps, *Acquire*, *Unpack* and *Calculate* are described in detail in [128, 129, 199], whereas this section only delivers a short overview over the main concepts.

5.2.2.1 Extraction of timing signals

In the first step of the data analysis all recorded voltage traces at both the ion and electron detector are translated into (arbitrary) timing signals through the application of peak-finding procedures applied to the raw voltage signals. As a result, each assigned voltage peak is reduced to a time position in relation to a trigger signal. In practice, this step can be carried out already on a hardware level. However, storing the raw voltage traces allows for post-acquisition optimisation of the peak finding settings for best peak recognition. Different algorithms are routinely

Table 5.1: Distribution of combinations of FEL and IR pulses during the measurement.

FEL pulse	IR pulse	Number of combinations
on	on	43
on	off	44
off	on	26

applied for peak finding, as the SearchHighRes (SHR) algorithm [200], the Constant Fraction Discriminator (CFD) algorithm [201] and the center of mass (COM) algorithm [202]. While the different algorithms all have their advantages and disadvantages, discussed for example in [128, 203], the CFD algorithm, based on the working principle of hardware CFD [204], was chosen for the extraction of peak positions in the data analysis in this project. It is applicable to double pulses and is robustly able to identify peaks with different height [201].

5.2.2.2 Extraction of time of flight and particle hit position

In the second step of the data analysis procedure, the detected signals from the MCP channel and the delay-line signals are translated into time-of-flight values of the particles and their hit position on the detector, respectively. For the precise determination of the time-of-flight signal, the detected signal from stray XUV light causing an MCP signal is used as the time-zero, i.e. the interaction time. The calibration of the position information is presented in section 4.1.3.2. More details on the calibration procedure are presented in [128, 129, 199]. The intrinsic time resolution of the detectors, which is on the order of 0.5 ns, is determined by the width of the signals travelling along the wires of the delay-line anode, which are broadened due to the spatial extension of the electron cloud emerging from the MCPs.

In this step also the initial sorting of the events according to the three combinations of laser pulses is done:

- FEL and IR pulse;
- only FEL and no IR pulse;
- only IR pulse and no FEL pulse.

Because of the double intrabunch pulse repetition rate of the FEL compared to the IR, an IR pulse is arriving only with every second of the 87 FEL pulse in the pulse train. With the number of pulses in one IR pulse burst, which is 70, this leads to the distribution of pulses, as listed in Table 5.1, taking into account that the first IR pulse arrives with the second FEL pulse.

5.2.2.3 Calculation of particle momenta

With the reconstructed time-of-flight to the detector and the hit position in the (x, y)-plane, the three-dimensional initial momentum of the detected ion or electron can be calculated from the equation of motion of the particle in the homogeneous magnetic and electric field. The combined action of both fields is included in the Lorentz force, such that the equation of motion takes the form:

$$m\ddot{\boldsymbol{x}} = q\,(\boldsymbol{E} + \dot{\boldsymbol{x}} \times \boldsymbol{B}), \tag{5.8}$$

where m and q are the particle's mass and charge, respectively, while $\boldsymbol{E}$ and $\boldsymbol{B}$ denote the electric and magnetic field, both having only a z non-zero component. This allows for decoupling of the longitudinal (along the z-axis) and transversal motion (in the (x, y)-plane) of the particle inside the spectrometer.

Longitudinal momentum reconstruction

The longitudinal equation of motion is then

$$m\ddot{z} = qE = q\frac{U}{d}, \tag{5.9}$$

with the applied voltage U over the distance d. The solution of the equation yields

$$d = \frac{1}{2}\frac{q}{m}\frac{U}{d}t_{\mathrm{TOF}}^2 + v_z t_{\mathrm{TOF}}. \tag{5.10}$$

Here, t_{TOF} denotes the time it takes for the particle to reach the detector, or its time of flight. The longitudinal momentum is then

$$p_z = \frac{md}{t_{\mathrm{TOF}}} - \frac{1}{2}\frac{qU}{d}t_{\mathrm{TOF}}. \tag{5.11}$$

The time of flight, on the other hand, is given by

$$t_{\mathrm{TOF}\pm} = \frac{p_z \pm \sqrt{p_z^2 + 2qUm}}{-qU/d}, \tag{5.12}$$

with $t_{\mathrm{TOF}}+$ corresponding to the flight time of the particles initially flying towards the detector and $t_{\mathrm{TOF}}-$ to those in opposite direction. In the limit of zero initial momentum one finds

$$t_{\mathrm{TOF}}(p_z = 0) = d\sqrt{\frac{2m}{qU}}, \tag{5.13}$$

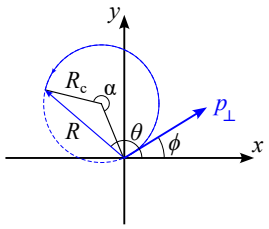

Figure 5.8: Illustration of a particle trajectory in the transversal (x,y)-plane. The vector $p_\perp$ indicates the initial momentum of the charged particle and $R = (x,y)$ is the position vector on the detector. R_c is the cyclotron radius.

which justifies the separation of ion species according to their mass-to-charge ratio, as discussed in section 4.1, describing the working principle of the reaction microscope.

Transversal momentum reconstruction

The applied magnetic field in the spectrometer forces all charged particles, ions and electrons, onto spiral trajectories to the respective detector. In the transversal (x,y)-plane, the particle moves along a circle with radius R_c, as illustrated in Figure 5.8. The cyclotron orbital frequency w_c of the motion is determined by the particle's charge q, mass m and by the amplitude of the constant magnetic field B:

$$w_c = \frac{qB}{m} \tag{5.14}$$

and the phase of the rotation along the circular trajectory at the particle's arrival time on the detector is given by

$$\alpha = w_c t_{\mathrm{TOF}} = \frac{qB}{m} t_{\mathrm{TOF}}. \tag{5.15}$$

During the particle's motion, the Lorentz force is balanced out by the centrifugal force, such that

$$q v_\perp B = \frac{m v_\perp^2}{R_c}, \tag{5.16}$$

with R_c being the radius of the cyclotron orbit. This leads to the transverse momentum

$$p_\perp = qBR_c = m w_c R_c. \tag{5.17}$$

The cyclotron radius, which is not directly measurable in the experiment, is connected to the impact position $R = (x, y)$ through the phase of rotation:

$$R_c = \frac{|R|}{2\sin\left(\frac{\alpha}{2}\right)} = \frac{|R|}{2\sin\left(\frac{w_c}{2}t_{\mathrm{TOF}}\right)}. \tag{5.18}$$

Inserting this result in Eq. (5.17) yields the absolute value of the initial transverse momentum

$$p_\perp = \frac{|R| m w_c}{2\sin\left(\frac{w_c}{2}t_{\mathrm{TOF}}\right)}. \tag{5.19}$$

With the initial emission direction of the charged particle under an angle ϕ with respect to the x-axis, the two components of the transversal momentum are:

$$\begin{aligned} p_x &= p_\perp \cos(\phi) \\ p_y &= p_\perp \sin(\phi), \end{aligned} \tag{5.20}$$

where

$$\phi = \theta - \frac{\alpha}{2} = \theta - \frac{w_c}{2}t_{\mathrm{TOF}}. \tag{5.21}$$

For heavy particles, i.e. as for ions, α becomes very small, such that the position vector $\vec{R}$ points along the direction of $p_\perp$, which takes the form:

$$p_\perp = v_\perp m. \tag{5.22}$$

This equation is also derived directly from the equation of motion (5.8), when neglecting the magnetic field, leading to

$$\begin{aligned} p_x &= m\left(\frac{x}{t} - v_{\mathrm{jet}}\right) \\ p_y &= m\frac{y}{t} \end{aligned} \tag{5.23}$$

with the impact coordinates x and y and the jet velocity along the x-axis v_{jet}.

5.2.2.4 Assignment of coincidences

The assignment of particle coincidences is based on momentum conservation, where the initial photon and particle momenta balance out the sum momentum of all outgoing particles. If no thermal excitation of the particles before the interaction is considered, the ions and electrons in the target have no initial momentum before the ionization. Additionally, the photon momentum can be neglected for most ionization processes, such that in the end the sum momentum of all released particles upon laser interaction has to be zero:

$$\sum_i \boldsymbol{p}_{\mathrm{ion},i} + \sum_j \boldsymbol{p}_{\mathrm{e},j} = 0, \tag{5.24}$$

where $\boldsymbol{p}_{\mathrm{ion},i}$ denotes the momentum of each detected i ion and $\boldsymbol{p}_{\mathrm{e},j}$ the momentum of each freed electron j. The momenta of all potentially coincident particles, ions and electrons from a certain ionization channel, are tested for the momentum sum condition and assigned to each other if the momentum conservation condition is met. Since the assumptions taken to arrive at the zero-sum condition are not met exactly, particles are assigned to be coincident if their sum is in a certain window, chosen as narrow as possible.

5.3 Ionization processes out of specifically excited states in helium

This section presents the results of applying state-selectivity to the initial state in laser ionization through specific preparation of doubly excited states in the helium atom and their subsequent exposure to a strong IR field. While the IR field with intensity of $\sim 10^{13}\,\mathrm{W/cm^2}$ is not strong enough to initiate ionization in the neutral helium atom, both single and double ionization are observed for the XUV-prepared doubly excited states, with the results presented in sections 5.3.1 and 5.3.2, respectively.

5.3.1 Single-ionization processes above the first ionization threshold in helium

Single ionization in a two-colour XUV-IR experiment is dominated by XUV-only single ionization for energy of the XUV photons above the first ionization threshold in the helium atom, in the presented experiment with XUV photons having energy between 59 eV and 80 eV. Here, already one single XUV photon is enough to overcome the binding energy of the first electron of 24.59 eV with considerably high photoionization cross section on the order of a few Mb [205]. For an ionizing field with photon energy of 59 eV the photoionization cross section is reported to be 1.56 Mb, while at photon energy of 80 eV, just above the total ionization threshold, the cross section decreases by more than a half to 0.693 Mb. Resonance photoionization cross sections through autoionization at the energies of the doubly excited states are of similar order of magnitude, meaning that the photoexcitation of the doubly excited states also happens with similar probability as ionization. An XUV-populated doubly excited state in the atom with binding energy of only a few electronvolt can then be ionized by the IR field in the two-colour configuration. The following sections discuss different possible ionization processes measured in the two-colour XUV-IR experiment, focussing predominantly on the IR-induced strong-field ionization but also pointing out XUV-only ionization being the source of a constant background in the detected ionization yield and photoion and photoelectron momentum distributions.

5.3.1.1 Single ionization for XUV pulse preceding the IR pulse

If the XUV and the NIR pulse do not interact with the target simultaneously, but one after each other, two types of ionization processes are possible: ionization induced by just one of the fields and two-colour sequential processes of pump-probe type. In the case presented here, the configuration of the two pulses is such that the XUV pulse arrives first and the IR pulse arrives later with a time delay of $\tau \approx 250\,\mathrm{fs}$. As the IR field strength is not high enough to ionize the helium atom out of its $1s^2$ ground state, the two possibilities for ionization are either XUV-only ionization, or IR-induced ionization out of the doubly excited states populated in a previous step, 250 fs earlier, by the XUV field.

An overview of the single-ionization yield as a function of XUV photon energy ranging in the scanned region between 59 eV and 80 eV is provided in Fig. 5.9, showing the measured photoelectron yield in coincidence with He^+ ions as a function of photoelectron kinetic energy $E_{\mathrm{kin,e}}$ and XUV photon energy. The interpretation of the XUV-only single-ionization yields, shown in the upper panel of the figure, is straightforward. Due to energy conservation the photoelectron energy, i.e. its kinetic energy, amounts to

$$E_{\mathrm{kin,e}} = E_{\mathrm{XUV}} - \mathrm{I}_n - E_{\mathrm{kin,ion}} \approx E_{\mathrm{XUV}} - \mathrm{I}_n, \tag{5.25}$$

where the approximation of very low energy sharing of the coincident ion being 3 orders of magnitude heavier than the electron is applied. While scanning through the XUV photon energy over the ionization thresholds I_n, ionization above the lower lying ionization thresholds is possible, as illustrated for the pathways 1 and 2 in Fig. 5.9 (b). Since the magnetic and electric field in the reaction microscope were set with focus on good momentum and energy resolution of slow electrons, the ionization products associated to the direct XUV ionization above $\mathrm{I}_1 = 24.59\,\mathrm{eV}$ were not efficiently detected, as they would have a minimum energy of $E_{\mathrm{kin,e}}(\mathrm{I}_1) = 34.41\,\mathrm{eV}$, if being ionized with XUV photon energy of 59 eV. Good detection efficiency is provided for the measurement parameters for photoelectrons with kinetic energy up to $\approx 10\,\mathrm{eV}$, the region depicted in Fig. 5.9. As the kinetic energy of the photoelectron is directly proportional to the rising XUV photon energy for ionization above a given threshold I_n, Eq. (5.25), the electron kinetic energy rises linearly with a slope of 1 for increasing E_{XUV}, starting at $E_{\mathrm{kin,e}} = 0\,\mathrm{eV}$ at each XUV photon energy corresponding to an ionization threshold position. The more ionization thresholds are crossed by the XUV photon energy, the more lines of increased ionization yield run parallel with increasing E_{XUV}, as shown in the upper panel of Fig. 5.9.

Adding the IR field to the picture, the IR-induced ionization channel opens up, when at matching XUV photon energies doubly excited states are excited from the $1s^2$ ground state in helium. IR-induced ionization then becomes possible through absorption of additional photons of the delayed IR field with moderate intensity on the order of $\sim 10^{12}\,\mathrm{W/cm^2}$. The gained kinetic energy by the electron upon ionization depends on the binding potential of the excited state and the number

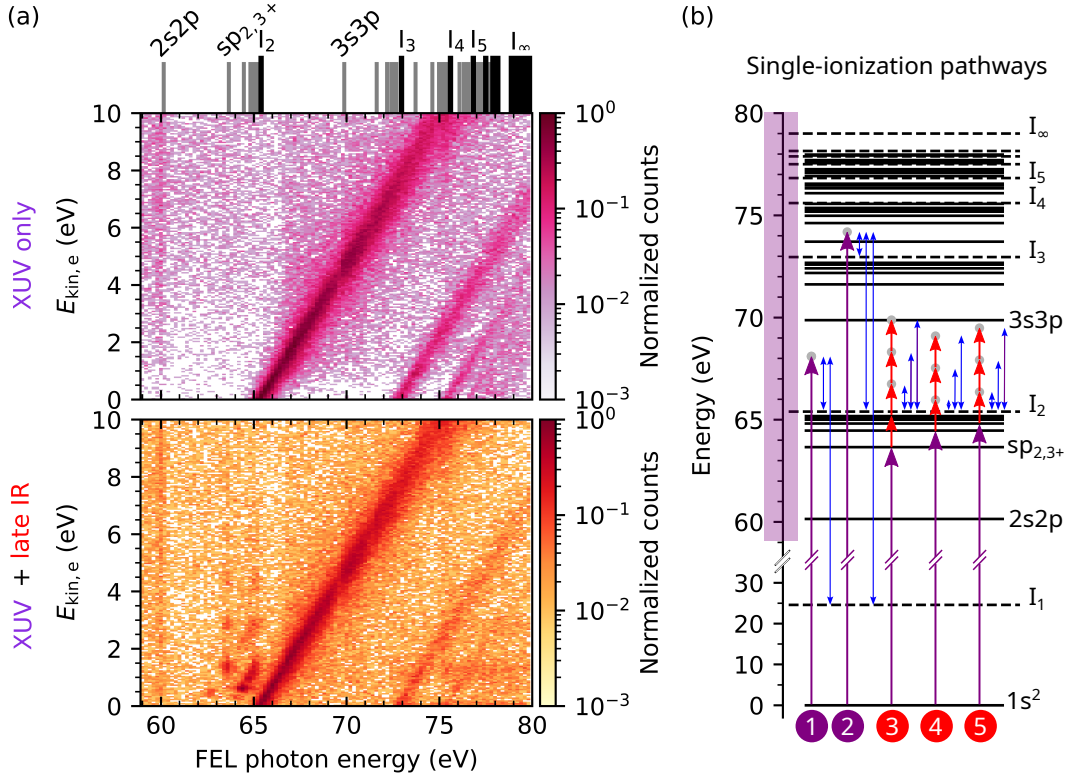

Figure 5.9: Single-ionization yield as a function of XUV photon energy, ranging between 59 eV and 80 eV, with XUV pulse arriving before the IR pulse. **(a)** Measured photoelectron yield in coincidence with He^+ ions as a function of photoelectron kinetic energy $E_{kin,e}$ and XUV photon energy in the XUV-only configuration (upper panel) and in the case of XUV pulse preceding the IR pulse (late IR) arriving at time delay $\tau \approx 250$ fs (lower panel). The gray lines in the top part of the figure indicate the positions of doubly excited states in helium as well as of the ionization thresholds I_2 to I_∞. **(b)** Sketch of single-ionization pathways indicated in the energy-level diagram of helium. The XUV-only ionization pathways (1 and 2) are marked in violet, with XUV photon energy indicated through the length of the violet arrows. In the XUV + late IR ionization pathways (3 to 5) the XUV photon is resonant to transition from the ground to an excited state, whereas the ionization is caused by the later arriving IR laser pulse (red arrows). The photoelectron kinetic energy $E_{kin,e}$ is indicated by blue arrows in all shown pathways.

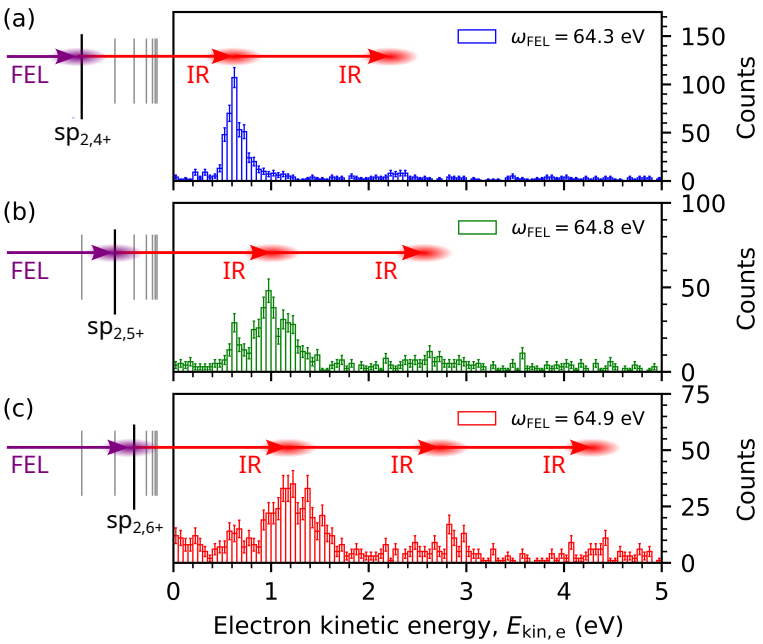

Figure 5.10: Distribution of electron kinetic energy $E_{\mathrm{kin,e}}$ for IR-induced above-threshold ionization out of the **(a)** $sp_{2,4+}$, **(b)** $sp_{2,5+}$ and **(c)** $sp_{2,6+}$ doubly excited states, prepared by the XUV field with photonenergy resonant to the transition energy between the ground states and the respective excited state. The lineouts for the three XUV photon energies are extracted from Fig. 5.9(a).

$n+s$ absorbed IR photons, with n photons needed to overcome the n-th ionization threshold and s additionally absorbed photons, leading to above-threshold ionization [37, 38, 206], as illustrated in the pathways 3 to 5 in Fig. 5.9 (b). This process, however, is only possible if the IR field arrives during the lifetime of the doubly excited states. As the 2s2p state, for example, is shorter lived than the time delay of 250 fs between the XUV excitation and the IR ionization, no significant rise in ionization yield is detected at $E_{\mathrm{XUV}} = (60.1 \pm 0.2)\,\mathrm{eV}$. Due to the jitter in the timing of both the XUV and the IR pulses, however, even for this state with an autoionization lifetime of $\approx 18\,\mathrm{fs}$ [56, 60] a non-vanishing IR-induced ionization yield is detected, even if only on the order of magnitude of the background. With lifetimes also on the order of $\approx 20\,\mathrm{fs}$ but excitation cross section almost an order of magnitude lower than the one of the 2s2p state, the 3s3p state and the states of the $sp_{3,n+}$ series do not exhibit IR-induced ionization after XUV excitation, as they are already autoionized.

The doubly excited states of the $sp_{2,n+}$ series, on the other hand, have longer lifetimes, such that ATI peaks are clearly detected at the corresponding XUV photon energy. While the ATI peaks out of the $sp_{2,3+}$ appear clearly separated, those corresponding to the higher-lying states start to overlap. Taking lineouts at XUV photon energies in this region, as done in Fig. 5.10, allows for visualisation of the ATI peaks out of the different doubly excited states. For example, for the ionization

pathway 5 in Fig. 5.9 (b) and Fig. 5.10 (b) of ionization through the $sp_{2,5+}$ state an absorption of just 1 IR photon is enough for ionization and already a second absorbed IR photon causes above-threshold ionization, as:

$$E_{\mathrm{XUV}}(64.8\,\mathrm{eV}) + 1 \cdot E_{\mathrm{IR}}(1.58\,\mathrm{eV}) - \mathrm{I}_2(65.4\,\mathrm{eV}) = E_{\mathrm{kin,e}}(0.98\,\mathrm{eV}). \tag{5.26}$$

In the case of the $sp_{2,4+}$ with resonance energy of 64.466 eV the XUV excitation energy of 64.3 eV is slightly off-resonant, but the resonance still lies in the bandwidth of the pulse and therefore the XUV photon energy is sufficient for the state's excitation. For the energy conservation condition, however, since the process is sequential and then out of the doubly excited state, the electron kinetic energy amounts to $E_{\mathrm{kin,e}}(0.646\,\mathrm{eV})$ instead to $E_{\mathrm{kin,e}}(0.48\,\mathrm{eV})$, Fig. 5.9 (a). In all three shown lineouts in the figure the ATI peaks are separated exactly by the energy of the IR field, as indicated by the red arrows with the corresponding length. For higher XUV photon energy, Fig. 5.9 (c), the XUV field with spectral bandwidth of around 1% of its central wavelength, is able to simultaneously excite a few doubly excited states, which leads to effective broadening of the ATI peaks, as the ionization out of all excited states takes place simultaneously.

Two additional ionization features in the region of the doubly excited states below the second ionization threshold have not been discussed yet: increased ionization yield for XUV photon energy of $(62.7 \pm 0.1)\,\mathrm{eV}$ at kinetic energy of $(0.5 \pm 0.1)\,\mathrm{eV}$ and for XUV photon energy of $(64.1 \pm 0.1)\,\mathrm{eV}$ at kinetic energy of $(0.35 \pm 0.05)\,\mathrm{eV}$. Ionization to those positions out of the states in the $sp_{2,n+}$ series is not possible, but ionization out of the weak $sp_{2,3-}$ and $sp_{2,4-}$ [56], respectively, as depicted in Fig. 5.11. The two ionization processes need two photons in the case of the $sp_{2,3-}$ state and just one photon for ionization out of the excited $sp_{2,4-}$ state. The missing peaks due to above-threshold ionization could be attributed to the smaller excitation cross section of those states compared to the states of the $sp_{2,n+}$ series, and thus decreased ionization yield of the sequential process.

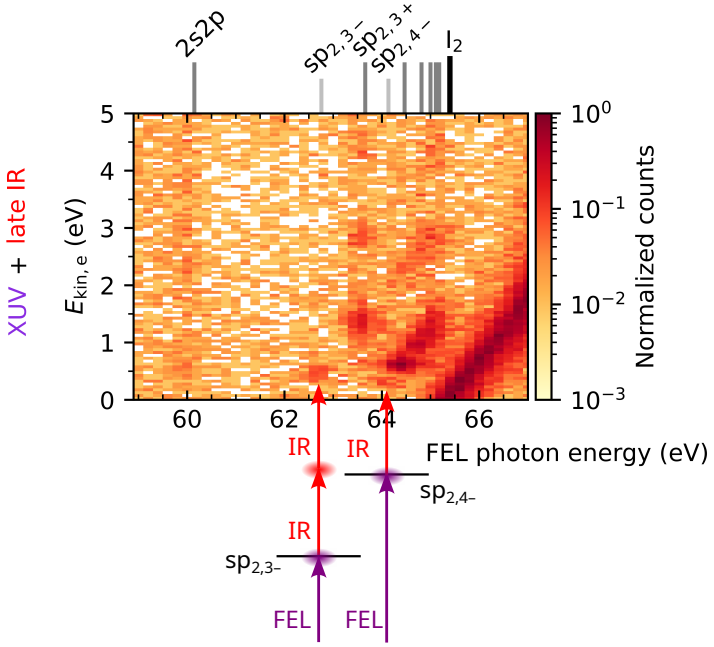

Figure 5.11: Single-ionization yield as a function of XUV photon energy, ranging between 59 eV and 67 eV, i.e. scanning the whole region of doubly excited states below the second ionization threshold I_2, with XUV pulse arriving before the IR pulse. The measured photoelectron yield is detected in coincidence with He^+ ions as a function of photoelectron kinetic energy $E_{kin,e}$ for XUV pulse preceding the IR pulse (late IR) arriving at time delay $\tau \approx 250$ fs . The gray lines in the top part of the figure indicate the positions of doubly excited states in helium as well as of the ionization threshold I_2, showing also the position of the weak states $sp_{2,3-}$ and $sp_{2,4-}$. IR-induced two-photon and one-photon ionization out of the XUV-excited $sp_{2,3-}$ and $sp_{2,4-}$ state, respectively, is indicated, leading to the increased ion yield at the energy positions of those states with photoelectron kinetic energy according to energy conservation.

5.3.1.2 Single ionization for two-colour XUV-IR pulse configuration

In the two-colour XUV-IR pulse configuration, when both pulses are in temporal overlap, the possible ionization processes change, as various excitation and ionization pathways open up. In this case, additionally, IR-induced ionization out of short-lived states becomes possible, as well as ionization pathways through otherwise dipole forbidden states become possible in the laser-dressed atom picture, as observed in photoelectron spectroscopy measurements in the region of the singly excited states below the first ionization threshold in laser-dressed atomic helium [206, 207].

To gain a first overview over the possible ionization pathways, opening up additionally to the sequential pathways, discussed above, which are still possible, Fig. 5.12 presents the single-ionization yield for measured photoelectrons in co-

incidence with He^+ ions as a function of photoelectron kinetic energy $E_{\mathrm{kin,e}}$ and XUV photon energy in the range between 59 eV and 80 eV. The XUV-only case, which is the same as in the previously discussed data set, is shown for the purpose of direct comparison to the XUV+IR case presented in the lower panel of subfigure (a). The most apparent additional ionization pathway is the above-threshold ionization out of the XUV-excited 2s2p state at XUV photon energy of 60.1 eV, with clear ≈ 1.58 eV spacing between the ATI peaks. Ionization to the laser-dressed continuum, pathway 2 in Fig. 5.12, becomes possible, as discussed later in this section. Furthermore, an ionization pathway through the excited 3s3p state also opens up, which is further investigated in the following.

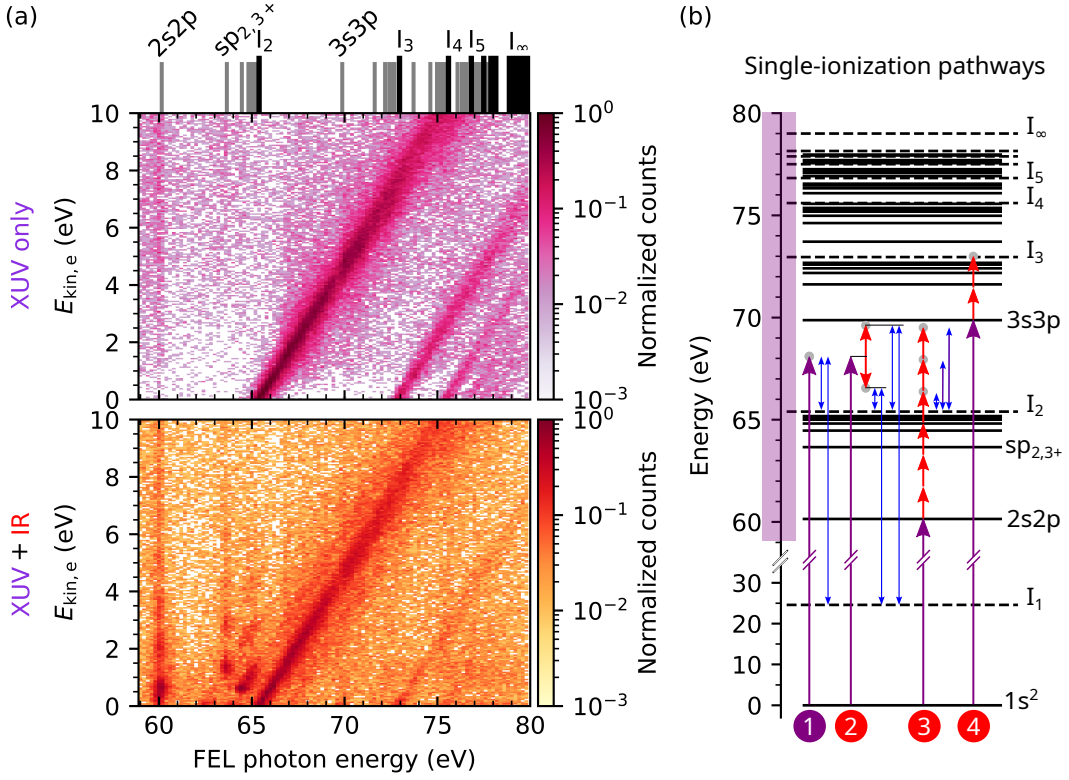

Figure 5.12: Single-ionization yield as a function of XUV photon energy, ranging between 59 eV and 80 eV, with XUV pulse arriving in time overlap with the IR pulse. **(a)** Measured photoelectron yield in coincidence with He^+ ions as a function of photoelectron kinetic energy $E_{kin,e}$ and XUV photon energy in the XUV-only configuration (upper panel) and in the case of XUV and IR pulse arriving together at the target (lower panel). The gray lines in the top part of the figure indicate the positions of doubly excited states in helium as well as of the ionization thresholds I_2 to I_∞. **(b)** Sketch of single-ionization pathways indicated in the energy-level diagram of helium. A single XUV-only ionization pathway(1), marked in violet, is depicted, as XUV-only pathways are discussed together with Fig. 5.9. In the XUV + IR ionization pathways (2 to 4) the XUV photon is indicated by a violet arrow, whereas red arrows show IR photons. The photoelectron kinetic energy $E_{kin,e}$ is indicated by blue arrows in all depicted pathways.

Single ionization out of doubly excited states below the I_2 ionization threshold

First, single ionization out of doubly excited states below the I_2 ionization threshold, specifically out of the $sp_{2,3+}$ state at photon energy of $E_{sp_{2,3+}} = 63.658\,\mathrm{eV}$, is considered. Ionization via excitation of this state is possible in a two-IR-photons process, as depicted in the schematic pathway in Fig. 5.13 for the absorption of one XUV and 2 IR photons. Absorption of additional IR photons leads to above-threshold ionization peaks with spacing of 1.58 eV (1 IR photon energy). The ATI peak distribution shows clear decrease in the intensity of the peaks, as the ionization rate scales exponentially with the number of absorbed IR photons. From the ATI spectrum, consisting of 4 clearly visible peaks and a fifth one just about the XUV-only background at $\approx 7.5\,\mathrm{eV}$, information on the laser intensity can be extracted through the ponderomotive energy gained by a free-moving electron in a linearly polarized laser field with electric field amplitude F and frequency ω. Without considering further interaction with the ionic core, the freed electron can be accelerated to a kinetic energy of up to twice the ponderomotive potential

$$U_\mathrm{p} = \frac{e^2 F^2}{4m\omega^2}. \tag{5.27}$$

While through recollision with the ion and subsequent backscattering even higher energies up to $10U_\mathrm{p}$ can be reached, thus extending the ATI cut-off [49, 50, 208], an order of magnitude estimate for the electric field strength can be extracted from the ATI spectrum. Assuming a cut-off at the energy of the fifth ATI peak, i.e. $E_\mathrm{cut-off} = (7.5 \pm 0.5)\,\mathrm{eV}$, a $2U_\mathrm{p}$ cut-off leads to an estimate of the IR intensity of $I_\mathrm{IR} = (6.6 \pm 0.4) \times 10^{13}\,\mathrm{W/cm^2}$, which is consistent with the independent intensity estimate through the measured IR pulse energy and estimate of the focal size on the order of $\sim 10^{13}\,\mathrm{W/cm^2}$ IR intensity.

Besides evaluating the photoelectron kinetic energy obtained at a certain XUV photon energy, here $\omega_\mathrm{XUV} = (63.65 \pm 0.70)\,\mathrm{eV}$, a further step in the data evaluation bringing further insight into the ionization process is extraction of photoion and photoelectron momentum distributions. First, the recoil-ion momentum distribution of He^+ is considered, Fig. 5.14. The two upper rows show the distributions in the case of overlapping XUV and IR fields, both polarized along the x-axis, while the two lower rows depict the XUV-only distribution, which is the background distribution obtained in the XUV+IR case. While the upper rows in both cases show a projection on the respective p_i-p_j plane, i.e. integrating over the whole third axis, the lower rows depict a cut through the third plane for momentum between $-0.1\,\mathrm{a.u.}$ and $0.1\,\mathrm{a.u.}$ The XUV-only process is well understood [126]. Ionization out of the ground state with s symmetry via a one-photon transition, results in an angular momentum quantum number of $l = 1$, thus exhibiting an angular distribution of the shape $|Y_{1,0}(\theta)|^2 \propto \cos^2(\theta)$ along the polarization direction of the ionizing laser field, here the x-axis. With an XUV photon energy of $\omega_\mathrm{XUV} = 63.65\,\mathrm{eV}$ and ionization above the first threshold $I_1 = 24.59\,\mathrm{eV}$, the absolute value of the total recoil-ion mo-

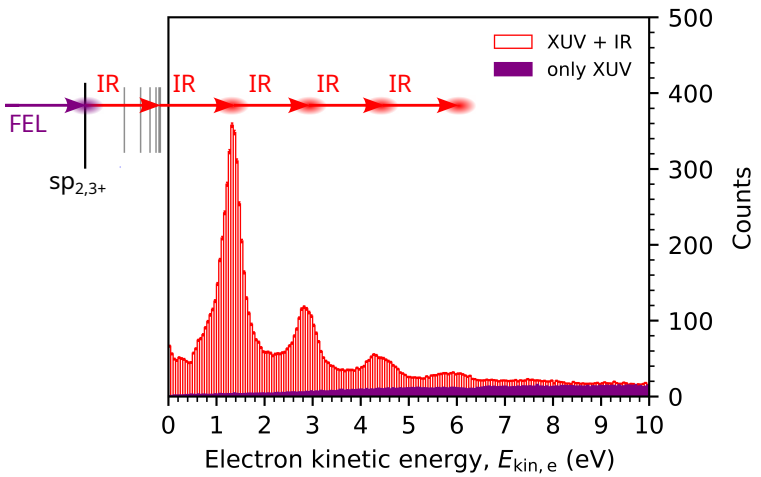

Figure 5.13: Distribution of electron kinetic energy $E_{\mathrm{kin,e}}$ for IR-induced above-threshold ionization out of the XUV-prepared $\mathrm{sp}_{2,3+}$ doubly excited state, interacting with XUV light with photon energy of $\omega_{\mathrm{XUV}} = 63.65\,\mathrm{eV}$ and IR light with photon energy $\omega_{\mathrm{IR}} = 1.58\,\mathrm{eV}$.

mentum given through the electron momentum and with this the electron kinetic energy calculated according to

$$|p_{\mathrm{recoil}}| = |p_{\mathrm{e}}| = \sqrt{2m_e E_{\mathrm{kin,e}}} = \sqrt{2m_e(E_{\mathrm{XUV}} - \mathrm{I}_n)} \tag{5.28}$$

amounts to 1.69 a u , as observed in the lower panels of Fig. 5.14 depicting the recoil-ion momentum distribution in the XUV-only case. While the projections show a considerable momentum spread, the cuts through the momentum distributions are sharper. In the XUV+IR case additionally to the XUV-only momentum distribution structure, also a low-momentum structure is detected, but the relatively low momentum resolution does not allow for clear reconstruction of the low-momentum distribution, resulting from IR-induced ionization, as it is not present in the XUV-only case.

Better momentum resolution is achieved in the photoelectron momentum distributions of the electrons detected in coincidence with He^+ ions, shown for total momentum lower than 1 a u , since higher momenta has already been attributed to the XUV-only ionization, Fig. 5.15. Here, momentum rings with spacing proportional to the square root of the IR photon energy arising due to above-threshold ionization, as discussed earlier, are observed, with highest yield along the IR polarization axis. The IR polarization is tilted with respect to the x-axis under an angle of $(18 \pm 2)^\circ$ due to imperfection in the setting of the IR polarization entirely parallel to the XUV polarization. Despite the polarization tilt, a clear directional pattern along the polarization direction is observed in all 5 visible ATI rings.

The electron momentum distributions associated to events corresponding to the first three ATI peaks, selected through a condition for the electron kinetic energy

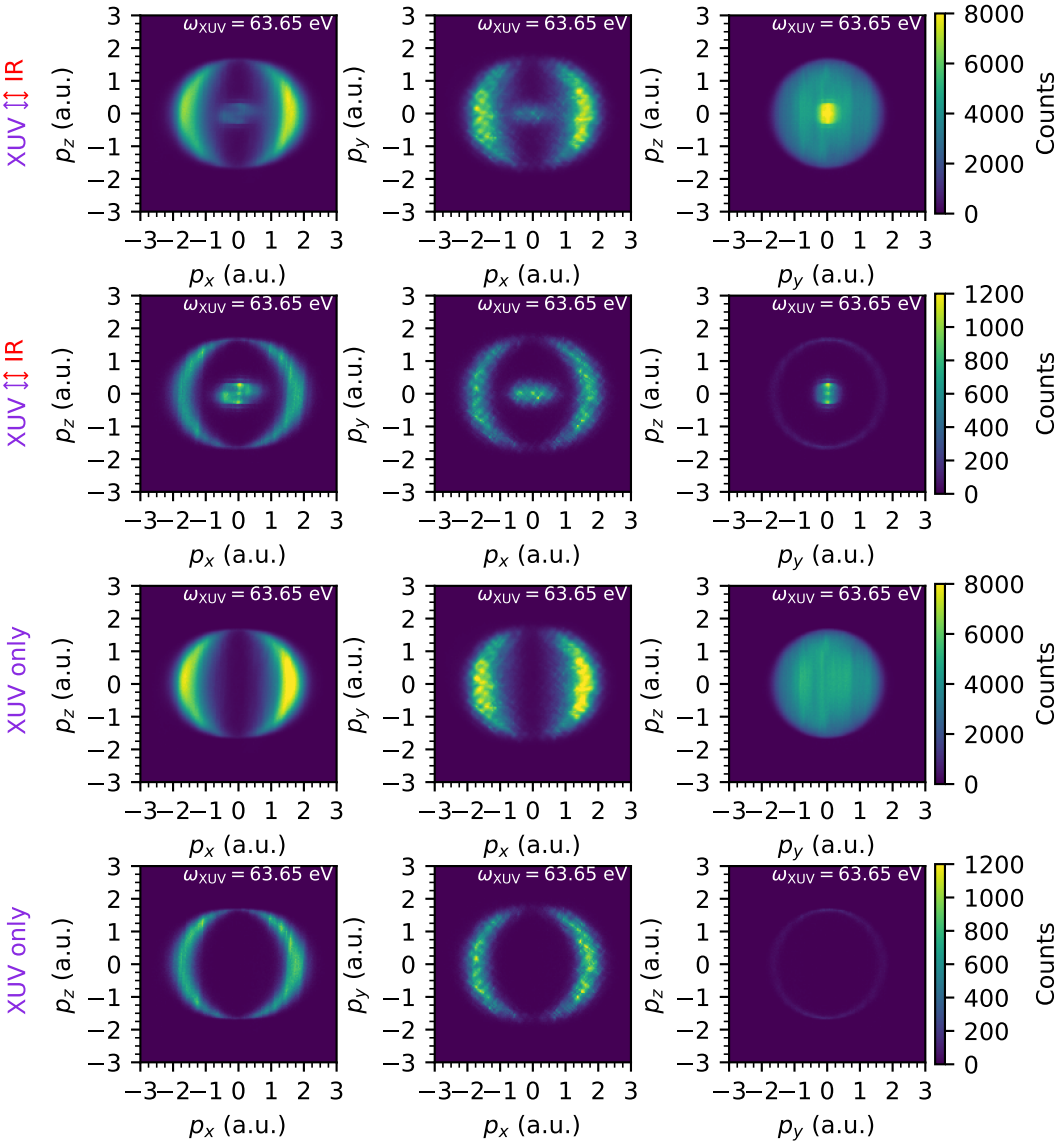

Figure 5.14: Recoil-ion momentum distribution of He^+ ions for XUV photon energy of $\omega_{XUV} = 63.65\,eV$ and polarization of the IR and XUV field along the x-axis. The two upper rows show the distributions in the case of overlapping XUV and IR fields, while the two lower rows depict the XUV-only distribution. In each set of two rows the upper one shows a projection on the respective p_i-p_j plane, i.e. integrating over the whole third axis, while the lower row depicts a cut through the third plane for momentum between $-0.1\,au$ and $0.1\,au$.

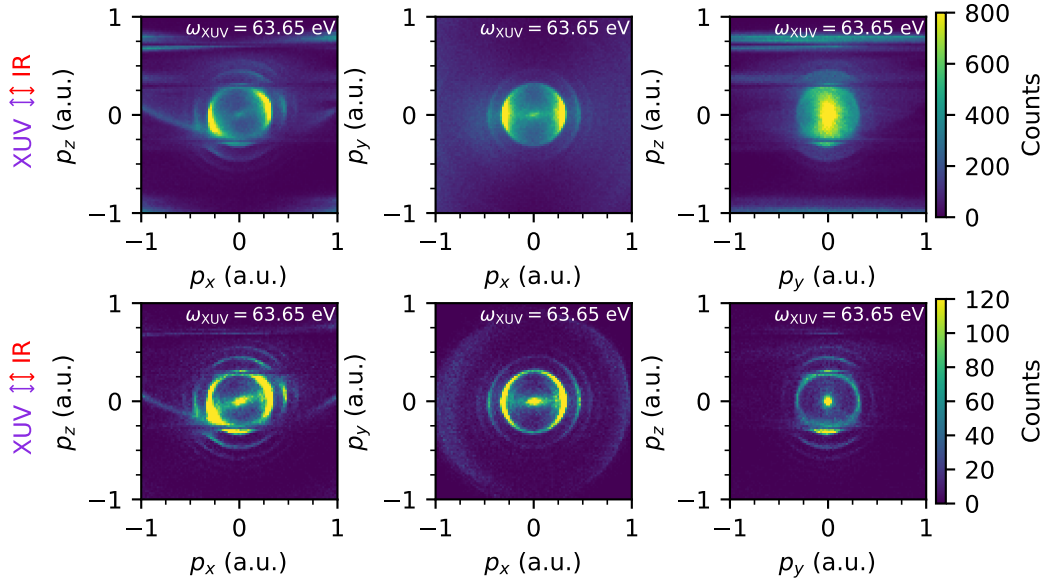

Figure 5.15: Photoelectron momentum distribution of electrons detected in coincidence with He^+ ions, i.e. single-ionization electrons, for XUV photon energy of $\omega_{XUV} = 63.65\,eV$ and polarization of the IR and XUV field along the x-axis. The upper row shows the distributions as a projection on the respective p_i-p_j plane, i.e. integrating over the whole third axis, while the lower row depicts a cut through the third plane for momentum between $-0.05\,a.u.$ and $0.05\,a.u.$

while looking for coincidences with He^+ ions, are presented in Fig. 5.16. As the electron kinetic energy in every next ATI peak is increased by the energy of the additionally absorbed IR photon $E_{IR} = 1.58\,eV$ and the total electron momentum scales proportional to the square of the electron kinetic energy, Eq. (5.28), the momentum distributions of the higher ATI electrons are bigger in extent. In contrast to the XUV-only case, shown in the recoil-ion distributions, which exhibits a clear minimum at $p_x = 0\,a.u.$ due to the $\cos(\theta)^2$ dependence of a p-wave, in the electron momentum distributions, detected in the case of XUV+IR in the ATI rings, it is clearly visible that also for $p_x = 0$, no full minimum is reached, which is consistent with even-component angular momenta as expected with the additional interaction with the IR (like s-wave or d-wave or higher-order distributions). It should be noted that the slight decrease in yield for $p_z \approx 0.25\,a.u.$ is due to the circular motion of the electrons towards the detector, which does not allow for efficient separation of the electrons arriving at the same time at a lot of different detector positions. Instead of showing a different symmetry, as it would be expected through the absorption of an additional IR photon [206], the symmetry of all ATI peaks appears nearly the same. A possible explanation for this is that in the strong-field regime the condition that a certain ATI peak can be reached through N photons holds only in the lowest-order process. The nth ATI peak can be reached not necessarily with n photons above the threshold, but also even 2, 4, etc. more photons can be absorbed/emitted. From

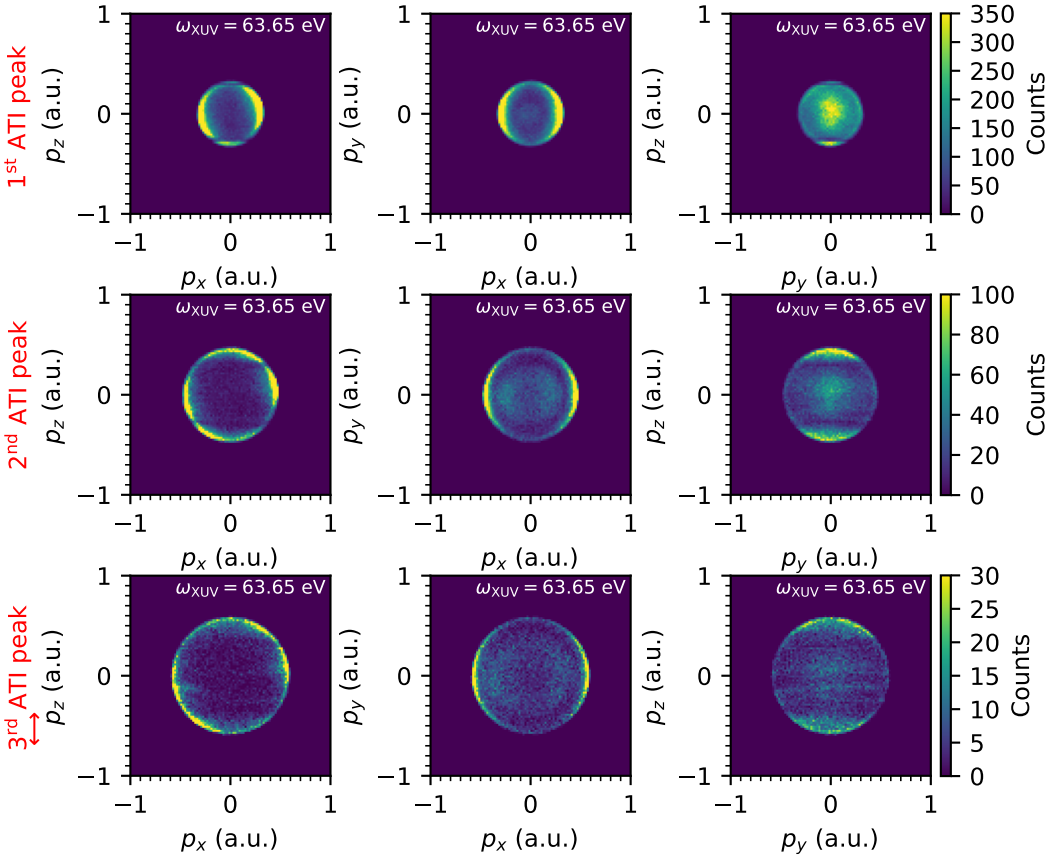

Figure 5.16: Photoelectron momentum distribution of ATI electrons detected in coincidence with He^+ ions for XUV photon energy of $\omega_{XUV} = 63.65\,eV$ and polarization of the IR and XUV field along the x-axis. The upper row shows the distributions corresponding to the first ATI peak, the middle row those of the second ATI peak and the bottom row of the third ATI peak. Each subfigure shows the distributions as a projection on the respective p_i-p_j plane, i.e. integrating over the entire third axis.

this viewpoint one can understand that also conditions for the higher-order processes leading to the formation of the nth ATI effectively weaken the conservation of angular momentum because both absorption and emission change the angular momentum state of the ionized electron.

To gain a further insight into the above-threshold ionization process, the momentum distributions of the recoil-ion and of the photoelectrons are shown for IR polarization perpendicular to the XUV polarization, i.e. along the z-axis, in Fig. 5.17 and Fig. 5.18, respectively. Compared to the case of the same polarization direction between both fields, the directionality of the IR-induced momentum components is now along the z-axis for all ATI momentum rings, Fig. 5.19, but still no clear additional ATI dependence on the momentum distribution is observed. Little dependence on the momentum distribution symmetry for different ATIs has been found

for above-threshold ionization due to circularly polarised laser fields [209–211], where the circular polarization, if looked at as a mix of two perpendicular to each other polarisations can drive simultaneously transitions to more than one state. A similar effect, where the contribution of pathways with different number of photons might be the cause for little structure in the ATI peak momentum distributions, which should be evaluated in detail in the future.

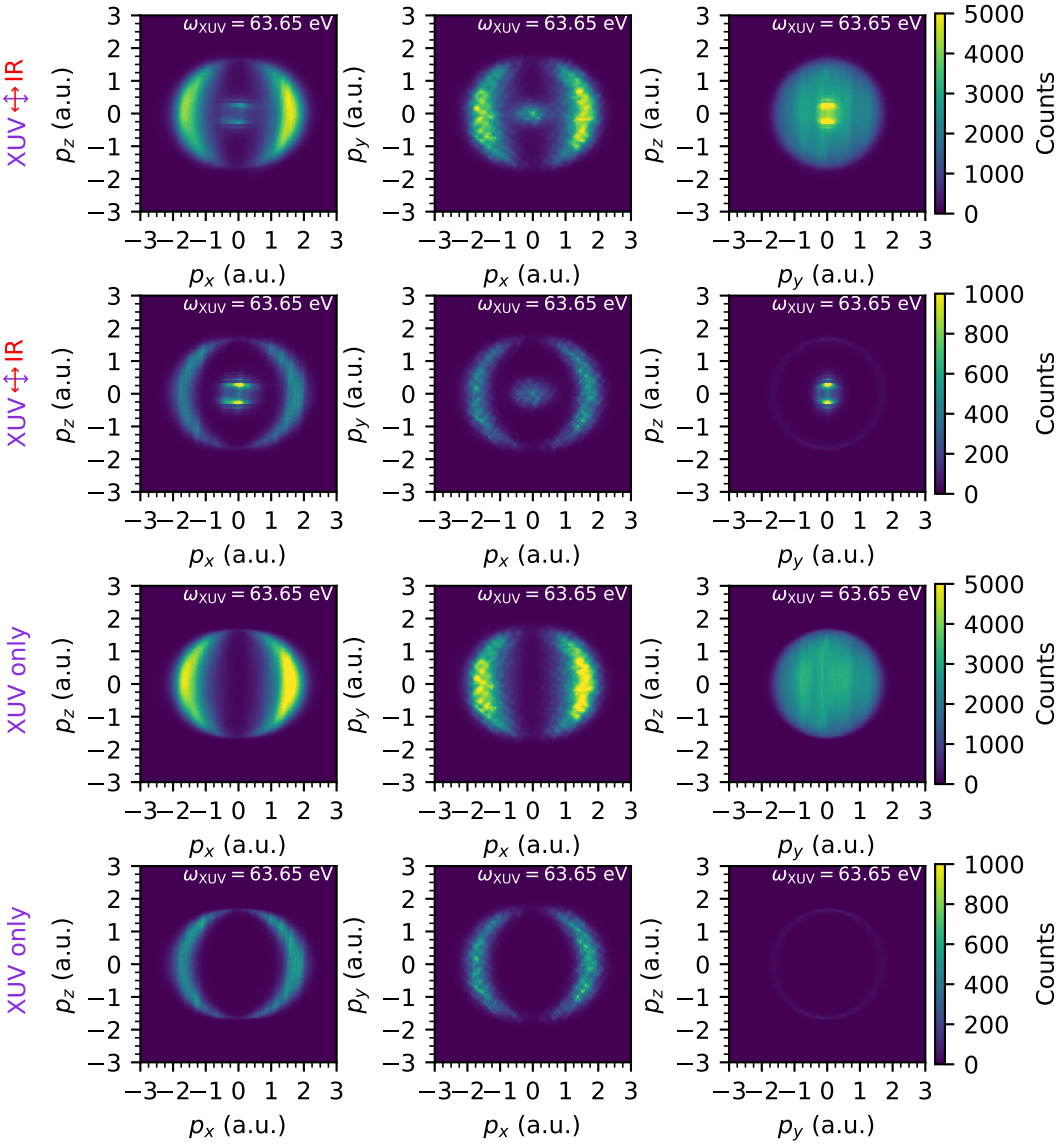

Figure 5.17: Recoil-ion momentum distribution of He^+ ions for XUV photon energy of $\omega_{XUV} = 63.65\,eV$ and XUV polarization along the x-axis, while the IR field is polarized perpendicularly to it along the z-axis. The two upper rows show the distributions in the case of overlapping XUV and IR fields, while the two lower rows depict the XUV-only distribution. In each set of two rows the upper one shows a projection on the respective p_i-p_j plane, i.e. integrating over the whole third axis, while the lower row depicts a cut through the third plane for momentum between $-0.1\,au$ and $0.1\,au$.

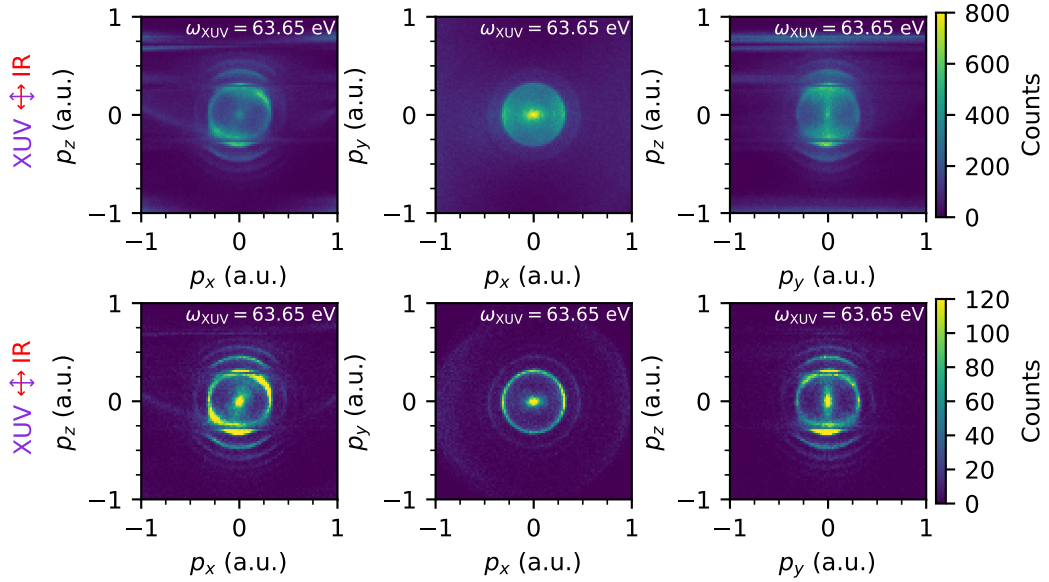

Figure 5.18: Photoelectron momentum distribution of electrons detected in coincidence with He^+ ions, i.e. single-ionization electrons, for XUV photon energy of $\omega_{XUV} = 63.65\,eV$ and XUV polarization along the x-axis, while the IR field is polarized perpendicularly to it along the z-axis. The upper row shows the distributions as a projection on the respective p_i-p_j plane, i.e. integrating over the whole third axis, while the lower row depicts a cut through the third plane for momentum between $-0.05\,au$ and $0.05\,au$.

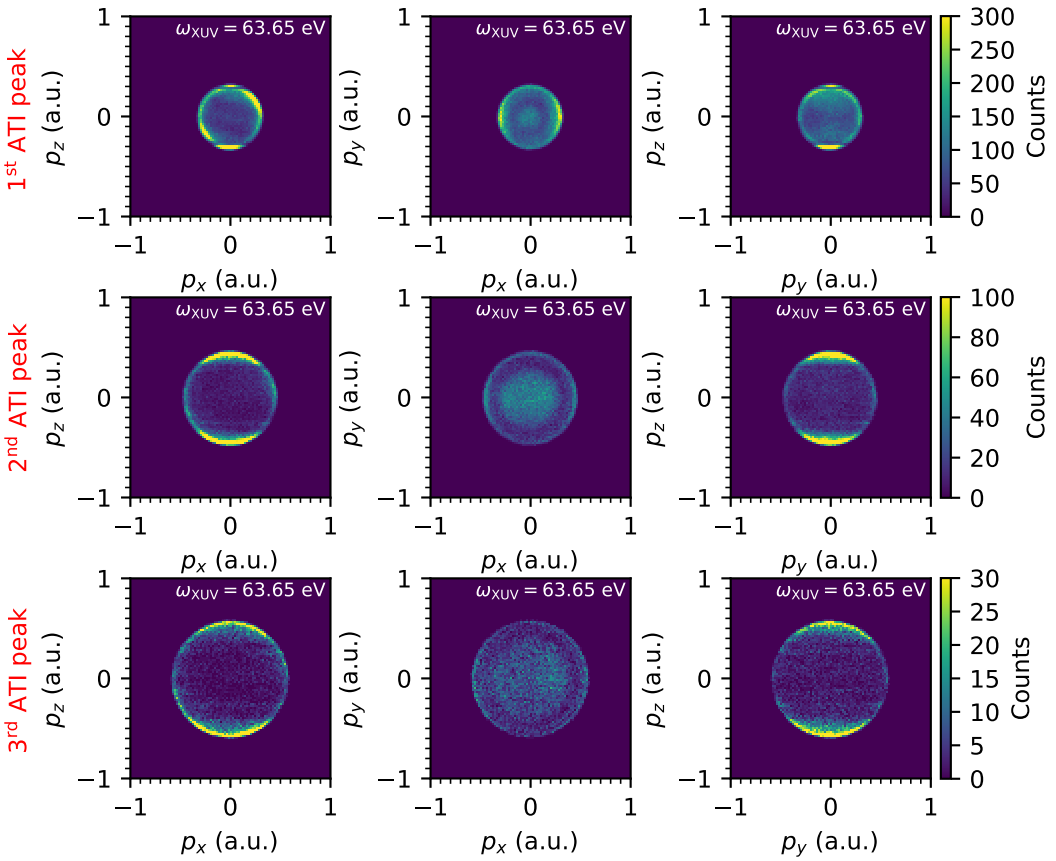

Figure 5.19: Photoelectron momentum distribution of ATI electrons detected in coincidence with He^+ ions for XUV photon energy of $\omega_{XUV} = 63.65\,eV$ and XUV polarization along the x-axis, while the IR field is polarized perpendicularly to it along the z-axis. The upper row shows the distributions corresponding to the first ATI peak, the middle row those of the second ATI peak and the bottom row of the third ATI peak. Each subfigure shows the distributions as a projection on the respective p_i-p_j plane, i.e. integrating over the whole third axis.

Single ionization out of highly doubly excited states between the I_2 and the I_3 ionization thresholds

To discuss further ionization pathways opening up when the XUV and the IR field overlap temporally, single ionization out of highly doubly excited states between the I_2 and the I_3 ionization thresholds is considered. An overview of the single-ionization yield in this energy region is presented in Fig. 5.20 for the XUV photon energy between 68.6 eV and 73.8 eV. The 3s3p state at energy 69.873 eV as well as the states of the $sp_{3,n+}$ series converging to the I_3 threshold at 72.957 eV are observed here. At the position of the 3s3p and the $sp_{3,4+}$ state electrons with almost zero kinetic energy are observed, which indicates a process as sketched in the pathway 4 of Fig. 5.12 (b) in the case of the 3s3p state, where the absorption of 2 IR photons is just enough for its ionization. The $sp_{3,4+}$ state at 71.623 eV can be ionized in a one-photon IR process, also with kinetic energy of the released photoelectron smaller than 0.25 eV. The kinetic energy of the ionized electron out of the higher lying states of the $sp_{3,n+}$ series increases with increasing energy of the states, as those are located closer to the I_3 threshold and one IR photon is enough to ionize one electron, thus more energy is transferred to the electron upon its ionization.

An interesting ionization pathway is the one to the laser-dressed continuum, observed along the XUV-only ionization diagonal starting at the I_2 threshold. In the here considered case of time-overlapping XUV and IR field, multiple sidebands in electron kinetic energy around the XUV-only ionization feature are detected. A sketch of the pathway leading to this type of ionization together with a distribution of the photoelectron kinetic energy $E_{\mathrm{kin,e}}$ measured for XUV photon energy of $\omega_{\mathrm{XUV}} = 70.2\,\mathrm{eV}$ is presented in Fig. 5.21. Here, in addition to the absorption of one XUV photon, the absorption of an additional IR photon can either increase or decrease the amount of the photoelectron kinetic energy, thus forming the sidebands around the XUV-only peak. A key difference however is, that the XUV-only process ionizes the photoelectron in the P continuum, while the XUV+1·IR process leads to ionization in the S or D continuum. The intensity of the XUV-only peak is additionally decreased, since now the probability of direct XUV-only ionization is suppressed by the IR-assisted ionization in the continuum. This process is similar in its nature to the process leading to sideband formation, exploited in the RABBITT (Reconstruction of attosecond beating by interference of two-photon transitions) technique to obtain the relative phase and amplitude of attosecond pulses for their temporal characterisation [30, 212] as well as to provide information on the dynamics of ultrafast processes in atoms and molecules [154, 213–215].

The recoil-ion momentum distribution of He^+ ions measured at the XUV photon energy of $\omega_{\mathrm{XUV}} = (70.0 \pm 0.6)\,\mathrm{eV}$ is shown in Fig. 5.22. Additionally to the high-momentum recoil ions being coincident with photoelectrons ionized over the first ionization threshold $I_1 = 24.59\,\mathrm{eV}$, now also recoil ions with lower momentum from the ionization process above the $I_2 = 65.399\,\mathrm{eV}$ are detected, corresponding to momentum of $(1.83 \pm 0.02)\,\mathrm{a.u.}$ and $(0.58 \pm 0.04)\,\mathrm{a.u.}$, respectively. The outer ring

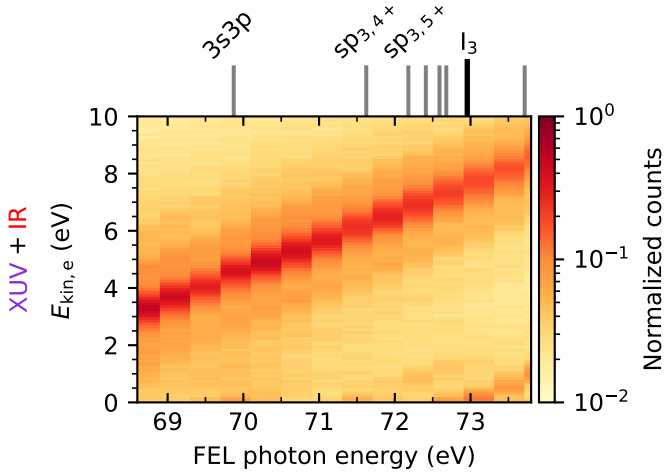

Figure 5.20: Single ionization yield as a function of XUV photon energy, ranging between 68.6 eV and 73.8 eV, i.e. scanning the whole region of doubly excited states between the second ionization threshold I_2 and the third ionization threshold I_3, with XUV and IR pulse arriving in time overlap. The measured photoelectron yield is detected in coincidence with He^+ ions as a function of photoelectron kinetic energy $E_{kin,e}$. The gray lines in the top part of the figure indicate the positions of doubly excited states in helium as well as of the ionization threshold I_3.

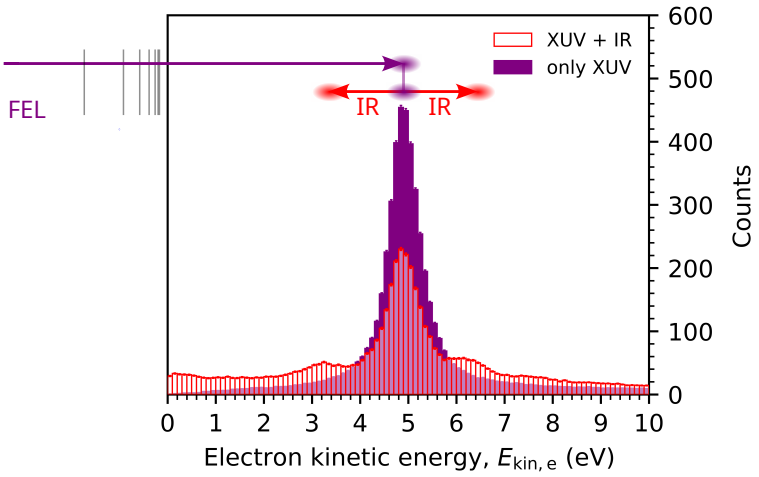

Figure 5.21: Distribution of electron kinetic energy $E_{kin,e}$ for two-colour XUV-IR direct ionization above the second ionization threshold I_2 measured for XUV photon energy of ω_{XUV} = 70.2 eV and XUV and IR field in time overlap. The depicted ionization pathway shows ionization into the two-colour continuum. The gray lines on the left denote the positions of doubly excited states of the $N = 2$ series, which are not relevant for the occurring ionization process.

corresponds to He^+ ions in the ground state, whereas the inner ring to He^+ ions in the 2p excited state. With additional IR interaction a feature around zero total momentum in the recoil-ion momentum distribution is detected. This low-energy feature is observed in the photoelectron momentum distribution of electrons detected in coincidence with He^+ ions, Fig. 5.23. In the $p_x - p_y$ momentum distribution additionally the rings corresponding to ionization in the S and D continuum via the absorption of one XUV and one IR photon are visible, but do not show a different symmetry than the ionization distribution corresponding to the direct XUV ionization. The momentum distributions of the recoil-ion and of the photoelectrons detected in the case of IR polarization perpendicular to the XUV polarization, i.e. along the z-axis, are presented in Fig. 5.24 and Fig. 5.25, respectively. While the distributions of the recoil He^+ ions barely show a difference, in the photoelectron momentum distributions strong directionality along the z-polarization axis is observed for the electrons detected with low momentum gained upon single ionization.

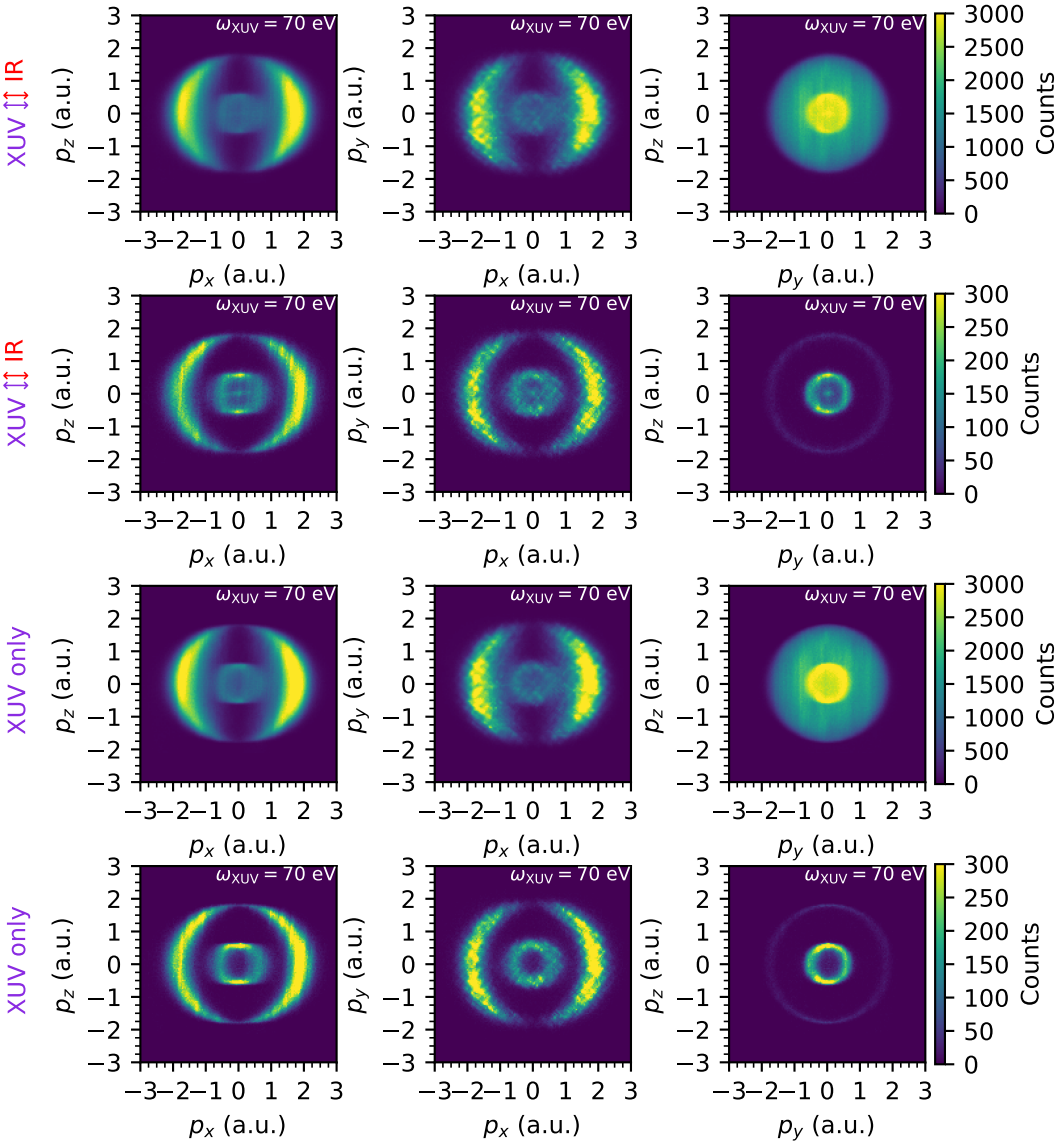

Figure 5.22: Recoil-ion momentum distribution of He^+ ions for XUV photon energy of $\omega_{XUV} = 70\,eV$ and polarization of the IR and XUV field along the x-axis. The two upper rows show the distributions in the case of overlapping XUV and IR fields, while the two lower rows depict the XUV-only distribution. In each set of two rows the upper one shows a projection on the respective p_i-p_j plane, i.e. integrating over the whole third axis, while the lower row depicts a cut through the third plane for momentum between $-0.1\,au$ and $0.1\,au$.

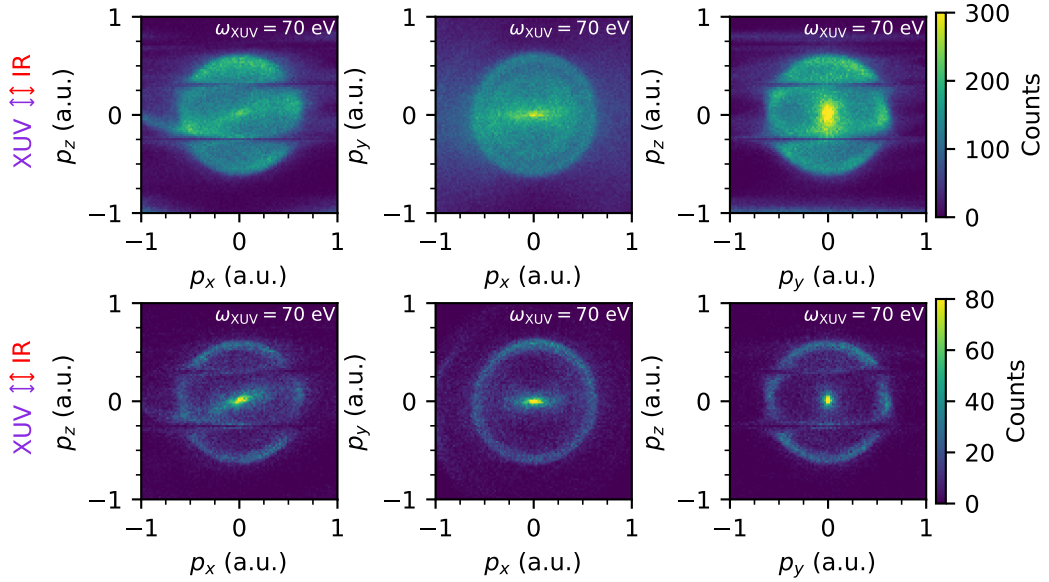

Figure 5.23: Photoelectron momentum distribution of electrons detected in coincidence with He^+ ions, i.e. single-ionization electrons, for XUV photon energy of $\omega_{XUV} = 70\,eV$ and polarization of the IR and XUV field along the x-axis. The upper row shows the distributions as a projection on the respective p_i-p_j plane, i.e. integrating over the whole third axis, while the lower row depicts a cut through the third plane for momentum between $-0.05\,a.u.$ and $0.05\,a.u.$

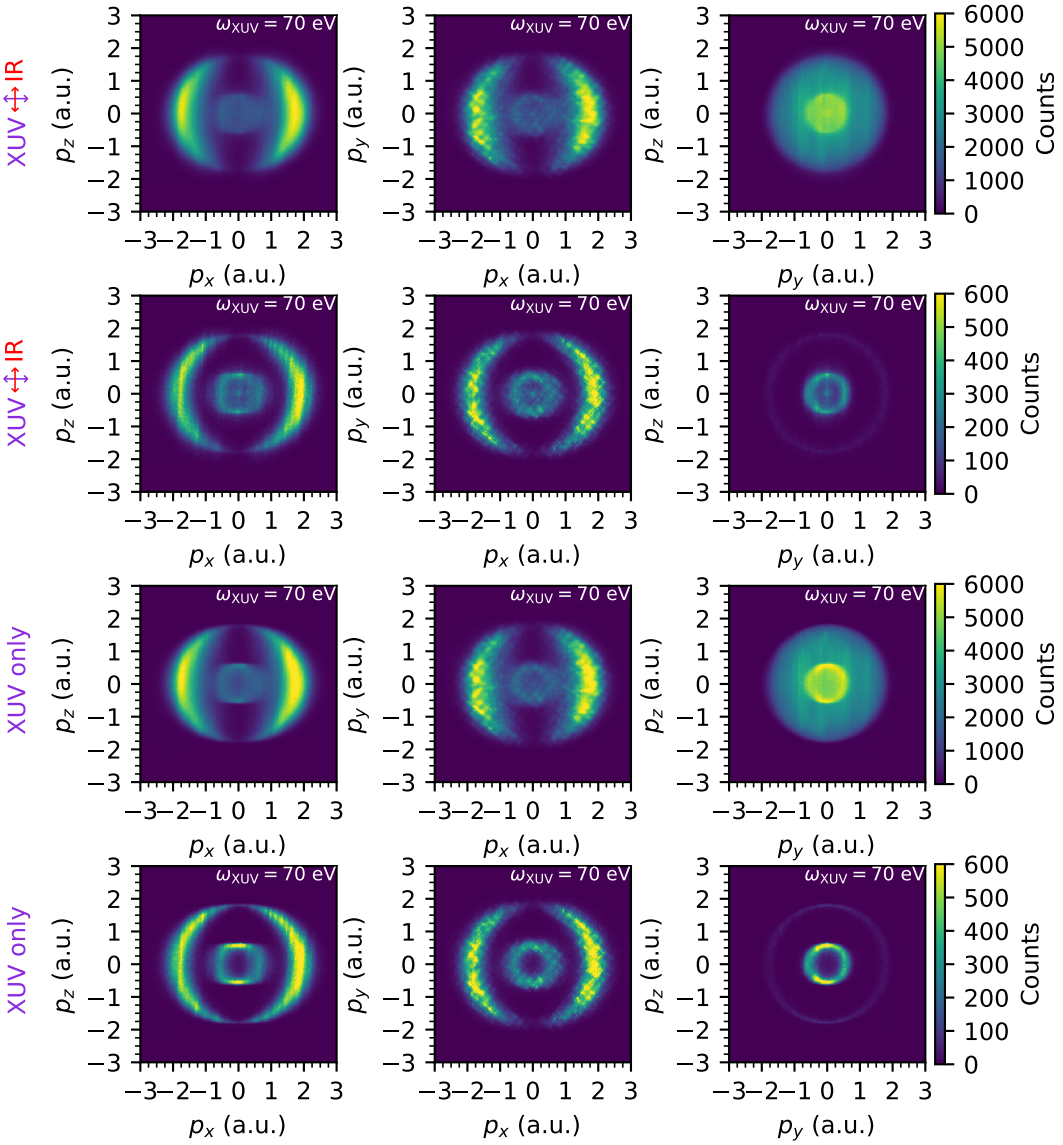

Figure 5.24: Recoil-ion momentum distribution of He^+ ions for XUV photon energy of $\omega_{XUV} = 70\,eV$ and XUV field with polarization along the x-axis, while the IR field is polarized perpendicularly to it along the z-axis. The two upper rows show the distributions in the case of overlapping XUV and IR fields, while the two lower rows depict the XUV-only distribution. In each set of two rows the upper one shows a projection on the respective p_i-p_j plane, i.e. integrating over the whole third axis, while the lower row depicts a cut through the third plane for momentum between $-0.1\,au$ and $0.1\,au$.

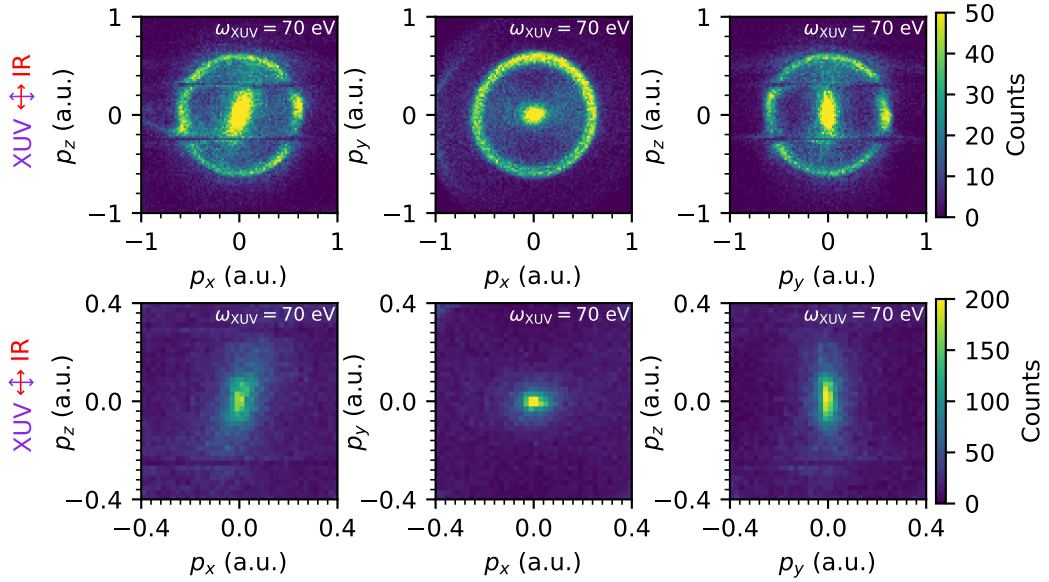

Figure 5.25: Photoelectron momentum distribution of electrons detected in coincidence with He^+ ions, i.e. single-ionization electrons, for XUV photon energy of $\omega_{XUV} = 70\,eV$ and XUV polarization along the x-axis, while the IR field is polarized perpendicularly to it along the z-axis. The upper row shows the distributions as a cut through the third plane for momentum between $-0.05\,a.u.$ and $0.05\,a.u.$, while the lower row shows a zoom for lower momenta of the same distribution.

5.3.2 Double-ionization processes above the first ionization threshold in helium

Having not only one, but two electrons, the helium atom cannot just undergo single ionization, but also double ionization. Double ionization can then be a result of a single photon transition, if the XUV energy is high enough to overcome the total ionization threshold in the helium atom of $I_\infty = 79.003\,\mathrm{eV}$, with a cross section of the single-photon double ionization process just above the double-ionization threshold I_∞ reported in [216] as 0.737 Mb. Considering also transitions including more than just a single photon, sequential and non-sequential double ionization pathways open up for XUV-only interaction, as well as for the combination of XUV and IR interaction.

In two-photon XUV absorption, the total energy required to doubly ionize the helium atom has to exceed $I_\infty = 79.003\,\mathrm{eV}$, as in the single-photon ionization process. Here, to overcome both the first and second ionization energies, at $I_1 = 24.59\,\mathrm{eV}$ and at $I_{\mathrm{He}^{2+}} = 54.4\,\mathrm{eV}$, either photons of energy grater than 54.4 eV have to interact with helium in two-photon ionization sequentially (or also non-sequentially), or two photons with energy between 39.5 eV and 54.4 eV have to be simultaneously absorbed in a direct non-sequential ionization process. This process is also possible for higher XUV photon energies, but it is suppressed due to the onsetting sequential ionization process, as discussed in the following. The non-sequential ionization process has been studied both theoretically [171, 217–221] and experimentally, together with the two-photon sequential process [222–226]. Since the XUV photon energy in the present study ranges between 59 eV and 80 eV, the non-sequential channel is dominated by the sequential process, happening with higher relative probability.

To get an overview over the possible ionization channels, first in the case of XUV light preceding the 250 fs later arriving IR light, a two-dimensional plot of the double-ionization yield as a function of XUV photon energy, ranging between 59 eV and 80 eV, and photoelectron kinetic energy $E_{\mathrm{kin,e}}$ is presented in Fig. 5.26. Here, measured 1 photoelectron yield in coincidence with He^{2+} ions is defined as double-ionization yield. In the XUV-only case, the rise in double-ionization yield for $\omega_{\mathrm{XUV}} > 79.003\,\mathrm{eV}$ (lower right corner of the distribution) is due to the single-photon channel. The single-ionization diagonal lines are barely visible, since the He^+ states populated in the single-ionization process are long-lived and have only a low probability to decay and with this free a second electron without further photon absorption. An additional diagonal line, however, is present in the double-ionization yield distribution in the region for ω_{XUV} between 59 eV and 65 eV at kinetic energies between 4 eV and 10 eV. This feature is due to the XUV-only double ionization in the sequential two-photon process, as sketched in Fig. 5.27 (a), which opens up for $\omega_{\mathrm{XUV}} > 54.4\,\mathrm{eV}$, as discussed above. At XUV photon energy of 62 eV, for example, the energy of the electron released in the second double-ionization step amounts to 7.6 eV.

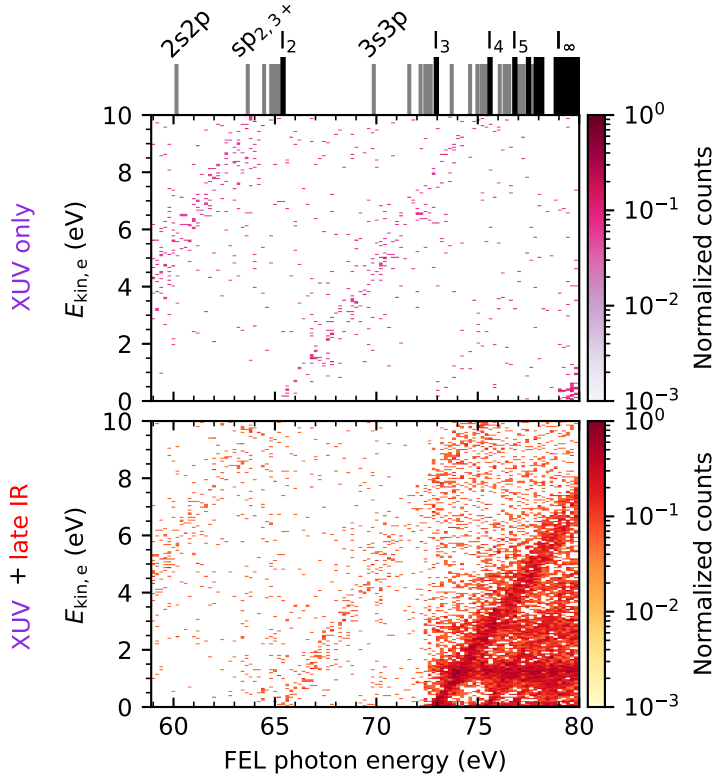

Figure 5.26: Double-ionization yield as a function of XUV photon energy, ranging between 59 eV and 80 eV, with the XUV pulse arriving before the IR pulse. The two panels show measured one-photoelectron yield in coincidence with He^{2+} ions as a function of photoelectron kinetic energy $E_{\mathrm{kin,e}}$ and XUV photon energy in the XUV-only configuration (upper panel) and in the case of XUV pulse preceding the IR pulse (late IR) arriving at time delay $\tau \approx 250$ fs (lower panel). The gray lines in the top part of the figure indicate the positions of doubly excited states in helium as well as of the ionization thresholds I_2 to I_∞.

Considering further the later arriving IR pulse, which can also contribute to double ionization, an additional ionization pathway opens up for energies above the third single-ionization threshold at $I_3 = 72.957$ eV. The pathway of this two-step process

$$\mathrm{He} \xrightarrow{\mathrm{XUV}} \mathrm{He}^{+*}(n=3) \xrightarrow{\mathrm{IR}} \mathrm{He}^{2+} \tag{5.29}$$

is sketched in Fig. 5.27 (b). Here, in a first step, the absorption of one XUV photon with energy enough to leave the produced He^+ in its state with quantum number $n = 3$ causes shake-up of the helium atom to the excited He^+ [48, 227–229]. The excited He^+ ion, which is long-lived, can then be ionized in strong-field multiphoton ionization through the absorption of four photons to just reach the ionization threshold to the He^{2+} continuum, as well as through the absorption of multiples of additional IR photons, as in the ATI process, leading to peaks in the kinetic energy

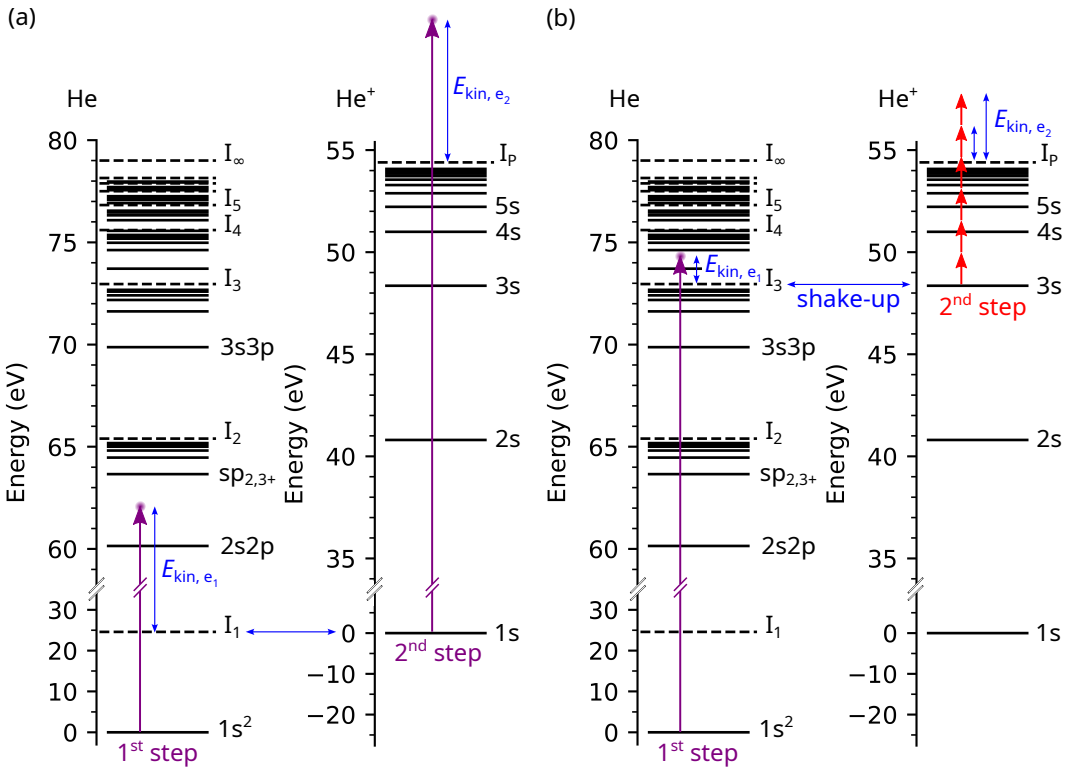

Figure 5.27: Sequential double-ionization pathways. **(a)** XUV-only two-step sequential double ionization with first step ionizing the He atom and leaving the created He^+ ion in its 1s ground-state configuration, such that in the second step an XUV photon ionizes the He^+ ion. **(b)** Sequential double ionization through XUV shake-up in the 3s state in He^+ (first step) and IR-induced above-threshold ionization in the second step.

of the electron spaced by 1.58 eV. Since shake-up into the $n = 3$ state of He^+ is possible for all XUV energies higher than the energy of 72.957 eV, horizontal lines with constant photoelectron kinetic energies are observed in the double-ionization yield.

The sequential double ionization process through shake-up is also possible in the case of time-overlapping XUV and IR pulses, Fig. 5.28, even if additional double ionization pathways out of the excited states densely populating the XUV region between 73 eV and 79 eV open up in this case. Increased double ionization yield here is also observed for XUV photon energy corresponding to the resonance energy of the 2s2p state, the 3s3p state, respectively, as well as for the lines of the $sp_{2,n+}$ series. These double ionization pathways are further discussed in relation to the measured He^{2+} recoil-ion momentum distributions. Those are presented in Fig. 5.29 and Fig. 5.30 in the case of measurement at XUV photon energy of $\omega_{XUV} = 63.65$ eV, as well as in Fig. 5.31 and Fig. 5.32 in the case of measurement at XUV photon energy of $\omega_{XUV} = 70$ eV.

The recoil-ion momentum distribution of the He^{2+} ions in the XUV-only case as a product of the sequential two-photon double ionization process shows two pairs of dipole-like half rings along the polarization direction of the XUV field, the x-axis. In the sequential ionization process both electrons are emitted independently of each other along the polarization direction, one from the neutral helium atom and one from the ground state of He^+, each forming then a dipole-like structure in the momentum distribution, where both are imprinted in the He^{2+} recoil-ion momentum distribution. For XUV photon energy of $\omega_{XUV} = 63.65\,eV$ the energy of the photoelectron in the first ionization step is 39.06 eV corresponding to a momentum of 1.69 au. The second electron, i.e. the additional ion recoil, has kinetic energy of 9.25 eV corresponding to a momentum of 0.82 au. This second recoil is added up to the first one after the first step. Since the second step can happen in either directions along the polarization axis, positive or negative, the resulting momentum distribution of the He^{2+} ions shows four peaks with momenta:

$-1.69\,au - 0.82\,au$	$-1.69\,au + 0.82\,au$	$1.69\,au - 0.82\,au$	$1.69\,au + 0.82\,au$
$-2.51\,au$	$-0.87\,au$	$0.87\,au$	$2.51\,au.$

For XUV photon energy of $\omega_{XUV} = 70\,eV$ the four peaks in the He^{2+} recoil ion momentum distribution are then positioned at

$-1.83\,au - 1.07\,au$	$-1.83\,au + 1.07\,au$	$1.83\,au - 1.07\,au$	$1.83\,au + 1.07\,au$
$-2.9\,au$	$-0.76\,au$	$0.76\,au$	$2.9\,au.$

The recoil-ion momentum distributions of the He^{2+} ions in the case of overlapping XUV and IR field shows additionally to the XUV-only distribution a broad signature around zero recoil-ion momentum with larger extent along the IR polarization axis, the x-axis in Fig. 5.29 and Fig. 5.31 and the z-axis in Fig. 5.30 and Fig. 5.32, respectively. While the momentum resolution in the recoil-ion momentum distributions is not sufficient to get an initial impression of the double-ionization distribution, induced by the IR field, except its extend along the polarization direction, the photoelectron momentum distributions in Fig. 5.33 and Fig. 5.34 show a dipole-like momentum distribution along the IR polarization direction with additional near-zero momentum yield for both XUV photon energies. Those distributions can be attributed to multiphoton double ionization out of the respective excited state to the He^{2+} continuum. Here, the near-zero-momentum distributions are much stronger in some projections than in others, which points at residual directionality of the ionization process, thus to electron correlations and different mechanisms in the strong-field ionization out of the FEL-prepared doubly excited states. Near-zero-momentum designates strongly a back-to-back emission of the two electrons, but still some directionality remains present.

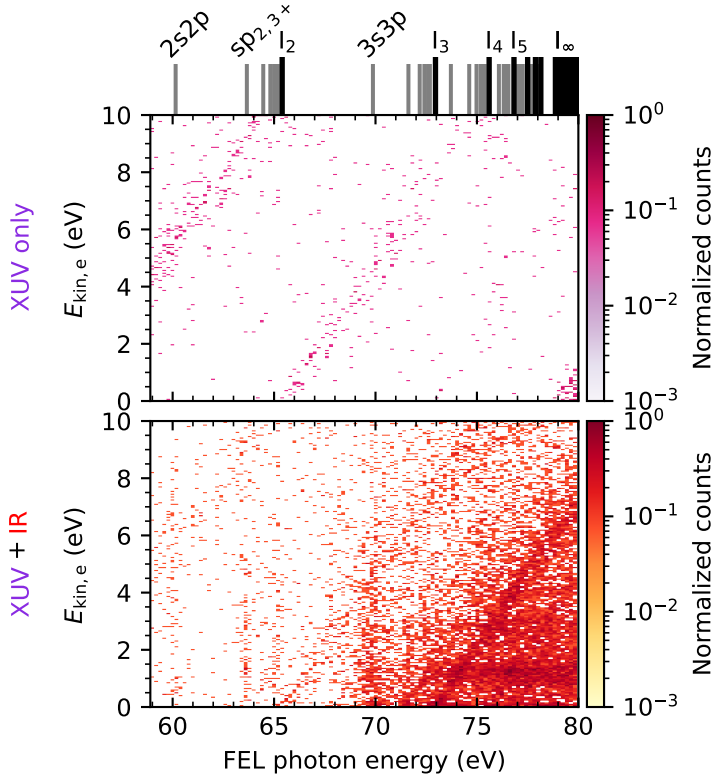

Figure 5.28: Double ionization as a function of XUV photon energy, ranging between 59 eV and 80 eV, with the XUV pulse arriving in time overlap with the IR pulse. The two panels show measured one-photoelectron yield in coincidence with He^{2+} ions as a function of photoelectron kinetic energy $E_{kin,e}$ and XUV photon energy in the XUV-only configuration (upper panel) and in the case of XUV and IR pulse arriving together at the target (lower panel). The gray lines in the top part of the figure indicate the positions of doubly excited states in helium as well as of the ionization thresholds I_2 to I_∞.

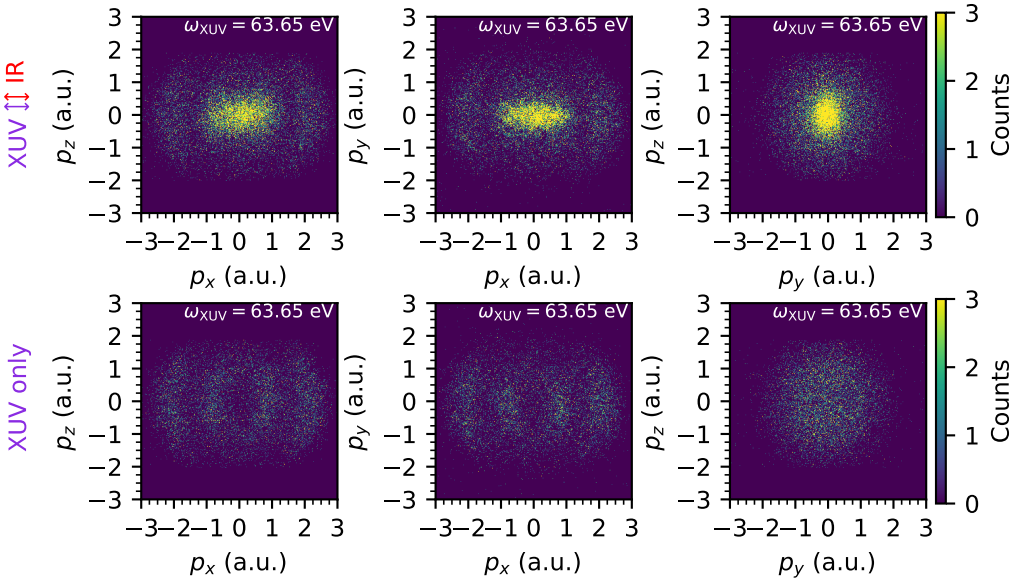

Figure 5.29: Recoil-ion momentum distribution of He^{2+} ions for XUV photon energy of $\omega_{XUV} = 63.65\,eV$ and polarization of the IR and XUV field along the x-axis. The upper row shows the distributions in the case of overlapping XUV and IR fields, while the lower row depicts the XUV-only distribution. Each subfigure shows a projection on the respective p_i-p_j plane, i.e. integrating over the whole third axis.

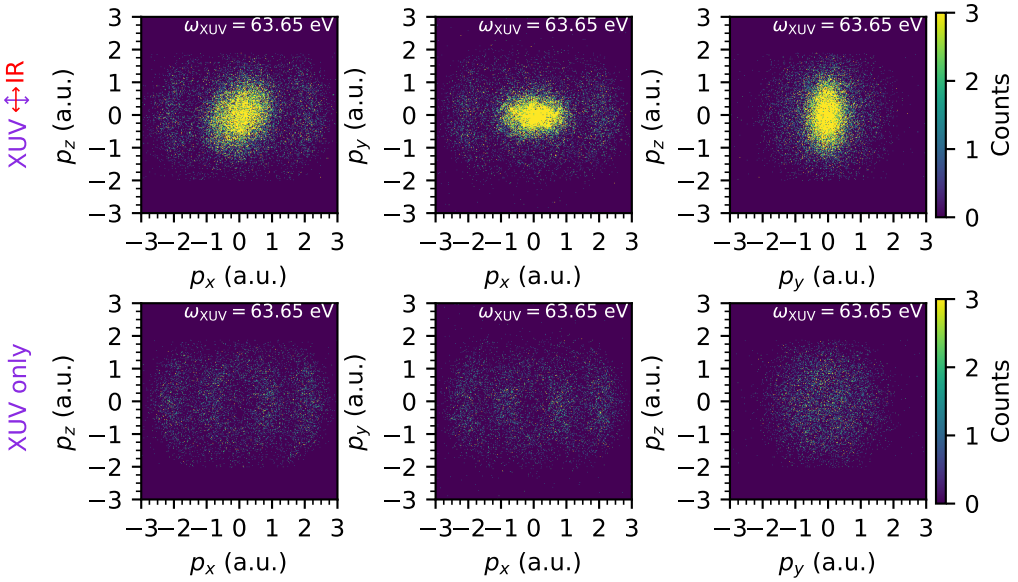

Figure 5.30: Recoil-ion momentum distribution of He^{2+} ions for XUV photon energy of $\omega_{XUV} = 63.65\,eV$ and XUV field with polarization along the x-axis, while the IR field is polarized perpendicularly to it along the z-axis. The upper row shows the distributions in the case of overlapping XUV and IR fields, while the lower row depicts the XUV-only distribution. Each subfigure shows a projection on the respective p_i-p_j plane, i.e. integrating over the whole third axis.

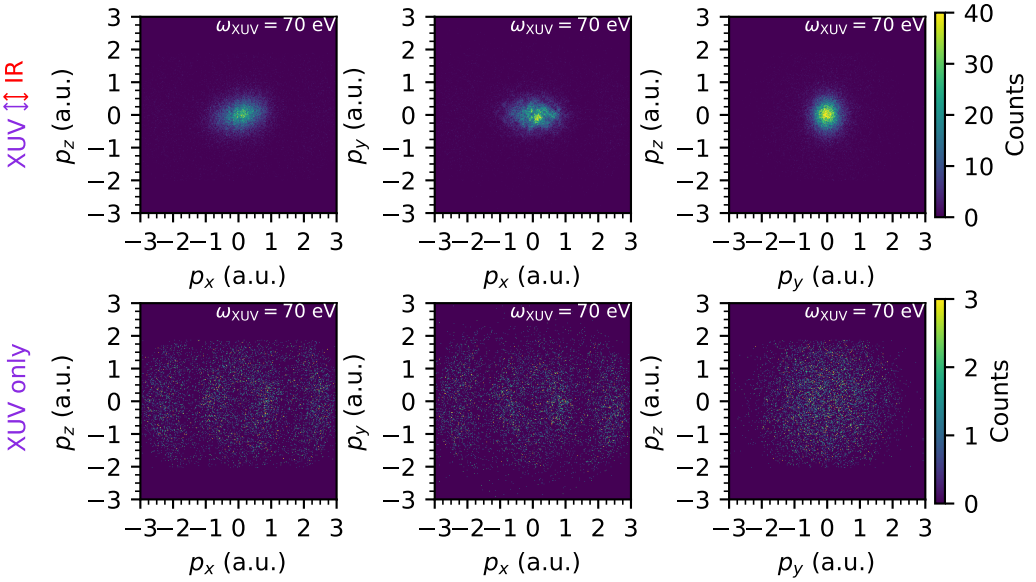

Figure 5.31: Recoil-ion momentum distribution of He^{2+} ions for XUV photon energy of $\omega_{XUV} = 70\,eV$ and polarization of the IR and XUV field along the x-axis. The upper row shows the distributions in the case of overlapping XUV and IR fields, while the lower row depicts the XUV-only distribution. Each subfigure shows a projection on the respective p_i-p_j plane, i.e. integrating over the whole third axis.

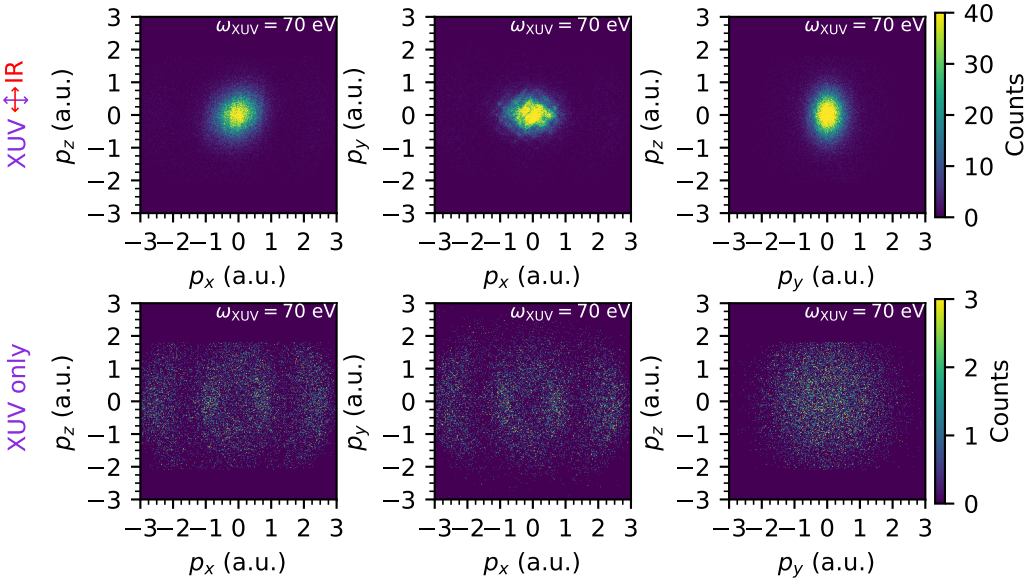

Figure 5.32: Recoil-ion momentum distribution of He^{2+} ions for XUV photon energy of $\omega_{XUV} = 70\,eV$ and XUV field with polarization along the x-axis, while the IR field is polarized perpendicularly to it along the z-axis. The upper row shows the distributions in the case of overlapping XUV and IR fields, while the lower row depicts the XUV-only distribution. Each subfigure shows a projection on the respective p_i-p_j plane, i.e. integrating over the whole third axis.

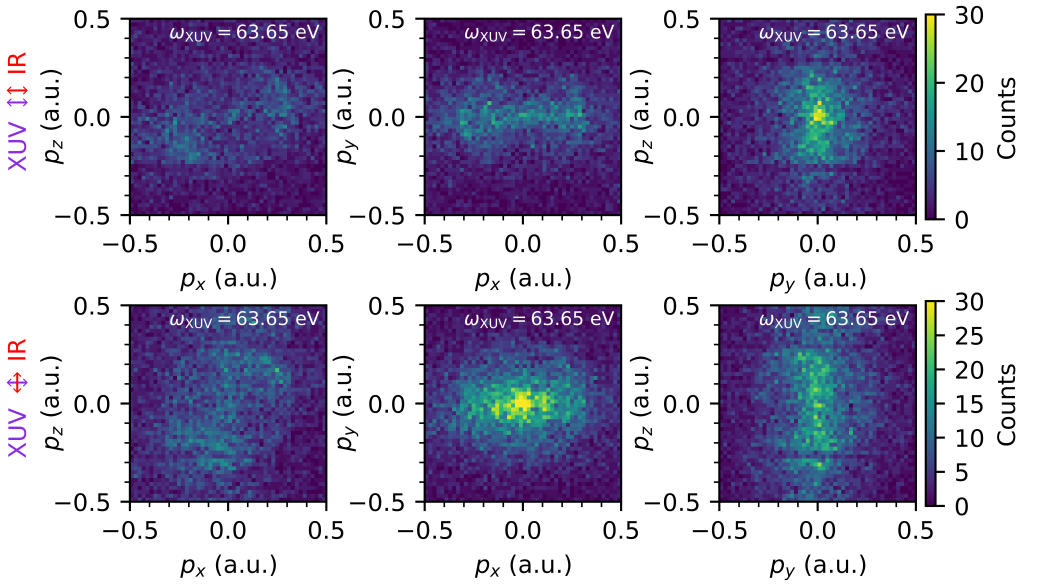

Figure 5.33: Photoelectron momentum distribution of electrons detected in coincidence with He^{2+} ions for XUV photon energy of $\omega_{XUV} = 63.65\,eV$. The upper row shows the distributions for polarization of the IR and XUV field along the x-axis, while those in the bottom row are for XUV polarization along the x-axis and IR polarized perpendicularly to it along the z-axis. All distributions are a projection on the respective p_i-p_j plane, i.e. integrating over the whole third axis.

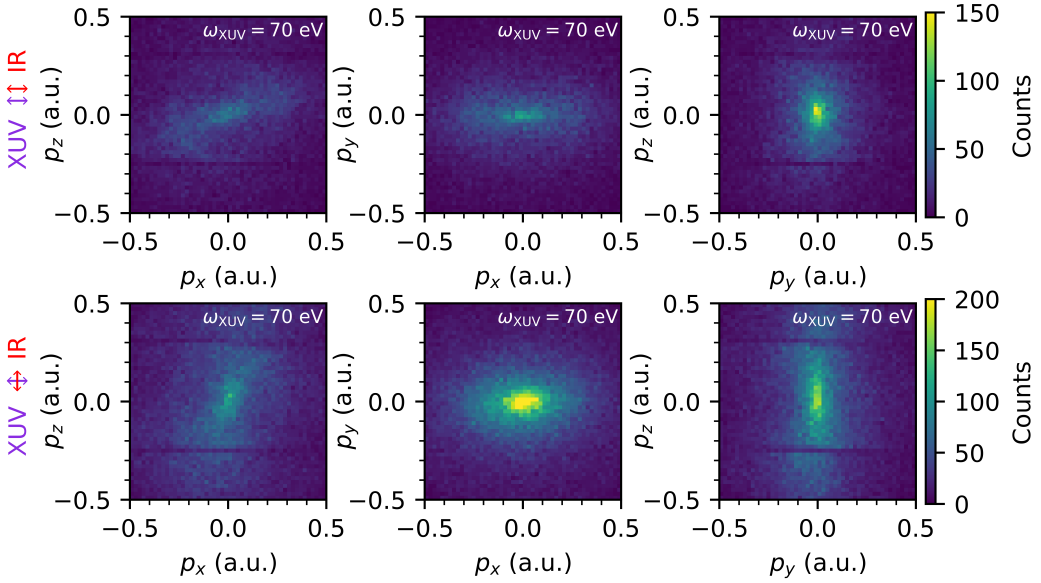

Figure 5.34: Photoelectron momentum distribution of electrons detected in coincidence with He^{2+} ions for XUV photon energy of $\omega_{XUV} = 70\,eV$. The upper row shows the distributions for polarization of the IR and XUV field along the x-axis, while those in the bottom row are for XUV polarization along the x-axis and IR polarized perpendicularly to it along the z-axis. All distributions are a projection on the respective p_i-p_j plane, i.e. integrating over the whole third axis.

5.4 Brief chapter summary and outlook

This chapter presented results on ionization out of specifically prepared doubly excited states in the helium atom. Selectively excited by a free-electron laser narrow-band XUV pulse, the doubly excited states were ionized either subsequently or directly by an intense IR field. With the aim to discover the dominating ionization pathways taking place, single and double ionization processes were discussed, also for the strong background XUV-only ionization mechanisms at play. Additional ionization pathways, like the ionization process in the laser-dressed continuum, also open up in the laser-dressed helium atom. The investigation of double-ionization pathways complements previous studies of sequential and non-sequential double ionization in the helium atom, while also finding new ionization IR-induced double-ionization pathways through shake-up ionization as well as directly out of the doubly excited states. One important next step here is to analyse and quantify in more detail the correlated angular distributions for the different configurations, as for example the ATI rings in single ionization as well as the correlated recoil-ion and two electrons emerging with low momentum after double ionization, all out of the specific doubly excited state, which will bring further insight into the nature of the electron correlations and its role for the ionization process.

The presented experimental results as well as the theoretical findings, which motivated the experimental study, contribute to understanding the role of the initial-state in the ionization process taking place in the same system, here the benchmark helium atom. With the effective preparation of individual excited states due to the availability of tunable narrowband XUV sources at free-electron lasers, as presented here, all processes studied so far out of the ground state in any system can now be investigated and possibly even new ionization mechanisms can be found out of the correlated initial states, not only in the simplest two-electron system, but also in bigger atoms and molecules.

6 LASER CONTROL OF A VIBRATIONAL WAVE PACKET IN THE NEUTRAL HYDROGEN MOLECULE

The key concepts and the presentation of some parts of this chapter follow closely the following reference:
Laser control of an excited-state vibrational wave packet in neutral H_2
Gergana D. Borisova, Paula Barber Belda, Shuyuan Hu, Paul Birk, Veit Stooß, Maximilian Hartmann, Daniel Fan, Robert Moshammer, Alejandro Saenz, Christian Ott and Thomas Pfeifer
arXiv:2301.03908 (2023).

Molecular dynamics covers a wide range of timescales: from the picosecond timescale of molecular rotations, through the femtosecond timescale characteristic of vibrations to the attosecond timescale of electronic dynamics [230–232]. To access one of those scales, suitably short laser radiation, comparable or shorter than the respective timescale, is needed to investigate the characteristic molecular dynamics, being rotational, vibrational or electronic. Rotational motion evolving on the slowest of the discussed timescales has been made accessible by picosecond laser radiation [21,233], while only femtosecond laser light, allowing for the generation of ultrashort light pulses has opened the door to the faster molecular vibrations studied widely in the thereafter emerging field of *femtochemistry* [25,26,234], with the aim to record snapshots of chemical reactions. Such snapshots become accessible in pump-probe experiments, implementing two laser pulses: a pump (initiating) pulse starting coherent molecular dynamics with a defined time zero, accurate on the femtosecond timescale, and a second probe pulse to map the system's current time-dependent state to a measurable observable. With the extension of the pump-probe technique also to the attosecond regime even electron dynamics has become accessible [235].

Pump-probe experiments have enabled monitoring the evolution of wave-packet dynamics in the smallest molecules H_2 and D_2. Here, however, most experiments study wave-packet vibration in the ground state of the respective molecular ion through controlling molecular dissociation via electron localization in the electronically excited ion [236–243]. Molecular wave-packet studies have been performed

also on other diatomics [244–248] but also for more complex molecules [249]. However, only a few experiments so far have treated the neural hydrogen molecule in time-delay pump-probe studies [250, 251]. The overall aim to control the wave-packet vibrational dynamics has been touched upon in [252, 253] in a pump-probe experiment. Meanwhile, a pump-control-probe scheme, employing three precisely timed laser pulses, has been employed to demonstrate strong-field control of a vibrational wave-packet [254, 255] in a limited number of molecular systems.

The majority of the experiments so far have typically employed detection of ionization/dissociation products to gain access to the natural evolution of the studied vibrational wave packet. An exception to this are the all-optical time-delay pump-probe studies of singly excited states in H_2 [250,251]. Here, the classical vibrational period of states is imprinted in an oscillating absorption signal in a short time-delay region after the wave-packet excitation. Through phase-fits on the oscillating absorption lineshapes along the time-delay a nuclear wave packet is reconstructed in the excited $B'\,^1\Sigma_u^+$ electronic state.

This chapter introduces an alternative approach to visualise a vibrational wave packet in an electronically excited state in the neutral H_2 molecule. Figure 6.1 illustrates the idea behind the experimental pump-control scheme for molecular wave-packet visualisation and control. Coherent extreme ultraviolet light is used to create (pump) a vibrational wave packet in the excited $D^1\Pi_u 3p\pi$ state of neutral H_2. Access to the wave-packet dynamics, in particular to the molecular vibrational revival, is gained through the XUV absorption spectra in the region of the resonances between the excited D vibronic band and the molecular ground state, from which the time-dependent coherent electronic dipole is reconstructed employing the technique for reconstruction of the real-time coherent dipole response [256], which probes the vibrating wave packet through the molecular ground state. To control the wave packet time evolution and through this its revival, an intense near-infrared (control) pulse, applied shortly after the wave-packet excitation is used. This second pulse, however, does not act as a probe pulse for the system, since the probe step is already fulfilled by the molecular ground state, self-probing the evolution of the excited wave packet, imprinted then in the coherent dipole emission. Thus, the second interacting pulse can be used to control the wave-packet's time evolution, while still utilizing the ground-state self-probing for the visualisation of the control mechanism.

This chapter presents a first demonstration of this non-destructive spectroscopic scheme to track molecular vibration in the smallest and fastest molecule, hydrogen. With the possibility to non-invasively, i.e. without destroying the quantum system, follow the coherent (time-resolved) dynamics of molecular vibration in a specific electronically excited state, the regime where electronic and nuclear degrees of freedom are coupled throughout the time-evolution becomes accessible. Learning to control either electronic, or nuclear motion, or even both simultaneously, can open the door to exploring the boundary of validity of the Born-Oppenheimer approximation, decoupling vibration and rotation from the fastest electronic movement.

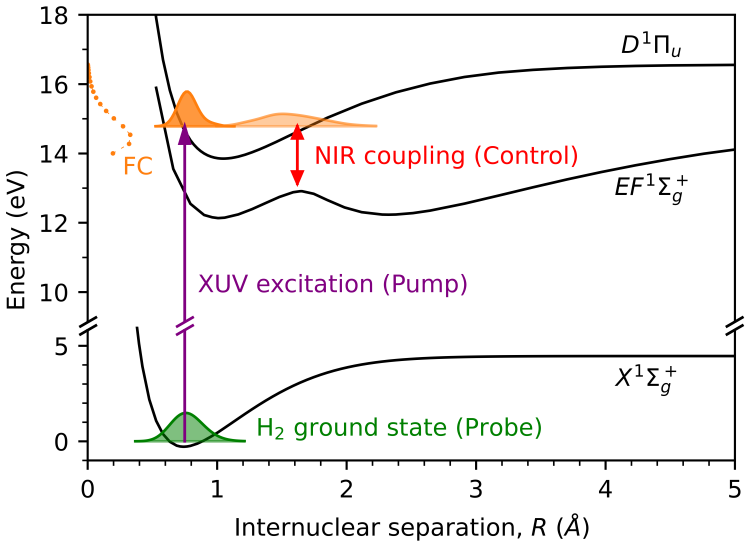

Figure 6.1: Illustration of the pump-control scheme for all-optical non-destructive wave-packet control in the neutral H_2 molecule. In the first pump step, initiated by an XUV-excitation pulse, a wave packet (orange) is promoted to the electronically excited $D^1\Pi_u 3p\pi$ bound state from the molecular $X^1\Sigma_g^+ 1s\sigma$ ground state (green) according to the Franck-Condon population distribution of the 18 bound vibrational states (labelled FC on the left side at the energy position of the respective states) in the electronically excited potential-energy curve. The excited wave packet oscillates as a function of internuclear separation R, leaving and (partially) re-entering the region of its initial excitation, the so called Franck-Condon region of overlap with the ground-state wave function, which acts as a probe to the wave packet, whenever the overlap between the ground state and the wave packet is non-vanishing. The free oscillating wave packet can then be coupled to other molecular bound states, as for example the resonant $EF^1\Sigma_g^+ 2s\sigma + 2p\sigma^2$. Here, an NIR-coupling pulse with variable intensity is introduced, which can deliberately change the wave packet and by this exert control on the wave packet, which, in turn, is detected by the quasi-stationary H_2 ground state acting as probe of the vibrating wave packet for all times of its evolution.

6.1 The vibrating diatomic molecule

A diatomic molecule, like the H_2 molecule, consists of two covalently bound atoms. Here, covalent bonding describes the stable balance of the attractive and repulsive forces between the two atoms: on the one hand, the nucleus of one atom attracts the electrons of the other atom, and vice versa, and on the other hand there is a repulsion between the two positively charged nuclei, as well as between the negatively charged electron distributions belonging to each of the two atoms. The attractive and repulsive Coulomb forces balance out at a certain mean internuclear

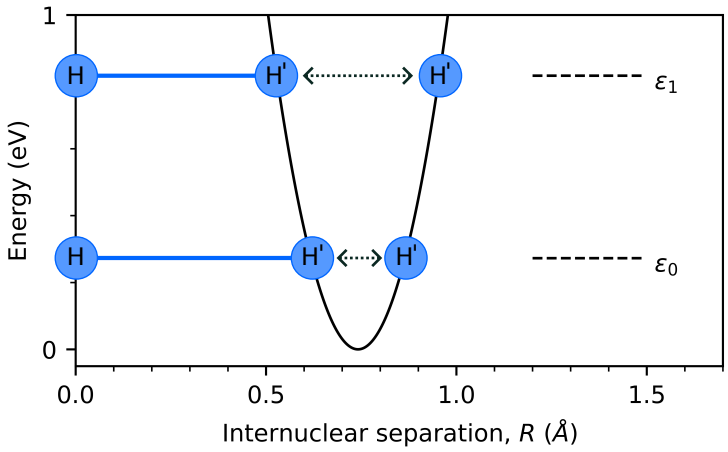

Figure 6.2: Bond compression and bond extension in the electronic ground state of the H_2 molecule. A hydrogen molecule is illustrated at the two depicted energy positions ε_0 and ε_1, where one of the atoms in the molecule, H, is located at position $R = 0$ Å and the second atom H′ can have a different position along the internuclear separation axis, i.e. can vibrate.

distance, where the total energy of the forming molecule is minimal. Bringing the two atoms further together would increase the repulsion in the system forcing molecular break-up, while a further atomic separation is prevented by the attractive force. Thus, any attempt to change the distance between the two atoms would increase the system's energy, as shown in Fig. 6.2. The compression and extension of the molecular bond, or in other words a vibrating diatomic molecule, very closely resembles the behaviour of an oscillating spring. Both systems represent a case of a harmonic oscillator. While a harmonic oscillator is a good starting point to understand the structure of vibrational spectra and overall molecular vibration, it fails to replicate observables like vibrational revival, which is a key characteristic of molecular vibration.

6.1.1 Time evolution of a molecular wave packet

The neutral hydrogen molecule has many excited electronic states, which can be populated out of the ground state after interaction with an XUV pulse [67]. The XUV pulse, used for the experiments presented in this chapter covers an energy region between 13 and 17 eV and therefore XUV excitation out of the molecular ground state leads to the population of multiple electronic states, with the corresponding occupation of many vibrational states according to the Franck-Condon overlap principle [34, 257–259]. In the Born-Oppenheimer approximation, allowing for the separation between the electronic and nuclear degrees of freedom [34,65, 258,259], then the resulting wave function can be written as a sum over the product functions of the n-th electronic wave function $\psi_R^n(\mathbf{x},t)$ and the nuclear wave packet

$\Phi^n(R,t)$ in the respective electronic state:

$$\Psi_{\mathrm{H_2}}^{\mathrm{excited}}(\mathbf{x},R,t) = \sum_n \Phi^n(R,t)\psi_R^n(\mathbf{x},t). \tag{6.1}$$

Here, the nuclear wave function is a coherent superposition of all vibrational eigenstates $\phi_\upsilon^n(R,t)$ of the corresponding potential-energy curve of an electronic state n

$$\Phi^n(R,t) = \sum_{\upsilon=0}^{\infty} c_\upsilon^n \phi_\upsilon^n(R,t), \tag{6.2}$$

weighted with the expansion coefficients c_υ^n, which quadratic value give the population amplitude of the corresponding vibrational eigenstate. The free time evolution of the vibrational eigenstates evolves with the state's eigenenergy E_υ^n, such that

$$\phi_\upsilon^n(R,t) = \mathrm{e}^{-iE_\upsilon^n t/\hbar}\phi_\upsilon^n(R) \tag{6.3}$$

Because of the linearity in the expansion of the total excited wave function in Eq. (6.1) the further discussion can be restricted to one electronic excited state together with the corresponding wave packet of nuclear wave functions. With the spacial representation of the nuclear wave functions and knowing their eigenenergy one can easily find the time evolution of a nuclear wave packet $\Phi(R,t)$ in the field-free case according to

$$\Phi(R,t) = \sum_{\upsilon=0}^{\infty} c_\upsilon \mathrm{e}^{-iE_\upsilon t/\hbar}\phi_\upsilon(R). \tag{6.4}$$

In an anharmonic potential-energy curve, as is the case for all electronic excited states in the hydrogen molecule, here specifically for the $D^1\Pi_u 3p\pi$ state, the energy separation between the vibrational states is not equidistant, which leads to spatial dispersion of the nuclear wave packet, as it evolves in time. At a specific later time the wave functions in the wave packet come back in phase again and a wave-packet revival is observed. Figure 6.3 shows four snapshots of the vibrational wave packet in the $D^1\Pi_u 3p\pi$ state, including the initially excited wave packet and its revival around 270 fs.

6.1.2 Wave-packet revivals in molecular potentials

To understand the emergence of a wave-packet revival as a rephasing of all wave-packet states, the eigenenergy of each individual state can be expanded in a Taylor series around a central vibrational state υ_e, as shown in for example [260, 261]. The expansion is justified in the case of many vibrational states with small

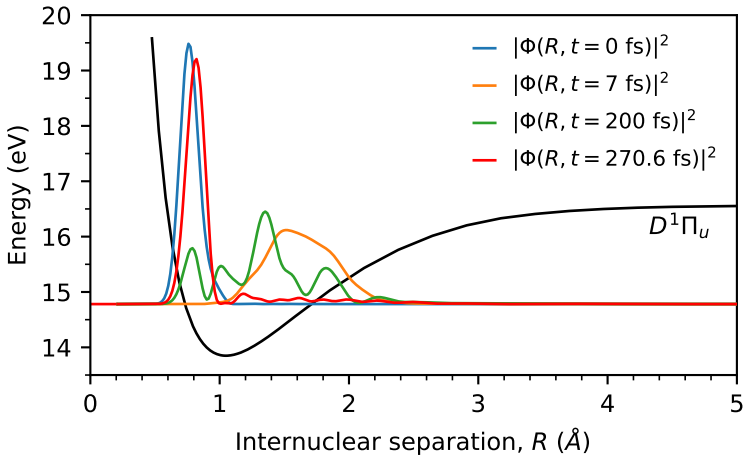

Figure 6.3: Time evolution of the bound-state vibrational wave packet in the $D^1\Pi_u 3p\pi$ state after excitation from the molecular ground state. The probability distribution of the nuclear wave packet $|\Phi(R,t)|^2$ along the internuclear separation coordinate R is shown for four different times. The initial wave packet distribution $|\Phi(R,t=0\,\text{fs})|^2$ resembles a well-localised copy of the molecular ground state. At the very beginning of its time evolution (here shown for time $t = 7\,\text{fs}$ the wave packets spreads spatially, while oscillating in the potential curve. At later times, the wave-packet is completely delocalised as in the depicted $|\Phi(R,t=200\,\text{fs})|^2$. At a later time a revival at $t = 270.6\,\text{fs}$ occurs and the wave packet is again localised around its initial excitation position.

energy-spacing compared to the energy of the expansion point $E(v_e)$

$$\frac{|E(v_e) - E(v_e \pm 1)|}{E(v_e)} \ll 1. \tag{6.5}$$

The expansion of the energy of a state with vibrational quantum number v then takes the form

$$E(v) \approx E(v_e) + \left.\frac{dE(v)}{dv}\right|_{v_e} (v - v_e) + \left.\frac{d^2E(v)}{dv^2}\right|_{v_e} (v - v_e)^2 + O(v^3), \tag{6.6}$$

which leads to the time evolution of each individual nuclear eigenstate according to Eq. (6.3):

$$\begin{aligned}\phi_v(R,t) &= \phi_v(R) \exp\left\{-\frac{i}{\hbar}\left[E(v_e) + \left.\frac{dE(v)}{dv}\right|_{v_e} (v - v_e) + \frac{1}{2}\left.\frac{d^2E(v)}{dv^2}\right|_{v_e} (v - v_e)^2 + \cdots\right] t\right\} \\ &= \phi_v(R) \exp\left\{-\frac{i}{\hbar}\left[E(v_e) + E'(v_e)(v - v_e) + \frac{1}{2}E''(v_e)(v - v_e)^2 + \cdots\right] t\right\}\end{aligned}. \tag{6.7}$$

Defining the characteristic timescales in the first and second expansion order as

$$T_{\mathrm{cl}} = \frac{2\pi\hbar}{|E'(\upsilon_e)|} \quad \text{and} \quad T_{\mathrm{rev}} = \frac{2\pi\hbar}{|E''(\upsilon_e)|/2}, \tag{6.8}$$

Eq. (6.7) simplifies to

$$\phi_\upsilon(R,t) = \phi_\upsilon(R) \exp\left\{-i\left[\frac{E(\upsilon_e)}{\hbar} + 2\pi(\upsilon-\upsilon_e)/T_{\mathrm{cl}} + 2\pi(\upsilon-\upsilon_e)^2/T_{\mathrm{rev}} + \cdots\right] t\right\}. \tag{6.9}$$

The first term is a υ-independent overall phase, accumulating equally for all times in all states in the wave packet, therefore not changing the phase relation between them and thus having no effect, when building the population density $|\Psi(R,t)|^2$.

Knowing that υ and υ_e are integer numbers, summands in the second or third term will deliver the same phase when they become multiples of 2π. The characteristic time scale of the second term is known as the classical period of motion in the bound electronic state and can be independently derived from correspondence principle arguments [262]. This component is relevant for the short-term wave-packet evolution and for the discussion of fractional revivals. The third expansion term is associated to the revival time scale, dependent on the quadratic term $(\upsilon-\upsilon_e)^2$. It is responsible for the spreading of the wave packet on a longer time scale and most notably, becomes very slowly varying around the time T_{rev} or multiples of it, when the classical motion given by the second expansion term becomes relevant. This effect is clearly visible in the time-evolution of the bound D vibrational wave packet, shown in Fig. 6.7(a).

6.1.2.1 Time evolution in a harmonic potential

Approximating a potential energy curve to a harmonic potential yields equidistant energy spacing for all vibrational levels:

$$E(\upsilon) = \left(\upsilon + \frac{1}{2}\right)\hbar\omega_0. \tag{6.10}$$

All higher derivatives of the energy with respect to the vibrational quantum number υ, except for the first derivative, vanish, such that the classical time scale takes the form

$$T_{\mathrm{cl}} = \frac{2\pi\hbar}{|E'(\upsilon_e)|} = \frac{2\pi}{\omega_0}. \tag{6.11}$$

Approximating the D-state potential with a harmonic potential and building a harmonic D-state wave packet including harmonic vibrational states with energy up to the dissociation energy of the real D potential-energy curve, one can find the time-evolution of the wave packet in Fig. 6.4. The wave packet does not disperse, i.e. all states remain in phase for all times, which, in turn, prevents the emergence of a wave packet revival, as indicated at the beginning of the section.

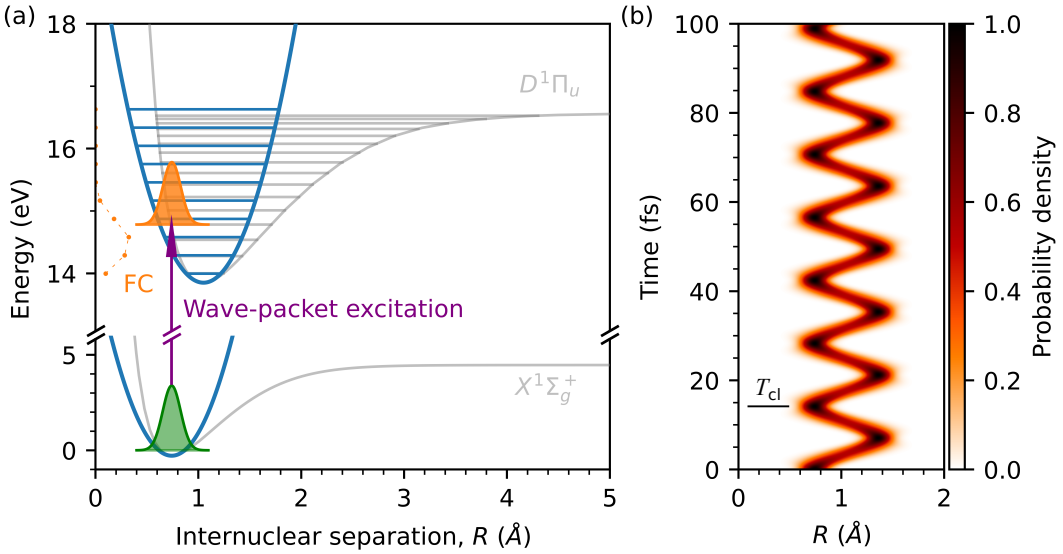

Figure 6.4: Time evolution of a vibrational wave packet excited in a harmonic potential approximating the $D^1\Pi_u 3p\pi$ potential energy curve. **(a)** Harmonic approximation (blue) for the molecular ground state and the excited $D^1\Pi_u 3p\pi$ state. The ground state (green) is mapped to the excited state according to the FC factors for the harmonic eigenstates below the dissociation threshold of the real $D^1\Pi_u 3p\pi$ potential (grey), where the energy position of the included eigenstates is indicated as vertical blue lines. **(b)** Wave-packet time evolution for the first 100 fs after the wave-packet excitation. In the harmonic potential approximation only classical vibration motion with the time constant T_{cl} of the wave packet is observed. In the absence of anharmonicity no dephasing of the wave packet occurs and therefore no subsequent revival.

6.1.2.2 Time evolution in an anharmonic potential

Going beyond the harmonic potential approximation, which is a good approximation for the potential of a diatomic molecule in the vicinity of the equilibrium internuclear distance $R = R_e$, a more realistic description of a potential-energy curve should consider its anharmonicity. Here, the empirically found analytic Morse potential is a good approximation for bound potential-energy curves [263]:

$$V_{\text{Morse}}(R) = D_e\left[\mathrm{e}^{-2a(R-R_e)} - 2\mathrm{e}^{-a(R-R_e)}\right], \tag{6.12}$$

where apart from the equilibrium internuclear separation R_e, the two additional parameters D_e, being the depth of the potential, and a, a parameter to control the width of the potential, offer flexibility for more accurate description of the molecular potential. Hereby, D_e is connected to the dissociation energy D_0 by

$$D_0 = D_e - \frac{\hbar\omega_0}{2}, \tag{6.13}$$

with ω_0 being the vibrational ground state energy of the Morse potential. An alternative form of the Morse potential, which can be applied also for excited bound molecular states is

$$V_{\text{Morse}}^{\text{excited}}(R) = E_0^{\text{excited}} + D_e\left[1 - \mathrm{e}^{-a(R-R_0)}\right]^2, \tag{6.14}$$

which differs from Eq. (6.12) by the shift of the dissociation energy of the potential from zero to $E_0^{\text{excited}} + D_e$. The exact energy eigenvalues of the Morse potential [258, 263] are given by

$$E_{\text{Morse}}(\upsilon) = \hbar\omega_0\left(\upsilon + \frac{1}{2}\right) - \frac{\hbar^2\omega_0^2}{4D_e}\left(\upsilon + \frac{1}{2}\right)^2, \tag{6.15}$$

and in the case of electronic excited states

$$E_{\text{Morse}}^{\text{excited}}(\upsilon) = E_{\text{Morse}}(\upsilon) + E_0^{\text{excited}}. \tag{6.16}$$

The vibrational levels are then no longer equidistant and their time evolution does not remain in phase for all times as in the harmonic case. The vibrational frequency

$$\omega_0 = a\sqrt{2D_e/\mu}, \tag{6.17}$$

with μ being the reduced mass, corresponds to the frequency of a harmonic oscillator with force constant $k = 2a^2D_e$. The energy expression for the Morse potential inserted in Eq. (6.8) yields for the characteristic vibrational timescales

$$T_{\text{cl}} = \frac{2\pi}{\left|\omega_0\left[1 - 2\frac{\hbar\omega_0}{4D_e}\left(\upsilon + \frac{1}{2}\right)\right]\right|} \quad \text{and} \quad T_{\text{rev}} = \frac{2\pi}{\left|-\frac{\hbar\omega_0^2}{4D_e}\right|}. \tag{6.18}$$

The classical time scale is bigger than the one obtained in the harmonic case due to the anharmonicity of the Morse potential. The revival time in this case is non-vanishing but higher order revivals cannot appear, as higher order derivatives of the energy expression vanish. The fist reconstruction of the initial wave packet occurs at time $t = T_{\text{rev}}/2$ and is termed a half-revival. According to Eq. (6.9) all eigenstates are phase-synchronised, however the phase of the even-numbered states is shifted by a factor of π compared to the odd-numbered states. The initial wave-packet appears to have restored its original shape, however its overall phase is shifted by π.

For an accurate description of the H_2 potentials even higher order anharmonicity has to be taken into account, which would lead to even higher order periodicity of the phase evolution of the states according to Eq. (6.7), see [261] for derivation of e.g. the so-called super-revival T_{super}. A full revival of the wave-packet would therefore be observed on a very long time scale. For this reason, in the following, the half-revival restoring the initially excited wave-packet is referred to as the first wave-packet revival.

6.1.3 Few-level model system for the vibrating H_2 molecule

To understand the vibrational dynamics in the neutral hydrogen molecule under the influence of a strongly interacting field, we consider a multi-level system and solve the time-dependent Schrödinger equation to find its time evolution. The TDSE is solved by expanding the time-dependent wave-function in a basis of field-free eigenstates, yielding a set of coupled differential equations. Owing to find the minimal set of states, allowing to understand the laser-coupled dynamics of the molecular wave packet, the numerical simulation only includes the most dominant spectroscopic signatures observed in the XUV spectra, here the XUV dipole-allowed resonances from the ground state to the electronically excited D state. Thus, the eigenstates included in the model are the following:

- the absolute ground $X^1\Sigma_g^+ 1s\sigma$ state with rovibrational quantum numbers $J = 0$ and $\upsilon = 0$,
- the bound states of the electronically excited $D^1\Pi_u 3p\pi$ state, with $J = 1$ and $\upsilon = 0, ..., 17$ and
- the bound states with $J = 0$ and $\upsilon = 0, ..., 33$ of the electronically excited $EF^1\Sigma_g^+ 2s\sigma + 2p\sigma^2$ potential-energy curve.

The numerical framework used for the few-level model simulation discussed in the following was in part developed together with a bachelor and a master student, who were supervised in the scope of this work: Daniel Fan [264] and Paula Barber Belda [265].

6.1.3.1 Eigenenergies and transition-dipole elements for the states in the few-level model system

The eigenenergy of all included field-free eigenstates as well as the spatial representation of the bound nuclear wave functions are obtained by solving the time-independent radial Schrödinger equation of nuclear motion using a B-spline basis of 600 B-spline functions of order 10 on a linear knot sequence in a radial box with maximal nuclear separation $R_{\text{max}} = 30$ a.u. and fixed-boundary conditions within the Born-Oppenheimer approximation, with the potential-energy curves from literature [67, 266, 267]. The bound nuclear wave-functions for all states are calculated for a radial size $R_{\text{bound}} = 24$ a.u.. Figure 6.5 shows all bound vibrational states of the excited $D^1\Pi_u 3p\pi$ potential-energy curve at their corresponding energy position, whereas Fig. 6.6 depicts the bound vibrational levels of the excited $EF^1\Sigma_g^+$ electronic potential.

The transition matrix elements between two states, an initial i and a final f state, are calculated as the expectation value of the transition operator $\hat{\boldsymbol{T}}$ according to

$$T_{f\leftarrow i} = \langle \Psi_f(\boldsymbol{x}, \boldsymbol{R}) | \hat{\boldsymbol{T}} | \Psi_i(\boldsymbol{x}, \boldsymbol{R}) \rangle . \tag{6.19}$$

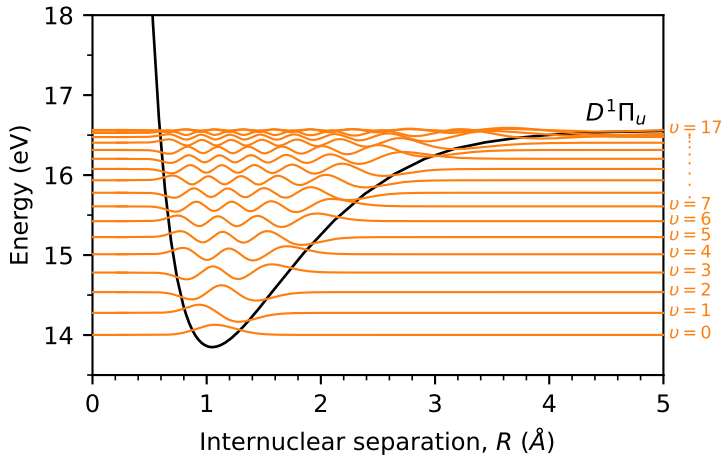

Figure 6.5: All bound vibrational states of the excited $D^1\Pi_u 3p\pi$ potential-energy curve in the neutral H_2 molecule. Every nuclear wave function is shown with an offset corresponding to its eigenenergy.

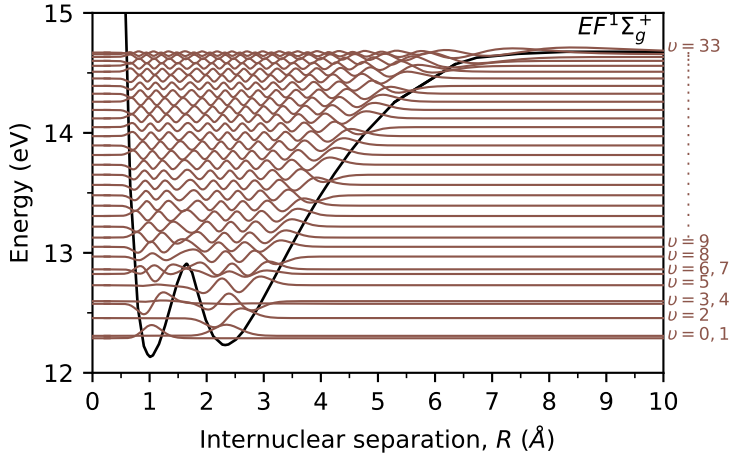

Figure 6.6: All bound vibrational states of the excited $EF^1\Sigma_g^+$ potential-energy curve in the neutral H_2 molecule.

Their squared value is the transition probability between two states:

$$P_{f\leftarrow i} = \left|T_{f\leftarrow i}\right|^2. \tag{6.20}$$

In the dipole approximation, considered throughout this thesis, the general transition operator $\hat{\boldsymbol{T}}$ is approximated by the transition dipole operator $\hat{\boldsymbol{D}}$, such that

$$T_{f\leftarrow i} \approx \langle \Psi_f(\boldsymbol{x},\boldsymbol{R})|\,\hat{\boldsymbol{D}}\,|\Psi_i(\boldsymbol{x},\boldsymbol{R})\rangle \equiv d_{f\leftarrow i}. \tag{6.21}$$

Applying the Born-Oppenheimer approximation to separate the nuclear $\phi(R)$ and electronic $\psi(\boldsymbol{x};R)$ wave function, the transition elements become

$$d_{f\leftarrow i} = \langle\phi_f(R)|\langle\psi_f(\boldsymbol{x};R)|\,\hat{\boldsymbol{D}}\,|\psi_i(\boldsymbol{x};R)\rangle|\phi_i(R)\rangle\,. \tag{6.22}$$

Due to the orthogonality of the electronic wave functions the dipole operator part of the nuclear coordinates does not contribute to the final expectation value, vanishing upon integration, such that the electronic part can be separately computed, leading to the expression

$$d_{f\leftarrow i} = \langle\phi_f(R)|\,D_{fi}(R)\,|\phi_i(R)\rangle\,, \tag{6.23}$$

depending only on the internuclear separation, with the electronic dipole transition moments $D_{fi}(R) = \langle\psi_f(\boldsymbol{x};R)|\,\hat{\boldsymbol{D}}\,|\psi_i(\boldsymbol{x};R)\rangle$.

Knowing the nuclear wave functions from the solution of the radial Schrödinger equation and the electronic dipole transition moments from literature [268, 269] the transition dipole moments between all the BO field-free eigenstates contained within the model were calculated according to Eq. (6.23) and compared for consistency to the values reported in literature [270–273].

6.1.3.2 Solution of the time-dependent Schrödinger equation

The dipole transition moments, together with the energies of the states, are used to construct the Hamiltonian of the model system, interacting with both XUV and NIR light. The laser interaction is considered in the length gauge of the dipole approximation and only dipole-allowed couplings between the states are included, which leads do the Hamiltonian, being the sum of the free and the interaction Hamiltonian:

$$\mathcal{H} = \mathcal{H}_0 + \mathcal{H}_{\text{int}} = \mathcal{H}_0 + \mathcal{H}_{\text{int,XUV}} + \mathcal{H}_{\text{int,NIR}} = \mathcal{H}_0 + \mathcal{H}_{\text{int,XUV}} + \mathcal{H}_{\text{int,NIR}}, \tag{6.24}$$

with the two interaction contributions - due to the XUV and due to the NIR, denoted as $\mathcal{H}_{\text{int,XUV}}$ and $\mathcal{H}_{\text{int,NIR}}$, respectively.

Building a basis set $\mathcal{S}$ out of the free states included in the model, listed out at the beginning of this section, i.e.

$$\mathcal{S} = \left\{|\phi_0^X\rangle\right\} \cup \left\{|\phi_\upsilon^D\rangle\,|\phi_\upsilon^D \text{ bound}\right\}_{\upsilon=0}^{N_D-1} \cup \left\{|\phi_\upsilon^{EF}\rangle\,|\phi_\upsilon^{EF} \text{ bound}\right\}_{\upsilon=0}^{N_{EF}-1} \equiv \{|s\rangle\}_{s=0}^{N_D+N_{EF}}\,,$$

the explicit $(1+N_D+N_{EF})\times(1+N_D+N_{EF})$-dimensional matrix form of the Hamiltonian becomes

$$\mathcal{H}(t) = \begin{pmatrix} E_X & d_{X\leftrightarrow D_0}\mathcal{E}(t) & d_{X\leftrightarrow D_1}\mathcal{E}(t) & \cdots & 0 & 0 & \cdots & 0 \\ d_{X\leftrightarrow D_0}\mathcal{E}(t) & E_{D_0} & 0 & \cdots & d_{D_0\leftrightarrow EF_0}\mathcal{E}(t) & d_{D_0\leftrightarrow EF_1}\mathcal{E}(t) & \cdots & d_{D_0\leftrightarrow EF_{33}}\mathcal{E}(t) \\ d_{X\leftrightarrow D_1}\mathcal{E}(t) & 0 & E_{D_1} & \cdots & d_{D_1\leftrightarrow EF_0}\mathcal{E}(t) & d_{D_1\leftrightarrow EF_1}\mathcal{E}(t) & \cdots & d_{D_1\leftrightarrow EF_{33}}\mathcal{E}(t) \\ \vdots & \vdots & \vdots & \ddots & \vdots & \vdots & \vdots & \vdots \\ 0 & d_{D_0\leftrightarrow EF_0}\mathcal{E}(t) & d_{D_1\leftrightarrow EF_0}\mathcal{E}(t) & \cdots & E_{EF_0} & 0 & \cdots & 0 \\ 0 & d_{D_0\leftrightarrow EF_1}\mathcal{E}(t) & d_{D_1\leftrightarrow EF_1}\mathcal{E}(t) & \cdots & 0 & E_{EF_1} & 0 & 0 \\ \vdots & \vdots & \vdots & \vdots & \vdots & \vdots & \ddots & \vdots \\ 0 & d_{D_0\leftrightarrow EF_{33}}\mathcal{E}(t) & d_{D_1\leftrightarrow EF_{33}}\mathcal{E}(t) & \cdots & 0 & 0 & 0 & E_{EF_{33}} \end{pmatrix}, \tag{6.25}$$

where the subindex of the states refers to the vibrational quantum number υ.

To account for the finite life time of the excited states an exponential decay of the population of the states is introduced through an imaginary term added to the eigenenergies of the states. For a lifetime of $1/\Gamma$, the corresponding transformation including the decay rate is

$$E \leftarrow E - i\frac{\Gamma}{2}, \tag{6.26}$$

with $\Gamma = 1 \times 10^{-4}$ a.u. for all excited states, comparable to the values reported in literature [73]. The ground state $X_{\upsilon=0}$ has no decay rate.

For the numerical solution of the time-dependent Schrödinger equation

$$i\frac{\partial}{\partial t}|\Psi(t)\rangle = \mathcal{H}(t)|\Psi(t)\rangle \tag{6.27}$$

the state vector of the model system $|\Psi(t)\rangle$ is represented in the $\mathcal{S}$ basis of the Hamiltonian as

$$|\Psi(t)\rangle = \sum_{s=0}^{N_D+N_{EF}} c_s(t)\,|s\rangle, \tag{6.28}$$

with the expansion coefficients $c_s(t)$, which squared value is the probability of the system to populate the state $|s\rangle$. Inserting the state vector representation in the TDSE and using the orthogonality of the eigenvectors, the remaining coupled differential equations for the expansion coefficients vector

$$\boldsymbol{c}(t) = \begin{pmatrix} c_0(t) \\ c_1(t) \\ \vdots \\ c_{N_D+N_{EF}}(t) \end{pmatrix} \tag{6.29}$$

remains to be solved.

The formal solution of the TDSE is the exponential time-evolution

$$\boldsymbol{c}(t) = e^{-i\mathcal{H}(t)\cdot t}\,\boldsymbol{c}(t=0), \tag{6.30}$$

with the initial coefficient vector $\boldsymbol{c}(0)$, in which only the ground state is populated, i.e.

$$\boldsymbol{c}(t=0) = \begin{pmatrix} 1 \\ 0 \\ \vdots \\ 0 \end{pmatrix}. \tag{6.31}$$

Since the Hamiltonian of the system, however, is not a diagonal matrix, the differential equation can be solved either by diagonalisation of the Hamiltonian at every time step, or through a split-step algorithm [176]. The latter choice was adopted, since it requires only two matrix diagonalisations, which makes it computationally faster than the full diagonalisation of the Hamiltonian at every time step.

The second-order split-step algorithm for the numerical TDSE solution implemented in the described model simulation relies on the separation of the Hamiltonian in two parts, the field-free part $\mathcal{H}_0$ and the interaction part $\mathcal{H}_{\text{int}}$, which are propagated independently of each other according to

$$|\Psi(t_n)\rangle = e^{-i\mathcal{H}_0 \cdot \frac{\Delta t}{2}} \, e^{-i\mathcal{H}_{\text{int}}(t_n)\cdot \Delta t} \, e^{-i\mathcal{H}_0 \cdot \frac{\Delta t}{2}} \, |\Psi(t_{n-1})\rangle \,. \tag{6.32}$$

The field-free Hamiltonian $\mathcal{H}_0$ is a diagonal matrix, which can be directly applied in the time-evolution. To compute the interaction part, however, a further separation in the interaction part by the XUV and the one by the NIR is introduced, accurate up to first order:

$$e^{-i\mathcal{H}_{\text{int}}(t)\cdot t} = e^{-i\left(\mathcal{H}_{\text{int,XUV}}(t)+\mathcal{H}_{\text{int,NIR}}(t)\right)\cdot t} \approx e^{-i\mathcal{H}_{\text{int,XUV}}(t)\cdot t} \, e^{-i\mathcal{H}_{\text{int,NIR}}(t)\cdot t}. \tag{6.33}$$

This separation is justified given very low XUV intensity, which is well in the perturbative regime, as well as with the moderate NIR intensities up to $10^{13}\,\text{W/cm}^2$. It further enables the independent propagation of both parts of the interaction Hamiltonian, requiring just a single diagonalisation at the beginning of the calculation. The time-dependent electric field can be factored out of each of the matrices $\mathcal{H}_{\text{int,XUV}}$ and $\mathcal{H}_{\text{int,NIR}}$, such that their unitary eigenvectors remain constant in time and the eigenvalues depend on the electric field through the multiplicative factor of the electric field strength. The basis change is then applied

$$\mathcal{H}^D_{\text{int,XUV}}(t) = T^{-1}_{\text{XUV}} \mathcal{H}_{\text{int,XUV}}(t) T_{\text{XUV}}, \tag{6.34}$$

$$\mathcal{H}^D_{\text{int,NIR}}(t) = T^{-1}_{\text{NIR}} \mathcal{H}_{\text{int,NIR}}(t) T_{\text{NIR}}, \tag{6.35}$$

where the matrices T_{XUV} and T_{NIR} are time independent and the superscript D denotes the diagonal matrix form.

Applying all necessary transformations, the complete time evolution for one step in time Δt takes the form

$$|\Psi(t_n)\rangle = e^{-i\mathcal{H}_0\cdot\frac{\Delta t}{2}}\, T_{\mathrm{NIR}}\, e^{-i\mathcal{H}^D_{\mathrm{int,NIR}}(t_n)\cdot\Delta t}\, T^{-1}_{\mathrm{NIR}}\, T_{\mathrm{XUV}}\, e^{-i\mathcal{H}^D_{\mathrm{int,XUV}}(t_n)\cdot\Delta t}\, T^{-1}_{\mathrm{XUV}}\, e^{-i\mathcal{H}_0\cdot\frac{\Delta t}{2}}\, |\Psi(t_{n-1})\rangle\,. \tag{6.36}$$

6.1.3.3 Numerical pulse parameters

Through the interaction term of the Hamiltonian in the dipole approximation

$$\mathcal{H}_{\mathrm{int}} = \boldsymbol{d}\,\mathcal{E}(t) \tag{6.37}$$

the laser field strength directly influences the system's dynamical evolution with time. Numerically, both the XUV and NIR laser fields are approximated by an oscillating cosine wave under a Gaussian envelope

$$\mathcal{E}(t) = \mathcal{E}_0 \cos(\omega t + \phi)\, \mathrm{e}^{\left(\frac{t-t_0}{\tau_{\mathrm{G}}}\right)^2}. \tag{6.38}$$

Here, $\mathcal{E}_0$ is the maximum of the electric field strength, ω is the central frequency, ϕ is the carrier-envelope phase and τ_{G} is the envelope duration of the pulse, which is connected to the laser pulse duration τ_{P}, defined as the full width at half maximum (FWHM) of $|\mathcal{E}(t)|^2$. For a Gaussian envelope the pulse duration is calculated according to $\tau_{\mathrm{P}} = \sqrt{2\log 2}\tau_{\mathrm{G}}$.

The parameters for the considered XUV and the NIR pulse are the following: central photon energy $\hbar\omega_{\mathrm{NIR}} = 1.6\,\mathrm{eV}$ and pulse duration $\tau_{\mathrm{NIR}} = 5\,\mathrm{fs}$ for the NIR pulse, and $\hbar\omega_{\mathrm{XUV}} = 14\,\mathrm{eV}$ and pulse duration $\tau_{\mathrm{XUV}} = 0.5\,\mathrm{fs}$ for the XUV pulse, respectively. For both pulses the carrier envelope phase was kept constant at $\phi = 0$. The maximal laser field strength of the XUV pulse was set to $\mathcal{E}_{0,\mathrm{XUV}} = 5\times10^{-5}$ a.u., remaining well in the perturbative regime, such that the ground-state depopulation does not exceed 10^{-6}. The NIR field strength $\mathcal{E}_{0,\mathrm{NIR}}$, on the other hand, was scanned in the range between 0 a.u. and 0.02 a.u.. Choosing the XUV-pulse maximum to arrive at $t_{0,\mathrm{XUV}} = 0\,\mathrm{fs}$, then an adjustable time-delay between the pulses can be set through the NIR-pulse maximum $t_{0,\mathrm{NIR}} = \tau$, which unless stated otherwise was chosen to be at $\tau = 7\,\mathrm{fs}$.

6.2 XUV absorption spectroscopy for wave-packet imaging

As discussed in the introduction of this chapter, the initiated wave-packet dynamics in the H_2 molecule is probed by the molecule itself, more specifically by the molecular ground state remaining localised in the molecule after the wave-packet excitation. This way, the excited wave packet is free to evolve on its excited

potential-energy curve/surface and whenever it overlaps again with the ground state the probability for dipole transition rises. The time-dependent dipole interferes with the XUV spectrum, thus being directly translated to a spectroscopic signal. Coming from the other side, i.e. knowing first the absorption spectrum, in this case the XUV absorption spectrum, one can reconstruct the time-dependent dipole and with this access the wave-packet evolution. This section gives more details on the method of reconstruction of the time-dependent dipole response, applied specifically to the case of molecular dynamics.

6.2.1 Reconstruction of the time-dependent dipole response

If a quantum system interacts with a weakly perturbing field $\mathcal{E}(t)$, introducing a transition in the system, i.e. charge redistribution, an oscillating dipole moment $d(t)$ arises as the system's response. During the lifetime of the dipole it can be modified by another interaction $V(t)$, which can be, for example, a strong near-infrared laser pulse with maximal intensity I_{NIR}. According to the connection between absorption signal and dipole moment, Eq. (2.38), the modified dipole moment $d(t, V(\tau))$ is encoded in the measured absorption signal at a particular time delay τ between the exciting and the perturbing pulse

$$A(\omega, V(\tau)) \propto \Im\mathrm{m}\left[\frac{\mathfrak{F}[d(t, V(\tau))]}{\mathfrak{F}[\mathcal{E}(t)]}\right]. \tag{6.39}$$

For an initial excitation $\mathcal{E}(t)$ much shorter than the life time of the system the impulsive limit applies to the problem and the excitation pulse can be treated as a Dirac delta function $\mathcal{E}(t) = \mathcal{E}\delta(t)$. In this limit, due to causality, implying that the time-dependent dipole arises only after the initial excitation, the dipole response can be reconstructed from a single absorption spectrum [256]:

$$d(t, V(t)) \propto \mathfrak{F}^{-1}\{iA[\omega; V(\tau)]\}(t) = \frac{1}{2\pi}\int_{-\infty}^{\infty} iA[\omega; V(\tau)]\,\mathrm{e}^{-i\omega t}d\omega \qquad \text{for} \quad t > 0, \tag{6.40}$$

with $d(t, V(t))$ being a complex quantity having an amplitude and a phase component.

The impulsive limit is for example met for an XUV excitation pulse with a duration up to a femtosecond, or considerably shorter than the natural time scale, on which the excited system evolves. Moreover, the above expression holds even for a strongly driven system beyond the perturbation limit, as in the case of an interaction with a strong NIR field with high intensity I_{NIR}. Emphasising the strong-interaction response imprinted in the time-dependent dipole, the expression in Eq. (6.40) takes

the form:

$$d(t, I_{\mathrm{NIR}}) \propto \mathfrak{F}^{-1}\left\{iA\left[\omega; I_{\mathrm{NIR}}(\tau)\right]\right\}(t) = \frac{1}{2\pi}\int_{-\infty}^{\infty} iA\left[\omega; I_{\mathrm{NIR}}(\tau)\right] \mathrm{e}^{-i\omega t} d\omega \qquad \text{for} \quad t > 0. \tag{6.41}$$

In Eq. (6.40), $A\left[\omega, V(\tau)\right]$ is the full absorption spectrum measured for interaction V at time τ, and similarly for $A\left[\omega; I_{\mathrm{NIR}}(\tau)\right]$ in Eq. (6.41). Because of the linearity of the time-dependent dipole response of different states, one could restrict the absorption spectrum used for the reconstruction only to resonances corresponding to a particular excitation. Formally, this restriction is introduced through a window function $w(\omega)$, which is non-zero only in the region including the spectral features of interest, such that the corresponding reconstructed dipole $d_w(t, I_{\mathrm{NIR}})$ shows dynamics of the part of the system accessible through the spectral selection, i.e.

$$d_w(t, I_{\mathrm{NIR}}) \propto \mathfrak{F}^{-1}\left\{i\, w(\omega) A\left[\omega; I_{\mathrm{NIR}}(\tau)\right]\right\}(t). \tag{6.42}$$

The reconstruction window used in the data analysis presented in this chapter is a band-pass filter with $\cos^2$-shaped rising and falling edge over an energy region of 0.1 eV and is otherwise constant 1 between the two edges and vanishes outside them. The reconstruction window is applied multiplicatively to the measured absorption data according to Eq. (6.42).

6.2.2 The time-dependent dipole in a molecular system

The above expression in Eq. (6.40) is valid for any quantum system. In the atomic system of helium it has been shown that the reconstructed dipole from a single absorption line shape accurately reproduces the amplitude and phase time evolution induced by a strong laser field, indicating for example Rabi oscillations due to resonant couplings [256]. The method has further proven its applicability also to non-resonant absorption in the continuum delivering information on recollision dynamics upon interaction with both linear and circularly polarised laser field [4]. The reconstructed dipole from the whole resonant series of doubly excited states in helium also shows the applicability of the method to access the strong-field induced fall time of an atomic wave packet consisting of coherently excited Rydberg states [11].

This section discusses what information about a molecular wave packet is encoded in the corresponding time-dependent dipole. For this, let's consider the general time-dependent dipole expression:

$$d(t) = \langle \Psi(t) | \hat{\boldsymbol{D}} | \Psi(t) \rangle, \tag{6.43}$$

where Ψ is the total wave function of the molecule including both electronic and nuclear contribution and $\hat{\boldsymbol{D}}$ is the dipole operator. For the sake of simplicity, let Ψ include the molecular ground state X and one excited electronic state $\psi_R^E(\mathbf{x}, t)$ with

its bound vibrational wave packet $\Phi^E(R,t)$, such that

$$\Psi(\mathbf{x},R,t) = c_0^X(t)\phi_0^X(R)\psi_R^X(\mathbf{x},t) + \Phi^E(R,t)\psi_R^E(\mathbf{x},t) \tag{6.44}$$

with

$$\Phi^E(R,t) = \sum_\upsilon c_\upsilon^E(t)\,\phi_\upsilon^E(R) \quad \text{for} \quad \upsilon \in \left\{\upsilon|\phi_\upsilon^E(R)\,\text{bound}\right\}. \tag{6.45}$$

Here, the Born-Oppenheimer approximation has been adopted, allowing for the separation of the nuclear and electronic degrees of freedom. Note that the rotational part of the nuclear wave function has not been considered, since the time scale of rotation is on the order of picoseconds, which is much longer than the femtosecond time scale considered in the following.

Without loss of generality, the time-evolution coefficients in the wave packet do not necessarily have to exhibit the trivial time evolution according to their eigenenergy $c_\upsilon(t) = c_\upsilon^0\,\mathrm{e}^{-i\omega_\upsilon t}$ but can also be modified in phase and amplitude by an interaction with an intense laser field. The following discussion therefore applies for both the static case as well as for a laser-driven molecular wave packet. While the static case has already been discussed by Heller *et al.* in the linear regime, extracting temporal information from incoherently measured spectroscopic data [274, 275], the applied generalisation, allowing for non-trivial interaction, aims at extending the time-domain interpretation of absorption spectroscopy through the technique of reconstruction of the time-dependent dipole beyond the linear regime.

If only transitions between the ground and the excited state, but no transitions between the states in the bound vibrational wave packet in the excited state are allowed, then the time-dependent dipole takes the form:

$$d(t) = \sum_\upsilon c_0^{X*}(t)c_\upsilon^E(t)\,\langle\phi_0^X(R)\psi_R^X(\mathbf{x},t)|\hat{\boldsymbol{D}}|\phi_\upsilon^E(R)\psi_R^E(\mathbf{x},t)\rangle + \text{c.c.}, \tag{6.46}$$

with the notation $c^*(t)$ for the complex conjugate of the evolution coefficients.

Every summand in the dipole expression is weighted with the transition dipole amplitude between the ground state and the corresponding excited state as well as with the time-dependent evolution coefficient. Since the nuclear component $Z\boldsymbol{R}e$ of the dipole transition operator does not contribute to the transition dipole matrix element due to the orthogonality of the electronic wave functions, the time-dependent dipole further simplifies to

$$d(t) = \sum_\upsilon c_0^{X*}(t)c_\upsilon^E(t)\,\langle\phi_0^X(R)|D_{XE}(R,t)|\phi_\upsilon^E(R)\rangle + \text{c.c.}. \tag{6.47}$$

The electronic transition dipole between the ground and the excited state $D_{XE}(R,t)$ depends on the nuclear coordinate R and for the discussed time-dependent electronic wave function also on time. Averaging $D_{XE}(R,t)$ over R and using the mean value $\overline{D_{XE}}$ in the Franck-Condon approximation, i.e. assuming no dependence on R, the transition dipole becomes proportional to the overlap between the ground state and

the vibrational wave packet:

$$d(t) = \overline{D_{XE}} \left\langle c_0^X(t)\phi_0^X(R) \middle| \sum_\upsilon c_\upsilon^E(t)\phi_\upsilon^E(R) \right\rangle + \text{c.c.}. \tag{6.48}$$

Equation (6.48) directly shows the connection between the time-dependent dipole and the ground state probing the excited vibrational wave packet in the Franck-Condon approximation. This connection also holds outside of the Franck-Condon approximation, when taking into account the R-dependence of the electronic transition dipole. Thus, the dipole amplitude rises whenever the overlap between the ground state and the excited wave packet becomes significant and when they are out of overlap, the dipole amplitude vanishes.
The connection between the wave-packet time evolution and the time-dependent dipole is illustrated in Fig. 6.7, showing the calculated field-free time evolution of the D vibrational wave packet in the hydrogen molecule in the upper panel (a) and the corresponding time-dependent dipole in the lower panel (b). The computed time-dependent Franck-Condon overlap integral

$$FC = \int_0^\infty \phi_0^{X*}(R,t)\,\Phi^E(R,t)\,dR \tag{6.49}$$

(dotted line in Fig. 6.7 (b)), normalized to time zero, and the time-dependent dipole, also normalized to time zero, match almost perfectly for all times, as predicted by Eq. (6.48) derived in the Franck-Condon approximation. The peaks of the dipole amplitude coincide with times when the vibrational wave packet localises inside the region it was created, i.e. the Franck-Condon region. Further confirmation for the localisation of the excited wave packet in the Franck-Condon region at times, when the dipole amplitude rises, is the computed integral of the probability density of the excited state wave packet inside the FC region

$$P_{\text{FC}} = \int_{R_1}^{R_2} \Phi^{E*}(R,t)\,\Phi^E(R,t)\,dR, \tag{6.50}$$

with $R_1 = 0.638\,\text{Å}$ and $R_2 = 0.889\,\text{Å}$. Thus, through the time-dependent dipole the molecular ground state acts as an intrinsic probe of the vibrational wave packet and its time evolution for all times after the wave-packet excitation. In the case of an interaction with an additional field after the wave-packet creation, the time-dependent evolution coefficients of the wave-packet states would be altered and through them the interaction will also be imprinted in the time-dependent dipole, as discussed later in section 6.4.2.

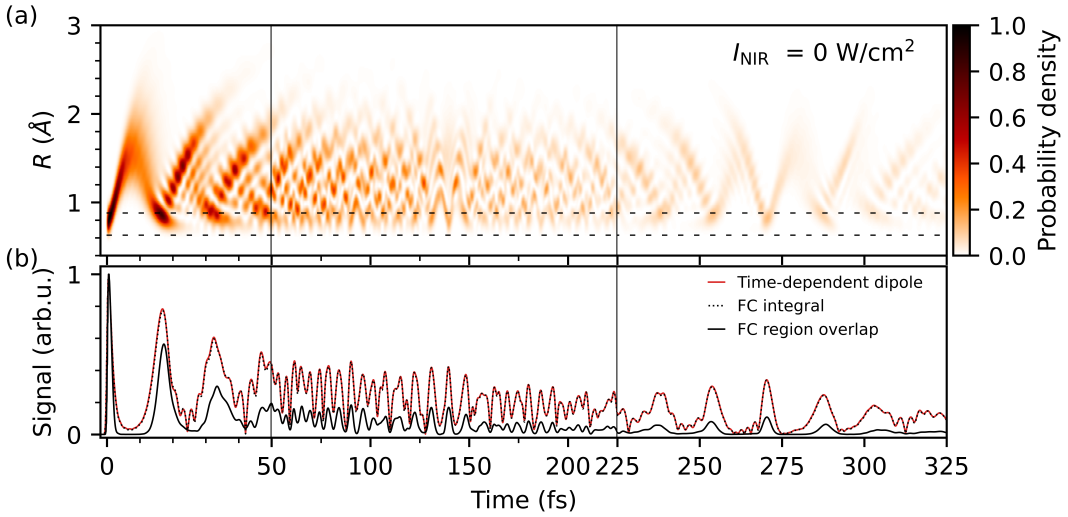

Figure 6.7: Connection between vibrational wave-packet time evolution and the time-dependent dipole amplitude. **(a)** Calculated time evolution of the vibrational wave packet in the electronically excited D state of H_2 for XUV-only interaction with the system at time zero, exciting the vibrational wave packet. **(b)** Time-dependent dipole amplitude, Franck-Condon overlap integral and integral inside the FC region.

6.3 Experimental methods

The all-optical approach to image and control a molecular wave packet, introduced in this chapter, could be implemented in any spectroscopy setup with the possibility to utilise two laser pulses:

1) a pulse in the spectral range of the resonances of the transition between all wave-packet states and the chosen self-probing state, which should be the mostly occupied one. The excitation pulse should also be shorter than the time-scale, on which the wave packet evolves, and

2) a pulse acting as a control pulse for the excited state, but not disturbing the self-probing state.

Note that if the control pulse is left out, wave-packet visualisation is possible with just one pulse as listed above under 1) in a combination with the dipole reconstruction technique, delivering the time-evolution of the emission dipole.

In the presented proof-of-principle case, the self-probing state is the molecular ground state $X^1\Sigma_g^+ 1s\sigma, \upsilon = 0$ of the hydrogen molecule and the nuclear wave packet of interest is in the singly excited electronic state of the $D^1\Pi_u 3p\pi$ potential-energy curve. In fact, not only the $D^1\Pi_u 3p\pi$ state is populated but also nuclear wave packets are excited in other states, as for example the $B^1\Sigma_u^+ 2p\sigma$, the $C^1\Pi_g 2p\pi$ or the $B'^1\Sigma_u^+ 3p\sigma$ electronic state. Because of the linearity of the superposition of states of

the whole molecular system after the excitation, all excited wave packets can be separated and treated independently, provided the relevant states are spectrally isolated and resolved. The relevant transitions from the ground state to the above mentioned electronically excited states are in the XUV spectral range, which then makes XUV spectroscopy or, with the possibility to control the wave packet of interest, XUV time-domain absorption spectroscopy the preferred spectroscopy technique. The experimental setup for time-domain XUV absorption spectroscopy used to obtain the results discussed in this chapter is described in detail in [3, 75, 86, 87], and a short summary of the laser source and the experimental beamline components, with focus on the characteristics relevant for the discussed experiment, are presented in sections 3.1.2 and 4.2, respectively. The following section gives a brief summary of the experimental conditions during the measurement delivering the results demonstrating laser control over a molecular wave packet from Sec. 6.4.2.

6.3.1 Experimental scheme for wave-packet imaging through XUV absorption spectroscopy

As discussed above, for the experimental scheme for wave-packet imaging through XUV absorption spectroscopy, a coherent short XUV pulse is needed to set off the wave-packet dynamics. In the experiment, the XUV pulse with less than a femtosecond duration is generated in the process of high-harmonic generation, driven by a few-cycle pulse, with duration $\approx 5\,\mathrm{fs}$ full width at half maximum and a central wavelength of 750 nm focussed into xenon gas. The generated XUV radiation, together with the NIR pulse, delayed such that it arrives at a fixed time delay of 7 fs after the XUV pulse, are jointly refocussed in the target cell filled with H_2 gas at a pressure of 10 mbar over 3 mm interaction length. Besides the time delay, an additional control parameter for the NIR pulse is its intensity, which is scanned in the range between $10^{11}\,\mathrm{W/cm^2}$ and $10^{13}\,\mathrm{W/cm^2}$. The recorded XUV absorption signal after the target interaction shows a multitude of resonances, with highest amplitude of those associated to transitions between the $X^1\Sigma_g^+ 1s\sigma, \upsilon = 0$ state and the vibronic resonances of the $C^1\Pi_g 2p\pi$ and $D^1\Pi_u 3p\pi$ electronic state, called the C and D band in the following. Figure 6.8 shows a typical absorption spectrum together with a sketch of the experimental scheme, with emphasize on the pulse configuration, including an XUV pulse, interacting first with the H_2 molecules for wave-packet excitation and an NIR pulse with adjustable NIR intensity, which arrives at a later time to change the wave-packet evolution.

6.3.2 Data collection and data evaluation

Two key features of the experimental setup for XUV time-delay absorption spectroscopy presented in section 4.2 stand out immediately, namely:

1) the exceptional temporal resolution of a few tenths of attoseconds, recently reported to reach down to 26.9 as [3], which is due to the shared propaga-

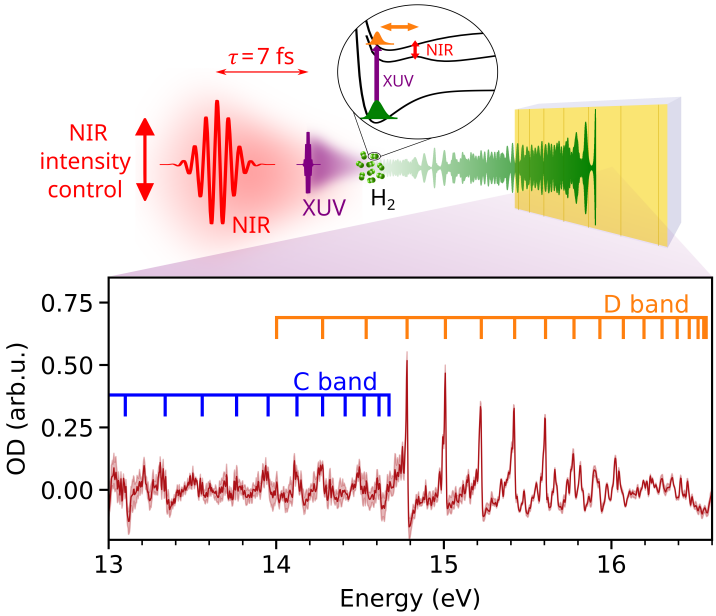

Figure 6.8: Experimental scheme for wave-packet imaging through XUV absorption spectroscopy, showing schematically the pulse configuration for XUV wave-packet excitation and subsequent wave-packet control via an NIR pulse with adjustable intensity. The direct experimental observable is an absorption spectrum in the XUV. The strongest resonances are indicated by the orange and blue vertical lines, for the resonances of the *D* and *C* band, respectively.

tion pathway of the HHG-generated XUV pulse and the HHG-driving NIR pulse reused in the target interaction region, both temporally separated after reflection off the split-mirror assembly;

2) the reproducible intensity control of the NIR field intensity with a closed-loop motorized iris aperture.

Both features take advantage of the higher divergence of the NIR laser beam of $\sim 15\,\mathrm{mrad}$ compared to the lower divergence of the XUV radiation of $\sim 1\,\mathrm{mrad}$ for the implemented focussing geometry.

Time-delay experiments with comparably good stability, reported as 25 as, have contributed to studies of wave-packet dynamics in the hydrogen molecule [250], where the time evolution of the vibrational wave packet within the excited $B'\,^1\Sigma_u^+ 3p\sigma$ electronic state of H_2 has been reconstructed through the laser-perturbed transient absorption spectrum. This reconstruction, however, has been restricted to a very short time region of $\sim 10\,\mathrm{fs}$ and relies on NIR interaction for the holographic coupling of the wave packets in the $B^1\Sigma_u^+$ and $B'\,^1\Sigma_u^+$ electronic state through an intermediate state. The applicability of the presented holographic scheme, however, is restricted to the perturbative regime of interaction, allowing to controllably

map wave packets evolving in one electronic state to another. Aiming not only at wave-packet imaging/reconstruction but most importantly at wave-packet control, the presented experiment in the following largely exploits the possibility for precise intensity control of the interacting NIR pulse, section 6.4.2, including the case of no NIR pulse interaction, presented in section 6.4.1, to reveal information on vibrational wave-packet dynamics and the possibility to change it through laser interaction.

6.3.2.1 From transmission to absorption data

The measurement signal in absorption spectroscopy is a spectrally resolved signal $I_{\mathrm{Sig}}(\omega)$ transmitted through the target sample of interest. Hereby, non-resonant absorption results in attenuation of the incoming reference spectrum $I_{\mathrm{Ref}}(\omega)$ over a broad region, whereas resonant absorption signatures change the incoming light only at the respective resonance position.

In the experiment discussed in the following, sets of XUV spectra were recorded as a function of both time delay and NIR-pulse intensity. Time delays between $-39\,\mathrm{fs}$ and $17\,\mathrm{fs}$ in steps of $\approx 170\,\mathrm{as}$ were set, with negative values corresponding to arrival of the NIR pulse before the XUV pulse. For the NIR intensity control 10 iris opening settings were used, however, only the 6 with the lower NIR intensity, as calibrated in section 6.3.2.4, were used in the data analysis due to the possible onset of nonlinear NIR-only interaction for intensities higher than a few $10^{13}\,\mathrm{W/cm^2}$ and increasing importance of the pre- and post-pulses around the main NIR pulse. Due to the low-transmission of the used indium filters each measured spectrum is an average over ≈ 3700 laser shots, while binning over a region of 144 pixels ($\approx 2.88\,\mathrm{mm}$) along the XUV spatial beam profile in the far field imaged on the vertical axis of the CCD camera chip, i.e. along the non-dispersive direction of the spectrometer. Reference XUV spectra without H_2 target gas were recorded directly after the signal data measurement.

In XUV absorption spectroscopy the usual data analysis procedure includes the calculation of an absorbance signal out of the measured signal and reference spectra according to

$$A = -\log_{10}\left(\frac{I_{\mathrm{Sig}}(\omega)}{I_{\mathrm{Ref}}(\omega)}\right). \tag{6.51}$$

Hereby, different options for the reference can be chosen. If the reference spectrum is the XUV light transmitted through the interaction region without any target gas, then through Lambert-Beer's law, Eq. (2.28), the obtained absorbance, now called optical density, is directly proportional to the photo-absorption cross section $\sigma(\omega)$:

$$OD(\omega) = -\log_{10}\left(\frac{I_{\mathrm{Sig}}(\omega)}{I_{\mathrm{Ref}}(\omega)}\right) = \frac{\rho\, l\, \sigma(\omega)}{\ln 10}, \tag{6.52}$$

with the optical-path-length-density product $\rho\, l$ as a measure for the optical thickness of the target medium. Ideally, a reference spectrum of incoming light obtained

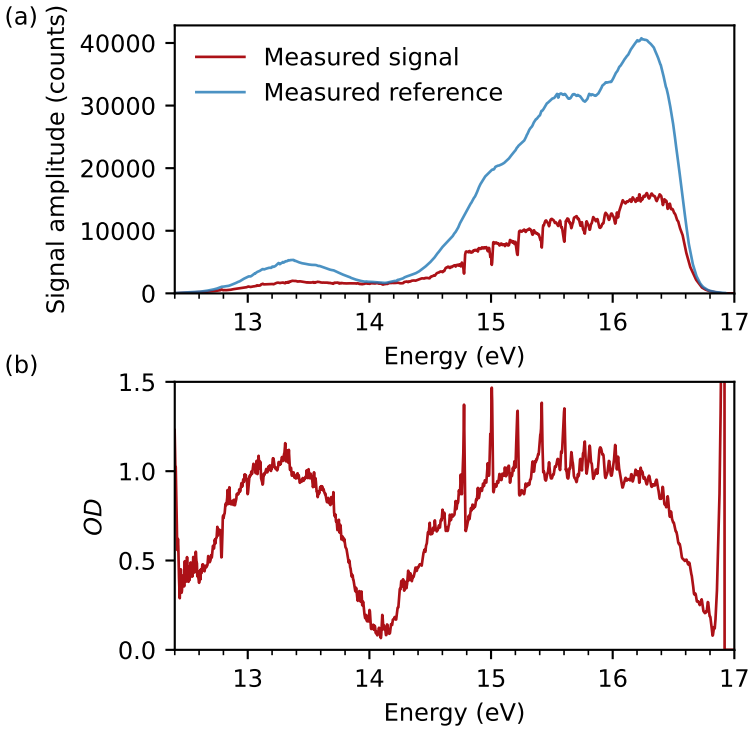

Figure 6.9: Optical density calculation through referencing with mean of measured XUV-only spectra. **(a)** Measured signal (red) and XUV reference (blue) after background correction. **(b)** Optical density $OD(\omega)$ obtained according to Eq. (6.52).

simultaneously with the signal should be recorded, such that no effects of shot-to-shot light fluctuations enter the absorption signal. A technique enabling this was introduced in our group through the implementation of an *in situ* reference spectrometer, which uses a copper-mesh microgrid for transmission electron microscopy (TEM) [276, 277] to disperse the incoming XUV light. The 0th dispersion order is then used as the signal, whereas the +1st dispersion order does not pass through the target and is used as the reference spectrum, as described in detail in [3]. This dispersion technique unfortunately attenuates the XUV flux by an order of magnitude and thus requires very long integration times of full-chip CCD images, which proved unviable for the measurements in the region of singly excited vibronic resonances in H_2. In a first attempt to obtain the optical density therefore the averaged reference spectrum recorded after the signal data acquisition was used as $I_{\mathrm{Ref}}(\omega)$. The resulting $OD(\omega)$ is shown in Fig. 6.9. The broad spectral signatures on top of the resonant absorption lines originate from residual harmonic modulation, as the intensity of the recorded spectra fluctuates with time.

An alternative established technique to obtain reference spectra for the calculation of the absorbance is the approximation of the optical density signal only by the resonant XUV absorption [3, 74, 153]. Here, a Fourier low-pass filter is used to directly reconstruct a reference spectrum from the measured signal $I_{\mathrm{Sig}}(\omega)$. This

method assumes that only the sharp resonant absorption signatures are of interest to the data analysis, whereas any non-resonant broad absorption signatures are filtered out together with the slowly modulating harmonic background. Focussing on dynamics imprinted on the sharp vibronic resonances in H_2 this method was used in the data analysis of the experiment discussed in the following.

To obtain the Fourier reference $I_{\mathrm{FT-Ref}}(\omega)$, first, the absorption spectrum $I_{\mathrm{Sig}}(\omega)$ is Fourier transformed (FT), which results in the Fourier decomposition of the measured spectrum, showing symmetrical FT frequency components around the 0th FT frequency. The lowest FT frequency components, both positive and negative, correspond to the slow modulation of the harmonics signal. Applying a generalised normal distribution with standard deviation α and order β of the form

$$G(x) = \mathrm{e}^{-\left(\frac{|x-x_0|}{\alpha}\right)^{\beta}} \tag{6.53}$$

as a low-pass filter selects only the low-frequency components, such that the back-transformed spectrum $I_{\mathrm{FT-Ref}}(\omega)$ after the filtering includes only the slow modulation in the original spectrum, i.e. follows the harmonics modulation. An illustration of this method to obtain reference spectra is shown in Fig. 6.10. Hereby, both the choice of the filter width and the steepness of the filter edges are crucial to filter out only the harmonics modulation and not the resonances. The parameters in the Gaussian low-pass filter thus have been chosen as $\alpha = 11$ frequency-space units and $\beta = 4$, while making sure that the reconstructed reference remains monotonic over the bandwidth of each vibronic resonance. By this method not the absolute optical density, which might also have non-resonant contributions, is obtained. To arrive at the right OD, the $I_{\mathrm{FT-Ref}}(\omega)$ reference has to be scaled with the exponential factor of Lambert-Beer's law, including the non-resonant absorption cross section $\sigma_{\mathrm{non-resonant}}(\omega)$ and the optical-path-length-density product $\rho\, l$. This correction provides an energy-dependent offset to the optical density, varying only weakly with energy, which is why it is omitted in the data evaluation.

An additional, commonly used technique in the data taking of absorption signals is the measurement of laser-induced changes in the absorption $\Delta OD(\omega)$, where the dressing laser is either switched on or off during the signal acquisition. This is typically realised through a beam chopper in the corresponding interferometer arm [278]. In the collinear geometry of the XUV absorption spectroscopy setup used to obtain the presented data the setup of a chopper is not possible. An equivalent approach is the measurement of a reference signal at a different time delay position, as for example at a very negative time-delay position, assuming the NIR field cannot affect the system. This approach was in fact used during the data acquisition but the obtained $\Delta OD(\omega)$ signal still included remaining modulation of the harmonics because of the long integration time required. Additionally, the change in absorption was not straightforward to interpret in the context of the molecular movement in contrast to the obtained OD signal after Fourier referencing, hence the Fourier-based method was used for extracting the OD from the measured spectra.

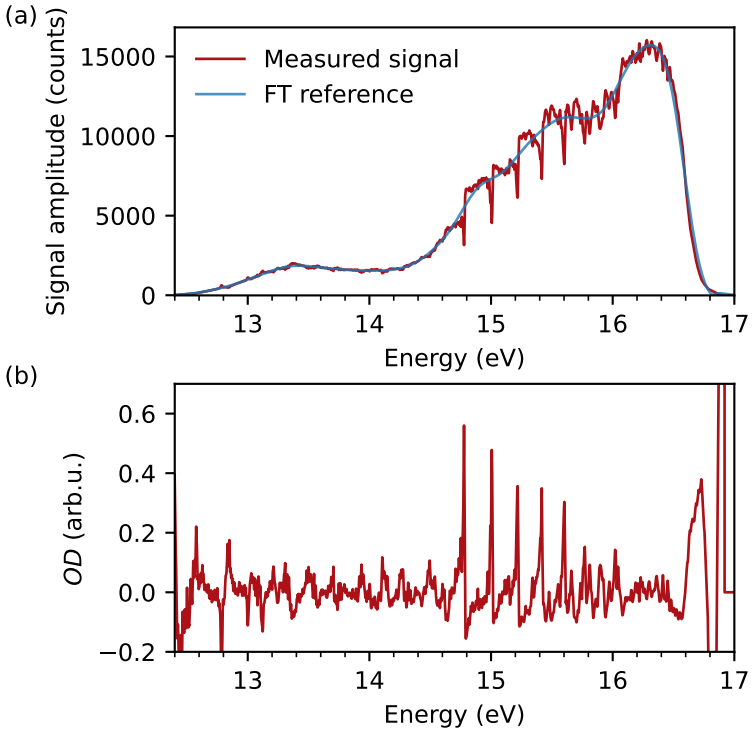

Figure 6.10: Reference reconstruction with a Fourier-transform method. **(a)** Measured signal (red) and reconstructed reference (blue) after applying a low-pass filter in Fourier space to filter out all sharp features in the signal. The chosen filter parameters according to Eq. 6.53 are $\alpha = 11$ frequency-space units and $\beta = 4$. **(b)** Calculated optical density OD using the reconstructed reference.

6.3.2.2 Data averaging and error estimation

The main control parameter in the experiments discussed in this chapter is the NIR intensity. All presented absorption data is a result of five individual measurements for each of the six considered NIR intensities, see Section 6.3.2.4, where a time delay $\tau = 7$ fs between the XUV and the NIR pulse was set. For better statistics the considered time-delay region around the chosen fixed time delay is a quarter of an NIR-pulse cycle, i.e. a data set at five different time steps of 0.17 fs around the chosen time-delay position is built. The absorption OD data is then a result of the averaging of all 5 measurements for each NIR intensity, which improves the signal-to-noise ratio of the absorption data for the line-shape analysis and for the dipole reconstruction. The estimation of the error bars for the absorption OD data is determined as the statistical error of the mean over all individual experiments at each NIR intensity. The shown reconstructed time-dependent emission dipole is the mean over all reconstructions of all individual 5 experiments. The error bars of the reconstruction are estimated with an upper and lower value, respectively, the highest and lowest reconstructed value of the dipole emission amplitude at a given real time

among all dipole reconstructions used to calculate the mean at each NIR intensity. This calculation of the error of the dipole emission amplitude is more conservative than simply taking the statistical error estimation, as it does not decrease with increasing number of considered data sets. In all figures, the error bars are shown as a shaded area around the corresponding plotted curves.

6.3.2.3 Photon-energy calibration

The dipole reconstruction method utilized to gain access to the molecular vibrational wave packet in Section 6.4 largely relies on the correct energy spacing between the resonances used to reconstruct the associated time-dependent dipole. For this reason, the energy calibration of the spectroscopic data is a crucial step in the data evaluation process.

As mentioned in section 4.2, which lays out the experimental setup, the spectrometer for data collection consists of a reflection diffraction VLS grating and a CCD camera. The diffraction grating separates the different photon energies in the XUV spectrum upon reflection and the CCD camera positioned in the focal plane of the concave VLS grating detects the photons reaching the camera chip surface at a respective position, i.e. pixel on the chip. The energy calibration thus can be performed knowing the exact setting geometry of the spectrometer and the typical characteristics of the grating, sketched in Fig. 4.11, all inserted in the grating equation

$$m\lambda = d\left[\sin\alpha - \frac{1}{\sqrt{\left(\frac{x}{a}\right)^2 + 1}}\right], \tag{6.54}$$

with m being the diffraction order, λ the wavelength of the light, d the grating constant and the remaining geometrical values x, a and α as depicted in Fig. 4.11. Although derived for a flat grating with equidistant spacing of the grooves, this grating equation is approximately applicable also for the curved grating geometry in the experimental setup. In particular, a calibration according to Eq. (6.54) is more accurate than a calibration with a polynomial fit, which deviates very fast outside of the fitting region.

The mapping of pixel to photon energy is done by imaging a known photon energy in the spectrometer. The more resonance lines with known photon energy are used to obtain the fitting curve and the wider they are spread in the imaging field, the better the mapping between pixel and photon energy. In the best case, easily recognisable resonances energetically in the same spectral region as the resonances of interest should be used. In the low energy region, confined between 11.2 eV and 16.8 eV due to the necessity to use NIR-blocking indium filters in the experimental setup, singly excited argon resonances are a sensible choice.

The ground-state electronic configuration of the argon atom is $1s^2 2s^2 2p^6 3s^2 3p^6 = [\mathrm{Ne}]\, 3s^2 3p^6$. XUV radiation in the spectral region between 11.2 eV and 16.8 eV pro-

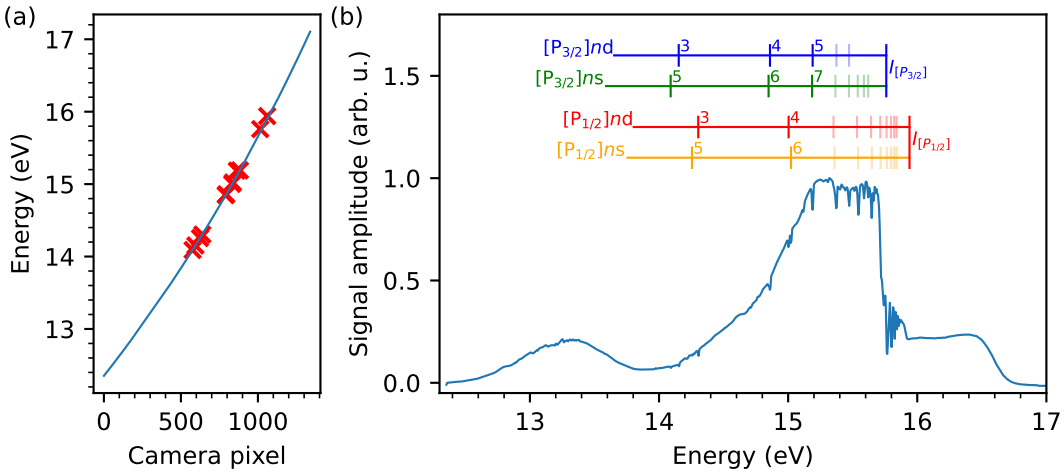

Figure 6.11: Energy calibration procedure. **(a)** Energy calibration curve obtained by fitting the grating equation to the position of the argon resonances listed in table 6.1 as well as the position of the two ionization thresholds $I_{P_{3/2}} = 15.76\,\text{eV}$ and $I_{P_{1/2}} = 15.94\,\text{eV}$. **(b)** Energy calibrated XUV absorption spectrum in argon together with the position of the four Rydberg series of single excitation, where the ten resonances used for the energy calibration are marked in solid colour and denoted by their quantum number n.

motes a 3p valence electron into the four dipole-allowed Rydberg series

$$3s^2 3p^6 \rightarrow 3s^2 3p^5 \left[^2P_{1/2,3/2}\right] n\text{s}, n\text{d}.$$

According to the total angular momentum quantum number $J = 1/2$ or $J = 3/2$, the respective series $3s^2 3p^6 \rightarrow 3s^2 3p^5 \left[^2P_{1/2}\right] n\text{s}, n\text{d}$ and $3s^2 3p^6 \rightarrow 3s^2 3p^5 \left[^2P_{3/2}\right] n\text{s}, n\text{d}$ converge to the ionization thresholds $I_{P_{1/2}} = 15.94\,\text{eV}$ and $I_{P_{3/2}} = 15.76\,\text{eV}$, respectively, as depicted in Fig. 6.11 (b). The 10 most distinctive spectral resonances as well as the energy positions of the two ionization thresholds were used for the energy calibration, with energy values taken from the Atomic Spectra Database [279], as listed in Table 6.1. All resonances are fitted by a Lorentzian line shape to obtain the pixel to energy mapping. The resulting energy calibration curve is shown in Fig. 6.11 (a). Because of the nonlinear pixel-to-energy relation, the photon energy is not sampled evenly through the whole energy region between 12.353 eV and 17.105 eV, but with a resolution of 3 meV and 5 meV at the lower and at the higher energy, respectively, i.e. the lower the photon energy, the better the spectrometer resolution.

A typical XUV absorption spectrum of H_2 obtained in the measurement is shown with the appropriate energy axis in Fig. 6.12. From the corresponding energy position of the different vibronic resonances one can assign the respective transition from the molecular ground state $X^1\Sigma_g^+ 1s\sigma$ with $\upsilon = 0$ to the respective excited state, being the $C^1\Pi_u\, 2p\pi$ or $D^1\Pi_u\, 3p\pi$ electronic state with the corresponding

Table 6.1: Energy positions of the argon resonances used in the calibration procedure

Series	Final state configuration	Energy (eV)
$3s^2 3p^6 \rightarrow s^2 3p^5 \left[^2P_{1/2}\right] ns$	$3s^2 3p^5 \left[^2P_{1/2}\right] 5s$	14.2551
	$3s^2 3p^5 \left[^2P_{1/2}\right] 6s$	15.0221
$3s^2 3p^6 \rightarrow s^2 3p^5 \left[^2P_{1/2}\right] nd$	$3s^2 3p^5 \left[^2P_{1/2}\right] 3d$	14.3037
	$3s^2 3p^5 \left[^2P_{1/2}\right] 4d$	15.0036
$3s^2 3p^6 \rightarrow s^2 3p^5 \left[^2P_{3/2}\right] ns$	$3s^2 3p^5 \left[^2P_{3/2}\right] 5s$	14.0900
	$3s^2 3p^5 \left[^2P_{3/2}\right] 6s$	14.8484
	$3s^2 3p^5 \left[^2P_{3/2}\right] 7s$	15.1855
$3s^2 3p^6 \rightarrow s^2 3p^5 \left[^2P_{3/2}\right] nd$	$3s^2 3p^5 \left[^2P_{3/2}\right] 3d$	14.1525
	$3s^2 3p^5 \left[^2P_{3/2}\right] 4d$	14.8592
	$3s^2 3p^5 \left[^2P_{3/2}\right] 5d$	15.1898

vibrational quantum number υ as indicated in the figure. The relative strength of the resonances in one vibronic band decreases with increasing vibrational quantum number υ, as expected from literature [273]. There is an exception to this behaviour for the resonances of the D band below $\upsilon = 3$, which is due to the non-dissociative character of those states, located energetically below the first dissociation continuum in H_2, which makes them long-lived [71, 73] and therefore the resonances very narrow and thus weak in the XUV absorption spectrum.

6.3.2.4 Intensity calibration

Calibration measurements for the intensity of the control NIR pulse were performed directly after the data recording. In doing so, first, the average power for the iris openings used in the experiment was measured shortly before the interaction region, after the last optical component such that the influence of all optical components reflecting or transmitting the laser beam before the interaction with the target is taken into account. Second, the beam profile in the focus, where the interaction with the H_2 molecules takes place, is recorded for every iris position. This is necessary, since a cut of the collimated laser beam with a circular aperture does not only attenuate the beam but also changes its diameter in the far field and therefore additionally the focus size. Assuming a Gaussian beam profile, the fit of the 2D focus image delivers a value for the beam waist W. The peak intensity is then calculated

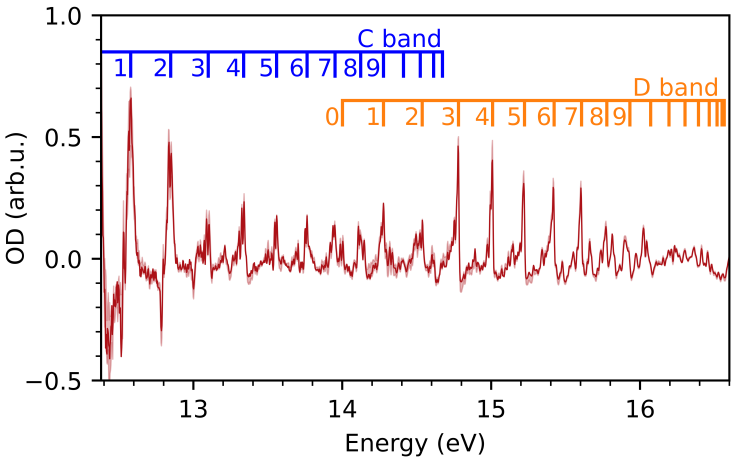

Figure 6.12: Typical XUV absorption spectrum of molecular hydrogen in the region of singly excited vibronic resonances with indicated position of the vibrational *C* (blue) and *D* (orange) bands.

as

$$I_0 = \frac{2P}{\pi W^2} \frac{1}{T_{\mathrm{NIR}} f_{\mathrm{rep}}} \tag{6.55}$$

from the measured power P, the fitted beam waist W, the pulse duration T_{NIR} as retrieved from the D-Scan measurement, see section 3.1.2.3, and the repetition rate of the laser f_{rep}. The actual intensity in the experiment, which could be assumed to be the average intensity, is a factor of 2 smaller than the estimated peak intensity by the described method, as also found in experiments measuring the ionization yields of noble gases as a function of the laser intensity [280]. Figure 6.13 shows the intensity calibration obtained using this method. The error of the calculated value, which is on the order of 10%, has its origin mostly in the uncertainty of the pulse duration T_{NIR}.

The maximal intensity of the used NIR pulse is $\approx 10^{13}\,\mathrm{W/cm^2}$, limited by the onset of strong-field effects out of the molecular ground state for higher intensity. This intensity limitation was determined through recording reference spectra where the NIR light for all considered intensities in the experiment interacts just with the target H_2 gas, without previous production of XUV light in xenon in the upstream HHG interaction region, Fig. 6.14 (a). Only for the highest considered intensities the NIR pulse produces high harmonics in H_2, but with an order of magnitude lower count rate compared to the XUV flux from the upstream HHG source with xenon as the driving medium, shown in Fig. 6.14 (b). Note that since the NIR pulse is reused for the target interaction, after generating the XUV pulses in xenon upstream, the NIR field strength is in general lowered in the actual experiment due to (plasma) dispersion and attenuation in xenon, hence there is no signature of XUV light generated in the target in the experimental data even for the highest considered intensity.

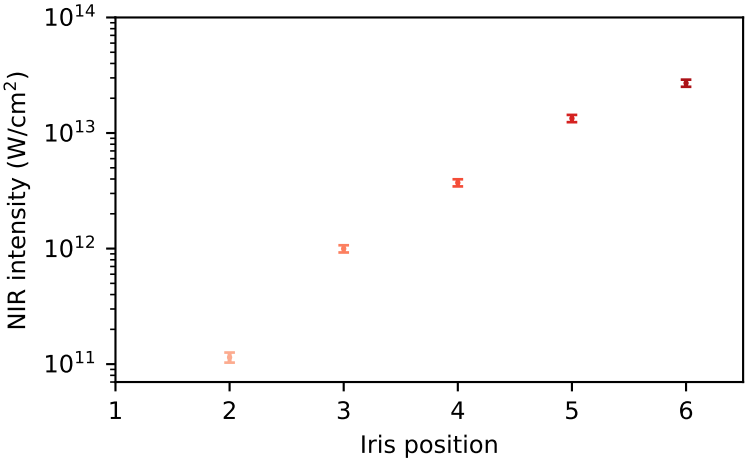

Figure 6.13: NIR intensity calibration showing the average intensity as a function of iris opening as calculated from the power measurements for every iris setting and the corresponding beam profile. Iris position 1 corresponds to no NIR intensity in the case of smallest opening where all NIR light passing through the iris is subsequently filtered out by the metal filters separating the XUV and NIR.

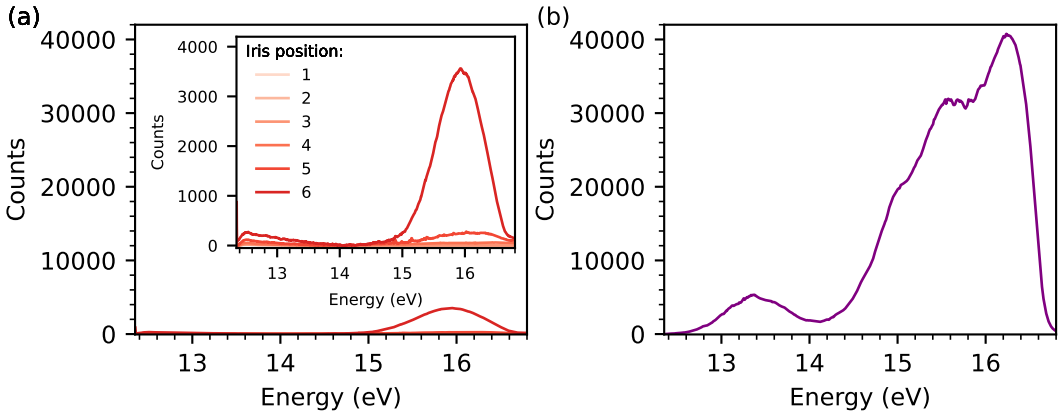

Figure 6.14: Detected XUV light **(a)** produced in the H_2 target in the absence of XUV light from the HHG source and **(b)** in the spectrum of the XUV pulse generated in the HHG process in Xe. Note that both subplots share the same axis for counts, whereas the inset of **(a)** zooms in on the target-only XUV spectrum for all iris settings, as used in the experiment.

6.4 Visualisation and laser control of a molecular wave-packet revival

This section presents the results of applying the all-optical technique for molecular wave-packet visualisation through the reconstruction of the time-dependent emission dipole to the hydrogen molecule. First, in section 6.4.1 molecular dynam-

ics of a freely evolving vibrational wave packet after its impulsive XUV excitation is considered, before a second interacting pulse is added as a control pulse to achieve strong-field reshaping of the molecular vibrational wave packet, shown in section 6.4.2. The control pulse in this case is an NIR pulse, fixed at time delay $\tau = 7\,\mathrm{fs}$ after the initial XUV excitation.

6.4.1 Dipole reconstruction for vibrational wave-packet revival imaging

The XUV pulse used to initiate molecular dynamics in the hydrogen molecule spans spectrally between 12.4 eV and 16.7 eV, such that simultaneously multiple electronic excited states are excited, like for example the $C^1\Pi_u\,2p\pi$ and $D^1\Pi_u\,3p\pi$ states, with their strong vibronic resonances, indicated in Fig. 6.12. Those detected vibronic resonances indicate that a vibrational wave packet belongs to every excited electronic state. The overall excited molecular wave packet consists therefore of the sum of all separate vibrational wave packets. The spectral signatures, associated to each of the different vibrational wave packets evolving in a particular excited state, are energetically separated. For example, the resonances of the D vibronic band are located at energies higher than those of the C vibronic band. This energetic separation allows for decoupling of the wave packets belonging to those electronic states. In the following only the D-state vibrational wave packet is considered. For this, spectrally only the region of the D band is selected, by applying a spectral window function in the energy region between 13.85 eV and 16.4 eV, as shown in Fig. 6.15.

The method for reconstruction of the time-dependent dipole is then applied to the resulting spectrum, now including mainly signatures of only the D vibrational band. The reconstructed dipole amplitude, Fig. 6.16 (a) exhibits a complicated structure for times up to a few hundred femtoseconds. Owing to the finite spectral resolution of 4 meV at 15 eV photon energy, the dipole of the D vibrational wave packet can be reconstructed up to a real time of around 400 fs. After an initial decrease in the dipole peaks, higher-in-intensity peak structure appears in the dipole amplitude around 270 fs. The two main peaks in this region are separated by 18 fs, corresponding to the classical vibrational time period in the D potential energy curve. A comparison of the reconstructed dipole to the calculated time evolution of a model D vibrational wave packet, Fig. 6.16 (b), and the corresponding calculated dipole, Fig. 6.16 (c), reveal the peaks in the time region around 270 fs to correspond directly to the vibrational wave packet revival, marked with an arrow at its time position. The vibrational wave packet is a distinct observable for a particular wave packet, and in particular for the time dynamics in the vibrational wave packet. The method of reconstruction of the time-dependent dipole therefore allows access to the wave-packet revival, directly connected to the molecular wave-packet dynamics.

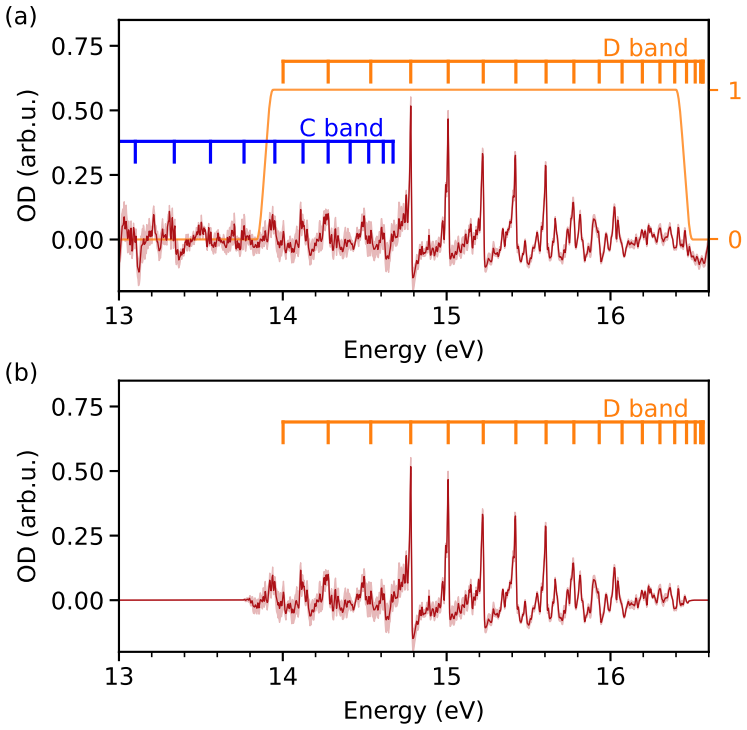

Figure 6.15: Spectral selection of the resonances belonging to the D vibrational wave packet. **(a)** Detected XUV absorption spectrum including resonances of different vibronic bands together with the window function (orange) used to select the D band. **(b)** Spectrally selected resonances of the D band.

Through the selection of the D band with a continuous spectral window function, not only the D resonance, but also low-intensity resonances of other electronically excited states, as for example those of the B' band, are included in the dipole reconstruction. To decrease the amount of included undesired resonances a complex window *comb* structure consisting of windows around each different D vibronic resonance was used to again reconstruct the dipole of the D vibrational wave packet. Due to the decreasing intensity of the D-band resonances with increasing vibrational quantum number, only the first 12 resonances up to $v = 11$ were selected with the comb-like window, as depicted in Fig. 6.17 (a). The corresponding reconstructed dipole, Fig. 6.17 (b), shows two differences in comparison to the dipole reconstructed with the simple one-window selection, including the D band together with low-intensity resonances of other bands. First, the reconstructed dipole is now able to reproduce the increase in dipole amplitude at the beginning of the wave-packet evolution, around 20 fs and around 40 fs, at the return time of the wave packet in the first two periods of the classical vibration, before the significant dephasing of the wave-packet. Second, the dipole at the time of the revival shows higher amplitude compared to the dipole reconstructed with the continuous window selection. The more complex comb-like window, precisely selecting the D

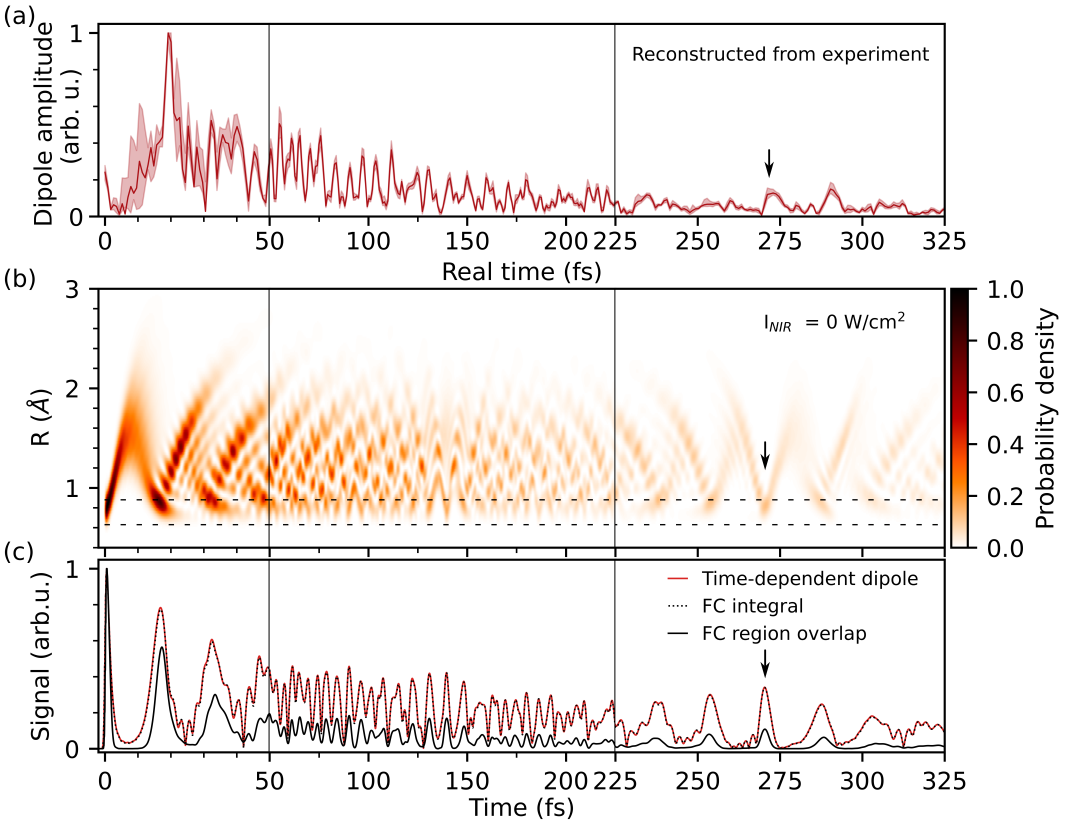

Figure 6.16: Visualisation of the free time evolution of the *D* vibration wave packet after initial XUV excitation. **(a)** Reconstructed time-dependent dipole emission amplitude from the spectral data inside the reconstruction window including the whole *D* vibronic band. **(b)** Calculated time evolution of the vibrational wave packet in the electronically excited *D* state of H_2 for XUV-only interaction with the system at time zero, exciting the vibrational wave packet. **(c)** Time-dependent dipole amplitude, Franck-Condon overlap integral and integral inside the FC region. All three subfigures share the same kind of division of the time axis in three different parts, with the same bigger scale for the first and third part, and smaller scale for the second.

band resonances, therefore allows for reconstruction of the time-dependent dipole revealing additional dynamics signatures compared to the case of using a simple selection of the band.

6.4.2 Experimental demonstration of laser control of a molecular wave packet

Adding a second interacting pulse, arriving at the target after the initial XUV excitation, we will now aim to change the wave-packet dynamics and observe this

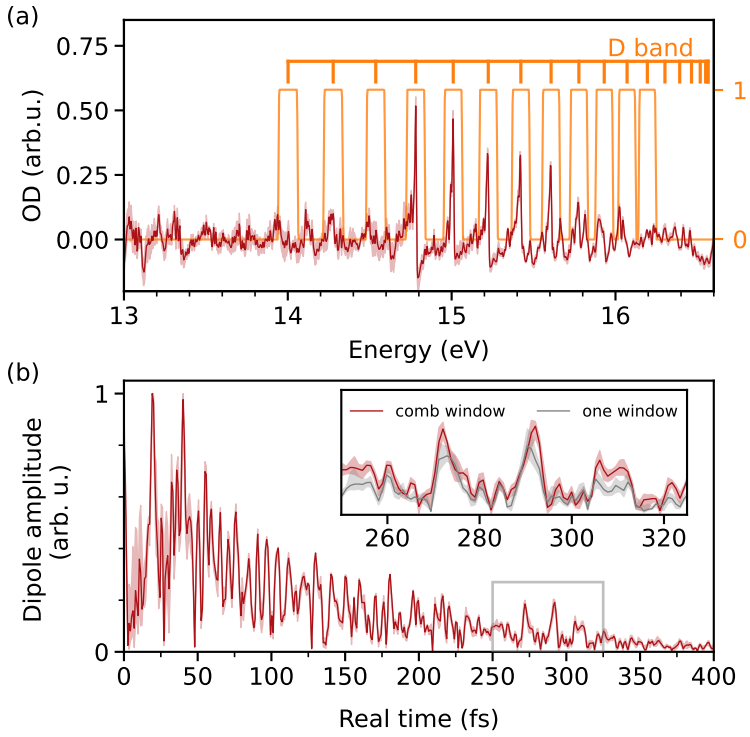

Figure 6.17: Time-dependent dipole reconstruction from measured absorption data after applying a comb-like window function (orange) selecting precisely only the D-band resonances from $v = 0$ up to resonance $v = 11$, as shown in **(a)**. **(b)** Reconstructed dipole amplitude up to real time 400 fs, with the inset showing the region around the wave-packet revival signature. For comparison, also the reconstructed dipole after one-window selection (gray) as in Fig. 6.15 is shown together with the dipole amplitude reconstructed after selection of the D-band resonances with a comb-like window function.

change in the reconstructed time-dependent dipole, in particular, in the signature of the wave-packet revival. Gradually tuning the NIR intensity between 10^{11} and $10^{13}\,\mathrm{W/cm^2}$ XUV absorption spectra in the region of the D vibronic band at different NIR intensities were recorded, as shown in Fig. 6.18 (a). The asymmetric line-shapes of the resonances become broader and assume a more symmetrical form with increasing NIR intensity. Such line-shape changes are known and understood for isolated atomic states [281,282], but their interpretation in the context of molecular dynamics remained elusive. In the case of H_2, recent experiments have studied resonances in the energy range of singly excited vibronic excitations for a fixed moderately strong NIR intensity by scanning the time delay between the transition-driving XUV pulse and the NIR perturbation pulse and detecting as a result beatings in the absorption spectra, connected to vibrational [251, 283] and rotational [284] motion in the molecule.

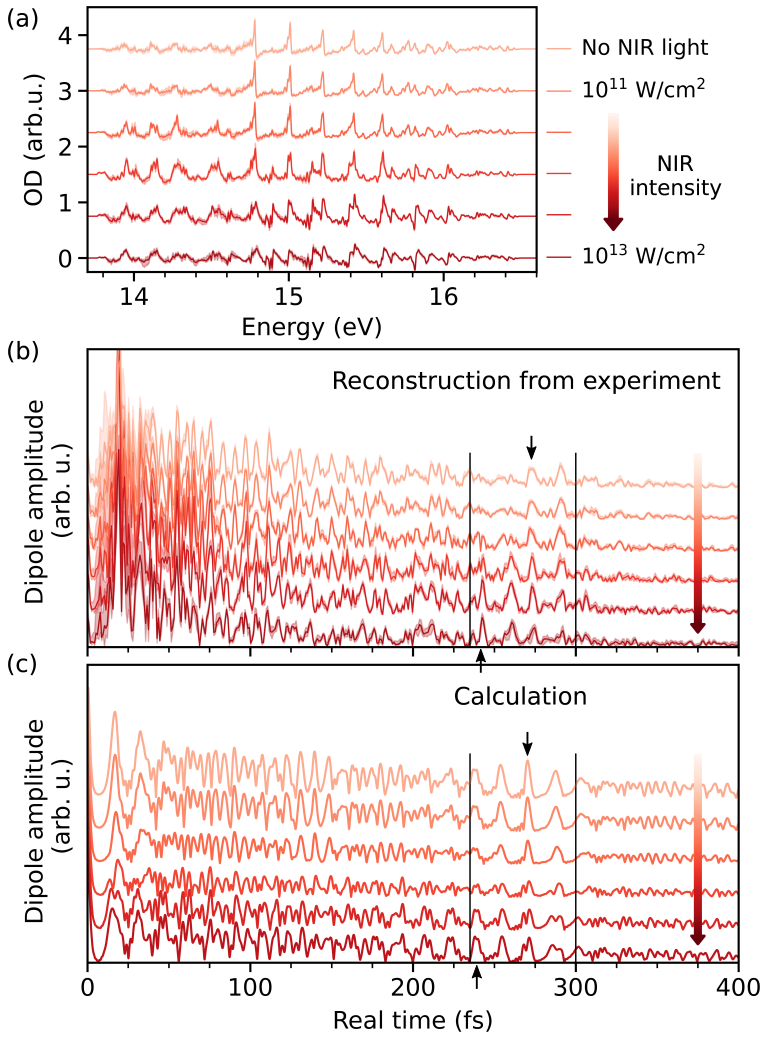

Figure 6.18: NIR-intensity-induced change of the D-state vibrational wave-packet dynamics. **(a)** Measured absorption spectrum (OD) in the region of the D band for NIR intensities between 10^{11} (top) and $10^{13}\,\mathrm{W/cm^2}$ (bottom), shown after applying the reconstruction window from Fig. 6.15. **(b)** and **(c)** Reconstructed and calculated time-dependent dipole emission amplitude of the D vibrational wave packet for different NIR intensities, respectively. The vertical black lines show the region around the revival of the wave packet. Black arrows point to the dipole maxima associated to the revival of the wave packet, shifting to earlier times with increasing NIR intensity. All subfigures share the same intensity colorscale. For better visibility the individual lines are ordered from lower ($10^{11}\,\mathrm{W/cm^2}$) intensity at the top to higher ($10^{13}\,\mathrm{W/cm^2}$) intensity at the bottom for all presented data. The six intensity values in $\mathrm{TW/cm^2}$ (from low to high) according to the calibration in Fig. 6.13 are: (0.010 ± 0.001), (0.115 ± 0.012), (0.997 ± 0.072), (3.71 ± 0.26), (13.40 ± 0.97), (27.0 ± 1.9).

The reconstruction of the time-dependent dipole emission amplitude of the D vibronic band for different NIR control intensities is shown in Fig. 6.18 (b). The most distinct change in the dipole amplitude as a function of NIR control intensity occurs in the wave-packet revival region between 235 and 300 fs. In particular, the peaks associated with the wave-packet localization in the Franck-Condon region shift to earlier times and become more prominent for higher intensity. However, no gradual shift of the dipole peaks is observed, but in multiples of the classical vibrational period. This trend is in qualitative agreement with the multi-level model calculations, depicted in Fig. 6.18 (c) for increasing NIR intensity. Due to uncertainties in the exact control pulse shapes in the experiment, as well as the limitation to a finite number of states in the simulation, and no consideration of focal volume averaging to account for the distribution of different intensities across the laser focus, no exact quantitative agreement of the relative dipole amplitudes is achieved. Even though the NIR pulse interacts with the system only for a short time and impulsively right after the wave-packet excitation, the results of the dipole reconstruction bring experimental evidence that the subsequent wave-packet evolution is coherently modified for times at least until its first revival.

To illustrate better how also the wave-packet evolution is affected by an additionally acting NIR pulse, a calculation for NIR intensity of $3.5 \times 10^{13}\,\mathrm{W/cm^2}$ is presented in Fig. 6.19, with (a) showing the wave-packet time evolution and (b) the computed corresponding time-dependent dipole, FC integral and FC region overlap. For the duration of the NIR pulse, the D states are strongly coupled to the EF states, such that population is transferred between the states. This population transfer is directly visible in the disturbed wave-packet probability density at the NIR interaction time of 7 fs. This effect is not accessible in the time-dependent dipole due to the fact, that at 7 fs the wave packet is localised outside of the region of the molecular ground state. The time-localised distortion of the wave packet through the NIR does have a noticeable effect also for later times. The revival of the wave packet, in the NIR-unperturbed case around 270 fs, is now shifted to one classical vibrational period earlier around 253 fs.

6.4.3 Control mechanism

The 5-fs NIR pulse is much shorter than the 300-fs scale of the vibrational revival, which justifies a δ-like approximation for the NIR interaction at time $t = \tau$. In such an impulsive picture, the overall induced accumulated phase and amplitude shift at $t = \tau$ can be understood as effectively different initial conditions of the $c_v(t)$ coefficients for the following field-free time evolution for times $t > \tau$. Among this line of argument, the very short time delay can also be approximated to $\tau = 0$ fs, meaning that both the XUV excitation and the NIR interaction occur instantaneously and much faster than the time scale of the coherent dipole-emission

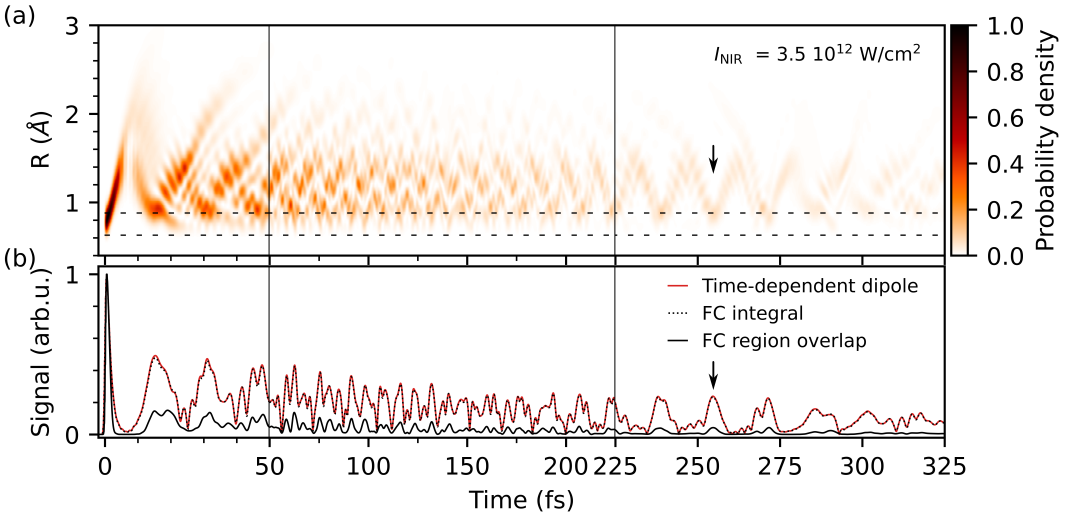

Figure 6.19: Vibrational wave-packet time evolution and the time-dependent dipole amplitude upon interaction with an NIR laser pulse. **(a)** Calculated time evolution of the vibrational wave packet in the electronically excited D state of H_2 for XUV excitation at time zero, followed by an interaction with an NIR control pulse arriving at 7 fs. **(b)** Time-dependent dipole amplitude, Franck-Condon overlap integral and integral inside the FC region, as marked by the horizontal dashed lines in (a). The black arrows point at the revival position, shifted in time to around 253 fs, one classical vibrational period earlier in comparison to the NIR-free case, shown in Fig. 6.7.

decay. Substituting then $c_\upsilon^0 \rightarrow c_\upsilon^0 a_\upsilon^{\mathrm{NIR}} \mathrm{e}^{i\phi_\upsilon^{\mathrm{NIR}}}$ leads to the expression

$$c_\upsilon(t) = c_\upsilon^0 \mathrm{e}^{-i\omega_\upsilon t} a_\upsilon^{\mathrm{NIR}} \mathrm{e}^{i\phi_\upsilon^{\mathrm{NIR}}} \tag{6.56}$$

for the wave-packet expansion coefficients and the modified initial conditions impact the complete wave-packet evolution. The complex coefficient c_υ^0 can in general be written in the form $c_\upsilon^0 = \tilde{c}_\upsilon \mathrm{e}^{i\phi_\upsilon^0}$, where the initial phase-shift accounts for non-adiabatic coupling of the state to other states. The overall time-independent part of the phase

$$\phi_\upsilon = \phi_\upsilon^0 + \phi_\upsilon^{\mathrm{NIR}} \tag{6.57}$$

of the coherent dipole emission of the vibrational state υ is further connected to the asymmetry parameter q_υ of the corresponding resonance through

$$q_\upsilon = -\cot\left(\frac{\phi_\upsilon}{2}\right). \tag{6.58}$$

The following short detour shall motivate this expression, derived in [281] in the case of a single resonance. For this purpose, first a two-level system is considered, consisting of a ground and an excited state, both labelled $|\psi_\mathrm{g}\rangle$ and $|\psi_\mathrm{e}\rangle$, respectively.

The time-dependent sum wave function then reads

$$|\psi(t)\rangle = c_\mathrm{g} \mathrm{e}^{-i\omega_\mathrm{g} t} |\psi_\mathrm{g}\rangle + \theta(t) c_\mathrm{e} \mathrm{e}^{-i\omega_\mathrm{e} t} \mathrm{e}^{-\frac{\Gamma_\mathrm{e}}{2} t} |\psi_\mathrm{e}\rangle , \tag{6.59}$$

where the Heaviside function $\theta(t)$ explicitly takes into account the excitation at time $t = 0$ of the state $|\psi_\mathrm{e}\rangle$, and the decay term $\mathrm{e}^{-\frac{\Gamma_\mathrm{e}}{2} t}$ accounts for the decay rate $\Gamma_\mathrm{e}/2$ of the excited state. The time-dependent emission dipole of this two-level system takes the form

$$d(t) = \langle \psi(t) | \hat{\boldsymbol{d}} | \psi(t) \rangle = \theta(t) c_\mathrm{g}^* c_\mathrm{e} \mathrm{e}^{-i(\omega_\mathrm{e} - \omega_\mathrm{g})t} \mathrm{e}^{-\frac{\Gamma_\mathrm{e}}{2} t} d_\mathrm{ge} + \mathrm{c.c.}, \tag{6.60}$$

with the transition dipole element between ground and excited state d_ge. Discarding the complex conjugate part at this point is equivalent to leaving the unphysical negative frequencies out of the remaining analysis.

A substitution of the coefficient c_e with an NIR-modified coefficient $c_\mathrm{e} \rightarrow c_\mathrm{e}\, a_\mathrm{e}^\mathrm{NIR}\, \mathrm{e}^{i\phi_\mathrm{e}^\mathrm{NIR}}$ leads to the NIR-modified expression for the time-dependent dipole:

$$d_\mathrm{NIR}(t) = \theta(t) c_\mathrm{g}^* c_\mathrm{e}\, a_\mathrm{e}^\mathrm{NIR}\, \mathrm{e}^{i\phi_\mathrm{e}^\mathrm{NIR}} \mathrm{e}^{-i(\omega_\mathrm{e} - \omega_\mathrm{g})t} \mathrm{e}^{-\frac{\Gamma_\mathrm{e}}{2} t} d_\mathrm{ge}. \tag{6.61}$$

The absorption line shape corresponding to this modified dipole is proportional to the imaginary part of the Fourier-transformed dipole, see Eq. (2.38), which leads to the expression

$$A \propto \Im\mathrm{m}\{\mathfrak{F}[d(t)]\} = \frac{c_\mathrm{g}^* c_\mathrm{e}\, a_\mathrm{e}^\mathrm{NIR} d_\mathrm{ge}}{\Gamma_\mathrm{e}/2} \frac{\left(\cos\phi_\mathrm{e}^\mathrm{NIR} - \frac{(\omega_\mathrm{e} - \omega_\mathrm{g})}{\Gamma_\mathrm{e}/2} \sin\phi_\mathrm{e}^\mathrm{NIR}\right)}{\left(1 + \left(\frac{\omega_\mathrm{e} - \omega_\mathrm{g}}{\Gamma_\mathrm{e}/2}\right)^2\right)}. \tag{6.62}$$

It is equivalent to the generalised Fano line-shape with its asymmetry q-parameter

$$A_\mathrm{Fano} = \frac{a}{(q^2+1)\pi\frac{\Gamma_\mathrm{e}}{2}} \left(\frac{\left(q + \frac{\omega_\mathrm{e} - \omega_\mathrm{g}}{\Gamma_\mathrm{e}/2}\right)^2}{1 + \left(\frac{\omega_\mathrm{e} - \omega_\mathrm{g}}{\Gamma_\mathrm{e}/2}\right)^2} - 1 \right), \tag{6.63}$$

assuming $\phi_\mathrm{e}^\mathrm{NIR} = 2\mathrm{Arg}(q - i)$ and $q = -\cot\left(\frac{\phi_\mathrm{e}^\mathrm{NIR}}{2}\right)$.

In a generalised picture, with not one but N excited states, which can all be accessed from the ground state, the full wave function takes the form

$$|\psi_{\mathrm{g},N}(t)\rangle = c_\mathrm{g} \mathrm{e}^{-i\omega_\mathrm{g} t} |\psi_\mathrm{g}\rangle + \sum_{n=1}^{N} \theta(t) c_n \mathrm{e}^{-i\omega_n t} \mathrm{e}^{-\frac{\Gamma_n}{2} t} |\psi_n\rangle , \tag{6.64}$$

with the corresponding time-dependent dipole emission expression

$$d_{\mathrm{g},N}(t) = \langle \psi_{\mathrm{g},N}(t)|\hat{\boldsymbol{d}}|\psi_{\mathrm{g},N}(t)\rangle = \sum_{n=1}^{N} \theta(t) c_{\mathrm{g}}^{*} c_n \mathrm{e}^{-i(\omega_n-\omega_{\mathrm{g}})t} \mathrm{e}^{-\frac{\Gamma_n}{2}t} d_{\mathrm{gn}} + \mathrm{c.c.} \tag{6.65}$$

Because of the linearity of the Fourier transformation and the imaginary operator, together with the linearity of the time-dependent dipole in Eq. (6.65), the NIR-modified absorption spectrum, now consisting of N interfering Fano line shapes takes the form

$$A \propto \Im\mathfrak{m}\{\mathfrak{F}[d(t)]\} = \sum_{n=1}^{N} \frac{c_{\mathrm{g}}^{*} c_n a_n^{\mathrm{NIR}} d_n}{\Gamma_n/2} \frac{\left(\cos\phi_n^{\mathrm{NIR}} - \frac{(\omega_n-\omega_{\mathrm{g}})}{\Gamma_n/2}\sin\phi_n^{\mathrm{NIR}}\right)}{\left(1+\left(\frac{\omega_n-\omega_{\mathrm{g}}}{\Gamma_n/2}\right)^2\right)}, \tag{6.66}$$

with the line asymmetry to dipole phase connection holding for each of the N states

$$q_n = -\cot\left(\frac{\phi_n}{2}\right). \tag{6.67}$$

6.4.3.1 Extraction of the NIR-induced phase shift

The NIR-induced phase shift can be extracted both experimentally and from the model simulation:

- **In the simulation** the NIR-induced phase shifts are obtained directly from the time-dependent expansion coefficients $c_\upsilon(t)$ for each state in the vibrational wave packet:

  The overall phase of the vibrational coefficients includes three contributions: the time-dependent contribution $\phi_\upsilon(t) = \omega_\upsilon t$ and the time-independent part as in Eq. (6.57). Two of them are NIR intensity independent, which allows to find the NIR induced phase when referencing $c_\upsilon(t)$ to the field-free case according to:

  $$\phi_{\upsilon,I}^{\mathrm{NIR}} = \arg\left(\frac{c_{\upsilon,I}(t)}{c_{\upsilon,I_0}(t)}\right), \tag{6.68}$$

  with $c_{\upsilon,I_0}(t)$ being the time-dependent coefficients for no NIR intensity, i.e. evolving with the corresponding eigenstate energy of the state υ. Strictly speaking, the obtained NIR phase shift is actually time dependent, since the calculation accounts for the NIR interaction at every time step Δt. To extract the accumulated NIR-induced phase $\Delta\phi_{\upsilon,I}^{\mathrm{NIR}}$, one has to find the phase difference of the values obtained between the end and the beginning of the NIR pulse, here $\phi_{\upsilon,I}^{\mathrm{NIR}}(t = 20\,\mathrm{fs})$ and $\phi_{\upsilon,I}^{\mathrm{NIR}}(t = 0\,\mathrm{fs})$, respectively, when in those two periods $\phi_{\upsilon,I}^{\mathrm{NIR}}$ remains unchanged.

  An example of the NIR-induced phase shift extraction from the numerical simulation is shown in Fig. 6.20 for NIR intensity of $I = 3.51\,\mathrm{TW/cm^2}$. Figure

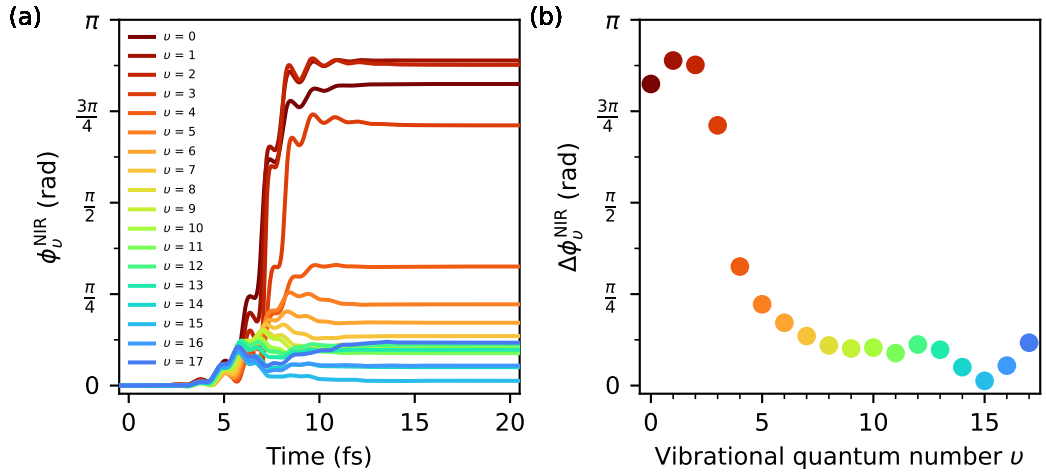

Figure 6.20: Extraction of the NIR-induced phase shift from the vibrational coefficients for the D bound states in the numerical simulation for NIR-intensity of $I = 3.51\,\mathrm{TW/cm^2}$. **(a)** Time-dependent evolution of $\phi_{\upsilon,I}^{\mathrm{NIR}}$ calculated according to Eq. (6.68) for all vibrational states in the D wave packet. Before and after the arrival of the NIR pulse at time $t = 7\,\mathrm{fs}$ the NIR-induced phase is constant. **(b)** Accumulated NIR-induced phase $\Delta\phi_{\upsilon,I}^{\mathrm{NIR}}$ extracted as the difference between $\phi_{\upsilon,I}^{\mathrm{NIR}}(t = 20\,\mathrm{fs})$ and $\phi_{\upsilon,I}^{\mathrm{NIR}}(t = 0\,\mathrm{fs})$.

6.20 (a) shows the time dependence of $\phi_\upsilon^{\mathrm{NIR}}$ for all 18 vibrational states in the D wave packet around $t = 7\,\mathrm{fs}$, when the NIR pulse arrives its amplitude maximum. The initially mostly populated states (compare to FC-coefficients) exhibit rapid rise of the NIR-induced phase of almost π until the NIR field reaches its maximum, whereas the higher vibrational states change their phase only up to $\pi/8$. The overall accumulated phase shift for each vibrational state is depicted in Fig. 6.20 (b). It exhibits a minimum for vibrational state $\upsilon = 15$.

- **In the experiment** the NIR-induced phase shifts are extracted through a state-resolved fit of an asymmetric Fano line shape for the corresponding vibrational resonances:

  According to Eq. (6.57), the fitted phase at every intensity $\phi_{\upsilon,I}$ includes both the non-adiabatic phase ϕ_υ^0, which is state-specific but independent of the NIR-intensity, as well as the intensity-dependent NIR-induced phase shift $\phi_{\upsilon,I}^{\mathrm{NIR}}$. The fitted phase ϕ_{υ,I_0} in the case of zero NIR intensity I_0 delivers the value of the intensity-independent contribution ϕ_υ^0, such that this can be subtracted from the intensity-dependent phase, providing the NIR-induced phase shift

$$\phi_{\upsilon,I}^{\mathrm{NIR}} = \phi_{\upsilon,I} - \phi_{\upsilon,I_0}. \tag{6.69}$$

As discussed above, the Fano asymmetry parameter q can be related to a phase shift ϕ of the temporal dipole response via

$$\phi = 2\arg(q - i). \tag{6.70}$$

Inserting this relation into the standard q-dependent expression for an asymmetric Fano line shape, Eq. (2.57), a ϕ-dependent equivalent version emerges:

$$S^{\phi}_{\mathrm{Fano}}(\omega) = a\frac{\cos(\phi) - \frac{\omega-\omega_\mathrm{r}}{\Gamma/2}\sin(\phi)}{\pi\frac{\Gamma}{2}\left(1+\left(\frac{\omega-\omega_\mathrm{r}}{\Gamma/2}\right)^2\right)} + b, \tag{6.71}$$

with parameters a for the line strength, background offset b, resonance position $E_\mathrm{r} = \hbar\omega_\mathrm{r}$ and decay width Γ. Before the fit procedure however, the spectrometer response function, i.e. the detector resolution, has to be taken into account. Since not directly the resonance cross section proportional to $S^{\phi}_{\mathrm{Fano}}(\omega)$ was measured, but transmitted intensity in the form of XUV spectrum, to account for the spectrometer resolution an inverted measured absorption spectrum has to be defined as 10^{-S_Fano}. The analytical fit formula for the ϕ-dependent fit applicable to the experimental data becomes

$$S^{\phi}_{\mathrm{Fano,exp}}(\omega) = -\log_{10}\left[10^{-S^{\phi}_{\mathrm{Fano}}(\omega)} * \frac{1}{\sqrt{2\pi}\sigma_\mathrm{res}}\exp\left(-\frac{\omega^2}{2\sigma^2_\mathrm{res}}\right)\right], \tag{6.72}$$

where $*$ denotes the convolution with the instrument response function with the detector resolution determined experimentally $\sigma_\mathrm{res} = 1\,\mathrm{meV}$.

The fits of the five most intense lines in the D band absorption spectrum, the $D\upsilon = 3$ to $D\upsilon = 7$ resonances, are depicted in Fig. 6.21 for all six considered NIR intensities. As for all data presented for increasing intensity throughout this chapter, the darkest red colour shows the data for NIR intensity $\sim 10^{13}\,\mathrm{W/cm^2}$ (bottom curves), whereas the lightest red colour corresponds to the case of no NIR intensity (top curves). The resonances show a clear broadening suggesting decrease of their life time, as well as change in the asymmetry form, i.e. in the line-shape q-parameter as a result of the NIR interaction. The retrieved NIR phase shift for each resonance as a function of NIR intensity is depicted in Fig. 6.22. The evolution of $\Delta\phi_\upsilon$ for each resonance shows increase of the accumulated phase shift with rising intensity. Qualitatively same behaviour is shown also from the phase-evolution for the considered states, retrieved from the simulation data (black curves in Fig. 6.22. The quantitative differences are accounted to the limitation of the simulation to a restricted set of states, thus overestimating the accumulated phase shift in the present model simulation.

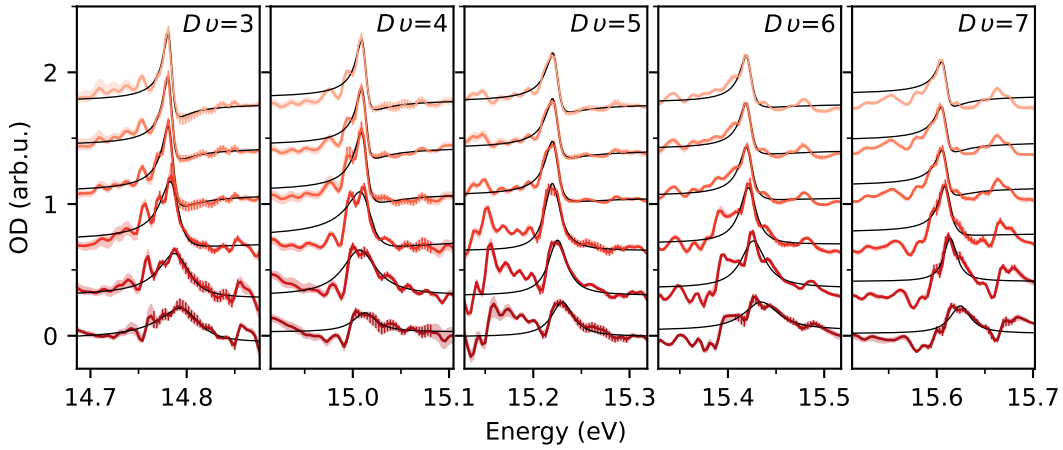

Figure 6.21: Extraction of the NIR-induced phase shift from the experimentally measured absorption line shapes as a function of intensity for the D-band resonances with vibrational quantum number $\upsilon = 3, ..., 7$. The fit, shown as a black line for every resonance and every intensity, is done according to Eq. (6.72). All subfigures share the same intensity colorscale. For better visibility the individual lines are ordered from lower ($10^{11}\,\mathrm{W/cm^2}$) intensity at the top to higher ($10^{13}\,\mathrm{W/cm^2}$) intensity at the bottom for all presented data. The six intensity values in $\mathrm{TW/cm^2}$ (from low to high) according to the calibration in Fig. 6.13 are: (0.010 ± 0.001), (0.115 ± 0.012), (0.997 ± 0.072), (3.71 ± 0.26), (13.40 ± 0.97), (27.0 ± 1.9).

6.4.3.2 NIR-induced phase shift and state-dependent polarizability

While the previous section laid out the extraction of the NIR induced phase shift out of the model simulation and of the experimentally measured absorption data, the present section points out the possible origin of NIR-induced phase shift.

The concept of additional laser-induced phase shift introduced to explain the transition of Fano to Lorentz line shapes in the helium atom points at the ponderomotive shift as the origin of the additionally observed phase shift, leading to line shape changes [281]. Here, the laser-induced AC stark shift of atomic energy levels is approximated by the ponderomotive energy shift derived in a classical picture for a free electron under the influence of a laser electric field. The gained kinetic energy by the electron amounts to

$$\Delta E_\mathrm{p} = U_\mathrm{p} = \frac{e^2 F^2}{4m\omega^2}, \tag{6.73}$$

with F and ω standing for the strength and the frequency of a monochromatic electric field, and e and m being the elementary charge and the electron mass. While the stronger bound energetically lower lying atomic states are also strongly affected by the Coulomb potential, the more loosely bound higher-lying Rydberg states are increasingly mostly affected by the ponderomotive shift, which turns out to be a good approximation for the higher electronic excitations in the helium atom [281]. The

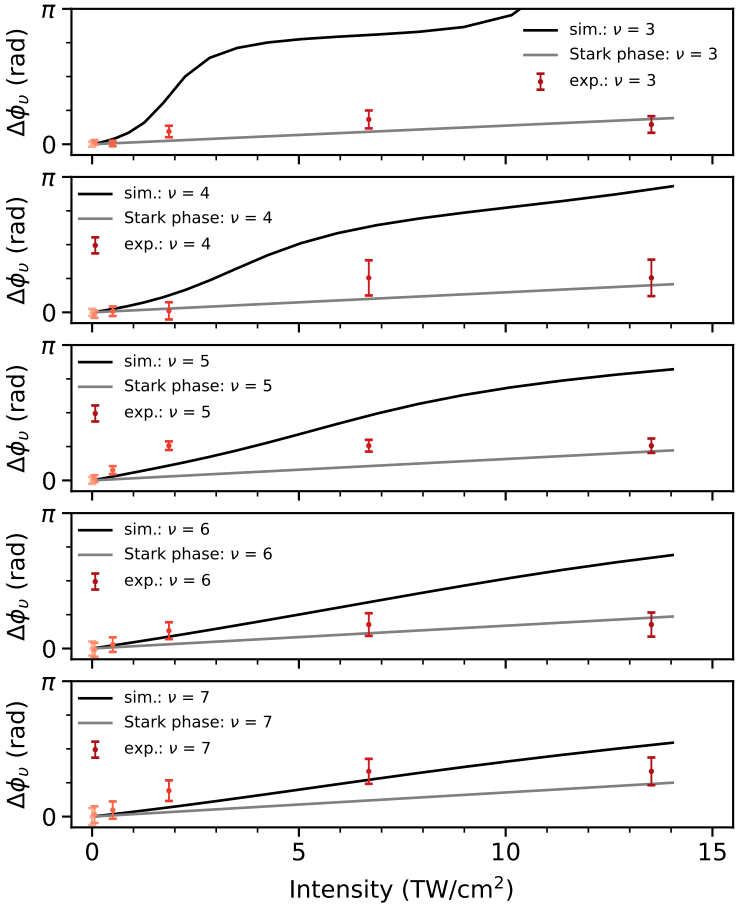

Figure 6.22: NIR-induced phase shift from the experimentally measured absorption line shapes (data points) and from the model calculation (black lines) as a function of intensity for the D-band resonances with vibrational quantum number $\upsilon = 3$ to $\upsilon = 7$ (top to bottom). The gray lines show computed phase change due to Stark shift over the duration of the NIR pulse for every considered state.

corresponding accumulated phase shift then is given by the integral over the time-dependent ponderomotive shift, as it in turn depends on the laser-field strength, which changes in time, such that:

$$\Delta\phi_{\mathrm{p}} = -\int \frac{\Delta E_{\mathrm{p}}(t')}{\hbar} \mathrm{d}t', \tag{6.74}$$

integrated over the NIR pulse duration.

Such a treatment of the NIR-induced phase shift, however, delivers the same NIR-induced phase shift for all states, if it would have been adopted for the present case treating the H_2 vibrational wave packet. A uniform phase shift would not change the rephasing condition for the emergence of a wave packet revival, as it

Table 6.2: State-dependent polarizabilities for the vibrational levels in the D electronically excited state. Values are extracted from Ref. [46] stating the polarizability of individual vibrational states of the ground state, and scaled up by a factor of 4.

v	α_v	v	α_v
0	21.7064	9	39.24776
1	23.59412	10	40.564
2	25.55344	11	41.40884
3	27.57224	12	41.58084
4	29.6312	13	41.68
5	31.70528	14	41.76
6	33.76116	15	41.8
7	35.74892	16	41.84
8	37.60456	17	41.88

would be accumulated equally for all states. Thus, a more realistic treatment would indeed include the state-dependent AC Stark shift with a state-dependent dynamic polarizability α_s, such that the instantaneous AC Stark shift for each state s

$$\Delta E_{\text{Stark}} = -\frac{\alpha_s}{2} F^2 \tag{6.75}$$

causes the state-dependent NIR-induced phase shift:

$$\Delta\phi_{\text{Stark}} = -\frac{\alpha_s}{2\hbar} \int F_{\text{NIR}}(t')^2 \mathrm{d}t'. \tag{6.76}$$

The calculation of the state-dependent polarizabilities α_s can be derived from the general from of the AC-stark shift including all possible transitions of a states $|\psi_s\rangle$ [285]:

$$\Delta E_{\text{AC Stark}} = -\sum_n \frac{|\langle\psi_s|\boldsymbol{dF}|\psi_n\rangle|^2}{E_n - E_s}. \tag{6.77}$$

While a state-dependent calculation of the polarizabilities of the vibrational states in the ground state of the hydrogen molecule has been computed [46, 286, 287], there are no current reports on polarizabilities of electronically excited states in H_2. Therefore, as a first approximation the vibrational-state resolved polarizabilities of the ground state are rescaled with a constant factor for all D states, such that the AC-Stark caused phase shift reproduces the order of magnitude of the experimentally retrieved NIR-induced phase shift, see Fig. 6.22. The values for the retrieved state-dependent polarizabilities, i.e. the rescaled ground-state polarizabilities by a factor of 4, are listed in table 6.2 in atomic units. The conversion factor from atomic to SI units follows the relation: 1 a.u. of polarizability $\approx 1.648\,78 \times 10^{-41}\,\mathrm{F}\cdot\mathrm{m}^2$.

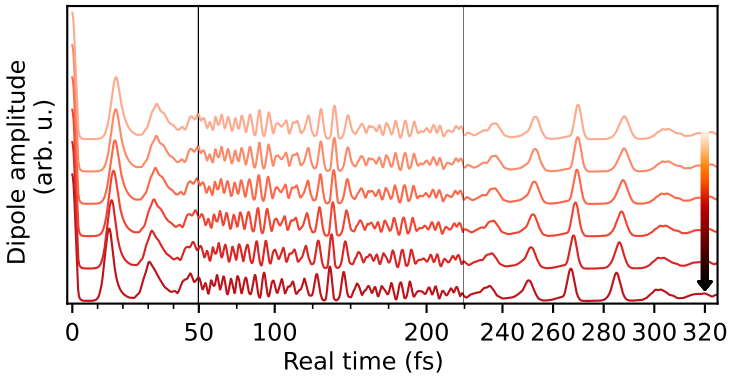

Figure 6.23: Calculated time-dependent dipole according to the control model with NIR-induced phase shift for each state in the wave packet due to the state-resolved AC Stark shift. For better visibility the individual lines are ordered from lower intensity at the top to higher intensity at the bottom. The intensities are the same as for the calculation presented in Fig. 6.18.

To illustrate the effect of the state-resolved AC Stark shift on the time-dependent dipole, the wave packet evolution is computed with the instantaneous time-dependent energy in the time-evolution operator for each state modified according to its dynamical Stark shift. The modified dipole as a function of NIR intensity is shown in Fig. 6.23. The revival of the computed dipoles indeed shifts to earlier times, however not in multiples of the classical revival time, but continuously. Additionally, a decrease of the classical revival time is observed at the beginning of the dipole due to the additional accumulated phase. The control model with state-resolved NIR-induced AC Stark shift, manages to reproduce an occurrence of the revival time towards earlier times, as well as change in the relative heights of the peaks in the revival region. The comparison of the phase-induced shifts to the experimentally retrieved shifts sheds a first light on the values for the state-dependent polarizabilities for the vibrational levels in the D electronically excited state.

6.5 Brief chapter summary and outlook

This chapter introduced a method for visualisation of vibrational wave-packet dynamics in a neutral molecular system, in particular in an excited state of the H_2 molecule. Access to the wave-packet dynamics is gained through reconstruction of the time-dependent dipole response of the wave packet to the quasistationary ground state, which acts as a probe to the dynamically evolving wave packet at every time step. The key observable in the wave-packet dynamics is the vibrational revival. The wave-packet visualisation method, applicable also in the case of additional laser interaction of the wave packet after its initial excitation, is further applied to demonstrate experimentally measured molecular wave-packet reshaping under the influence of a strong and short NIR laser field. Even if interacting with

the system only briefly and for a short time after the birth of the wave packet, the NIR field affects its subsequent time evolution reaching at least until the first revival time. The presented results show that by tuning the NIR intensity one can influence the wave-packet rephasing time through the accumulation of a state-resolved NIR induced phase shift, possibly attributed to the AC Stark shift. These results thus also demonstrate a novel way to access dynamic polarizabilities in ultrashort laser pulses to state-resolved control of excited-state molecular dynamics. While a wave-packet creation pulse and a control strong-field pulse are required, in the discussed scheme most notably no probe pulse is needed. Additional wavelength control of the intense fields, or even complex-shaped (e.g., chirped) laser pulses could create almost arbitrary sets of wave-packet coefficients and enhanced controllability of internuclear wave packets up to the fastest (hydrogen) oscillations, also in complex (organic) molecules. Thus, one can use intense laser fields as flexible control knobs to coherently steer the recovery of vibrational wave packets on electronically excited potential energy surfaces to critical points along a reaction coordinate (e.g., conical intersections), and with this initiating a chemical reaction at a desired later time becomes possible. The boundaries of the possibility to track coherent nuclear molecular movement in an electronically excited state and even steer it in a desired direction through laser control additionally could help find a regime where electronic and nuclear degrees of freedom are not anymore decoupled and thus the Born-Oppenheimer approximation starts to break.

7 CONCLUSION

In the last decades novel light sources for the production of ever shorter and more intense laser pulses in different photon energy ranges have led to the booming evolution of femtochemistry, ultrafast physics and attosecond science. Those very closely related fields studying fundamental light-matter interactions in all kinds of systems concentrate on different time scales, but are all united by the idea of understanding the (time-dependent) evolution of the investigated systems and using the gained knowledge to control it in a desired way by laser radiation. Typically, in all those three fields, pump–probe experimental schemes are realised, where a pump pulse initiates (non-trivial) dynamics in a system, and another probe pulse tracks the dynamics at different times or, in general, introduces new dynamics in the system. A variety of different detection techniques have evolved since the emergence of femtochemistry and attosecond science allowing to study the evolution of quantum systems after and during light–matter interaction processes. Two of those techniques, complementary in their approach, have been utilised for the presented studies of two-electron systems in their excited state under the influence of intense laser fields, namely coincidence photoelectron-photoion spectroscopy, as well as XUV time-delay absorption spectroscopy, allowing to access, on the one side, bound-free state transitions, and on the other side, bound-bound transitions.

The first experimental study, motivated by a prior theoretical investigation of the role of the initial state in the ionization process, explores ionization out of specifically prepared doubly excited states in the helium atom. Here, in a first step, doubly excited states in helium were selectively populated by free-electron laser narrowband XUV radiation and either subsequently or directly ionization out of those states was induced. Aiming to discover the dominating ionization pathways, single and double ionization processes were discussed, also for the strong background XUV-only ionization mechanisms at play. The most prominent examples, for which also photelectron and recoil-ion momentum distributions were detected, include multi-photon above threshold ionization out of different doubly excited states and the ionization process in the laser-dressed continuum, to mention but a few. The investigation of double-ionization pathways complemented previous experimental and theoretical studies of sequential and non-sequential double ionization in the helium atom, while also finding new ionization IR-induced double-ionization processes through shake-up ionization as well as directly out of the doubly excited states. While the initial data analysis allows to point out those pathways, future

data evaluation may bring further insight into the role of electron correlation for the double ionization process through investigation of, for example, directionality and energy-sharing of the correlated electrons leaving the atom. Additionally, the concept of selective preparation of initial states can be extended to any system of interest to study fundamental light–matter interaction not only starting from a ground state in a system, but from an excited, thus correlated state as well.

While the aim of the first study was to investigate light–matter interaction, ideally out of a single state, in the second presented experiment collective wave-packet dynamics of a group of states was studied. Here, for the benchmark two-electron H_2 system a method for visualisation of vibrational wave-packet dynamics in the neutral molecule was introduced. Access to the wave-packet evolution, in particular to the wave packet revival, was gained through extension of the already established technique for reconstruction of the time-dependent dipole response to the molecular case. For this, the quasistationary molecular ground state acts as an intrinsic self-probe of the dynamically evolving wave packet. Provided that the ground state of the system remains intact also for a subsequent interaction, addressing only the excited wave packet, the wave-packet visualisation method remains applicable also if an additional laser interaction takes place. With this prerequisite, molecular wave-packet reshaping under the influence of a strong and short NIR laser field was demonstrated in the detection of time-shifts of the wave-packet revival for different NIR intensities. In an impulsive scheme, the NIR laser pulse could be understood to introduce state-resolved phase shifts of the involved wave-packet states and through this affect the rephasing time in the system. Attributing the phase shifts to the strong-field introduced AC Stark shift, their state-resolved extraction demonstrated a novel way to access dynamic polarizabilities in ultrashort laser pulses. Extending the presented pump-control scheme with the implementation of light fields with for example exotic spectral-phase properties can allow arbitrary phase changes in wave packets of quantum systems, both atomic and molecular, and with this non-trivial time-shifts or possibly even time-jumps in the collective dynamics of the studied system.

In conclusion, the results of both experimental studies of light–matter interaction out of excited states in atoms, as well as molecules, demonstrate the importance to look into light–matter interaction not only starting from a well-defined stable atomic or molecular ground state, but to consider also correlated multi-electron states under the influence of strong and short laser fields.

APPENDIX A: ATOMIC UNITS

Atomic units are a system of natural units used in the context of atomic and molecular physics, as well as in femtochemistry, ultrafast physics and attosecond science. In this thesis both SI units as well as atomic units (a u or a.u.) are used and the following short overview provides the necessary conversion factors between the different unit scales to 4 digits of precision.

Defining constants, all set to unity:

Constant	**Symbol**	**SI value of one atomic unit** 1 a u
elementary charge	e	$1.602 \times 10^{-18}\,\mathrm{C}$
reduced Planck constant	$\hbar$	$1.055\,\mathrm{J\,s}$
electron rest mass	m_e	$9.109 \times 10^{-13}\,\mathrm{kg}$
Coulomb constant	k_e	$8.988 \times 10^{9}\,\mathrm{kg\,m^3\,s^{-4}A^{-2}}$

Important quantities in atomic unit:

Atomic unit of	**Symbol**	**SI value of one atomic unit** 1 a u
length (Bohr radius)	a_0	$5.292 \times 10^{-11}\,\mathrm{m}$
time	$\hbar/E_\mathrm{h}$	$2.419 \times 10^{-17}\,\mathrm{s} = 24.19\,\mathrm{as}$
velocity	$a_0 E_\mathrm{h}/\hbar = \alpha c$	$2.188 \times 10^{6}\,\mathrm{m/s}$
momentum	$\hbar/a_0$	$1.993 \times 10^{-24}\,\mathrm{kg\,m\,s^{-1}}$
energy (hartree)	E_h	$4.360 \times 10^{-18}\,\mathrm{J} = 27.21\,\mathrm{eV}$
electric field	$E_\mathrm{h}/(e a_0^2)$	$5.142 \times 10^{11}\,\mathrm{V/m}$

Bibliography

[1] G.D. Borisova, P.B. Belda, S. Hu, P. Birk, V. Stooß, M. Hartmann, D. Fan, R. Moshammer, A. Saenz, C. Ott and T. Pfeifer, *Laser control of an excited-state vibrational wave packet in neutral H_2*, 2023. 10.48550/ARXIV.2301.03908.

[2] G.D. Borisova, V. Stooß, A. Dingeldey, A. Kaldun, T. Ding, P. Birk, M. Hartmann, T. Heldt, C. Ott and T. Pfeifer, *Strong-field-induced single and double ionization dynamics from single and double excitations in a two-electron atom*, *Journal of Physics Communications* **4** (2020) 055012.

[3] V. Stooß, M. Hartmann, P. Birk, G.D. Borisova, T. Ding, A. Blättermann, C. Ott and T. Pfeifer, *XUV-beamline for attosecond transient absorption measurements featuring a broadband common beam-path time-delay unit and in situ reference spectrometer for high stability and sensitivity*, *Review of Scientific Instruments* **90** (2019) 053108.

[4] T. Heldt, J. Dubois, P. Birk, G.D. Borisova, G.M. Lando, C. Ott and T. Pfeifer, *Attosecond real-time observation of recolliding electron trajectories in helium at low laser intensities*, *Phys. Rev. Lett.* **130** (2023) 183201.

[5] M. Straub, T. Ding, M. Rebholz, G.D. Borisova, A. Magunia, H. Lindenblatt, S. Meister, F. Trost, Y. Wang, S. Palutke, M. Braune, S. Düsterer, R. Treusch, C.H. Greene, R. Moshammer, T. Pfeifer and C. Ott, *Differential measurement of electron ejection after two-photon two-electron excitation of helium*, *Phys. Rev. Lett.* **129** (2022) 183204.

[6] M. Hartmann, L. Hutcheson, G.D. Borisova, P. Birk, S. Hu, A.C. Brown, H.W. van der Hart, C. Ott and T. Pfeifer, *Core-resonance line-shape analysis of atoms undergoing strong-field ionization*, *Journal of Physics B: Atomic, Molecular and Optical Physics* **55** (2022) 245601.

[7] M. Rebholz, T. Ding, L. Aufleger, M. Hartmann, K. Meyer, V. Stooß, A. Magunia, D. Wachs, P. Birk, Y. Mi, G.D. Borisova, C. da Costa Castanheira, P. Rupprecht, M. Magrakvelidze, U. Thumm, S. Roling, M. Butz, H. Zacharias, S. Düsterer, R. Treusch, G. Brenner, C. Ott and T. Pfeifer, *XUV-initiated dissociation dynamics of molecular oxygen (O_2)*, *The Journal of Physical Chemistry A* **125** (2021) 10138.

[8] M. Rebholz, T. Ding, V. Despré, L. Aufleger, M. Hartmann, K. Meyer, V. Stooß, A. Magunia, D. Wachs, P. Birk, Y. Mi, G.D. Borisova, C.d.C. Castanheira, P. Rupprecht, G. Schmid, K. Schnorr, C.D. Schröter, R. Moshammer, Z.-H. Loh,

A.R. Attar, S.R. Leone, T. Gaumnitz, H.J. Wörner, S. Roling, M. Butz, H. Zacharias, S. Düsterer, R. Treusch, G. Brenner, J. Vester, A.I. Kuleff, C. Ott and T. Pfeifer, *All-XUV pump-probe transient absorption spectroscopy of the structural molecular dynamics of di-iodomethane*, *Phys. Rev. X* **11** (2021) 031001.

[9] T. Ding, M. Rebholz, L. Aufleger, M. Hartmann, V. Stooß, A. Magunia, P. Birk, G.D. Borisova, D. Wachs, C. da Costa Castanheira, P. Rupprecht, Y. Mi, A.R. Attar, T. Gaumnitz, Z.-H. Loh, S. Roling, M. Butz, H. Zacharias, S. Düsterer, R. Treusch, A. Eislage, S.M. Cavaletto, C. Ott and T. Pfeifer, *Measuring the frequency chirp of extreme-ultraviolet free-electron laser pulses by transient absorption spectroscopy*, *Nature Communications* **12** (2021) 643.

[10] T. Ding, M. Rebholz, L. Aufleger, M. Hartmann, V. Stooß, A. Magunia, P. Birk, G.D. Borisova, C. da Costa Castanheira, P. Rupprecht, Y. Mi, T. Gaumnitz, Z.-H. Loh, S. Roling, M. Butz, H. Zacharias, S. Düsterer, R. Treusch, C. Ott and T. Pfeifer, *XUV pump–XUV probe transient absorption spectroscopy at FELs*, *Faraday Discuss.* **228** (2021) 519.

[11] V. Stooß, P. Birk, A. Blättermann, M. Hartmann, G.D. Borisova, C. Ott and T. Pfeifer, *Strong-field-gated buildup of a rydberg series*, *Phys. Rev. Res.* **2** (2020) 032041.

[12] P. Birk, V. Stooß, M. Hartmann, G.D. Borisova, A. Blättermann, T. Heldt, K. Bartschat, C. Ott and T. Pfeifer, *Attosecond transient absorption of a continuum threshold*, *Journal of Physics B: Atomic, Molecular and Optical Physics* **53** (2020) 124002.

[13] C. Ott, L. Aufleger, T. Ding, M. Rebholz, A. Magunia, M. Hartmann, V. Stooß, D. Wachs, P. Birk, G.D. Borisova, K. Meyer, P. Rupprecht, C. da Costa Castanheira, R. Moshammer, A.R. Attar, T. Gaumnitz, Z.-H. Loh, S. Düsterer, R. Treusch, J. Ullrich, Y. Jiang, M. Meyer, P. Lambropoulos and T. Pfeifer, *Strong-field extreme-ultraviolet dressing of atomic double excitation*, *Phys. Rev. Lett.* **123** (2019) 163201.

[14] T. Ding, M. Rebholz, L. Aufleger, M. Hartmann, K. Meyer, V. Stooß, A. Magunia, D. Wachs, P. Birk, Y. Mi, G.D. Borisova, C.D.C. Castanheira, P. Rupprecht, Z.H. Loh, A.R. Attar, T. Gaumnitz, S. Roling, M. Butz, H. Zacharias, S. Düsterer, R. Treusch, S.M. Cavaletto, C. Ott and T. Pfeifer, *Nonlinear coherence effects in transient-absorption ion spectroscopy with stochastic extreme-ultraviolet free-electron laser pulses*, *Physical Review Letters* **123** (2019) 103001.

[15] "Oxford learner's dictionary." https://www.oxfordlearnersdictionaries.com/definition/english/physics.

[16] "Oxford learner's dictionary." https://www.oxfordlearnersdictionaries.com/definition/english/matter.

[17] A.L. Schawlow and C.H. Townes, *Infrared and optical masers*, *Phys. Rev.* **112** (1958) 1940.

[18] T.H. Maiman, *Stimulated Optical Radiation in Ruby*, *Nature* **187** (1960) 493.

[19] A. Bauch and H.R. Telle, *Frequency standards and frequency measurement*, *Reports on Progress in Physics* **65** (2002) 789.

[20] L.E. Hargrove, R.L. Fork and M.A. Pollack, *Locking of He-Ne Laser Modes Induced by Synchronous Intracavity Modulation*, *Applied Physics Letters* **5** (1964) 4.

[21] A.J. DeMaria, D.A. Stetser and H. Heynau, *SELF MODE-LOCKING OF LASERS WITH SATURABLE ABSORBERS*, *Applied Physics Letters* **8** (1966) 174.

[22] D.E. Spence, P.N. Kean and W. Sibbett, *60-fsec pulse generation from a self-mode-locked ti:sapphire laser*, *Opt. Lett.* **16** (1991) 42.

[23] U. Keller, G.W. 'tHooft, W.H. Knox and J.E. Cunningham, *Femtosecond pulses from a continuously self-starting passively mode-locked ti:sapphire laser*, *Opt. Lett.* **16** (1991) 1022.

[24] A. Wirth, M.T. Hassan, I. Grguraš, J. Gagnon, A. Moulet, T.T. Luu, S. Pabst, R. Santra, Z.A. Alahmed, A.M. Azzeer, V.S. Yakovlev, V. Pervak, F. Krausz and E. Goulielmakis, *Synthesized light transients*, *Science* **334** (2011) 195.

[25] A.H. Zewail, *Laser femtochemistry*, *Science* **242** (1988) 1645.

[26] A.H. Zewail, *Femtochemistry: Atomic-scale dynamics of the chemical bond*, *The Journal of Physical Chemistry A* **104** (2000) 5660.

[27] A. McPherson, G. Gibson, H. Jara, U. Johann, T.S. Luk, I.A. McIntyre, K. Boyer and C.K. Rhodes, *Studies of multiphoton production of vacuum-ultraviolet radiation in the rare gases*, *J. Opt. Soc. Am. B* **4** (1987) 595.

[28] X.F. Li, A. L'Huillier, M. Ferray, L.A. Lompré and G. Mainfray, *Multiple-harmonic generation in rare gases at high laser intensity*, *Phys. Rev. A* **39** (1989) 5751.

[29] M. Ferray, A. L'Huillier, X.F. Li, L.A. Lompre, G. Mainfray and C. Manus, *Multiple-harmonic conversion of 1064 nm radiation in rare gases*, *Journal of Physics B: Atomic, Molecular and Optical Physics* **21** (1988) L31.

[30] H. Muller, *Reconstruction of attosecond harmonic beating by interference of two-photon transitions*, *Applied Physics B* **74** (2002) s17.

[31] R. Kienberger, E. Goulielmakis, M. Uiberacker, A. Baltuska, V. Yakovlev, F. Bammer, A. Scrinzi, T. Westerwalbesloh, U. Kleineberg, U. Heinzmann, M. Drescher and F. Krausz, *Atomic transient recorder*, *Nature* **427** (2004) 817.

[32] F. Krausz and M. Ivanov, *Attosecond physics*, *Rev. Mod. Phys.* **81** (2009) 163.

[33] B.E.A. Saleh and M. Teich, *Fundamentals of photonics*, in *Fundamentals of Photonics*, pp. 41–79, John Wiley & Sons, Ltd (1991), DOI.

[34] B.H. Bransden and C.J. Joachain, *Physics of atoms and molecules*, Pearson Education Limited (2003).

[35] I.V. Hertel and C.-P. Schulz, *Atoms, Molecules and Optical Physics 1, Atoms and Spectroscopy*, Springer-Verlag Berlin Heidelberg (2015).

[36] J.-C. Diels and W. Rudolph, *Ultrashort Laser Pulse Phenomena*, Academic Press, 2nd ed. (2006).

[37] P. Agostini, F. Fabre, G. Mainfray, G. Petite and N.K. Rahman, *Free-free transitions following six-photon ionization of xenon atoms*, *Phys. Rev. Lett.* **42** (1979) 1127.

[38] Y. Gontier, M. Poirier and M. Trahin, *Multiphoton absorptions above the ionisation threshold*, *Journal of Physics B: Atomic and Molecular Physics* **13** (1980) 1381.

[39] G. Petite, P. Agostini and H.G. Muller, *Intensity dependence of non-perturbative above-threshold ionisation spectra: experimental study*, *Journal of Physics B: Atomic, Molecular and Optical Physics* **21** (1988) 4097 .

[40] A.M. Perelomov, V.S. Popov and M.V. Terent'ev, *Ionization of Atoms in an Alternating Electric Field*, *Soviet Journal of Experimental and Theoretical Physics* **23** (1966) 924.

[41] M.V. Ammosov, N.B. Delone and V.P. Krainov, *Tunnel ionization of complex atoms and of atomic ions in an alternating electromagnetic field*, *Sov. Phys. JETP* **64** (1986) 1191.

[42] S. Augst, D.D. Meyerhofer, D. Strickland and S.L. Chin, *Laser ionization of noble gases by Coulomb-barrier suppression*, *Journal of the Optical Society of America B Optical Physics* **8** (1991) 858.

[43] M. Ammosov and N. Delone, *Tunneling ionization and above-barrier decay of atoms under the action of pulsed laser radiation*, *Laser Physics* **7** (1997) 79.

[44] L.V. Keldysh, *Ionization in the field of a strong electromagnetic wave*, *Sov. Phys. JETP* **20** (1965) 1307.

[45] R.R. Freeman and P.H. Bucksbaum, *Investigations of above-threshold ionization using subpicosecond laser pulses*, *Journal of Physics B: Atomic, Molecular and Optical Physics* **24** (1991) 325.

[46] J. Rychlewski, *An accurate calculation of the polarizability of the hydrogen molecule and its dependence on rotation, vibration and isotopic substitution*, *Molecular Physics* **41** (1980) 833.

[47] A. L'Huillier, L.A. Lompre, G. Mainfray and C. Manus, *Multiply charged ions formed by multiphoton absorption processes in the continuum*, *Phys. Rev. Lett.* **48** (1982) 1814.

[48] B. Walker, B. Sheehy, L.F. DiMauro, P. Agostini, K.J. Schafer and K.C. Kulander, *Precision measurement of strong field double ionization of helium*, *Phys. Rev. Lett.* **73** (1994) 1227.

[49] K.J. Schafer, B. Yang, L.F. DiMauro and K.C. Kulander, *Above threshold ionization beyond the high harmonic cutoff*, *Phys. Rev. Lett.* **70** (1993) 1599.

[50] P.B. Corkum, *Plasma perspective on strong field multiphoton ionization*, *Phys. Rev. Lett.* **71** (1993) 1994.

[51] G. Paulus, F. Grasbon, H. Walther, P. Villoresi, M. Nisoli, S. Stagira, E. Priori and S. Silvestri, *Absolute-phase phenomena in photoionization with few-cycle laser pulses*, *Nature* **414** (2001) 182.

[52] A.M. Sayler, T. Rathje, W. Müller, C. Kürbis, K. Rühle, G. Stibenz and G.G. Paulus, *Real-time pulse length measurement of few-cycle laser pulses using above-threshold ionization*, *Opt. Express* **19** (2011) 4464.

[53] T. Nubbemeyer, K. Gorling, A. Saenz, U. Eichmann and W. Sandner, *Strong-field tunneling without ionization*, *Phys. Rev. Lett.* **101** (2008) 233001.

[54] "NIST Atomic Spectra Database Levels Form." `http://physics.nist.gov/PhysRefData/ASD/levels_form.html`.

[55] A. Burgers, D. Wintgen and J.M. Rost, *Highly doubly excited S states of the helium atom*, *Journal of Physics B: Atomic, Molecular and Optical Physics* **28** (1995) 3163.

[56] M. Domke, K. Schulz, G. Remmers, G. Kaindl and D. Wintgen, *High-resolution study of $^1P^o$ double-excitation states in helium.*, *Phys. Rev. A* **53** (1996) 1424.

[57] K. Schulz, G. Kaindl, M. Domke, J.D. Bozek, P.A. Heimann, A.S. Schlachter and J.M. Rost, *Observation of New Rydberg Series and Resonances in Doubly Excited Helium at Ultrahigh Resolution*, *Phys. Rev. Lett.* **77** (1996) 3086.

[58] R.P. Madden and K. Codling, *New Autoionizing Atomic Energy Levels in He, Ne, and Ar*, *Phys. Rev. Lett.* **10** (1963) 516.

[59] J.W. Cooper, U. Fano and F. Prats, *Classification of two-electron excitation levels of helium*, *Phys. Rev. Lett.* **10** (1963) 518.

[60] D.R. Herrick and O. Sinanoğlu, *Comparison of doubly-excited helium energy levels, isoelectronic series, autoionization lifetimes, and group-theoretical configuration-mixing predictions with large-configuration-interaction calculations and experimental spectra*, *Phys. Rev. A* **11** (1975) 97.

[61] C.D. Lin, *Classification of doubly excited states of two-electron atoms*, *Phys. Rev. Lett.* **51** (1983) 1348.

[62] C. Lin, *Hyperspherical coordinate approach to atomic and other coulombic three-body systems*, *Physics Reports* **257** (1995) 1.

[63] G. Tanner, K. Richter and J.-M. Rost, *The theory of two-electron atoms: between ground state and complete fragmentation*, *Rev. Mod. Phys.* **72** (2000) 497.

[64] U. Fano, *Effects of Configuration Interaction on Intensities and Phase Shifts*, *Physical Review* **124** (1961) 1866.

[65] M. Born and R. Oppenheimer, *Zur Quantentheorie der Molekeln*, *Annalen der Physik* **389** 457.

[66] G. Dieke, *The molecular spectrum of hydrogen and its isotopes*, *Journal of Molecular Spectroscopy* **2** (1958) 494.

[67] T. Sharp, *Potential-energy curves for molecular hydrogen and its ions*, *Atomic Data and Nuclear Data Tables* **2** (1970) 119.

[68] I.V. Hertel and C.-P. Schulz, *Atoms, Molecules and Optical Physics 2, Molecules and Photons - Spectroscopy and Collisions*, Springer-Verlag Berlin Heidelberg (2015).

[69] J.J. Hopfield, *Absorption and emission spectra in the region λ600 – 1100*, *Phys. Rev.* **35** (1930) 1133.

[70] H. Beutler, A. Deubner and H.O. Jünger, *Über das Absorptionsspektrum des Wasserstoffs. II. Die Einordnung des Zustands d ins Thermschema des Wasserstoffs, nach Aufnahmen an H_2 und D_2*, *Zeitschrift für Physik* **98** (1935) 181.

[71] M. Glass-Maujean, J. Breton and P. Guyon, *A Fano-profile study of the predissociation of the* $3p\pi D^1\Pi_u^+$ *state of* H_2, *Chemical Physics Letters* **63** (1979) 591.

[72] G.D. Dickenson, T.I. Ivanov, M. Roudjane, N. de Oliveira, D. Joyeux, L. Nahon, W.-U.L. Tchang-Brillet, M. Glass-Maujean, I. Haar, A. Ehresmann and W. Ubachs, *Synchrotron vacuum ultraviolet radiation studies of the $D^1\Pi_u$ state of H_2*, *The Journal of Chemical Physics* **133** (2010) 144317.

[73] J.Z. Mezei, I.F. Schneider, M. Glass-Maujean and C. Jungen, *Resonances in photoabsorption: Predissociation line shapes in the* $3p\pi D^1\Pi_u^+ \leftarrow X^1\Sigma_g^+$ *system in* H_2, *The Journal of Chemical Physics* **141** (2014) 064305.

[74] C. Ott, *Attosecond multidimensional interferometry of single and two correlated electrons in atoms*, Dissertation, Ruperto-Carola-University of Heidelberg, Germany, 2012.

[75] V. Stooß, *Strong-Field Spectroscopy: From Absorption to Time-Resolved Dynamics in Strong Fields*, Dissertation, Ruperto-Carola-University of Heidelberg, Germany, 2018.

[76] J.-C. Diels and W. Rudolph, *Ultrashort laser pulse phenomena*, Elsevier (2006).

[77] T. Lang, S. Alisauskas, U. Große-Wortmann, T. Hülsenbusch, B. Manschwetus, C. Mohr, J. Müller, F. Peters, N. Schirmel, S. Schulz, A. Swiderski, J. Zheng and I. Hartl, *Versatile opcpa pump-probe laser system for the flash2 xuv fel beamline at desy*, in *2019 Conference on Lasers and Electro-Optics Europe & European Quantum Electronics Conference (CLEO/Europe-EQEC)*, pp. 1–1, 2019, DOI.

[78] H. Fattahi, H.G. Barros, M. Gorjan, T. Nubbemeyer, B. Alsaif, C.Y. Teisset, M. Schultze, S. Prinz, M. Haefner, M. Ueffing, A. Alismail, L. Vámos, A. Schwarz, O. Pronin, J. Brons, X.T. Geng, G. Arisholm, M. Ciappina, V.S. Yakovlev, D.-E. Kim, A.M. Azzeer, N. Karpowicz, D. Sutter, Z. Major, T. Metzger and F. Krausz, *Third-generation femtosecond technology*, *Optica* **1** (2014) 45.

[79] P. Russbueldt, T. Mans, G. Rotarius, J. Weitenberg, H. Hoffmann and R. Poprawe, *400 W Yb:YAG Innoslab fs-amplifier*, *Opt. Express* **17** (2009) 12230.

[80] S. Meister, H. Lindenblatt, F. Trost, K. Schnorr, S. Augustin, M. Braune, R. Treusch, T. Pfeifer and R. Moshammer, *Atomic, molecular and cluster science with the reaction microscope endstation at FLASH2*, *Applied Sciences* **10** (2020) .

[81] D. Strickland and G. Mourou, *Compression of amplified chirped optical pulses*, *Optics Communications* **56** (1985) 219.

[82] H. Telle, G. Steinmeyer, A. Dunlop, J. Stenger, D. Sutter and U. Keller, *Carrier-envelope offset phase control: A novel concept for absolute optical frequency measurement and ultrashort pulse generation*, *Applied Physics B* **69** (1999) 327.

[83] F. Lücking, A. Assion, A. Apolonski, F. Krausz and G. Steinmeyer, *Long-term carrier-envelope-phase-stable few-cycle pulses by use of the feed-forward method*, *Optics Letters* **37** (2012) 2076.

[84] M. Nisoli, S. De Silvestri and O. Svelto, *Generation of high energy 10 fs pulses by a new pulse compression technique*, *Applied Physics Letters* **68** (1996) 2793.

[85] M. Nisoli, S.D. Silvestri, O. Svelto, R. Szipöcs, K. Ferencz, C. Spielmann, S. Sartania and F. Krausz, *Compression of high-energy laser pulses below 5 fs*, *Opt. Lett.* **22** (1997) 522.

[86] P. Birk, *The Dipole Response of an Ionization Threshold within Ultrashort and Strong Fields*, Dissertation, Ruperto-Carola-University of Heidelberg, Germany, 2020.

[87] M. Hartmann, *Attosecond dynamics of strong-field generated ions*, Dissertation, Ruperto-Carola-University of Heidelberg, Germany, 2021.

[88] M. Miranda, T. Fordell, C. Arnold, A. L'Huillier and H. Crespo, *Simultaneous compression and characterization of ultrashort laser pulses using chirped mirrors and glass wedges*, *Opt. Express* **20** (2012) 688.

[89] M. Miranda, C.L. Arnold, T. Fordell, F. Silva, B. Alonso, R. Weigand, A. L'Huillier and H. Crespo, *Characterization of broadband few-cycle laser pulses with the d-scan technique*, *Opt. Express* **20** (2012) 18732.

[90] D.A.G. Deacon, L.R. Elias, J.M.J. Madey, G.J. Ramian, H.A. Schwettman and T.I. Smith, *First operation of a free-electron laser*, *Phys. Rev. Lett.* **38** (1977) 892.

[91] V. Ayvazyan *et al.*, *First operation of a free-electron laser generating GW power radiation at 32 nm wavelength*, *The European Physical Journal D* **37** (2006) 297.

[92] E. Allaria *et al.*, *Highly coherent and stable pulses from the FERMI seeded free-electron laser in the extreme ultraviolet*, *Nature Photonics* **6** (2012) 699.

[93] T. Ishikawa *et al.*, *A compact X-ray free-electron laser emitting in the sub-ångström region*, *Nature Photonics* **6** (2012) 540.

[94] C.J. Milne *et al.*, *Swissfel: The swiss x-ray free electron laser*, *Applied Sciences* **7** (2017) .

[95] P. Emma, R. Akre, J. Arthur, R. Bionta, C. Bostedt, J. Bozek, A. Brachmann, P. Bucksbaum, R. Coffee, F.J. Decker, Y. Ding, D. Dowell, S. Edstrom, A. Fisher, J. Frisch, S. Gilevich, J. Hastings, G. Hays, P. Hering, Z. Huang, R. Iverson, H. Loos, M. Messerschmidt, A. Miahnahri, S. Moeller, H.D. Nuhn, G. Pile, D. Ratner, J. Rzepiela, D. Schultz, T. Smith, P. Stefan, H. Tompkins, J. Turner, J. Welch, W. White, J. Wu, G. Yocky and J. Galayda, *First lasing and operation of an ångstrom-wavelength free-electron laser*, *Nature Photonics* **4** (2010) 641.

[96] W. Decking *et al.*, *A MHz-repetition-rate hard X-ray free-electron laser driven by a superconducting linear accelerator*, *Nature Photonics* **14** (2020) 391.

[97] H.-S. Kang *et al.*, *Hard X-ray free-electron laser with femtosecond-scale timing jitter*, *Nature Photonics* **11** (2017) 708.

[98] T. Ding, *Quantum dynamics in weak and strong fields measured by XUV nonlinear spectroscopy*, Dissertation, Ruperto-Carola-University of Heidelberg, Germany, 2018.

[99] E.A. Seddon, J.A. Clarke, D.J. Dunning, C. Masciovecchio, C.J. Milne, F. Parmigiani, D. Rugg, J.C.H. Spence, N.R. Thompson, K. Ueda, S.M. Vinko, J.S. Wark and W. Wurth, *Short-wavelength free-electron laser sources and science: a review*, *Reports on Progress in Physics* **80** (2017) 115901.

[100] J.M.J. Madey, *Stimulated Emission of Bremsstrahlung in a Periodic Magnetic Field*, *Journal of Applied Physics* **42** (2003) 1906.

[101] B. Faatz *et al.*, *Simultaneous operation of two soft x-ray free-electron lasers driven by one linear accelerator*, *New Journal of Physics* **18** (2016) 062002.

[102] A.M. Kondratenko and E.L. Saldin, *Generating of coherent radiation by a relativistic electron beam in an ondulator*, *Part. Accel.* **10** (1980) 207.

[103] R. Bonifacio, C. Pellegrini and L.M. Narducci, *Collective instabilities and high-gain regime in a free electron laser*, *Optics Communications* **50** (1984) 373.

[104] E. Saldin, E. Schneidmiller and M. Yurkov, *The physics of free electron lasers. an introduction*, *Physics Reports* **260** (1995) 187.

[105] U. Frühling, M. Wieland, M. Gensch, T. Gebert, B. Schütte, M. Krikunova, R. Kalms, F. Budzyn, O. Grimm, J. Rossbach, E. Plönjes and M. Drescher, *Single-shot terahertz-field-driven X-ray streak camera*, *Nature Photonics* **3** (2009) 523.

[106] T.A. Callcott, K.L. Tsang, C.H. Zhang, D.L. Ederer and E.T. Arakawa, *High-efficiency soft x-ray emission spectrometer for use with synchrotron radiation excitation*, *Review of Scientific Instruments* **57** (1986) 2680.

[107] C. Dallera, E. Puppin, G. Trezzi, N. Incorvaia, A. Fasana, L. Braicovich, N.B. Brookes and J.B. Goedkoop, *Soft X-ray Emission Spectroscopy at ESRF Beamline 26 Based on a Helical Undulator*, *Journal of Synchrotron Radiation* **3** (1996) 231.

[108] T. Tanikawa, A. Hage, M. Kuhlmann, J. Gonschior, S. Grunewald, E. Plönjes, S. Düsterer, G. Brenner, S. Dziarzhytski, M. Braune, M. Brachmanski, Z. Yin, F. Siewert, T. Dzelzainis, B. Dromey, M. Prandolini, F. Tavella, M. Zepf and B. Faatz, *First observation of SASE radiation using the compact wide-spectral-range XUV spectrometer at FLASH2*, *Nuclear Instruments and Methods in Physics Research Section A: Accelerators, Spectrometers, Detectors and Associated Equipment* **830** (2016) 170.

[109] S. Düsterer, P. Radcliffe, G. Geloni, U. Jastrow, M. Kuhlmann, E. Plönjes, K. Tiedtke, R. Treusch, J. Feldhaus, P. Nicolosi, L. Poletto, P. Yeates, H. Luna, J.T. Costello, P. Orr, D. Cubaynes and M. Meyer, *Spectroscopic characterization of vacuum ultraviolet free electron laser pulses*, *Opt. Lett.* **31** (2006) 1750.

[110] J. Rönsch-Schulenburg, B. Faatz, K. Honkavaara, M. Kuhlmann, S. Schreiber, R. Treusch and M. Vogt, *Experience with Multi-Beam and Multi-Beamline FEL-Operation*, *Journal of Physics: Conference Series* **874** (2017) 012023.

[111] P. Agostini and L.F. DiMauro, *The physics of attosecond light pulses*, *Reports on Progress in Physics* **67** (2004) 813.

[112] D. Attwood and A. Sakdinawat, *X-Rays and Extreme Ultraviolet Radiation: Principles and Applications*, Cambridge University Press, 2 ed. (2017).

[113] K.C. Kulander, K.J. Schafer and J.L. Krause, *Dynamics of Short-Pulse Excitation, Ionization and Harmonic Conversion*, in *Super-Intense Laser-Atom Physics III*, B. Piraux, A. L'Huillier and K. Rzazewski, eds., vol. 316, pp. 95–110, Springer, Boston, MA, 1993, https://doi.org/10.1007/978-1-4615-7963-$2_1$0.

[114] M. Lewenstein, P. Balcou, M.Y. Ivanov, A. L'Huillier and P.B. Corkum, *Theory of high-harmonic generation by low-frequency laser fields*, *Phys. Rev. A* **49** (1994) 2117.

[115] M. Protopapas, C.H. Keitel and P.L. Knight, *Atomic physics with super-high intensity lasers*, *Reports on Progress in Physics* **60** (1997) 389.

[116] K. Amini, J. Biegert, F. Calegari, A. Chacón, M.F. Ciappina, A. Dauphin, D.K. Efimov, C.F. de Morisson Faria, K. Giergiel, P. Gniewek, A.S. Landsman, M. Lesiuk, M. Mandrysz, A.S. Maxwell, R. Moszyński, L. Ortmann, J.A. Pérez-Hernández, A. Picón, E. Pisanty, J. Prauzner-Bechcicki, K. Sacha, N. Suárez, A. Zaïr, J. Zakrzewski and M. Lewenstein, *Symphony on strong field approximation*, *Reports on Progress in Physics* **82** (2019) 116001.

[117] M. Hentschel, R. Kienberger, C. Spielmann, G.A. Reider, N. Milosevic, T. Brabec, P. Corkum, U. Heinzmann, M. Drescher and F. Krausz, *Attosecond metrology*, *Nature* **414** (2001) 509.

[118] M.J. Abel, T. Pfeifer, P.M. Nagel, W. Boutu, M.J. Bell, C.P. Steiner, D.M. Neumark and S.R. Leone, *Isolated attosecond pulses from ionization gating of high-harmonic emission*, *Chemical Physics* **366** (2009) 9.

[119] G. Sansone, E. Benedetti, F. Calegari, C. Vozzi, L. Avaldi, R. Flammini, L. Poletto, P. Villoresi, C. Altucci, R. Velotta, S. Stagira, S.D. Silvestri and M. Nisoli, *Isolated single-cycle attosecond pulses*, *Science* **314** (2006) 443.

[120] I.J. Sola, E. Mével, L. Elouga, E. Constant, V. Strelkov, L. Poletto, P. Villoresi, E. Benedetti, J.-P. Caumes, S. Stagira, C. Vozzi, G. Sansone and M. Nisoli, *Controlling attosecond electron dynamics by phase-stabilized polarization gating*, *Nature Physics* **2** (2006) 319.

[121] M. Chini, K. Zhao and Z. Chang, *The generation, characterization and applications of broadband isolated attosecond pulses*, *Nature Photonics* **8** (2014) 178.

[122] H. Mashiko, S. Gilbertson, C. Li, S.D. Khan, M.M. Shakya, E. Moon and Z. Chang, *Double optical gating of high-order harmonic generation with carrier-envelope phase stabilized lasers*, *Phys. Rev. Lett.* **100** (2008) 103906.

[123] T.T. Luu, Z. Yin, A. Jain, T. Gaumnitz, Y. Pertot, J. Ma and H.J. Wörner, *Extreme–ultraviolet high–harmonic generation in liquids*, *Nature Communications* **9** (2018) 3723.

[124] T.T. Luu, M. Garg, S.Y. Kruchinin, A. Moulet, M.T. Hassan and E. Goulielmakis, *Extreme ultraviolet high-harmonic spectroscopy of solids*, *Nature* **521** (2015) 498.

[125] R. Moshammer, M. Unverzagt, W. Schmitt, J. Ullrich and H. Schmidt-Böcking, *A 4π recoil-ion electron momentum analyzer: a high-resolution "microscope" for the investigation of the dynamics of atomic, molecular and nuclear reactions*, *Nuclear Instruments and Methods in Physics Research Section B: Beam Interactions with Materials and Atoms* **108** (1996) 425.

[126] R. Dörner, V. Mergel, O. Jagutzki, L. Spielberger, J. Ullrich, R. Moshammer and H. Schmidt-Böcking, *Cold target recoil ion momentum spectroscopy: a 'momentum microscope' to view atomic collision dynamics*, *Physics Reports* **330** (2000) 95.

[127] J. Ullrich, R. Moshammer, A. Dorn, R. Dörner, L.P.H. Schmidt and H. Schmidt-Böcking, *Recoil-ion and electron momentum spectroscopy: reaction-microscopes*, *Reports on Progress in Physics* **66** (2003) 1463.

[128] K. Schnorr, *XUV Pump-Probe Experiments on Electron Rearrangement and Interatomic Coulombic Decay in Diatomic Molecules*, Dissertation, Ruperto-Carola-University of Heidelberg, Germany, 2014.

[129] G. Schmid, *Two-Color Pump-Probe Experiments on Small Quantum Systems at the Free-Electron Laser in Hamburg*, Dissertation, Ruperto-Carola-University of Heidelberg, Germany, 2018.

[130] G. Schmid, K. Schnorr, S. Augustin, S. Meister, H. Lindenblatt, F. Trost, Y. Liu, M. Braune, R. Treusch, C.D. Schröter, T. Pfeifer and R. Moshammer, *Reaction microscope endstation at FLASH2*, *Journal of Synchrotron Radiation* **26** (2019) 854.

[131] G. Scoles, *Atomic and Molecular Beam Methods: 1. Atomic and Molecular Beam Methods*, Oxford University Press (1988).

[132] W.C. Wiley and I.H. McLaren, *Time-of-Flight Mass Spectrometer with Improved Resolution*, *Review of Scientific Instruments* **26** (2004) 1150.

[133] O. Jagutzki, A. Cerezo, A. Czasch, R. Dorner, M. Hattas, M. Huang, V. Mergel, U. Spillmann, K. Ullmann-Pfleger, T. Weber, H. Schmidt-Bocking and G. Smith, *Multiple hit readout of a microchannel plate detector with a three-layer delay-line anode*, *IEEE Transactions on Nuclear Science* **49** (2002) 2477.

[134] J. Ladislas Wiza, *Microchannel plate detectors*, *Nuclear Instruments and Methods* **162** (1979) 587.

[135] S. Suzuki and T. Konno, *A computer simulation study on electron multiplication of parallel-plate electron multipliers*, *Review of Scientific Instruments* **64** (1993) 436.

[136] A.T.J.B. Eppink and D.H. Parker, *Velocity map imaging of ions and electrons using electrostatic lenses: Application in photoelectron and photofragment ion imaging of molecular oxygen*, *Review of Scientific Instruments* **68** (1997) 3477.

[137] D. Rolles, Z. Pešić, M. Perri, R. Bilodeau, G. Ackerman, B. Rude, A. Kilcoyne, J. Bozek and N. Berrah, *A velocity map imaging spectrometer for electron–ion and ion–ion coincidence experiments with synchrotron radiation*, *Nuclear Instruments and Methods in Physics Research Section B: Beam Interactions with Materials and Atoms* **261** (2007) 170.

[138] O. Jagutzki, V. Mergel, K. Ullmann-Pfleger, L. Spielberger, U. Spillmann, R. Dörner and H. Schmidt-Böcking, *A broad-application microchannel-plate detector system for advanced particle or photon detection tasks: large area imaging, precise multi-hit timing information and high detection rate*, *Nuclear Instruments and Methods in Physics Research Section A: Accelerators, Spectrometers, Detectors and Associated Equipment* **477** (2002) 244.

[139] M. Lampton, O. Siegmund and R. Raffanti, *Delay line anodes for microchannel-plate spectrometers*, *Review of Scientific Instruments* **58** (1987) 2298.

[140] S. Sobottka and M. Williams, *Delay line readout of microchannel plates*, *IEEE Transactions on Nuclear Science* **35** (1988) 348.

[141] T. Pflüger, *Electron Impact Ionization Studies of Small Rare Gas Clusters*, Dissertation, Ruperto-Carola-University of Heidelberg, Germany, 2012.

[142] *MACOR® Machinable Glass Ceramic For Industrial Applications*, Tech. Rep. , Corning Incorporated (2012).

[143] C. for X-Ray Optics (CXRO), "X-ray transmission of gases and solids." URL: https://henke.lbl.gov/optical_constants/, 2021.

[144] G.D. Borisova, *Theoretical and Experimental Studies of XUV Multielectron (Auto-)Ionization Dynamics in Helium and Molecular Hydrogen*, Master's thesis, Ruperto-Carola-University of Heidelberg, Germany, 2017.

[145] S. Hu, *Attosecond dynamics of dipole-coupled doubly excited states in helium*, Dissertation, Ruperto-Carola-University of Heidelberg, Germany, 2023.

[146] T. Kita, T. Harada, N. Nakano and H. Kuroda, *Mechanically ruled aberration-corrected concave gratings for a flat-field grazing-incidence spectrograph*, *Appl. Opt.* **22** (1983) 512.

[147] P. Rupprecht, L. Aufleger, S. Heinze, A. Magunia, T. Ding, M. Rebholz, S. Amberg, N. Mollov, F. Henrich, M.W. Haverkort, C. Ott and T. Pfeifer, *Laser control of electronic exchange interaction within a molecule*, *Phys. Rev. Lett.* **128** (2022) 153001.

[148] P.D. Rupprecht, *Ultrafast Laser Control of Molecular Quantum Dynamics from a Core-Electron Perspective*, Dissertation, Ruperto-Carola-University of Heidelberg, Germany, 2022.

[149] S.N. Pisharody and R.R. Jones, *Probing two-electron dynamics of an atom*, *Science* **303** (2004) 813.

[150] T. Morishita, S. Watanabe and C.D. Lin, *Attosecond light pulses for probing two-electron dynamics of helium in the time domain*, *Phys. Rev. Lett.* **98** (2007) 083003.

[151] J. Feist, S. Nagele, R. Pazourek, E. Persson, B.I. Schneider, L.A. Collins and J. Burgdörfer, *Nonsequential two-photon double ionization of helium*, *Phys. Rev. A* **77** (2008) 043420.

[152] Z.-H. Loh, C.H. Greene and S.R. Leone, *Femtosecond induced transparency and absorption in the extreme ultraviolet by coherent coupling of the He 2s2p (1Po) and $2p^2$ ($1S^e$) double excitation states with 800nm light*, *Chemical Physics* **350** (2008) 7.

[153] C. Ott, A. Kaldun, L. Argenti, P. Raith, K. Meyer, M. Laux, Y. Zhang, A. Blättermann, S. Hagstotz, T. Ding, R. Heck, J. Madroñero, F. Martín and T. Pfeifer, *Reconstruction and control of a time-dependent two-electron wave packet*, *Nature* **516** (2014) 374.

[154] V. Gruson, L. Barreau, A. Jiménez-Galán, F. Risoud, J. Caillat, A. Maquet, B. Carré, F. Lepetit, J.-F. Hergott, T. Ruchon, L. Argenti, R. Taïeb, F. Martín and P. Salières, *Attosecond dynamics through a fano resonance: Monitoring the birth of a photoelectron*, *Science* **354** (2016) 734.

[155] B. Bergues, M. Kübel, N.G. Johnson, B. Fischer, N. Camus, K.J. Betsch, O. Herrwerth, A. Senftleben, A.M. Sayler, T. Rathje, T. Pfeifer, I. Ben-Itzhak, R.R. Jones, G.G. Paulus, F. Krausz, R. Moshammer, J. Ullrich and M.F. Kling,

Attosecond tracing of correlated electron-emission in non-sequential double ionization, *Nature Communications* **3** (2012) 813.

[156] N. Camus, B. Fischer, M. Kremer, V. Sharma, A. Rudenko, B. Bergues, M. Kübel, N.G. Johnson, M.F. Kling, T. Pfeifer, J. Ullrich and R. Moshammer, *Attosecond correlated dynamics of two electrons passing through a transition state*, *Phys. Rev. Lett.* **108** (2012) 073003.

[157] R. Moshammer, J. Ullrich, B. Feuerstein, D. Fischer, A. Dorn, C.D. Schröter, J.R.C. López-Urrutia, C. Höhr, H. Rottke, C. Trump, M. Wittmann, G. Korn, K. Hoffmann and W. Sandner, *Strongly directed electron emission in non-sequential double ionization of ne by intense laser pulses*, *Journal of Physics B: Atomic, Molecular and Optical Physics* **36** (2003) L113.

[158] P. Ranitovic, X.-M. Tong, B. Gramkow, S. De, B. DePaola, K.P. Singh, W. Cao, M. Magrakvelidze, D. Ray, I. Bocharova, H. Mashiko, E. Gagnon, A. Sandhu, M.M. Murnane, H.C. Kapteyn, I. Litvinyuk and C.L. Cocke, *IR-assisted ionization of He by attosecond XUV radiation*, *Journal of Physics: Conference Series* **194** (2009) 032036.

[159] S. Gilbertson, M. Chini, X. Feng, S. Khan, Y. Wu and Z. Chang, *Monitoring and controlling the electron dynamics in helium with isolated attosecond pulses*, *Phys. Rev. Lett.* **105** (2010) 263003.

[160] E. Goulielmakis, Z.-H. Loh, A. Wirth, R. Santra, N. Rohringer, V.S. Yakovlev, S. Zherebtsov, T. Pfeifer, A.M. Azzeer, M.F. Kling, S.R. Leone and F. Krausz, *Real-time observation of valence electron motion*, *Nature* **466** (2010) 739.

[161] A. Kaldun, A. Blättermann, V. Stooß, S. Donsa, H. Wei, R. Pazourek, S. Nagele, C. Ott, C.D. Lin, J. Burgdörfer and T. Pfeifer, *Observing the ultrafast buildup of a Fano resonance in the time domain*, *Science* **354** (2016) 738.

[162] M. Lein, E.K.U. Gross and V. Engel, *Intense-field double ionization of helium: Identifying the mechanism*, *Phys. Rev. Lett.* **85** (2000) 4707.

[163] J. Guo, X.-S. Liu and S.-I. Chu, *Exploration of strong-field multiphoton double ionization, rescattering, and electron angular distribution of he atoms in intense long-wavelength laser fields: The coupled coherent-state approach*, *Phys. Rev. A* **82** (2010) 023402.

[164] D.K. Efimov, A. Maksymov, J.S. Prauzner-Bechcicki, J.H. Thiede, B. Eckhardt, A. Chacón, M. Lewenstein and J. Zakrzewski, *Restricted-space ab initio models for double ionization by strong laser pulses*, *Phys. Rev. A* **98** (2018) 013405.

[165] J. Madroñero and A. Buchleitner, *Ab initio quantum approach to planar helium under periodic driving*, *Phys. Rev. A* **77** (2008) 053402.

[166] S. Chen, C. Ruiz and A. Becker, *Double ionization of helium by intense near-infrared and VUV laser pulses*, *Phys. Rev. A* **82** (2010) 033426.

[167] J. Zhao and M. Lein, *Probing fano resonances with ultrashort pulses*, *New Journal of Physics* **14** (2012) 065003.

[168] L. Argenti and E. Lindroth, *Attosecond photoelectron spectroscopy of helium doubly excited states*, *Phys. Rev. Res.* **5** (2023) 033047.

[169] A. Palacios, D.A. Horner, T.N. Rescigno and C.W. McCurdy, *Two-photon double ionization of the helium atom by ultrashort pulses*, *Journal of Physics B: Atomic, Molecular and Optical Physics* **43** (2010) 194003.

[170] D.A. Horner, T.N. Rescigno and C.W. McCurdy, *Decoding sequential versus nonsequential two-photon double ionization of helium using nuclear recoil*, *Phys. Rev. A* **77** (2008) 030703.

[171] L.A.A. Nikolopoulos and P. Lambropoulos, *Multichannel theory of two-photon single and double ionization of helium*, *Journal of Physics B: Atomic, Molecular and Optical Physics* **34** (2001) 545.

[172] R. Grobe and J.H. Eberly, *Photoelectron spectra for a two-electron system in a strong laser field*, *Physical Review Letters* **68** (1992) 2905.

[173] R. Grobe and J.H. Eberly, *One-dimensional model of a negative ion and its interaction with laser fields*, *Physical Review A* **48** (1993) 4664.

[174] S.L. Haan, R. Grobe and J.H. Eberly, *Numerical study of autoionizing states in completely correlated two-electron systems*, *Phys. Rev. A* **50** (1994) 378.

[175] L. Roso, L. Plaja, P. Moreno, E.C. Jarque, J.R.V. de Aldana, J. San Roman and C. Ruiz, *Multielectron atomic models using the Rochester one-dimensional potential*, *Laser Physics* **15** (2005) 1393.

[176] A.D. Bandrauk and H. Shen, *Improved exponential split operator method for solving the time-dependent Schrödinger equation*, *Chemical Physics Letters* **176** (1991) 428.

[177] D. Bauer, *Two-dimensional, two-electron model atom in a laser pulse: Exact treatment, single-active-electron analysis, time-dependent density-functional theory, classical calculations, and nonsequential ionization*, *Physical Review A* **56** (1997) 3028.

[178] G. Lagmago Kamta and A.F. Starace, *Multielectron system in an ultrashort, intense laser field: A nonperturbative, time-dependent two-active-electron approach*, *Physical Review A* **65** (2002) 053418.

[179] S. Saugout, C. Cornaggia, A. Suzor-Weiner and E. Charron, *Ultrafast electronuclear dynamics of H_2 double ionization*, *Physical Review Letters* **98** (2007) 253003.

[180] G. Camiolo, G. Castiglia, P.P. Corso, E. Fiordilino and J.P. Marangos, *Two-electron systems in strong laser fields*, *Physical Review A - Atomic, Molecular, and Optical Physics* **79** (2009) 063401.

[181] M. Vafaee, F. Sami, B. Shokri, B. Buzari and H. Sabzyan, *Precise description of single and double ionization of hydrogen molecule in intense laser pulses.*, *The Journal of Chemical Physics* **137** (2012) 044112.

[182] J. Rapp and D. Bauer, *Effects of inner electrons on atomic strong-field-ionization dynamics*, *Phys. Rev. A* **89** (2014) 033401.

[183] V. Kapoor, *Autoionization in time-dependent density-functional theory*, *Phys. Rev. A* **93** (2016) 063408.

[184] H.R. Larsson and D.J. Tannor, *Control of concerted back-to-back double ionization dynamics in helium*, *The Journal of Chemical Physics* **155** (2021) 144105.

[185] R. Moshammer, B. Feuerstein, J.C. López-Urrutia, J. Deipenwisch, A. Dorn, D. Fischer, C. Höhr, P. Neumayer, C.D. Schröter, J. Ullrich, H. Rottke, C. Trump, M. Wittmann, G. Korn and W. Sandner, *Correlated two-electron dynamics in strong-field double ionization*, *Phys. Rev. A* **65** (2002) 035401.

[186] K. Henrichs, S. Eckart, A. Hartung, D. Trabert, K. Fehre, J. Rist, H. Sann, M. Pitzer, M. Richter, H. Kang, M.S. Schöffler, M. Kunitski, T. Jahnke and R. Dörner, *Multiphoton double ionization of helium at 394 nm: A fully differential experiment*, *Phys. Rev. A* **98** (2018) 043405.

[187] M. Feit, J. Fleck and A. Steiger, *Solution of the schrödinger equation by a spectral method*, *Journal of Computational Physics* **47** (1982) 412.

[188] G.D. Borisova, *Einfluss der Elektron-Elektron-Korrelation auf die Ionisation von Atomen in starken, ultrakurzen Laser-Impulsen*, Bachelor's thesis, Ruprecht-Karls-Universität Heidelberg, Deutschland, 2015.

[189] V. Schyja, T. Lang and H. Helm, *Channel switching in above-threshold ionization of xenon*, *Phys. Rev. A* **57** (1998) 3692.

[190] H. Zimmermann, S. Patchkovskii, M. Ivanov and U. Eichmann, *Unified time and frequency picture of ultrafast atomic excitation in strong laser fields*, *Phys. Rev. Lett.* **118** (2017) 013003.

[191] A. Kamor, F. Mauger, C. Chandre and T. Uzer, *How key periodic orbits drive recollisions in a circularly polarized laser field*, *Phys. Rev. Lett.* **110** (2013) 253002.

[192] R. Ivanov, J. Liu, G. Brenner, M. Brachmanski and S. Düsterer, *FLASH free-electron laser single-shot temporal diagnostic: terahertz-field-driven streaking*, *Journal of Synchrotron Radiation* **25** (2018) 26.

[193] R. Ivanov, I.J.B. Macias, J. Liu, G. Brenner, J. Roensch-Schulenburg, G. Kurdi, U. Frühling, K. Wenig, S. Walther, A. Dimitriou, M. Drescher, I.P. Sazhina, A.K. Kazansky, N.M. Kabachnik and S. Düsterer, *Single-shot temporal characterization of XUV pulses with duration from* $\sim 10\,\mathrm{fs}$ *to* $\sim 350\,\mathrm{fs}$ *at FLASH*, *Journal of Physics B: Atomic, Molecular and Optical Physics* **53** (2020) 184004.

[194] U. Frühling, *Light-field streaking for FELs*, *Journal of Physics B: Atomic, Molecular and Optical Physics* **44** (2011) 243001.

[195] A. Azima, J. Bödewadt, O. Becker, S. Düsterer, N. Ekanayake, R. Ivanov, M.M. Kazemi, L.L. Lazzarino, C. Lechner, T. Maltezopoulos, B. Manschwetus, V. Miltchev, J. Müller, T. Plath, A. Przystawik, M. Wieland, R. Assmann, I. Hartl, T. Laarmann, J. Rossbach, W. Wurth and M. Drescher, *Direct measurement of the pulse duration and frequency chirp of seeded XUV free electron laser pulses*, *New Journal of Physics* **20** (2018) 013010.

[196] A. Senftleben, *Kinematically complete study on electron impact ionisation of aligned hydrogen molecules*, Dissertation, Ruperto-Carola-University of Heidelberg, Germany, 2009.

[197] J. Adamczewski-Musch *et al.*, "The go4 project."

[198] R. Brun and F. Rademakers, *Root — an object oriented data analysis framework*, *Nuclear Instruments and Methods in Physics Research Section A: Accelerators, Spectrometers, Detectors and Associated Equipment* **389** (1997) 81.

[199] F. Trost, *Time-resolved Fragmentation of Diiodomethane studied in an XUV Pump-Probe Experiment*, Dissertation, Ruperto-Carola-University of Heidelberg, Germany, 2023.

[200] M. Mariscotti, *A method for automatic identification of peaks in the presence of background and its application to spectrum analysis*, *Nuclear Instruments and Methods* **50** (1967) 309.

[201] W.R. Leo, *Techniques for nuclear and particle physics experiments. a how-to approach*, Springer, Berlin (1987).

[202] M. Kurka, *Zwei- und Drei-Photonen Doppelionisation von Helium und Neon am Freie-Elektronen-Laser in Hamburg*, Diploma thesis, Ruperto-Carola-University of Heidelberg, Germany, 2007.

[203] L. Foucar, *Auslese von Delaylinedetektoren mit Hilfe von Transientenrekordern*, Dissertation, Johann Wolfgang Goethe-Universität Frankfurt, Germany, 2008.

[204] D. Gedcke and W. McDonald, *A constant fraction of pulse height trigger for optimum time resolution*, *Nuclear Instruments and Methods* **55** (1967) 377.

[205] J.A.R. Samson, Z.X. He, L. Yin and G.N. Haddad, *Precision measurements of the absolute photoionization cross sections of He*, *Journal of Physics B: Atomic, Molecular and Optical Physics* **27** (1994) 887.

[206] S. Meister, A. Bondy, K. Schnorr, S. Augustin, H. Lindenblatt, F. Trost, X. Xie, M. Braune, B. Manschwetus, N. Schirmel, H. Redlin, N. Douguet, T. Pfeifer, K. Bartschat and R. Moshammer, *Linear dichroism in few-photon ionization of laser-dressed helium*, *The European Physical Journal D* **75** (2021) 205.

[207] S. Meister, A. Bondy, K. Schnorr, S. Augustin, H. Lindenblatt, F. Trost, X. Xie, M. Braune, R. Treusch, B. Manschwetus, N. Schirmel, H. Redlin, N. Douguet, T. Pfeifer, K. Bartschat and R. Moshammer, *Photoelectron spectroscopy of laser-dressed atomic helium*, *Phys. Rev. A* **102** (2020) 062809.

[208] G.G. Paulus, W. Becker, W. Nicklich and H. Walther, *Rescattering effects in above-threshold ionization: a classical model*, *Journal of Physics B: Atomic, Molecular and Optical Physics* **27** (1994) L703.

[209] M.-H. Yuan and X.-B. Bian, *Angular distribution of photoelectron momentum in above-threshold ionization by circularly polarized laser pulses*, *Phys. Rev. A* **101** (2020) 013412.

[210] M.-M. Liu, Y. Shao, M. Han, P. Ge, Y. Deng, C. Wu, Q. Gong and Y. Liu, *Energy- and Momentum-Resolved Photoelectron Spin Polarization in Multiphoton Ionization of Xe by Circularly Polarized Fields*, *Phys. Rev. Lett.* **120** (2018) 043201.

[211] L. Arissian, C. Smeenk, F. Turner, C. Trallero, A.V. Sokolov, D.M. Villeneuve, A. Staudte and P.B. Corkum, *Direct test of laser tunneling with electron momentum imaging*, *Phys. Rev. Lett.* **105** (2010) 133002.

[212] P.M. Paul, E.S. Toma, P. Breger, G. Mullot, F. Augé, P. Balcou, H.G. Muller and P. Agostini, *Observation of a train of attosecond pulses from high harmonic generation*, *Science* **292** (2001) 1689.

[213] L. Cattaneo, L. Pedrelli, R.Y. Bello, A. Palacios, P.D. Keathley, F. Martín and U. Keller, *Isolating attosecond electron dynamics in molecules where nuclei move fast*, *Phys. Rev. Lett.* **128** (2022) 063001.

[214] D. Busto, L. Barreau, M. Isinger, M. Turconi, C. Alexandridi, A. Harth, S. Zhong, R.J. Squibb, D. Kroon, S. Plogmaker, M. Miranda, A. Jiménez-Galán, L. Argenti, C.L. Arnold, R. Feifel, F. Martín, M. Gisselbrecht, A. L'Huillier and P. Salières, *Time–frequency representation of autoionization dynamics in helium*, *Journal of Physics B: Atomic, Molecular and Optical Physics* **51** (2018) 044002.

[215] S. Haessler, B. Fabre, J. Higuet, J. Caillat, T. Ruchon, P. Breger, B. Carré, E. Constant, A. Maquet, E. Mével, P. Salières, R. Taïeb and Y. Mairesse, *Phase-resolved attosecond near-threshold photoionization of molecular nitrogen*, *Phys. Rev. A* **80** (2009) 011404.

[216] M. Pont and R. Shakeshaft, *Absolute cross sections for double photoionization of helium at energies from 0 to 80 eV above threshold*, *Journal of Physics B: Atomic, Molecular and Optical Physics* **28** (1995) L571.

[217] R. Shakeshaft, *Two-photon single and double ionization of helium*, *Phys. Rev. A* **76** (2007) 063405.

[218] L. Feng and H.W. van der Hart, *Two-photon double ionization of he*, *Journal of Physics B: Atomic, Molecular and Optical Physics* **36** (2002) L1.

[219] S.X. Hu, J. Colgan and L.A. Collins, *Triple-differential cross-sections for two-photon double ionization of he near threshold*, *Journal of Physics B: Atomic, Molecular and Optical Physics* **38** (2004) L35.

[220] A. Simonsen, S. Askeland and M. Førre, *Two-photon double ionization of helium: investigating the importance of correlation in the final state*, *Open Physics* **11** (2013) 1099.

[221] H. Hasegawa, E.J. Takahashi, Y. Nabekawa, K.L. Ishikawa and K. Midorikawa, *Multiphoton ionization of* He *by using intense high-order harmonics in the soft-x-ray region*, *Phys. Rev. A* **71** (2005) 023407.

[222] A. Rudenko, L. Foucar, M. Kurka, T. Ergler, K.U. Kühnel, Y.H. Jiang, A. Voitkiv, B. Najjari, A. Kheifets, S. Lüdemann, T. Havermeier, M. Smolarski, S. Schössler, K. Cole, M. Schöffler, R. Dörner, S. Düsterer, W. Li, B. Keitel, R. Treusch, M. Gensch, C.D. Schröter, R. Moshammer and J. Ullrich, *Recoil-Ion Momentum Distributions for Two-Photon Double Ionization of He and Ne by 44 eV Free-Electron Laser Radiation*, *Phys. Rev. Lett.* **101** (2008) 073003.

[223] M. Kurka, J. Feist, D.A. Horner, A. Rudenko, Y.H. Jiang, K.U. Kühnel, L. Foucar, T.N. Rescigno, C.W. McCurdy, R. Pazourek, S. Nagele, M. Schulz, O. Herrwerth, M. Lezius, M.F. Kling, M. Schöffler, A. Belkacem, S. Düsterer, R. Treusch, B.I. Schneider, L.A. Collins, J. Burgdörfer, C.D. Schröter, R. Moshammer and J. Ullrich, *Differential cross sections for non-sequential double ionization of He by 52 eV photons from the free electron laser in hamburg, flash*, *New Journal of Physics* **12** (2010) 073035.

[224] P. Antoine, E. Foumouo, B. Piraux, T. Shimizu, H. Hasegawa, Y. Nabekawa and K. Midorikawa, *Two-photon double ionization of helium: An experimental lower bound of the total cross section*, *Phys. Rev. A* **78** (2008) 023415.

[225] H. Shimada, K. Komatsu, W. Komatsubara, T. Mizuno, S. Miyake, S. Minemoto, H. Sakai, T. Majima, S. Owada, T. Togashi, M. Yabashi and A. Yagishita, *Two- and three-photon double ionization of helium by soft x-ray free-electron laser pulses*, *Journal of Physics B: Atomic, Molecular and Optical Physics* **52** (2019) 065602.

[226] M. Straub, *Multiphoton Ionization of Helium with Extreme Ultraviolet Light at the Free-Electron Laser in Hamburg*, Master's thesis, Ruperto-Carola-University of Heidelberg, Germany, 2021.

[227] D.N. Fittinghoff, P.R. Bolton, B. Chang and K.C. Kulander, *Observation of nonsequential double ionization of helium with optical tunneling*, *Phys. Rev. Lett.* **69** (1992) 2642.

[228] S. Donsa, M. Ederer, R. Pazourek, J. Burgdörfer and I. Březinová, *Angle-resolved time delays for shake-up ionization of helium*, *Phys. Rev. A* **102** (2020) 033112.

[229] S. Mehmood, E. Lindroth and L. Argenti, *Coherence control in helium-ion ensembles*, *Phys. Rev. Res.* **3** (2021) 023233.

[230] M. Domke, R.M. Bowman and A.H. Zewail, *Femtosecond laser observations of molecular vibration and rotation*, *Nature* **343** (1990) 737.

[231] M. Nisoli, P. Decleva, F. Calegari, A. Palacios and F. Martín, *Attosecond electron dynamics in molecules*, *Chemical Reviews* **117** (2017) 10760.

[232] N. Saito, H. Sannohe, N. Ishii, T. Kanai, N. Kosugi, Y. Wu, A. Chew, S. Han, Z. Chang and J. Itatani, *Real-time observation of electronic, vibrational, and rotational dynamics in nitric oxide with attosecond soft x-ray pulses at 400 eV*, *Optica* **6** (2019) 1542.

[233] P.P. Sorokin, J.R. Lankard, E.C. Hammond and V.L. Moruzzi, *Laser-pumped stimulated emission from organic dyes: Experimental studies and analytical comparisons*, *IBM Journal of Research and Development* **11** (1967) 130.

[234] M.J. Rosker, M. Dantus and A.H. Zewail, *Femtosecond clocking of the chemical bond*, *Science* **241** (1988) 1200.

[235] M.F. Kling and M.J. Vrakking, *Attosecond electron dynamics*, *Annual Review of Physical Chemistry* **59** (2008) 463.

[236] F. Kelkensberg, C. Lefebvre, W. Siu, O. Ghafur, T.T. Nguyen-Dang, O. Atabek, A. Keller, V. Serov, P. Johnsson, M. Swoboda, T. Remetter, A. L'Huillier, S. Zherebtsov, G. Sansone, E. Benedetti, F. Ferrari, M. Nisoli, F. Lépine, M.F. Kling and M.J.J. Vrakking, *Molecular dissociative ionization and wave-packet dynamics studied using two-color XUV and IR pump-probe spectroscopy*, *Phys. Rev. Lett.* **103** (2009) 123005.

[237] T. Ergler, A. Rudenko, B. Feuerstein, K. Zrost, C.D. Schröter, R. Moshammer and J. Ullrich, *Spatiotemporal imaging of ultrafast molecular motion: Collapse and revival of the D_2 nuclear wave packet*, *Phys. Rev. Lett.* **97** (2006) 193001.

[238] B. Feuerstein, T. Ergler, A. Rudenko, K. Zrost, C.D. Schröter, R. Moshammer, J. Ullrich, T. Niederhausen and U. Thumm, *Complete characterization of molecular dynamics in ultrashort laser fields*, *Phys. Rev. Lett.* **99** (2007) 153002.

[239] Y. Furukawa, Y. Nabekawa, T. Okino, S. Saugout, K. Yamanouchi and K. Midorikawa, *Nonlinear fourier-transform spectroscopy of D_2 using high-order harmonic radiation*, *Phys. Rev. A* **82** (2010) 013421.

[240] F. Kelkensberg, W. Siu, J.F. Pérez-Torres, F. Morales, G. Gademann, A. Rouzée, P. Johnsson, M. Lucchini, F. Calegari, J.L. Sanz-Vicario, F. Martín and M.J.J. Vrakking, *Attosecond control in photoionization of hydrogen molecules*, *Phys. Rev. Lett.* **107** (2011) 043002.

[241] K.P. Singh, F. He, P. Ranitovic, W. Cao, S. De, D. Ray, S. Chen, U. Thumm, A. Becker, M.M. Murnane, H.C. Kapteyn, I.V. Litvinyuk and C.L. Cocke, *Control of electron localization in deuterium molecular ions using an attosecond pulse train and a many-cycle infrared pulse*, *Phys. Rev. Lett.* **104** (2010) 023001.

[242] G. Sansone, F. Kelkensberg, J.F. Pérez-Torres, F. Morales, M.F. Kling, W. Siu, O. Ghafur, P. Johnsson, M. Swoboda, E. Benedetti, F. Ferrari, F. Lépine, J.L. Sanz-Vicario, S. Zherebtsov, I. Znakovskaya, A. L'Huillier, M.Y. Ivanov, M. Nisoli, F. Martín and M.J.J. Vrakking, *Electron localization following attosecond molecular photoionization*, *Nature* **465** (2010) 763.

[243] A. Fischer, A. Sperl, P. Cörlin, M. Schönwald, H. Rietz, A. Palacios, A. González-Castrillo, F. Martín, T. Pfeifer, J. Ullrich, A. Senftleben and R. Moshammer, *Electron localization involving doubly excited states in broadband extreme ultraviolet ionization of H_2*, *Phys. Rev. Lett.* **110** (2013) 213002.

[244] T. Baumert, M. Grosser, R. Thalweiser and G. Gerber, *Femtosecond time-resolved molecular multiphoton ionization: The Na_2 system*, *Phys. Rev. Lett.* **67** (1991) 3753.

[245] M.J.J. Vrakking, D.M. Villeneuve and A. Stolow, *Observation of fractional revivals of a molecular wave packet*, *Phys. Rev. A* **54** (1996) R37.

[246] S. De, M. Magrakvelidze, I.A. Bocharova, D. Ray, W. Cao, I. Znakovskaya, H. Li, Z. Wang, G. Laurent, U. Thumm, M.F. Kling, I.V. Litvinyuk, I. Ben-Itzhak and C.L. Cocke, *Following dynamic nuclear wave packets in N_2,O_2, and CO with few-cycle infrared pulses*, *Phys. Rev. A* **84** (2011) 043410.

[247] T. Okino, Y. Furukawa, Y. Nabekawa, S. Miyabe, A.A. Eilanlou, E.J. Takahashi, K. Yamanouchi and K. Midorikawa, *Direct observation of an attosecond electron wave packet in a nitrogen molecule*, *Science Advances* **1** (2015) e1500356.

[248] M. Magrakvelidze, O. Herrwerth, Y.H. Jiang, A. Rudenko, M. Kurka, L. Foucar, K.U. Kühnel, M. Kübel, N.G. Johnson, C.D. Schröter, S. Düsterer, R. Treusch, M. Lezius, I. Ben-Itzhak, R. Moshammer, J. Ullrich, M.F. Kling and U. Thumm, *Tracing nuclear-wave-packet dynamics in singly and doubly charged states of N_2 and O_2 with XUV-pump–XUV-probe experiments*, *Phys. Rev. A* **86** (2012) 013415.

[249] M. Dantus, M. Janssen and A. Zewail, *Femtosecond probing of molecular dynamics by mass-spectrometry in a molecular beam*, *Chemical Physics Letters* **181** (1991) 281.

[250] Y. Cheng, M. Chini, X. Wang, A. González-Castrillo, A. Palacios, L. Argenti, F. Martín and Z. Chang, *Reconstruction of an excited-state molecular wave packet with attosecond transient absorption spectroscopy*, *Phys. Rev. A* **94** (2016) 023403.

[251] W. Cao, E.R. Warrick, A. Fidler, S.R. Leone and D.M. Neumark, *Excited-state vibronic wave-packet dynamics in H_2 probed by xuv transient four-wave mixing*, *Phys. Rev. A* **97** (2018) 023401.

[252] H. Niikura, P.B. Corkum and D.M. Villeneuve, *Controlling vibrational wave packet motion with intense modulated laser fields*, *Phys. Rev. Lett.* **90** (2003) 203601.

[253] D. Brinks, F.D. Stefani, F. Kulzer, R. Hildner, T.H. Taminiau, Y. Avlasevich, K. Müllen and N.F. van Hulst, *Visualizing and controlling vibrational wave packets of single molecules*, *Nature* **465** (2010) 905.

[254] W.A. Bryan, C.R. Calvert, R.B. King, G.R.A.J. Nemeth, J.D. Alexander, J.B. Greenwood, C.A. Froud, I.C.E. Turcu, E. Springate, W.R. Newell and I.D. Williams, *Redistribution of vibrational population in a molecular ion with nonresonant strong-field laser pulses*, *Phys. Rev. A* **83** (2011) 021406.

[255] E.R. Warrick, A.P. Fidler, W. Cao, E. Bloch, D.M. Neumark and S.R. Leone, *Multiple pulse coherent dynamics and wave packet control of the N_2 $a''\,^1\Sigma_g^+$ dark state by attosecond four-wave mixing*, *Faraday Discuss.* **212** (2018) 157.

[256] V. Stooß, S.M. Cavaletto, S. Donsa, A. Blättermann, P. Birk, C.H. Keitel, I. Březinová, J. Burgdörfer, C. Ott and T. Pfeifer, *Real-time reconstruction of the strong-field-driven dipole response*, *Phys. Rev. Lett.* **121** (2018) 173005.

[257] E.U. Condon, *Nuclear motions associated with electron transitions in diatomic molecules*, *Phys. Rev.* **32** (1928) 858.

[258] H. Haken and H.C. Wolf, *Molekülphysik und Quantenchemie: Einführung in die experimentellen und theoretischen Grundlagen*, Springer Berlin (2006).

[259] W. Demtröder, *Atoms, Molecules and Photons: An Introduction to Atomic-, Molecular- and Quantum Physics*, Springer Heidelberg (2010).

[260] R. Bluhm, V. Alan Kostelecký and B. Tudose, *Wave-packet revivals for quantum systems with nondegenerate energies*, *Physics Letters A* **222** (1996) 220.

[261] R. Robinett, *Quantum wave packet revivals*, *Physics Reports* **392** (2004) 1.

[262] N. Bohr, *Über die Anwendung der Quantentheorie auf den Atombau*, *Zeitschrift für Physik* **13** (1923) 117.

[263] P.M. Morse, *Diatomic molecules according to the wave mechanics. II. vibrational levels*, *Phys. Rev.* **34** (1929) 57.

[264] D. Fan, *A few-level simulation of the time-dependent dynamics of singly excited resonances of molecular hydrogen under the influence of moderately strong, ultrashort laser pulses*, Bachelor's thesis, Ruperto-Carola-University of Heidelberg, Germany, 2022.

[265] P. Barber Belda, *Strong-field effects on singly excited vibronic resonances in the hydrogen molecule*, Master's thesis, Ruperto-Carola-University of Heidelberg, Germany, 2022.

[266] L. Wolniewicz and K. Dressler, *The $B\,^1\Sigma_u^+$, $B'\,^1\Sigma_u^+$, $C\,^1\Pi_u$, and $D\,^1\Pi_u$ states of the H_2 molecule. Matrix elements of angular and radial nonadiabatic coupling and improved abâ€^initio potential energy curves*, *The Journal of Chemical Physics* **88** (1988) 3861.

[267] H. Nakashima and H. Nakatsuji, *Solving the Schrödinger equation of hydrogen molecule with the free complement-local Schrödinger equation method: Potential energy curves of the ground and singly excited singlet and triplet states, Σ, Π, Δ, and Φ*, *Journal of Chemical Physics* **149** (2018) 244116.

[268] L. Wolniewicz and G. Staszewska, $^1\Sigma_u^+ \rightarrow X\,^1\Sigma_g^+$ *transition moments for the hydrogen molecule*, *Journal of Molecular Spectroscopy* **217** (2003) 181.

[269] L. Wolniewicz and G. Staszewska, *Excited* $^1\Pi_u$ *states and the* $^1\Pi_u \rightarrow X\,^1\Sigma_g^+$ *transition moments of the hydrogen molecule*, *Journal of Molecular Spectroscopy* **220** (2003) 45.

[270] M. Glass-Maujean, P. Quadrelli, K. Dressler and L. Wolniewicz, *Transition probabilities for spontaneous emission in the adiabatic and nonadiabatic approximations for all bound vibrational levels of the* $E,F\,^1\Sigma_g^+$, $G,K\,^1\Sigma_g^+$, *and* $H,\overline{H}\,^1\Sigma_g^+$ *states of* H_2, *Phys. Rev. A* **28** (1983) 2868.

[271] M. Glass-Maujean, *Transition probabilities for the D and B′ vibrational levels to the X vibrational levels and continuum of* H_2, *Atomic Data and Nuclear Data Tables* **30** (1984) 301.

[272] M. Glass-Maujean, P. Quadrelli and K. Dressler, *Band transition moments between excited singlet states of the* H_2 *molecule, nonadiabatic eigenvectors, and probabilities for spontaneous emission*, *Atomic Data and Nuclear Data Tables* **30** (1984) 273.

[273] W. Chan, G. Cooper and C. Brion, *Absolute optical oscillator strengths (11–20 eV) and transition moments for the photoabsorption of molecular hydrogen in the Lyman and Werner bands*, *Chemical Physics* **168** (1992) 375.

[274] K. Hirai, E.J. Heller and P. Gaspard, *Spectroscopy and intramolecular dynamics via molecular vibrogram analysis*, *The Journal of Chemical Physics* **103** (1995) 5970.

[275] E.J. Heller, *Photofragmentation of symmetric triatomic molecules: Time dependent picture*, *The Journal of Chemical Physics* **68** (2008) 3891.

[276] R. Gauvin, *Review of transmission electron microscopy for the characterization of materials*, in *Materials Characterization and Optical Probe Techniques: A Critical Review*, R.A. Lessard and H. Franke, eds., vol. 10291, p. 102910C, International Society for Optics and Photonics, SPIE, 1997, DOI.

[277] D.B. Williams and C.B. Carter, *Transmission Electron Microscopy*, Springer (2009).

[278] M. Huppert, I. Jordan and H.J. Wörner, *Attosecond beamline with actively stabilized and spatially separated beam paths*, *Review of Scientific Instruments* **86** (2015) 123106.

[279] A. Kramida, Yu. Ralchenko, J. Reader and NIST ASD Team. NIST Atomic Spectra Database (ver. 5.10), `https://physics.nist.gov/asd`. National Institute of Standards and Technology, Gaithersburg, MD., 2022.

[280] W.C. Wallace, O. Ghafur, C. Khurmi, S. Sainadh U, J.E. Calvert, D.E. Laban, M.G. Pullen, K. Bartschat, A.N. Grum-Grzhimailo, D. Wells, H.M. Quiney, X.M. Tong, I.V. Litvinyuk, R.T. Sang and D. Kielpinski, *Precise and accurate measurements of strong-field photoionization and a transferable laser intensity calibration standard*, *Phys. Rev. Lett.* **117** (2016) 053001.

[281] C. Ott, A. Kaldun, P. Raith, K. Meyer, M. Laux, J. Evers, C.H. Keitel, C.H. Greene and T. Pfeifer, *Lorentz meets fano in spectral line shapes: A universal phase and its laser control*, *Science* **340** (2013) 716.

[282] A. Kaldun, C. Ott, A. Blättermann, M. Laux, K. Meyer, T. Ding, A. Fischer and T. Pfeifer, *Extracting phase and amplitude modifications of laser-coupled fano resonances*, *Phys. Rev. Lett.* **112** (2014) 103001.

[283] Y. Cheng, M. Chini, X. Wang, A. González-Castrillo, A. Palacios, L. Argenti, F. Martín and Z. Chang, *Reconstruction of an excited-state molecular wave packet with attosecond transient absorption spectroscopy*, *Phys. Rev. A* **94** (2016) 023403.

[284] P. Peng, Y. Mi, M. Lytova, M. Britton, X. Ding, A.Y. Naumov, P.B. Corkum and D.M. Villeneuve, *Coherent control of ultrafast extreme ultraviolet transient absorption*, *Nature Photonics* **16** (2022) 45.

[285] J. Mitroy, M.S. Safronova and C.W. Clark, *Theory and applications of atomic and ionic polarizabilities*, *Journal of Physics B: Atomic, Molecular and Optical Physics* **43** (2010) 202001.

[286] W.C. Marlow, *Mean polarizability of excited molecular hydrogen*, *Proceedings of the Physical Society* **86** (1965) 731.

[287] D. Sun, Y.P. Zhang, X.J. Wei, L.M. Wang and Z.-C. Yan, *Polarizabilities of hydrogen molecules calculated without using the born-oppenheimer approximation*, *Phys. Rev. A* **103** (2021) 062813.

ACKNOWLEDGMENTS

Scientific research is like puzzling - putting small pieces together one after each other. In an infinitely big puzzle, there is no clear ending of the puzzle process, thus one has to take a step back at some point and look into the established picture so far. In this sense, this thesis is a momentary picture of the never-ending puzzling called research and I would like to thank to everybody that has puzzled with me or helped me in any sense along the way:

Thomas Pfeifer, who shines contagious curiosity and is always enthusiastically involved in any discussion arising from just a short question. I have learned a lot from you, not only about Physics!

Christian Ott for his great art of understanding and encouragement in any situation and for the sense of scientific trust I have experienced in your group!

Selim Jochim, whose interest in fundamental light–matter interactions prevailed over his busy schedule and agreed to become the second referee of this thesis.

Maurits Haverkort and **Jörg Evers**, who friendly joined my exam committee.

Robert Moshammer, who found time for my questions whenever I had them.

José Crespo for the occasional "How is it going?" and caring for an answer.

The **InterAtto** ant **X-Music** teams, present and past, for the help in the lab and the open ear for questions of any kind. **Veit Stooß**, **Paul Birk**, **Maximilian Hartmann**, **Shuyuan Hu**, **Yu He**, I learned a lot from and with you and enjoyed the time spend together in the lab. Thank you for the enjoyable time in the group also to **Thomas Ding**, **Marc Rebholz**, **Lennart Aufleger**, **Patrick Rupprecht**, **Alexander Magunia**, **Carina da Costa Castanheira**, **Maximilian Richter**, **Carlo Kleine**, **Lina Hedewig**, **Harijyoti Mandal**, **Arikta Saha**.

The **FLASH-REMI** team for the help to find my way in the world of photoion and photoelectron spectroscopy, in particular **Hannes Lindenblatt** for joining forces with me whenever go4 didn't cooperate, and **Florian Trost** for the discussions on data evaluation.

The students, who trusted me in supervising them: **Daniel Fan** and **Paula Barber Belda**, and those I could help in addition co-supervising: **Tobias Heldt**, **Sabine Rockenstein**, **Michael Straub**. The discussions with all of you contributed immensely to my own understanding of Physics.

Nikola Mollov for teaching me all I know about the laser system and the continuous support even after he left the institute. Благодаря!

The **FLASH-Team**: Harald Redlin, Nora Schirmel, Rolf Treusch, Markus Braune, who contributed for the successful beamtime.

Everybody who proofread some parts of this thesis, some of your comments were very insightful for me.

Carlos für die *gute Laune*, **Patrick** für das tägliche "Du schaffst das!", Деничка за утехата в трудни времена и за търпението с мен, Дърдораните - Дени, Лени, Петя, Дони и Деничка - за приятелството и подкрепата особено през последните три трудни години, Грациите - Яна, Тони и Хрис - за дългогодишното приятелство независимо от делящото ни разстояние, както и Стефан Гандев и Леля Маргарита за опората при нужда.

Andreas for bringing back a smile to my face and making me trust myself again.

Моето семейство - майка ми Цветанка и сестра ми Мария, които са до мен от далече. Най-много благодаря на мама, която винаги е вярвала, че ще завърша, каквото съм започнала и се надявам, че и баща ми Димитър щеше да се гордее с мен. Благодаря много и на Дани, както и на любопитното ми племенниче Мишо.

And all those, who have shared some of their time with me, no matter long or short.

Vielen Dank, Thank you and Благодаря!